

Copyright © 1991, by the author(s).  
All rights reserved.

Permission to make digital or hard copies of all or part of this work for personal or classroom use is granted without fee provided that copies are not made or distributed for profit or commercial advantage and that copies bear this notice and the full citation on the first page. To copy otherwise, to republish, to post on servers or to redistribute to lists, requires prior specific permission.

**RESIST MECHANISMS AND MODELS  
IN ELECTRON-BEAM LITHOGRAPHY**

by

Nelson Ngai-Sang Tam

Memorandum No. UCB/ERL M91/102

19 November 1991

UCB/ERL M91/102

**RESIST MECHANISMS AND MODELS  
IN ELECTRON-BEAM LITHOGRAPHY**

by

Nelson Ngai-Sang Tam

Memorandum No. UCB/ERL M91/102

19 November 1991

**ELECTRONICS RESEARCH LABORATORY**

College of Engineering  
University of California, Berkeley  
94720

TITLE PAGE

# RESIST MECHANISMS AND MODELS IN ELECTRON-BEAM LITHOGRAPHY

by

Nelson N. Tam

## ABSTRACT

An in-depth examination of chemical and physical mechanisms in resist materials has been made to support the applications of electron-beam (e-beam) lithography with high beam current exposure systems and advanced resist systems. Novel resist models and extensions to the lithography simulator *SAMPLE* have been developed to provide a CAD capability for inexpensive and rapid evaluation of new e-beam lithographic processes.

Due to the small thermal conductivity of resists, e-beam induced heating of resists during exposure can be quite significant. Resist deformation and irregular dissolution behaviors have been observed in the RD-2000N resist when the beam current density exceeds  $25 \text{ A/cm}^2$ . A massively parallel computer program using an explicit Euler algorithm has been developed to simulate the temperature rise in the resist during exposure as a function of pattern, tool and resist parameters.

A novel approach of using empirically-modeled parameters in the mechanism-based rate model is introduced to include additional process variables. An application to developer concentration and post-exposure bake (PEB) makes possible profile simulation for the optimization of these processing steps in chemically-amplified resists.

A practical model based on a linear approximation of the “cage effect” is developed for the acid-hardening crosslinking resists. This model is derived from measurements of the extent of the reaction obtained with FTIR. The new model accurately characterizes both optically and e-beam exposed SNR-248 resists and a comparison of the kinetic parameters shows effects attributed to initial crosslinking with e-beam. The correlation between dissolution rate and the extent of reaction is a single valued function which, when combined with the “cage effect” bake model, can be used to determine the resist behaviors during exposure, PEB, and development.

Processing strategies and a quantitative model for resist profile improvement through interrupted development of an IBM DQN resist are investigated. It is found that rinsing is the critical step in improving resist performance. Dissolution measurements show that no resist loss occurs during rinsing and that the latent induction period upon redevelopment of up to 40 seconds is an exponential function of exposure dose. Implementation of this time-delay model in *SAMPLE* allows the simulation of interrupted development with any interrupted schedules and differentiation of developer-related induction effects and spin-cast-layer-related surface rate retardation effects in other resist systems.



Professor Andrew R. Neureuther  
Committee Chairman

**Resist Mechanisms and Models  
in Electron-Beam Lithography**

**Copyright © 1991**

**by**

**Nelson N. Tam**

# Table of Contents

Table of Contents .....	ii
Acknowledgements.....	vii
Chapter 1: Introduction.....	1
Chapter 2: General Modeling Techniques .....	9
2.1: Historical Perspective .....	9
2.1.1: Exposure Modeling .....	11
2.1.2: Characterization and Modeling of Resist Dissolution .....	12
2.1.2.1: In-situ Monitoring of Resist Development.....	13
2.1.2.2: Resist Dissolution Rate Model .....	14
2.1.3: Dissolution Simulation.....	16
2.2: Advances in Resist and Processing Technology.....	17
2.2.1: Hitachi RD-2000N Negative Crosslinking Resist .....	18
2.2.2: Shipley ECX-1033 Negative Chemically-Amplified Resist.....	19
2.2.3: Interrupted Development of DQN Resist.....	20
2.2.4: Heating Effects.....	24
2.3: Resist Modeling Extensions in this Thesis .....	24
Chapter 3: Applications and Limitations of Energy Deposition Rate Models .....	33
3.1: Introduction.....	33
3.2: Exposure Simulation.....	35
3.3: Dissolution Characterization and Modeling .....	39
3.3.1: Dissolution Rate Measurements of Negative e-beam Resists....	39
3.3.2: Parameter Extraction .....	40
3.3.3: Profile Simulation and Experimental Comparison .....	42
3.3.4: Interrupt Effect in the Development of a DNQ Resist.....	47
3.3.4.1: Rate Dependence on Deposited Energy and Interrupt .....	49

3.3.4.2: Modeling the Rate Data of Interrupted Development ..	50
3.3.4.3: Comparison of Experiment and Simulation .....	52
3.3.5: Summary .....	54
Chapter 4: Thermal Effects of Electron-Beam Exposure .....	56
4.1: Introduction.....	56
4.2: Thermal Effects on the Hitachi RD-2000N Resist .....	58
4.2.1: Beam Current Effects.....	58
4.2.2: Oxide Thickness.....	60
4.2.3: Resist Thickness .....	61
4.3: Temperature Rise Simulation .....	63
4.4: Simulation Results .....	66
4.4.1: Beam Current Density, Resist Thickness, and Flash Size .....	66
4.4.2: Pixel Placement.....	68
4.5: Conclusion .....	70
Chapter 5: Empirical Extensions to Dissolution Rate Model for Chemically-Amplified Resists .....	75
5.1: Empirical Extension of Mechanism-based Resist Model.....	75
5.2: Factorial Experiment Design .....	78
5.3: Factorial Experiment .....	79
5.3.1: Resist Preparation .....	79
5.3.2: Levels of the Factors .....	80
5.4: Dissolution Rate Data .....	80
5.5: First Experimental Stage and Linear Effects .....	82
5.5.1: Effect Calculation for $E_0$ .....	83
5.5.2: Effect Calculation for $R_0$ .....	83
5.6: Second Experimental Stage and Quadratic Effects .....	85
5.6.1: Effect between First and Second Experimental Stage .....	85

5.7: Quadratic Models for $\sqrt{R_0}$ and $E_0$ .....	87
5.8: Analysis of the Residuals.....	88
5.9: Analysis of Variance .....	90
5.10: Estimation of Confidence Interval for the Main Model.....	91
5.10.1: Variance of fitted $\sqrt{R_0}$ and $E_0$ .....	91
5.11: Comparison of Simulated and Experimental Resist Profiles .....	93
5.11.1: Samples within the Parameter Space .....	94
5.11.2: Samples outside the Parameter Space.....	95
5.12: Process Optimization .....	97
5.13: Summary .....	101
 Chapter 6: Mechanism and Model of the Crosslinking Reaction in Acid-Hardening Chemically-amplified Resists.....	 105
6.1: Introduction.....	105
6.2: Acid-Catalyzed Crosslinking Reaction.....	108
6.2.1: Melamine-hydroxyl Crosslinking Reaction Mechanism .....	108
6.2.2: “Cage Effect” Model by Seligson et al. ....	110
6.2.3: Acid Loss Mechanism by Ferguson et al. ....	112
6.3: Novel Model of the “Cage Effect” .....	117
6.4: Comparison of Deep-UV and e-Beam Exposed SNR-248.....	128
6.4.1: Post-Exposure Bake Effects .....	129
6.5: Dissolution Rate as a Function of Extent of Crosslinking Reaction ..	137
6.6: Summary.....	139
6.7: Appendix.....	141
6.7.1: Fourier Transformed Infrared Spectrometry.....	141
6.7.2: Experimental .....	141
6.7.3: Extracting Data from FTIR Spectra .....	143
 Chapter 7: Effects of Interrupted Development on Resist Profiles.....	 146

7.1: Introduction.....	146
7.2: Experimental.....	147
7.2.1: Exposure.....	147
7.2.2: Interrupted Development without the Drying Step.....	148
7.2.2.1: Interrupted Spray Development .....	148
7.2.2.2: Original Interrupted Development without Drying (OIDWOD).....	150
7.2.3: Interrupted Development with Drying .....	151
7.2.3.1: Interrupted Spray Development with Drying (ISDWD) .....	152
7.2.3.2: Interrupted Development with Wetted Resist (RIDWDW) .....	153
7.3: Comparison of Techniques .....	154
7.4: Summary.....	155
Chapter 8: Time-Delay Model of Interrupted Development .....	157
8.1: Introduction.....	157
8.2: Dissolution Characteristics after Interruption Treatment .....	158
8.3: Input for Interrupted Development Simulation .....	163
8.4: Dissolution Rate in Straight Development .....	164
8.5: Comparison of Simulation and Experiment for Straight Development .....	165
8.6: Comparison of Simulation and Experiment for Interrupted Development.....	168
8.6.1: Effects of Shorter Development Cycle .....	170
8.6.2: Effects of Additional Induction Time .....	171
8.7: Summary.....	172
Chapter 9: Conclusions and Future Research .....	175
9.1: Conclusions.....	175

<b>9.2: Future Work .....</b>	<b>178</b>
<b>9.3: A Final Perspective .....</b>	<b>182</b>

## ACKNOWLEDGEMENTS

I would first like to thank my Research Advisor, Professor Andrew R. Neureuther for his guidance, support and friendship throughout the course of this research. His patience and editorial skills are also greatly appreciated. I would also like to thank Professor William G. Oldham for being the chairman of my qualifying committee, and for being a reader of my thesis. The encouragement he gave me while preparing for the qualifying examination is greatly appreciated. I am also indebted to Professor Ping Ko, Professor Ronald Gronsky and Professor Eugene E. Petersen who served on my qualifying committee and discussions with them have further enhanced my technical understanding.

Special thanks also must go to my colleagues in 550 Cory Hall, especially those in the SAMPLE group, for their contributions. It is not possible to list all their names here. Nevertheless, I would like to thank Timothy Hu for the countless times I asked him for advice and help. I would also like to thank Richard Ferguson, Kenny Toh, William Partlo, Alex Wong, Edward Scheckler, Alfred Wong, and John Hutchinson for making life in Berkeley much more interesting.

Part of the research which went into this thesis was a collaborative effort with people at the IBM T. J. Watson Research Center in Yorktown Heights, New York. I would like to thank Michael G. Rosenfield for giving me the opportunity to work at IBM and also for his encouragement and many helpful suggestions. Thanks are also to be extended to Alan Wilson, Fritz Hohn, David Seeger, David Klaus, Keith Kwietniak, Philip Coane, and Chris Blair for their support.

Last but not least, I would like to thank my parents, Chun-Hing and Shui-Kwan Tam, brother Kit, and sisters, Grace and Christine for their love and support through the

years. The immeasurable love, support, and patience of my wife, Addy, over the last three years have made even the difficult times seem easy. In order to provide me with an excellent education, they have made many sacrifices.

# Chapter 1

## Introduction

The development of integrated circuit processing techniques has decreased the cost per component on a silicon chip over 10,000-fold in the last thirty years. This achievement is due to advances in processing technology which have enabled the shrinking of device dimensions to less than a micrometer and the integration of millions of devices on a chip with area of only a few square centimeters. A key technology driver for the reduction of device geometry is the printing of these small features with high resolution lithography. In lithography, the two-dimensional circuit design is transferred onto a radiation-sensitive resist material by imaging a mask with either UV light, deep-UV light, an X-ray, or an electron-beam, or by scanning a finely focused electron beam over the surface of the resist. Although electron-beam direct-write exposure cannot currently compete with optical projection printing in throughput, it plays an important role in the overall lithography process. Electron-beam (e-beam) lithography is essential in the making of masks for optical and X-ray lithography.[1] Even in device fabrication, e-beam lithography has advantages for advanced VLSI devices with fine features [2] and application-specific integrated circuits with low volumes [3].

E-beam lithography fundamentally involves three steps: 1) formation of a latent image in the resist through electron-resist interactions during exposure, 2) modification of the latent image by means of subsequent processing such as baking, and 3) creation of the physical resist profile from the latent image by developing the resist in a selective solvent. For a positive resist, the solvent preferentially dissolves the exposed region, and for a negative resist, the solvent selectively dissolves the unexposed region. Successful application of e-beam lithography depends on an understanding of how processing technology impacts the

key phenomena in these three steps. This thesis investigates the key phenomena of these steps by establishing quantitative characterization methods and a mechanistic foundation for modeling. This characterization and modeling of advanced e-beam lithography requires knowledge from various disciplines, including the massively-parallel computing technique, statistical experiment design, response surface analysis, chemistry and kinetics of catalytic reaction in resist polymers, and mechanism-based dissolution rate modeling. The techniques reported here are widely applicable to future e-beam and even optical resist materials. The practical focus of the research reported here is on predicting the temperature rise in resists during exposure, extending the dissolution rate models of conventional resists to chemically-amplified negative resists, and exploring the possibility of improving resist profiles by interrupting their development.

E-beam lithography has evolved to meet modern demands on throughput with new technologies in exposure systems, resist materials, and resist processing. High-current variable-shape beam exposure systems in conjunction with character or cell projection [4]-[7] are being used to minimize the number of pixels required in writing a wafer by exposing multiple pixels simultaneously. Throughput is also being improved by using highly sensitive resists to reduce the exposure time. For example, a new class of resists was introduced recently which utilizes chemical amplification to achieve sensitivity 1 to 2 orders of magnitude higher than conventional e-beam resists [8]. Processing technology has also been used to achieve higher resolution and better process latitude by introducing techniques such as interrupted development with Diazoquinone-Novolak (DQN) resists [9]-[11]. These e-beam technology advances introduce complex new thermal, physical, and chemical mechanisms, and it is imperative that they be well characterized to develop robust processes.

A basic example of how changes in e-beam technology affect lithography is the thermal heating during exposure with high-current variable-shape beam systems. These thermal effects can change the resist sensitivity [12] and in some cases, cause physical damage to the resist. For example, foaming of the resist can be observed on the Hitachi RD-2000N after exposure on the AEBLE-150 when high-current density-beam and high dose are used [13]. The amount of heating depends on the beam current, beam size, resist thickness, thermal properties of the resist and substrate, and exposure pattern.

A second example of how changes in e-beam technology affect lithography is chemically-amplified resists. They are different from conventional resists because the electron irradiation does not affect their solubility rates directly. Instead, the electrons activate the radiation sensitive compounds in the resist film, which generate either acid or base moieties. During a post-exposure bake (PEB), these acid or base moieties catalyze the thermodynamic reactions which will ultimately determine the dissolution rate of the exposed regions of the resist. Since a single catalyst can produce multiple chemical events, the number of chemical events occurring per absorbed radiation unit is much greater. Special exploratory and systematic experimental techniques are needed to investigate these catalytic reaction mechanisms.

To avoid the use of costly dark field exposure, it is necessary to have both negative and positive resists in e-beam lithography. Unfortunately, most positive e-beam resists either have very poor sensitivity or very poor plasma etch resistance. With the advent of high-current exposure systems and the desire for dry etching processes, the criterion for resists has shifted from sensitivity to dry etch resistance. As a result, despite their relative low sensitivity, novolak-based positive resists are widely used in today's e-beam lithography, because they can provide very good dry etch resistance.

The use of novolak-based resists has led to another change in the processing technology in e-beam lithography. Various special development techniques such as interrupted development [9] are introduced to improve the process latitude and contrast of these resists. Since these positive resists have a finite minimum dissolution rate, they are more susceptible to over-development than negative resists. For example, a 20% over-development of a DQN resist can reduce the critical dimension (CD) by over 50%. However, by taking advantage of the unique interactions between the novolak resin, the dissolution inhibitor, and the base developer, two special development techniques have been shown to improve the contrast and process latitude of these resists. Typically, these development processes modify the surface of the resist either before or during the development. In the first case, the resist is soaked in a dilute developer before development [11]. In the second case, water rinse and air dry are applied to interrupt the development. A 0.25  $\mu\text{m}$  process with tolerance of 20% over development has been demonstrated with the interrupted development of an IBM DQN resist [15].

A major problem in the evaluation and optimization of modern processes in e-beam lithography is the number of physical parameters involved and the complexity of their interactions. For a particular process application, it is important to understand the effects of tool, substrate, resist, and processing parameters to achieve a desired resist profile with good process latitude. These parameters include electron-beam voltage and shape, exposure dose, PEB temperature and time, developer concentration, development time, and schedule of interrupted development. Simulation is a powerful tool for studying e-beam lithography, because it provides an inexpensive and rapid means for systematically determining the effects of the many process parameters on the lithographic pattern transfer process. The simulation must use mechanism-based rather than parametric models to understand the

chemical and physical processes in advanced e-beam lithography. However, a methodology based on a combination of semi-empirical modeling and response surface analysis can provide very general resist dissolution models [17]. These models can be used to simulate resist line-edge profiles under a wide range of processing conditions, as well as to optimize the resist processing.

The work described in this thesis is aimed at establishing quantitative characterization methods and a mechanistic foundation to support resist profile simulation and process optimization of the state-of-the-art e-beam lithography. Both semi-empirical and mechanistic approaches are used. Specific results of this research include a simulator for temperature rise in resists during exposure, semi-empirical and mechanism-based dissolution models for chemically-amplified negative resists, techniques to control the pattern bias of a DQN resist with interrupted development, and a model for the simulation of interrupted development.

## References

- [1] J. Warlaumont, "X-ray Lithography: On The Path To Manufacturing," *J. Vac. Sci. Technol. B*, vol. 7, no. 6, Nov/Dec 1989.
- [2] A. H. Perera and J. P. Krusius, "All-level Electron-Beam Lithography For Trench Isolated Nano-metal-oxide Semiconductor Devices," *J. Vac. Sci. Technol. B*, vol. 8, no. 6, pp. 1343-1347, Nov/Dec 1990.
- [3] F. J. Hohn, "Electron Beam Lithography: Its Applications," *J. Vac. Sci. Technol. B*, vol. 7, no.6, pp. 1405-1411, Nov/Dec 1989.
- [4] U.S. Patent 4,213,053 (1980), IBM.
- [5] H. C. Pfeiffer, T. R. Groves, T. H. Newman, "High-throughput, High-resolution Electron-beam Lithography," *IBM J. Res. Develop.*, vol. 32, no. 4, pp.494-501, 1988.
- [6] R. Yoshikawa, H. Wada, M. Goto, H. Kusakabe, O. Ikenaga, S. Tamamushi, M. Ninomiya, and T. Takigawa, "A High Dose And High Accuracy Variable Shaped Beam Electron Beam Exposure System For Quartermicron Device Fabrication," *J. Vac. Sci. Technol. B*, vol. 5, no. 1, pp. 70-74, Jan/Feb 1987.
- [7] Y. Nakayama, S. Okazaki, N. Saitou, and H. Wakabayashi, "Electron-beam Cell Projection Lithography: A New High-throughput Electron-beam Direct-writing Technology Using A Specially Tailored Si Aperture," *J. Vac. Sci. Technol. B*, vol. 8, no. 6, pp. 1836-1840, Nov/Dec 1990.

- [8] M. deGrandpré, K. Graziano, S. D. Thompson, H. Liu, and L. Blum, "High Resolution, Novolak based Negative Tone Electron Beam Resist," *Proceedings of SPIE, Electron-Beam, X-ray, and Ion-Beam Technology: Submicrometer Lithographies VII*, vol. 923, pp. 158-171, 1988.
- [9] S. J. Gillespie, "Resist Profile Control in E-beam Lithography," *IBM J. Res. Develop.*, vol. 28, no. 4, July 1984.
- [10] J. Frackoviak, R. G. Tarascon, S. Vaidya, and E. Reichmanis, "Process Parameters for Submicron Electron Beam Lithography of NPR," *Proceedings of SPIE, Advances in Resist Technology and Processing IV*, vol. 771, pp. 120-127, 1987.
- [11] T. Yoshimura, F. Murai, H. Shiraishi, and S. Okazaki, "PRISM: Process for Resist Profile Improvement with Surface Modification," *J. Vac. Sci. Technol. B*, vol. 6, no. 6, pp. 2249-2253, Nov/Dec 1988.
- [12] N. K. Eib and R. J. Kvitek, "Thermal Distribution And The Effect On Resist Sensitivity In Electron-beam Direct Write," *J. Vac. Sci. Technol. B*, vol. 7, no. 6, pp. 1502-1506, Nov/Dec 1989.
- [13] N. N. Tam and A. R. Neureuther, "Effects of High Electron Beam Current Density on the Dissolution of RD-2000N Resist," *Proceedings MicroProcess Conference*, pp. 174-175, Tokyo, July 1988.
- [14] S. A. MacDonald, C. D. Snyder, N. J. Clecak, H. R. Wendt, C. G. Wilson, C. J. Knors, and N. B. Deyoe, "Air Borne Chemical Contamination of a Chemically Amplified Resist," *Proceedings of SPIE Symposium on Microlithography*, 1991.

- [15] K. G. Chiong, K. Pettilo, F. J. Hohn, and A. D. Wilson, "Contrast and Sensitivity Enhancement of Resists for High-Resolution Lithography," *J. Vac. Sci. Technol. B*, vol. 6, no. 6, pp. 2238-2244, Nov/Dec 1988.
- [16] S. Asaumi and H. Nakane, "Mechanism of Photoresist Resolution Improvement by Pre-exposure Treatment," *J. Electrochem. Soc.*, vol. 137, no. 8, pp. 2546-2549, 1990.
- [17] N. N. Tam, H. Y. Liu, C. Spanos, A. R. Neureuther, "A Statistically Based Model of Electron-beam Exposed, Chemically Amplified Negative Resist," *Proceedings of 34th International Symposium on Electron, Ion, and Photon Beams*, Seattle, 1991.

## Chapter 2

# General Modeling Techniques

The simulation of e-beam lithography involves the modeling of the exposure, the post-exposure processing, and the time evolution of the resist profile in a developer. Historically, the exposure and the development processes have been the subjects of extensive theoretical and experimental research. While the majority of the modeling efforts have concentrated on PMMA, advanced resist technologies such as alkaline soluble resists and chemical amplification have recently begun to receive considerable attention. These new resist materials require additional post-exposure processing, such as baking or interrupted development, which cannot be easily characterized and modeled with traditional dissolution rate functions of absorbed energy. In this chapter, the status and difficult issues in characterization measurements, modeling, and simulation are described.

### 2.1 Historical Perspective

The origins of e-beam lithography can be traced to the 1970s. Many early e-beam lithography tools were modified scanning electron microscopes, and they were successfully used to fabricate semiconductor devices with dimensions much smaller than could be achieved with optical lithography [1]. E-beam lithography also benefited from the established theoretical framework for electron scattering interactions in scanning electron microscopy. To understand the production of secondary electrons, X-ray, and backscattered electrons when high energy electrons strike a solid, both analytic [2][3] and computational (Monte Carlo calculation) [4] models of electron scattering interactions were developed. These models of electron scattering laid the foundation for the modeling of the energy deposition in e-beam exposed resists. For example, Everhart and Hoff developed a universal depth-dose function from measurements of steady-state e-beam-induced current through a

thin insulating layer of SiO<sub>2</sub> of a MOS capacitor [3] which can be applied to calculate the energy deposition in the resist as a function of depth in a large area exposure.

The development of resist modeling and characterization techniques of e-beam exposed resists soon followed to support the simulation of e-beam lithography. Most of the early modeling efforts were focused on PMMA because it is a relatively simple system, and it can provide very high resolution. The first resist profile model for PMMA was a threshold energy model where the development step could be ignored [5]. However, as faster developers such as MIBK:IPA were developed, the amount of resist removed became a function of development time. To model the development of PMMA in these developers, a hypothesis that the dissolution rate is a function of deposited energy in the resist was postulated and verified originally by Ting [6] and later by Hawryluk [7]. When combined with an etching algorithm, this energy deposition rate model enabled the simulation of time evolution of resist profiles.

The e-beam resist characterization techniques and the dissolution simulation algorithms required were very similar to the ones that were being developed for the modeling of optical lithography. As a result, the rapid resist characterization techniques such as in-situ interferometry [8], and fast algorithms for simulating the etching of resists in developer, such as the ray tracing [9], and the string algorithms [10] developed for the modeling of optical lithography, were also applied to the modeling of e-beam lithography. Some of the exposure, resist, and dissolution models have been implemented in a number of e-beam lithography simulation programs [11]-[13], including the *SAMPLE* simulation program at U. C. Berkeley. Since *SAMPLE* was introduced in April 1979, it has been used with great success for studying the issues involved in the exposure and development of PMMA.

However, with the advent of new resist and processing technologies, new resist models must be developed for these process simulators.

The following sections provide a historical perspective on the exposure simulation, resist modeling, and development simulation algorithms involved in the modeling of e-beam lithography. The important issues associated with the advances in exposure systems, resist materials and processing, such as exposure induced thermal effects, chemically-amplified resists, and interrupted development of a DQN resist, are then discussed.

### **2.1.1 Exposure Modeling**

The most rigorous method to model electron energy deposition in resists during exposures is the Monte Carlo technique. In general, the Monte Carlo technique calculates the trajectories of a large number of electrons and determines the energy deposited in resists using the continuous slowing down approximation (CSDA) and Bethe energy loss formula [15][16]. Shimizu *et al.* [17] and Adesida *et al.* [18] included statistical effects in the energy loss calculation by using more exotic inelastic scattering events such as conduction electrons, excitation of plasmon, and L-shell excitation, in their Monte Carlo simulations. In addition, knock-on effect and secondary electron generation have also been modeled [19]. More recently, the Mott cross-section was used in place of the Rutherford cross-section in Monte Carlo simulation to improve energy deposition in heavy substrates such as those used in the fabrication of X-ray masks [20]. Johnson and MacDonald extended the Monte Carlo simulation for lower energy electrons with a quantum-mechanical elastic scattering differential cross-section [21]. These simulation programs have been successfully used to optimize exposure and minimize proximity effects. [22]

## 2.1.2 Characterization and Modeling of Resist Dissolution

The concept of the dissolution rate of absorbed energy model was originated by Ting for PMMA and based on hand measurements [6]. Today automated techniques are used. A schematic diagram of the methodology in obtaining the dissolution rate data as a function of absorbed energy is illustrated in Figure 2.1. First, the resist film thicknesses removed from large area exposures, which received different exposure doses, are measured as a function of development time. The dissolution rate as a function of depth,  $R(z)$ , is then obtained by taking the derivative of the thickness versus time data with respect to time.  $E(z)$  can be evaluated with the Monte Carlo simulation or the Everhart and Hoff equation [23]. Since both the rate and the energy are functions of the depth, they can be combined to give  $R(E)$ .

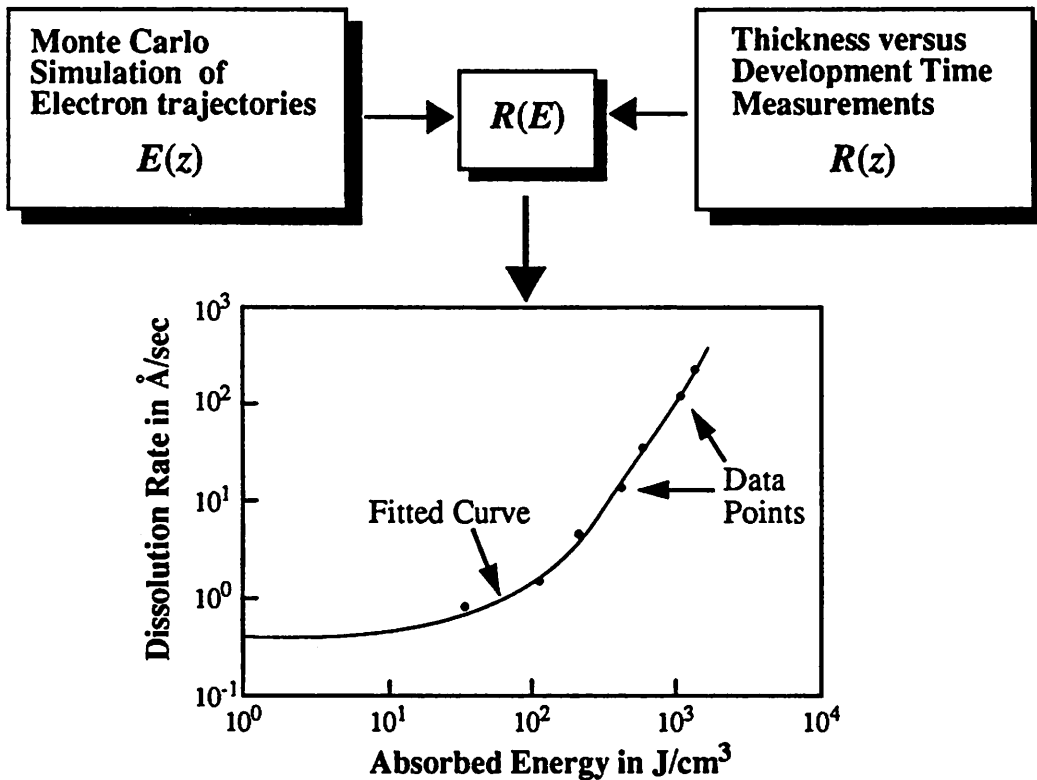


Figure 2.1. A schematic diagram of characterization and modeling of an electron-beam exposed positive resist with dissolution rate of absorbed energy function. Before the use of in-situ laser interferometry, only a few data points were gathered and fitted to the rate equation.

### 2.1.2.1 In-situ Monitoring of Resist Development

Before the introduction of an in-situ development monitor, very few dissolution rate data points were collected because the film thickness removed had to be measured at discrete time intervals. Currently, there are two major techniques for in-situ measurement of resist dissolution. The first technique is laser interferometry, which monitors the reflected intensity of a non-exposing laser beam from the resist substrate sandwich as the thickness of the resist film changes due to developer etching. The thickness removed as a function of development time can be calculated from the reflectivity versus time data using the inverted two-beam interference equation. Dill *et al.* [8] pioneered the use of reflectivity measurements with a multiple wavelength technique to monitor resist dissolution. Since that time, the Perkin-Elmer Development Rate Monitor (DRM) has become the primary instrument for rapid acquisition of resist dissolution data. Although employing only a single wavelength laser beam, its 256-pixel photodiode array dramatically reduces the time required to characterize the dissolution because multiple exposure zones can be measured simultaneously.

Quartz crystal microbalance (QCM) is another technique that can monitor the variations in the thickness of a thin film. This instrument measures the shift in the resonant frequency of a piezoelectric quartz crystal as the mass of the sample changes. This technique has been successfully applied by Hinsberg *et al.* [24] to measure the dissolution rate of several optical resists. The advantage of this technique over interferometry is that it can measure very fast dissolution rates and resists with high absorption or rough surfaces. However, a special piezoelectric quartz wafer with gold electrodes is needed for this technique, which increases the contribution of exposure from backscattered electrons. Also, the measurement throughput is very low because only one sample can be measured at a time.

### 2.1.2.2 Resist Dissolution Rate Model

For simple polymeric resist systems, the variation of dissolution rates with deposited energy is usually a result of changes in the molecular weight of the resist molecules. These changes are caused by the chain scission and crosslinking reactions initiated by the exposure. In a positive resists, the chain scission reactions dominate, whereas in a negative resist the crosslinking reactions are favored. For example, the exposure of a positive polymeric resist produces molecules having a mean molecular weight,  $M_f$  which is less than the original molecular weight,  $M_n^\dagger$ . Greeneich [25] has shown that

$$M_f = M_n / (1 + N_g) \quad (\text{EQ 2.1})$$

where  $N_g$  is the number of scission events per molecule given by

$$N_g = (g_s E M_n) / (\rho A_0) \quad (\text{EQ 2.2})$$

where  $E$  is the absorbed energy density,  $g_s$  is the radiation chemical yield for scission events,  $\rho$  is the resist density, and  $A_0$  is Avogadro's number. The combination of Equations (2.1) and (2.2) yields,

$$M_f = M_n / (1 + K M_n) \quad (\text{EQ 2.3})$$

with  $K = (g_s E) / (\rho A_0)$ . Since the dissolution rate  $R$  of a polymer in a solvent generally follows a power law dependence on the molecular weight,

$$R \propto (M_f)^{-\alpha} \quad (\text{EQ 2.4})$$

the dissolution rate versus absorbed energy data can be fitted with this function. In order to characterize the removal of very high molecular weight materials such as the unexposed

---

†. These are number average molecular weight.

regions, and the effects of the developer, Greeneich [26] developed an empirical relationship for  $R(E)$  based on Equations (2.3) and (2.4)

$$R = R_0 + \beta/M_f^\alpha \quad (\text{EQ 2.5})$$

where  $R_0$ ,  $\beta$ , and  $\alpha$  are empirical constants that depend upon the resist and the developer. Combining Equations (2.3) and (2.5) gives the rate in term of the absorbed energy density

$$R(E) = R_1 \left( C_m + \frac{E}{E_0} \right)^\alpha \quad (\text{EQ 2.6})$$

In the above equation,  $R_1 C_m^\alpha$  is the unexposed resist dissolution rate,  $C_m$  is proportional to  $1/M_n$ , and  $E_0$  is the critical energy which is proportional to  $g_s/\rho$ . These dissolution rate functions of deposited energy have been used successfully to determine the effect of initial molecular weight on the performance of PMMA as well as calculating the dissolution rates in the simulation of time evolution of resist profiles [14]. Moreover, since this function is based on the molecular weight changes in the resist, it is general enough to model the development rate of non-swelling negative resists, which will be discussed in Chapter 3.

With the advent of new resist systems such as DQN systems, new rate functions were developed to model the development data of these resists. Generally, these models were not based on theory but instead were obtained from the use of an engineering curve fitting approach. For example, Kyser and Pyle [12] added an exponential function to Equation 2.6 to describe the depth dependence of dissolution rate in diazo-type positive resists. Eib *et al.* [27] later used highly non-linear functions which had their origins in the Bose-Einstein approximations to the low temperature heat capacity and internal energy associated with phonons in nonmetallic crystalline insulators. These models are most useful in evaluat-

ing and optimizing the processing of a given resist but are generally less useful in terms of understanding how the resist properties affect the performance of the resist.

### 2.1.3 Dissolution Simulation

To simulate the time evolution of the resist profile, a robust and accurate model of the development process is needed. The first step in the simulation is to use the dissolution rate model to calculate the local dissolution rate in the resist based on the absorbed energy density and in some cases, the depth into the resist. Once the spatial distribution of energy is converted to dissolution rate, the resist profile can be evaluated, in principle, for any development time, by tracking the volume of resist removed. The most common volumetric algorithm is the cell method in which the resist is divided into a matrix of small cells. On the other hand, since the dissolution of the resist takes place in a thin layer at the resist/developer interface, this problem can be generalized to that of etching an inhomogeneous and isotropic medium. Algorithms to track the advancement of the resist/developer interface such as the string [10] and ray tracing [9] algorithms, have been applied to simulate the dissolution of the resist in two dimensions.

In the cell removal model originated by Dill *et al.* [8], the resist is subdivided into stacks of cells. The dissolution rate of each cell is determined by the energy deposited in that cell. The developer dissolves only those cells with which it is in contact, at a rate determined by the local dissolution rate. If a cell is dissolved, then the developer can attack the surrounding cells. The resist profile is tracked by noting the state of each cell in the resist. The removal method was extended to simulate three dimensional resist development. [13]

Both the string and the ray tracing algorithms are based on the same mathematical solution to the general problem of tracing a surface or profile as it evolves in time [28]. In two dimensions, they both construct the resist/developer boundary out of a string of points.

However, they differ in their implementations of the surface advancement algorithm. In the string model, the string advances according to the local dissolution rate along the line that bisects the angle formed by the adjoining points. In the ray tracing algorithm, each node follows the trajectory of a ray and the surface is moved by connecting nodes at given times. That is each point is an independent ray whose trajectory is dependent only on its previous trajectory and the local dissolution rate. These algorithms are both faster but less robust than the cell method. Since in the string algorithm, the string is moved perpendicular to the surface, it tends to propagate any surface errors and is susceptible to the formation of artificial loops. The ray tracing algorithm has the advantage that the ray is independent of the local surface and is less sensitive to error. But in the ray tracing algorithm, there are often insufficient rays to adequately describe the entire surface. For a more detailed discussion of dissolution algorithms including the variations of the ray approach proposed by Barouch, see Toh[28] and Scheckler [29]. For the profile modeling in this work, the *SAMPLE* program, which utilizes the string algorithm with “delooping” capability for resist etching, is used to simulate the resist dissolution.

## **2.2 Advances in Resist and Processing Technology**

In this section, three advanced resists which have greatly changed e-beam lithography as well as heating effects are described. All three resists have good dry etch resistance because of the presence of aromatic phenolic groups in the resin. Another attractive feature of these resists for e-beam lithography is that they are soluble in an aqueous alkaline developer. The first resist is the Hitachi RD-2000N resist, which is a deep-UV azide phenolic resin resist. Its use with e-beam exposure has been studied by Okazaki *et al.* [30] and Liu *et al.* [31]. The second example is a prototype chemically-amplified resist from Shipley, ECX-1033, which utilizes thermodynamically driven acid-hardening reactions to achieve high

sensitivity and high contrast [32]. The third example is a DQN resist developed with an interrupted development process [33]. Heating of the resist during exposure has become a new concern as beam current densities have exceeded  $25 \text{ A/cm}^2$ .

### 2.2.1 Hitachi RD-2000N Negative Crosslinking Resist

The RD-2000N resist is composed of 3,3'-diazidodiphenyl sulfone (20 wt%) as a radiation-sensitive azide compound, and poly(*p*-vinylphenol) as a phenolic resin matrix [34]. The structural formulas for the resist components are shown in Figure 2.2. Upon

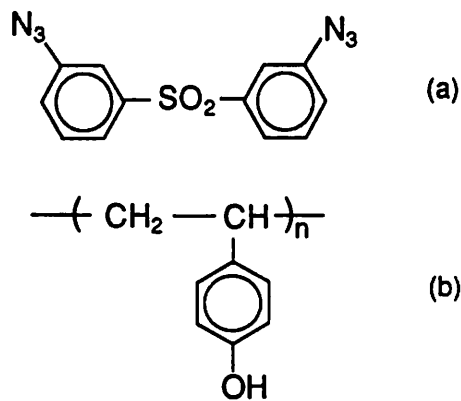


**Figure 2.2.** Structural formulas for the two major components of RD-2000N: (a) 3,3'-diazidodiphenyl sulfones; (b) poly(*p*-vinylphenol).

exposure, the nitrogen trimers lose a nitrogen molecule to produce a nitrene intermediate, which may exist either in the triplet biradical state or in the singlet state (Figure 2.3). The nitrenes are very reactive and can undergo many insertion, addition, or reduction reactions with other azides and the resin polymers [35]. It is believed that the diazides react with the phenolic resins to form a cross-linked polymer matrix and increase the molecular weight of the resin polymers. This cross-linked network becomes insoluble in any organic solvents as well as in aqueous bases [36]. In an aqueous alkaline developer, the resist dissolves in a manner similar to AZ-type positive photoresists and does not swell after development. This

non-swelling development characteristic not only increases the resolution limit of the resist, but enables the use of the dissolution rate of absorbed energy function to simulate its development. Profile modeling of this resist under deep-UV exposure with *SAMPLE* has been reported by Matsuzawa *et al.* [37]. The dissolution characterization and time evolution profile modeling under e-beam exposure will be given in the following chapter.

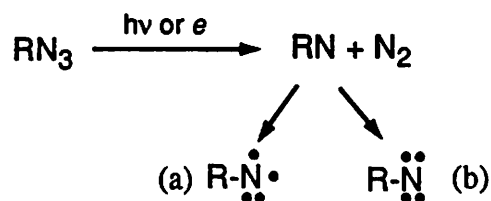


**Figure 2.3.** The nitrene intermediate states: (a) triplet biradical state and (b) the singlet state.

## 2.2.2 Shipley ECX-1033 Negative Chemically-Amplified Resist

ECX-1033 is a negative resist composed of a novolak resin, a melamine compound, and a radiation-sensitive acid generating (RSAG) species [38]. The melamine compound has multiple amine sites which, in the presence of protons ( $\text{H}^+$ ) and high temperatures, will react with the novolak resin molecules to form a cross-linked network. The reaction mechanism proposed by Blank [39] is illustrated in Figure 2.4. The unique feature about this reaction is that the acid acts as a catalyst; it provides an alternative path with lower activation energy for the reaction and is regenerated after the completion of the reaction. During exposure, some of the PAG is excited and acid is released into the resist. After the exposure, a bake is applied to drive the acid-catalyzed crosslinking reaction. Since a single exposure event (generation of an acid) can produce many chemical events during the post-exposure bake, this resist has much higher sensitivity and contrast than RD-2000N, and its mechanism is called “chemical amplification”.

Although chemically-amplified resists have the advantages of high sensitivity and contrast, the added process complexity complicates the lithography. Since a post-exposure baking (PEB) step is needed to drive the acid-catalyzed reaction, two more processing variables are introduced: the PEB temperature and the PEB time. Thus, the determination of an optimal processing condition would require many characterization experiments. However, for a specific PEB, the dissolution characteristic of the negative acid-hardening chemically-amplified resist such as ECX-1033 is very similar to that of the RD-2000N. As a result, it is possible to obtain a dissolution rate function for this resist and use it in a process simulation program such as *SAMPLE* to study processing issues such as the tradeoffs in exposure dose and development time. The characterization and modeling of ECX-1033 will be given in Chapter 3.

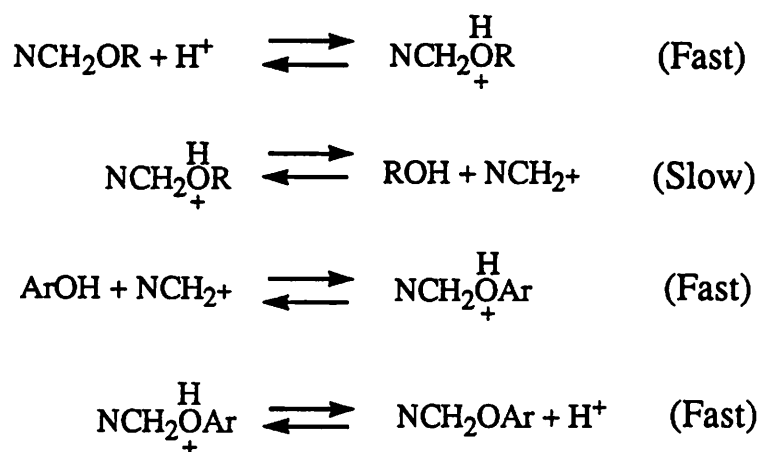


**Figure 2.4.** The reaction mechanism of the hydroxyl group on the resin polymer with the amine group on the melamine crosslinking agent.

### 2.2.3 Interrupted Development of DQN Resist

The DQN resists consist of a smaller radiation-sensitive component of diazonaphthoquinone (DNQ) dispersed in a novolak resin. When the hydrophobic DNQ is added to the alkali-soluble resin (novolak), the resin dissolution is inhibited. The destruction of the

DNQ dissolution inhibitors by the exposure then releases the uncomplexed resin and enables dissolution of the exposed resist. Upon exposure, the DNQ generates in Wolff rearrangement a carbene, which then rearranges to a ketene. The ketene reacts with absorbed moisture present in the resin to form an indene acid,

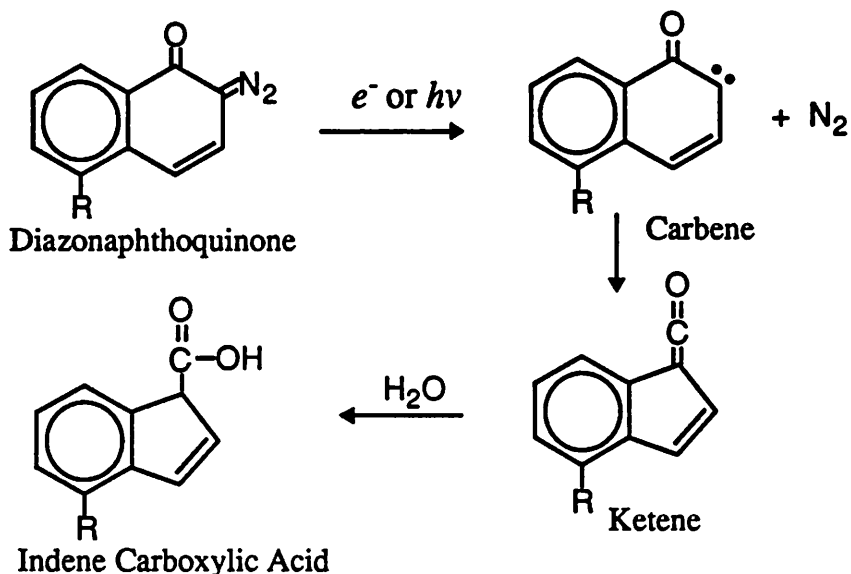


**Figure 2.5.** Photochemical transformation of DNQ.

The indene carboxylic acid photoproduct leads to a substantial increase in the dissolution rate even beyond that of the pure resin matrix. Modern resists show a dissolution rate ratio of about 2 to 3 in orders of magnitude of exposed versus unexposed resist regions with DNQ loadings of approximately 20% of solid. However, due to the finite dissolution rate in the unexposed resist, these resist systems do not provide enough contrast and process latitude for sub-half micron e-beam lithography.

Recently, an interrupted development process was discovered which can substantially improve the performance of an IBM DQN resist [40]. The procedure for interrupted development is illustrated in Figure 2.6. Contrary to the standard development process, the development of the resist is carried out in small time intervals in interrupted development.

### Straight Development

### Interrupted Development

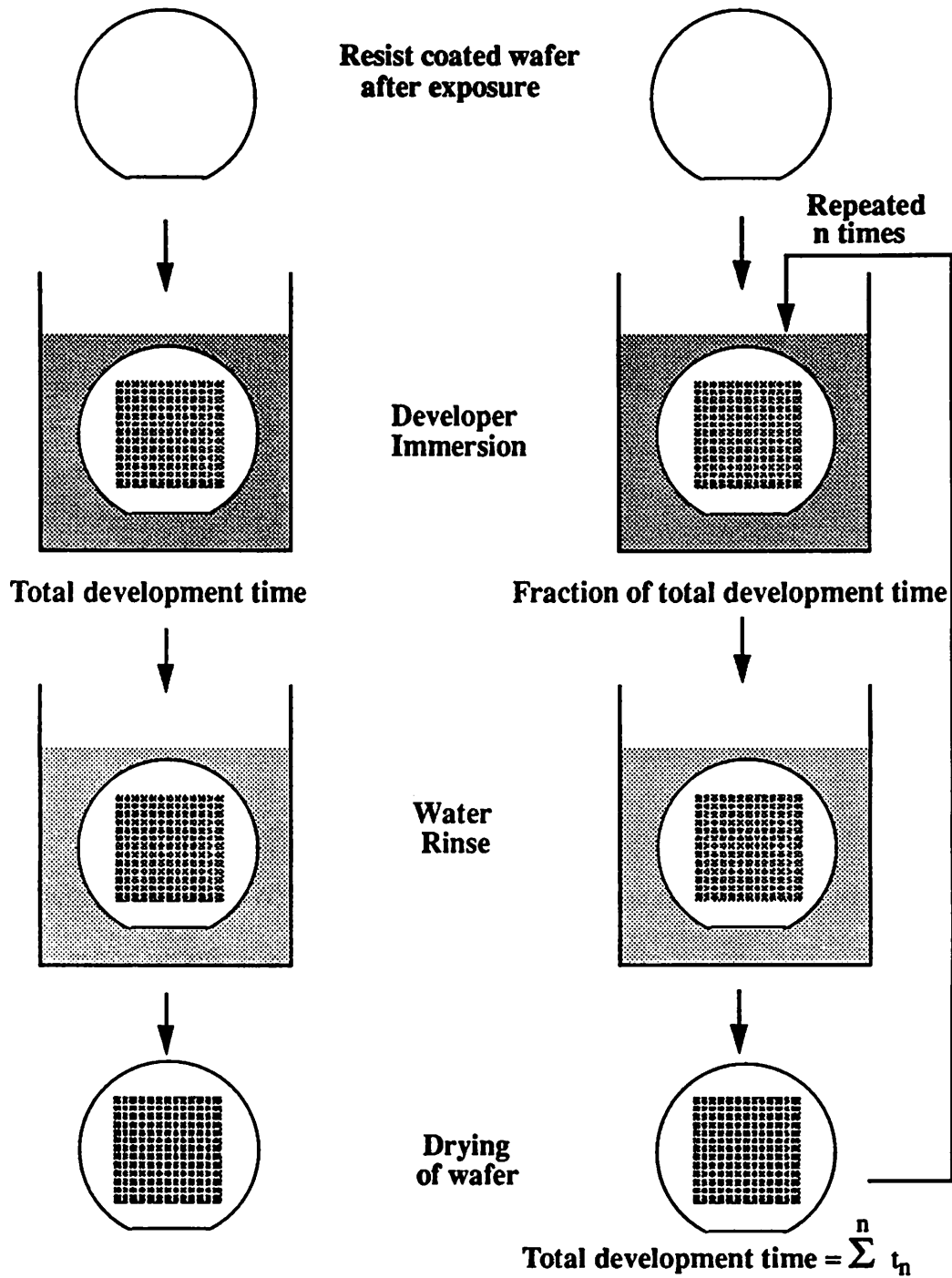
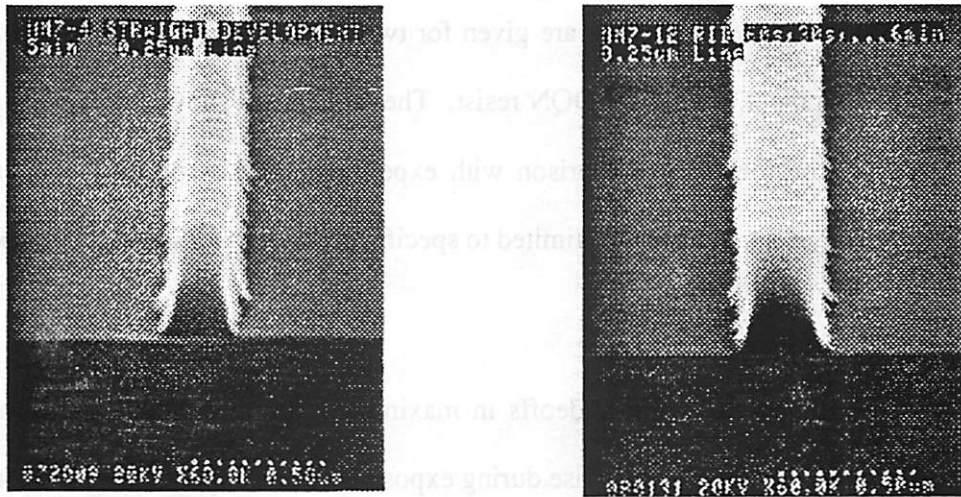


Figure 2.6. Schematic diagrams of the regular and the interrupted development procedures.

A typical development schedule would be 60, 30, 30,...., 30 seconds, until the endpoint of development is reached. At the end of each development interval, the wafer is taken out of the developer and rinsed in DI water. After the rinse, the wafer is dried with an N<sub>2</sub> gun and later developed in the developer for the duration of the next interval. Figure 2.6 shows the improved resist profiles obtained with a 6 minute interrupted development process with interruptions at 60, 90, 120, 150, 180, 210, 240, 270, 300, and 330 seconds, corresponding to 60, 30,...., 30 second development intervals. The resist line-edge profile in Figure 2.7b has steeper sidewalls and less bias when compared to the one in Figure 2.7a. In addition, the features obtained with interrupted development are very insensitive to over-development. However, the complicated development procedure makes it very difficult to develop a resist dissolution model for simulation.



(a) Straight Development

(b) Interrupted Development

**Figure 2.7.** Comparison of resist profiles of a 0.25  $\mu\text{m}$  isolated line delineated in an 0.5  $\mu\text{m}$  IBM DQN resist with straight and interrupted development. (a) Straight development gives poor sidewall angle and more top loss. (b) Interrupted development produces more desirable resist profile.

## **2.2.4 Heating Effects**

One of the problems with high beam current density exposures is that resist materials often suffer exposure-induced thermal effects. These effects have been shown to affect the dissolution of RD-2000N exposed on the AEBLE-150 at high doses and high currents [41]. These thermal effects have also been observed in PMMA [42]. In the case of RD-2000N, thermal effects manifest in the form of a frosty surface on resist exposed with high doses. Although chemically-amplified resists such as ECX-1033 can reduce the thermal effects significantly due to their low dose-requirement, it is not clear whether their sensitivity is affected by the temperature rise during exposure.

## **2.3 Resist Modeling Extensions in this Thesis**

This thesis applies the traditional dissolution rate as a function of absorbed energy models to modern e-beam resists and then makes four major extensions to the modeling approach. In Chapter 3, models are given for two advanced negative resists and the interrupted development of an IBM DQN resist. The models are shown to be adequate for predicting resist profiles via comparison with experimental resist profiles obtained with the SEM. The models are, however, limited to specific process conditions and low beam current density exposures.

In order to study the tradeoffs in maximizing the throughput and minimizing the thermal effects, the temperature rise during exposure and its dependence on resist, substrate, and exposure conditions must be known. The thermal effects observed in the resist profiles in Chapter 3 are examined by further experimental studies augmented with numerical simulations of temperature rise using a massively-parallel approach. The experimental and theoretical studies concerning thermal effects during exposure are discussed in Chapter 4.

There is a need in the applications of process optimization and process control in manufacturing to generalize the resist model so that simulation can include many more process parameters, which have not been characterized in terms of physical mechanisms. These parameters might, for example, include the concentration of developer and the temperature and the duration of the post-exposure bake in the processing of chemically-amplified resists. One strategy for generalizing the resist dissolution model is to use response surface analysis to fit the parameters of the dissolution rate function as the processing conditions vary. Using a factorial experiment of dissolution rate measurements, correlations between the parameters in the dissolution rate function and the processing conditions can be obtained with linear regression. Once these rate-model parameter functions are determined, a rate equation can be obtained for any processing condition. These empirical extensions to the mechanism-based dissolution rate function of absorbed energy can extend the range of profile modeling for chemically-amplified resists. Hence, the advantage of this technique is that through response surface analysis, the basic nature of the resist is still captured by the non-linear rate curve. This approach to characterize and simulate the post-exposure bake and development of a chemically-amplified resist is discussed in detail in Chapter 5.

The second strategy is to extend the basic understanding of the physical and /or chemical mechanisms that govern the resist's behavior. This model is especially useful in the case of the acid-hardening chemically-amplified resist because the absorbed energy is no longer the fundamental variable that determines the resist's dissolution rate. Instead, it is the acid-catalyzed crosslinking reaction which occurs during the post-exposure bake step that determines the solubility of the resist. Quantitative information about the extent of the acid-catalyzed crosslinking reaction must be measured and modeled. The experimentation and

the post-exposure bake models for the acid-hardening chemically-amplified resists are given in Chapter 6.

In order to use simulation to evaluate and optimize the interrupted development of the IBM DQN resist, both extensions to the rate model and a basic understanding of the process are required. In Chapter 3, the average development rates of the resist in each development interval are characterized and modeled. Chapter 7 examines the effect of different processing conditions on the resist profiles with interrupted development. Since the increase in the contrast of the resist is believed to be caused by the formation of a surface insoluble layer in the low dose region, the dissolution of the resist before and after the interrupt must be measured. The DRM experiments and the modeling of the surface induction effects are discussed in Chapter 8.

## References

- [1] A. N. Broers and M. Hatzakis, "Microcircuits by Electron Beam," *Scientific American*, vol. 227, no. 5, pp. 34-44, 1972.
- [2] T. E. Everhart, "Simple Theory Concerning the Reflection of Electrons from Solids," *J. Appl. Phys.*, vol. 31, no. 8, pp. 1483-1490, 1960.
- [3] T. E. Everhart and P. H. Hoff, "Determination of Kilovolt Electron Energy Dissipation vs. Penetration Distance in Solid Materials," *J. Appl. Phys.*, vol. 42, no. 13, pp. 5837-5846, 1971.
- [4] R. Shimizu and K. Murata, "Monte Carlo Calculations of the Electron-Sample Interactions in the Scanning Electron Microscope," *J. Appl. Phys.*, vol. 42, no. 1, pp. 387-394, 1971.
- [5] J. S. Greeneich and T. Van Duzer, "An Exposure Model for Electron-Sensitive Resists," *IEEE Trans. Electron Devices*, vol. ED-21, no. 5, pp. 286-299, 1974.
- [6] C. H. Ting, *Record of 11th Symposium on Electron, Ion, and Laser Beam Technology*, edited by R. F. M. Thornley (San Francisco Press, San Francisco), p. 345, 1971.
- [7] R. J. Hawryluk, Ph. D. dissertation, Massachusetts Institute of Technology, Cambridge, Mass. 1974.
- [8] F. H. Dill, A. R. Neureuther, J. A. Tuttle, and E. J. Walker, "Modeling Projection Printing of Positive Photoresists," *IEEE Trans. Electron Devices*, vol. ED-22, no. 7, pp. 445-452, 1975.

- [9] P. I. Hagouel, "X-ray Lithographic Fabrication of Blazed Diffraction Gratings," *Ph.D. Dissertation*, Department of Electrical Engineering and Computer Sciences, University of California, Berkeley, 1976.
- [10] R. E. Jewett, P. I. Hagouel, A. R. Neureuther, and T. Van Duzer, "Line-Profile Resist Development Simulation Techniques," *Polymer Eng. Sci.*, vol. 17, no. 6, pp. 381-384, 1977.
- [11] M. G. Rosenfield, "Simulation of Developed Resist Profiles for Electron-Beam Lithography," *Master Report*, Department of Electrical Engineering and Computer Sciences, University of California, Berkeley, 1981.
- [12] D. F. Kyser and R. Pyle, "Computer Simulation of Electron-Beam Resist Profiles," *IBM J. Res. Develop.*, vol. 24, no. 4, pp. 426-437, 1980.
- [13] F. Jones and J. Paraszczak, "RD3D (Computer Simulation of Resist Development in Three Dimensions)," *IEEE Trans. Electron Devices*, vol. ED-28, no. 12, 1981.
- [14] A. R. Neureuther, D. F. Kyser, and C. H. Ting, "Electron-Beam Resist Edge Profile Simulation," *IEEE Trans. Electron Devices*, vol. ED-26, no. 4, pp.686-693, 1979.
- [15] D. F. Kyser and K. Murata, "Monte Carlo Simulation of Electron Beam scattering and Energy Loss in Thin Films on Thick Substrates," *Proceedings of 6th Int. Conf. on Electron and Ion Beam Science and Technology*, pp. 205-223, (Electrochemical Society, 1974).
- [16] I. Adesida, "Electron Energy Dissipation in Layered Media," *Ph.D. Dissertation*, Department of Electrical Engineering and Computer Sciences, University of California, Berkeley, 1979.

- [17] R. Shimizu, Y. Kataoka, T. Ikuta, T. Koshikawa, and H. Hashimoto, "A Monte Carlo Approach to the Direct Simulation of Electron Penetration in Solids," *J. Phys. D: Appl. Phys.*, vol. 9, pp. 101-114, 1976
- [18] I. Adesida, T. E. Everhart, and R. Shimizu, *J. Vac. Sci. Technol.*, vol. 16, pp. 1743, 1979.
- [19] K. Murata, D. F. Kyser, and C. H. Ting, "Monte Carlo Simulation of Fast Secondary Electron Production in Electron Beam Resists," *J. Appl. Phys.*, vol. 52, no. 7, pp. 4396-4405, July 1981.
- [20] K. Murata, H. Kawata, and K. Nagami, "Studies of Energy Dissipation in Resist Films by a Monte Carlo Simulation Based on the Mott Cross Section," *J. Vac. Sci. Technol. B.*, vol. 5, no. 1, pp. 124-128, Jan/Feb 1987.
- [21] S. Johnson and N. C. MacDonald, "A Program for Monte Carlo Simulation of Electron Energy Loss Nanostructures," *J. Vac. Sci. Technol. B.*, vol. 7, no. 6, pp. 1513-1518, Nov/Dec 1989.
- [22] R. J. Hawryluk, "Exposure and Development Models Used in Electron Beam Lithography," *J. Vac. Sci. Technol.*, vol. 19, pp. 1-17, May/June 1981.
- [23] G. R. Brewer, ed., J. S. Greeneich, *Electron-Beam in Microelectronic Fabrication*, pp. 98-99, Academic Press, New York, 1980.

- [24] W. D. Hinsberg, C. G. Wilson, and K. K. Kanazawa, "Use of a Quartz Crystal MicroBalance Rate Monitor to Examine Photoproduct Effects on Resist Dissolution," *Proceedings SPIE: Advances in Resist Technology and Processing II*, vol. 539, pp. 6-13, 1985.
- [25] J. S. Greeneich, "Time Evolution of Developed Contours in PMMA Electron Resist," *J. Appl. Phys.*, vol. 45, pp. 5264-5268, 1974.
- [26] J. S. Greeneich, *J. Electrochem. Soc.*, vol. 121, pp. 1669, 1974; and J. S. Greeneich, *J. Electrochem. Soc.*, vol. 122, pp. 970, 1975.
- [27] N. Eib, D. Kyser, and R. Pyle, *VLSI Electronics: Microstructure Science*, vol. 16, pp. 103-145, Academic Press, 1987.
- [28] Kenny K.H. Toh, "Algorithm for Three-Dimensional Simulation of Photoresist Development," *Ph.D. Dissertation*, Department of Electrical Engineering and Computer Sciences, University of California, Berkeley, 1990.
- [29] Edward W. Scheckler, "Algorithms for Three-Dimensional Simulation of Etching and Deposition Processes in Integrated Circuit Fabrication," *Ph.D. Dissertation*, Department of Electrical Engineering and Computer Sciences, University of California, Berkeley, 1991.
- [30] S. Okazaki, F. Murai, O. Suga, and H. Shiraishi, "A Practical Electron Beam Direct Writing Process Technology for Submicron Device Fabrication," *J. Vac. Sci. Technol. B*, vol. 5, no. 1, pp. 402-404.

- [31] H. Liu and E. D. Liu, "Application of GHOST Proximity Effect Correction Method to Conventional and Nonswelling Negative E-beam Resists," *SPIE Proceedings: Advances in Resist Technology and Processing III*, vol. 632, pp. 244, 1986.
- [32] H. Liu, M. P. deGrandpre, and W. E. Feely, "Characterization of a High Resolution Novolak Based Negative E-beam Resist with  $4 \mu\text{C}/\text{cm}^2$  Sensitivity," *J. Vac. Sci. Technol. B*, vol. 6, no. 1, pp. 379-383, 1988.
- [33] K. G. Chiong, K. Petrillo, F. J. Hohn, and A. D. Wilson, "Contrast and Sensitivity Enhancement of Resists for High-Resolution Lithography," *J. Vac. Sci. Technol. B*, vol. 6, no. 6, pp. 2238-2244, Nov/Dec 1988.
- [34] T. Iwayanagi, T. Kohashi, S. Nonogaki, T. Matsuzawa, K. Douta, and H. Yanazawa, "Azide-Phenolic Resin Photoresists for Deep UV Lithography," *IEEE Trans. on Electron Devices*, vol. ED-28, no. 11, 1981.
- [35] W. M. Moreau, *Semiconductor Lithography*, pp. 178, Plenum Press, New York and London, 1988.
- [36] T. Iwayanagi, M. Hashimoto, and S. Nonogaki, "Azide-Phenolic Resin UV Resist (MRL) for Microlithography," *Polymer Engineering and Sciences*, vol. 23, no. 17, pp. 935-940, 1983.
- [37] T. Matsuzawa, A. Kishimoto, and H. Tomioka, "Profile Simulation of Negative Resist MRS Using the SAMPLE Photolithography Simulation," *IEEE Electron Device Letter*, vol. EDL-3, no. 3, 1982.

- [38] M. deGrandpre, K. Graziano, S. D. Thompson, H. Liu, and L. Blum, "High Resolution, Novolak based Negative Tone Electron-Beam Resist," *Proceedings SPIE: Electron-Beam, X-Ray, and Ion-Beam Technology: Submicrometer Lithographies VII*, vol. 923, pp. 158-171, 1988.
- [39] W. Blank, "Reaction Mechanism of Melamine Resins," *Journal of Coatings Technology*, vol. 51, no. 656, pp. 61-70, September 1979.
- [40] S. J. Gillespie, "Resist Profile Control in E-beam Lithography," *IBM J. Res. Develop.*, vol. 28, no. 4, pp. 454-460, July 1984.
- [41] N. Tam and A. Neureuther, "Effects of High Electron-Beam Current Density on the Dissolution of RD-2000N Resist," *Proceedings of MicroProcess Conference*, July 1988.
- [42] L. H. Veneklasen, "Optimizing EBL Writing Strategy Subject to Electron Optical, Pattern and Resist Constraints," *Proceedings of the 35th International Symposium on Electron, Ion and Photon Beams*, Seattle, 1991.

# Chapter 3

## Applications and Limitations of Energy Deposition Rate Models

In this chapter, the current state of the general modeling techniques used in *SAMPLE* is discussed. These are the techniques used throughout this thesis and their limitations form the motivation for the extensions in Chapters 4 to 8. In exposure modeling, a new pseudorandom number generator is implemented in the Monte Carlo simulation program which improves the statistical precision of the energy deposition calculation. In the resist characterization, a parameter extraction program with graphical user-interface is developed to support the data analysis of the in-situ development rate measurements and non-linear regression in the curve-fitting of dissolution rate data. Examples of using these characterization and modeling techniques are illustrated using two advanced negative resists and a positive DQN resist with interrupted development. Within each of the exposure, dissolution, and experimental characterization sections, the particular approach used in this work and the importance of the dominant physical mechanisms are considered.

### 3.1 Introduction

The exposure simulation in *SAMPLE* is based on Monte Carlo calculations of electron trajectories, in which pseudorandom numbers are used to determine the scattering angles, weighted probabilities of atomic interaction, and path length between collisions, etc. In the simulation, a large number of electron trajectories (e.g.,  $10^5$ ) must be calculated to provide sufficient statistical precision. However, if the pseudorandom number generator does not provide a sufficiently long series of random numbers, the statistical precision will suffer despite the use of a large number of electrons. Due to the speed constraint of the

Monte Carlo simulation used in *SAMPLE*, the original random number generator compromised the statistical precision for faster execution. As a result, artifacts such as kinks are sometimes observed in the simulated resist profiles. With the recent increase in the performance of computer workstations, the use of more sophisticated pseudorandom number generation algorithms becomes much more attractive.

After the spatial distribution of electron energy deposition is determined, *SAMPLE* utilizes a dissolution rate function of absorbed energy to convert the energy matrix into a rate matrix. This dissolution rate function is obtained from a combination of DRM data and the Monte Carlo simulation of energy as a function of depth into the resist. With the advent of new resist and processing technologies such as negative chemically-amplified resists and the interrupted development of positive DQN resists, new resist characterization techniques and models must be developed for *SAMPLE*.

For the advanced resists, the feasibility of using a dissolution rate formula similar to the molecular-weight-based dissolution model is demonstrated. The two negative resists Hitachi RD-2000N and Shipley ECX-1033 are then used for illustration of the general modeling technique. For the interrupted development of the DQN resist, a model of the overall effect of the interruptions is developed which is based on the resist film thickness versus development time data measured at the end of each interruption. Comparisons of simulated and experimental resist profiles are then used to verify the models. Despite the good agreement between the simulations and experiments, there is a need to develop advanced characterization and modeling techniques if simulation is to be used to understand the underlying mechanisms and to evaluate and optimize these new resists and processing technologies.

TABLE 3.1. Exposure systems used in the characterization experiments.

Systems	Beam Voltage	Beam Shape
AEBLE-150	20 keV	Variable, square
EL-3	50 keV	Variable, square

### 3.2 Exposure Simulation

The exposure energy deposition simulations used in the characterization studies are based on the Monte Carlo technique using extensions of the technique of Adesida [1]. This Monte Carlo technique is also used to prepare the spatial deposited energy distribution for *SAMPLE*. Two different exposure systems were used with the characteristics listed in Table 3.1. The exposure system used in the study of the two negative resists was the Etec AEBLE-150. To simulate the exposure by the AEBLE-150, a Monte Carlo program which utilizes the standard Rutherford scattering and Bethe energy loss theories to calculate the energy deposition was used. For the DQN resist, the exposure was performed on an IBM EL-3 system. Since EL-3 is a 50 keV system, secondary electrons significantly contributed to the deposited energy. Therefore, a Monte Carlo program\* which adds the occurrence and effects of fast secondary electron production was used.

The input to the Monte Carlo simulation program included the resist and substrate atomic compositions, and the acceleration voltage of the exposure system. For RD-2000N, the relative atomic composition of (73C:9.6O:69H:6N:1S) and a density of 1.3 g/cm<sup>3</sup> were used. Unfortunately, the composition of ECX-1033 cannot be determined because it is an experimental product and its formulation is proprietary. Nevertheless, since the major elements in most resists are very similar, the energy deposition for RD-2000N can be used for

---

\*. This version of the Monte Carlo program was written by M. G. Rosenfield.

ECX-1033 as well. In the simulation, a large number of electron trajectories (e.g.,  $10^5$ ) were calculated to provide sufficient statistical precision for the analysis.

The statistical precision depends equally on the number of electrons simulated and the pseudorandom number generator, which is used to determine scattering angles, weighted probabilities of atomic interaction, path lengths between collisions, etc. A generator without a sufficiently long period of pseudorandom number generation could lead to errors in the

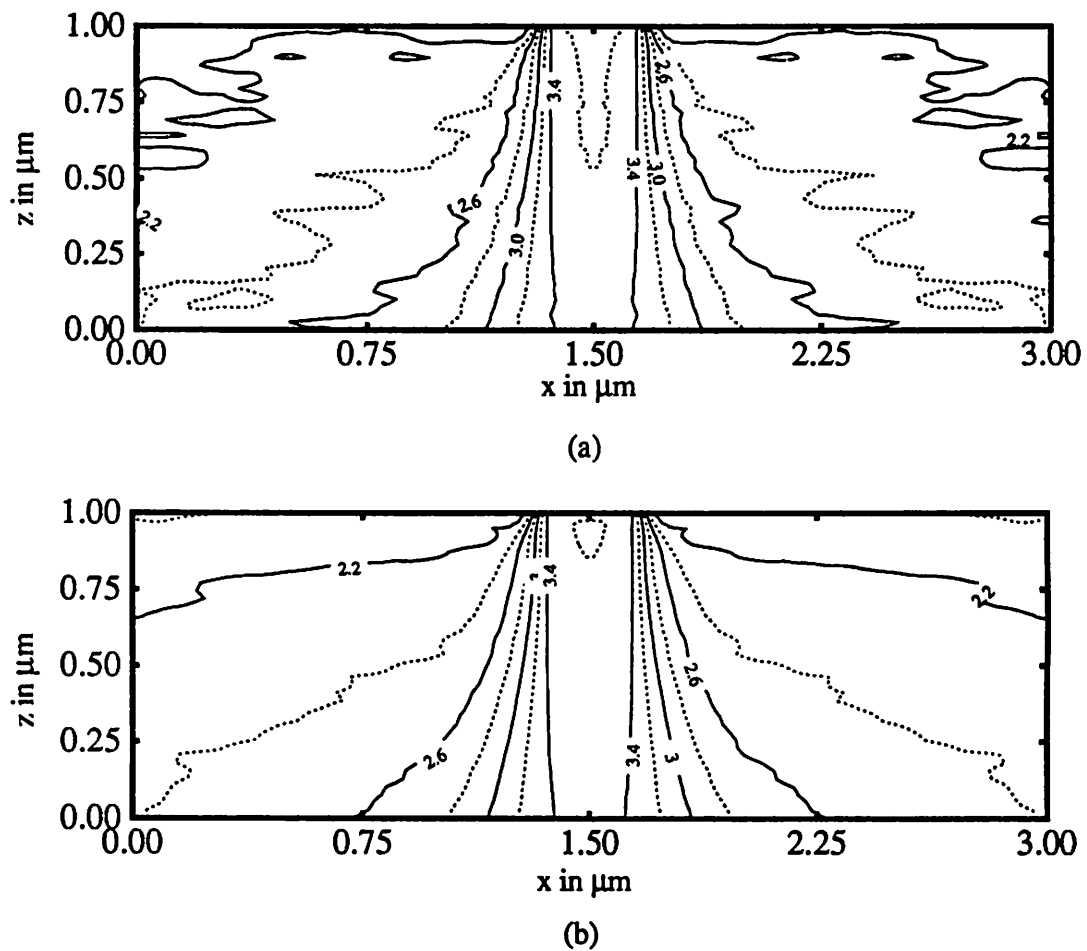


**Figure 3.1.** Contours of constant absorbed energy density (in  $\text{J}/\text{cm}^3$  and in log scale) calculated with *SAMPLE* for a  $0.3 \mu\text{m}$  line exposed with  $250 \mu\text{C}/\text{cm}^2$  in a  $1 \mu\text{m}$  thick PMMA. (a) Striation and local maximum away from the main feature are due to the bias in the energy deposition of the delta-function of the line source, which is calculated with a simple congruential algorithm. (b) Using a mixed congruential algorithm, the contours are much smoother.

electron energy deposition calculation. Figure 3.1 compares the absorbed energy profiles in the cross-section of an isolated  $0.3 \mu\text{m}$  line exposed with  $250 \mu\text{C}/\text{cm}^2$  in  $1 \mu\text{m}$  thick PMMA as calculated by *SAMPLE* using energy data files prepared with two different pseudorandom number generators. The data file used in Figure 3.1a is prepared with a simple congruential algorithm, which is used in the original Monte Carlo program for *SAMPLE*. Striations in the constant energy contours and local maxima of absorbed energy away from the center of the beam can be observed in Figure 3.1a. On the other hand, the contours in Figure 3.1b are obtained from data files which are calculated with a mixed-congruential algorithm [2], and they are much smoother. As a result, to obtain better precision, the pseudorandom number generator in the Monte Carlo program has been modified to use the mixed-congruential algorithm. However, the computational time for this method is more than double that for the simple congruential method. On a DEC3100, a run time of about 3 hours is required to compute the trajectories of 50,000 electrons.

The equi-energy contours shown in Figures 3.1a and 3.1b are obtained by convolving the Monte Carlo data, which gives the spatial distribution of energy deposited in the resist by a delta-function line source, with a  $0.3 \mu\text{m}$  exposure profile. In *SAMPLE*, the exposure profile can be a pattern of arrayed Gaussian or rectangular shaped electron-beams. The convolution operation to calculate the energy deposition in two-dimensions is illustrated in Figure 3.2. The convolution is performed in a "window" of resist profile simulation using the superposition of effects from a larger pattern writing window. In the window of resist profile simulation, the resist is actually represented by a two-dimensional array to store the absorbed energy density. The energy deposition in each row of the array, which corresponds to a depth in the resist, is computed by adding the contribution of absorbed energy density from each of the delta functions in the window of interest. The convolution is com-

plete when the procedure has been carried out for each row of the Monte Carlo data which extends to a range of, for example, 5  $\mu\text{m}$  from the center of the exposure.

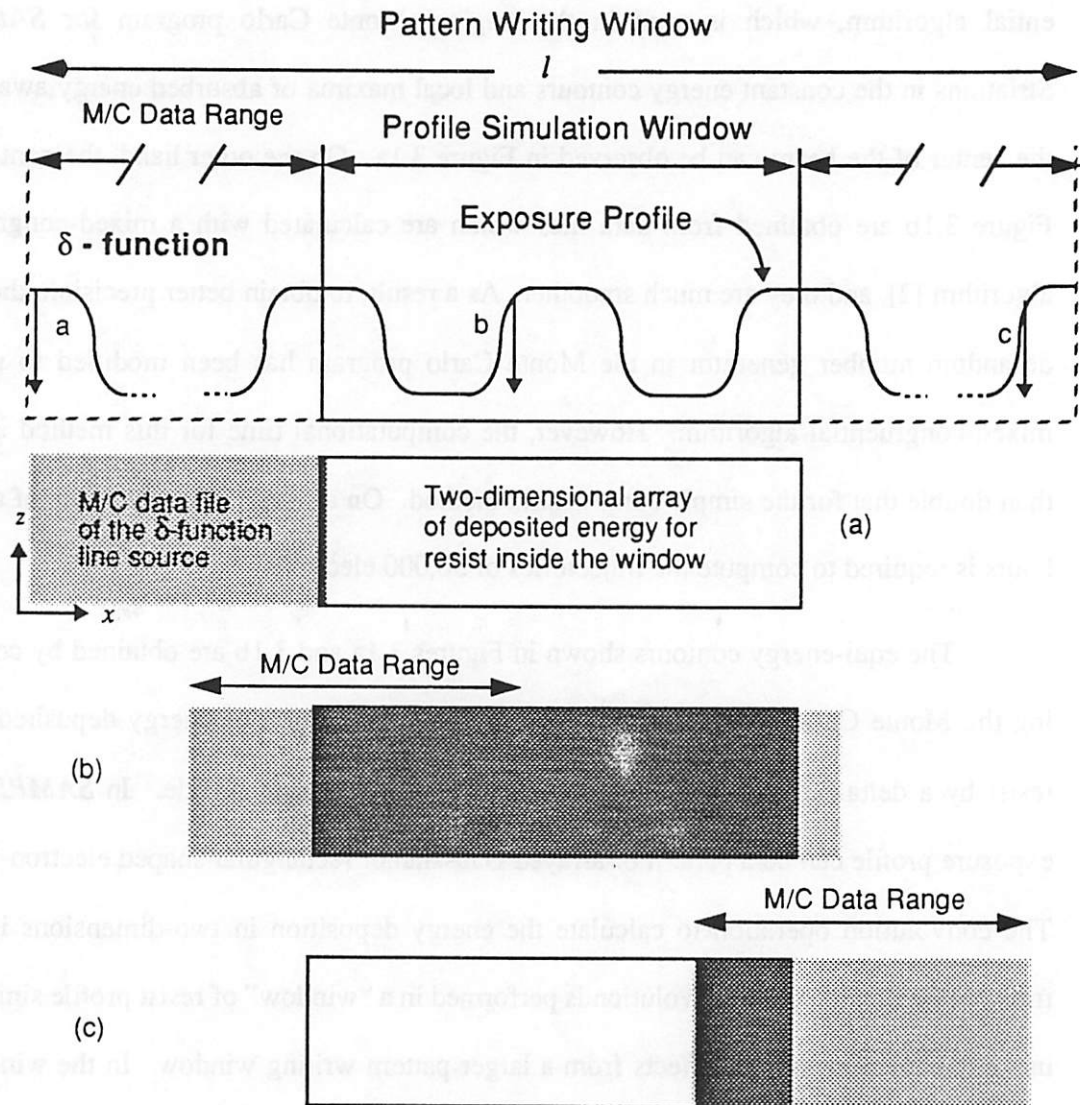


**Figure 3.2.** An example to illustrate the convolution operation. The delta function is convolved with the exposure profile and the energy deposition inside the user-defined resist window. The contribution of energy deposition by the line source is represented by the overlapping region of the arrays. The final energy deposition is the summation of all the overlapping regions.

### 3.3 Dissolution Characterization and Modeling

In this section, the dissolution characterization experiments and the determination of resist dissolution models are described. For the chemically-amplified resist ECX-1033, after the post-exposure bake was applied the development processing was identical to that of RD-2000N. As a result, the characterization experiments for the two negative e-beam resists were very similar and in fact, were the extensions of the approach outlined in Figure 2.3. For the interrupted development of the DQN resist, the development procedure involves interruptions in which the resist is rinsed and dried after partial development.

#### 3.3.1 Dissolution Rate Measurements of Negative e-beam Resists

The characterization experiments of the dissolution of the two resists were performed on the DRM. Table 3.2 lists the processing conditions of the resists for the DRM experiments. The exposure pattern was a matrix of twelve 8 by 2 mm<sup>2</sup> rectangles with exposure doses ranging from 2.5 to 100  $\mu\text{C}/\text{cm}^2$ . For ECX-1033, a bake at 105°C for two minutes was applied on a hot plate, after exposure and prior to development. A beam current of 25 A/cm<sup>2</sup> was used in all cases, except where specifically noted.

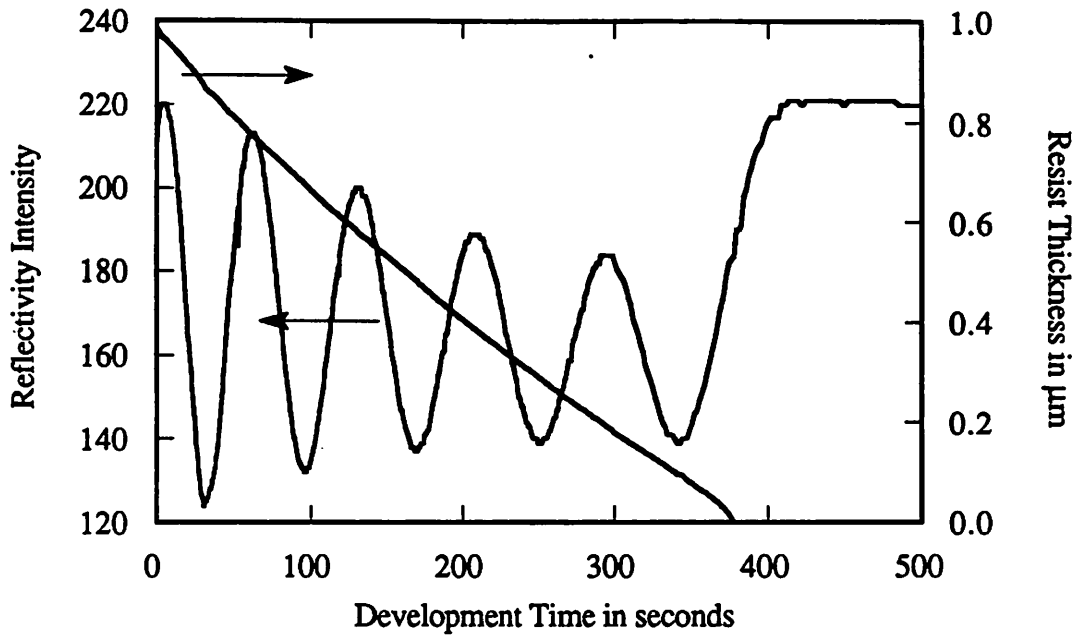
TABLE 3.2. Processing conditions for Development Rate Measurements of RD-2000N and ECX-1033.

	RD-2000N	ECX-1033
Substrate	HMDS Primed 4" wafer	HMDS Primed 4" wafer
Resist thickness	1 $\mu\text{m}$	1 $\mu\text{m}$
Prebake	90°C, 30 min	90°C, 30 min
Post-Exposure Bake	none	105°C, 2 min
Developer	RD-2000N	MF-312
Developer Temp.	21°C	21°C

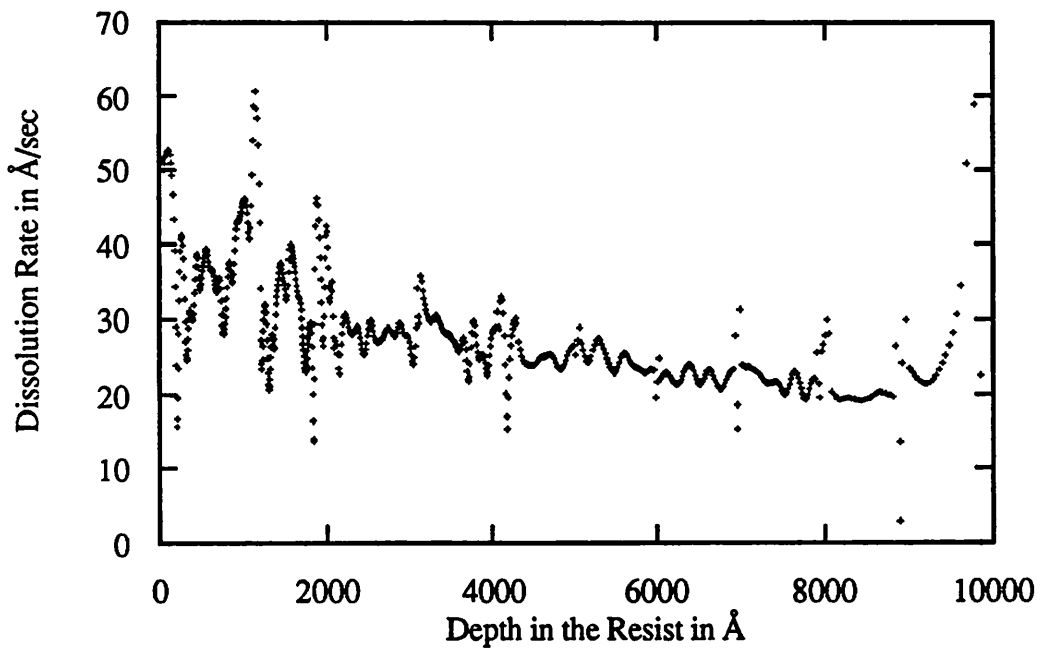
### 3.3.2 Parameter Extraction

Even with the use of the automated DRM, characterizing a resist still requires many experiments. The data reduction and analysis following the measurements are a major bottleneck in the data acquisition. After collecting the dissolution rate data, a model is needed to fit the experimental data. Due to the complexity of the dissolution rate data, usually various forms of the rate equations have to be tried before a satisfactory model can be obtained. Moreover, because of the non-linearity in the data, sophisticated non-linear regression techniques have to be used to calculate the best fit parameter. To automate this data analysis and parameter extraction process, the program *PARMEX* [3] has been developed at the University of California at Berkeley. It provides a powerful and user-friendly software package so that various highly non-linear dissolution rate models can be evaluated and fit to the experimental data.

The generation of dissolution rate versus absorbed energy density data requires three stages of data processing: 1) conversion of reflectivity versus time data to thickness of resist removed versus time data, 2) calculation of dissolution rate as a function of depth into the resist, and 3) calculation of rate versus energy data from the rate versus depth data. Figure 3.3a shows a typical reflectivity versus development time curve and the resulting thickness versus development time curve obtained from the DRM measurement. The measurements were collected from one of the zones on a 1  $\mu\text{m}$  thick RD-2000N exposed with a dose of 15  $\mu\text{C}/\text{cm}^2$ . The dissolution rates as a function of depth into the resist are plotted in Figure 3.3b. As expected for a negative resist, the dissolution rate decreases at lower depths because the deposited energy is an increasing function of depth for the range of accelerating voltage and resist thickness used in the characterization experiment. The rate data in Figure 3.3b are then converted to  $R(E)$  data using the Everhart and Hoff equation [4]. The resulting



(a)



(b)

**Figure 3.3.** Intermediate results in the data analysis of dissolution rate versus absorbed energy data for a 1  $\mu\text{m}$  thick RD-2000N resist exposed with  $15 \mu\text{C}/\text{cm}^2$ . (a) The intensity versus time curve and the resulting thickness versus time curve. (b) Dissolution rate versus depth data calculated from the thickness versus time curve.

data as a function of absorbed energy of RD-2000N is shown in Figure 3.4a. As a comparison, similar data for ECX-1033 are plotted in Figure 3.4b.

To fit these data, a model similar to the one that was used for the effects of molecular weight on dissolution rate was chosen, and the dissolution rate as a function of absorbed energy density is given by

$$R = \frac{R_0}{\left(1 + \frac{E}{E_0}\right)^\alpha} \quad (\text{EQ 3.1})$$

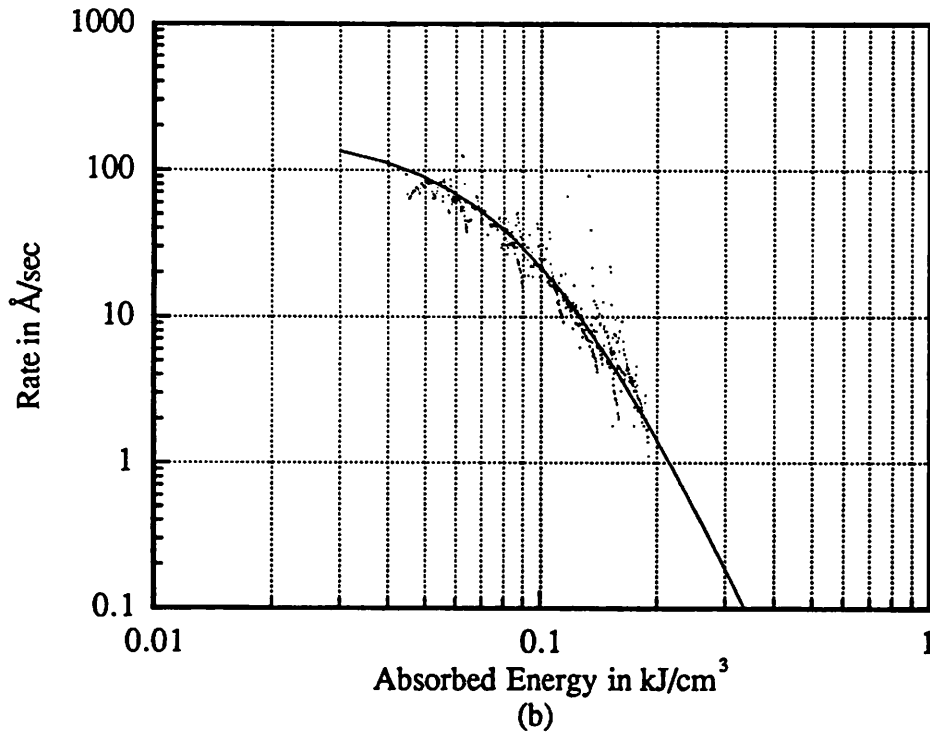
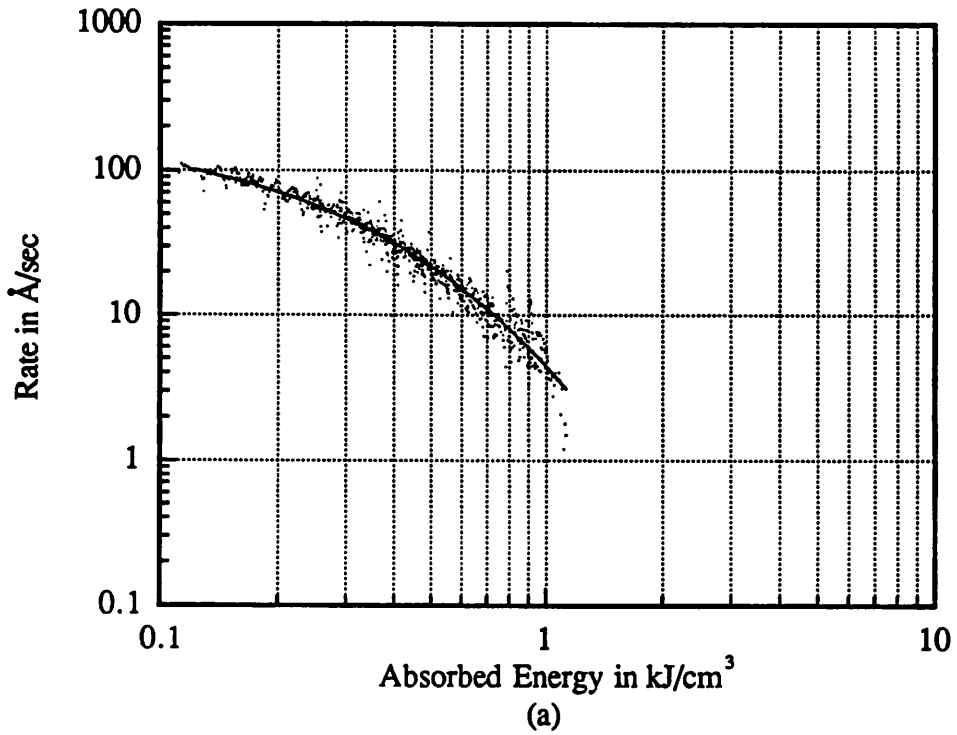
Here  $R_0$  denotes the development rate of the unexposed resist, and  $E_0$  and  $\alpha$  are semi-empirical fitting parameters. The model is fitted to the experimental data using *PARMEX* and the extracted parameters are listed in Table 3.3. The solid lines in Figures 3.4a and 3.4b are the dissolution rate curves calculated with these parameters. The smaller  $E_0$  and higher  $\alpha$  of ECX-1033 indicate that the chemically amplified resist is superior in both sensitivity and contrast to RD-2000N.

TABLE 3.3. Extracted dissolution rate parameters for RD-2000N and ECX-1033.

	RD-2000N	ECX-1033
$R_0$	180 Å/sec	216 Å/sec
$E_0$	1360 J/cm <sup>3</sup>	300 J/cm <sup>3</sup>
$\alpha$	6.72	8.27

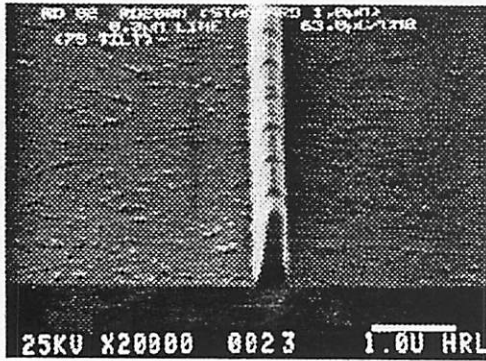
### 3.3.3 Profile Simulation and Experimental Comparison

Equation (3.1) is implemented in *SAMPLE* to test the validity of the model and study resist development profile effects. Comparisons between simulated and experimental resist profiles of RD-2000N are given in Figures 3.5 and 3.6. Figure 3.5 shows the cross-



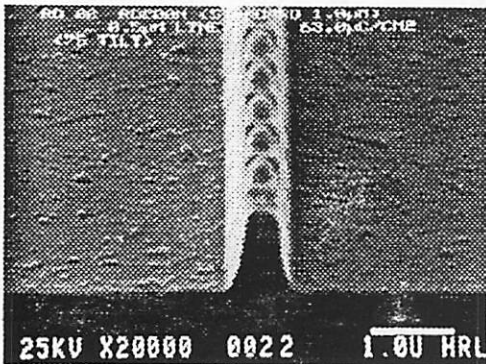
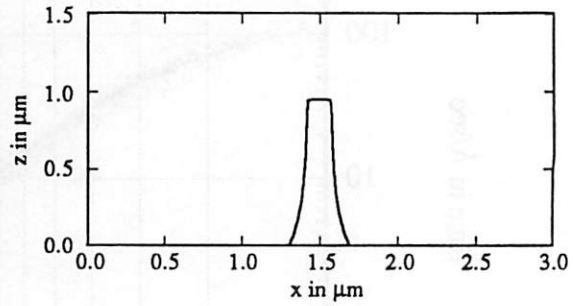
**Figure 3.4.** Dissolution rate versus absorbed energy density for (a) RD-2000N exposed with  $25 \text{ A/cm}^2$  beam current density, and (b) for ECX-1033 exposed with  $5 \text{ A/cm}^2$  beam current density. ECX-1033 is much more sensitive than RD-2000N.

### Experimental

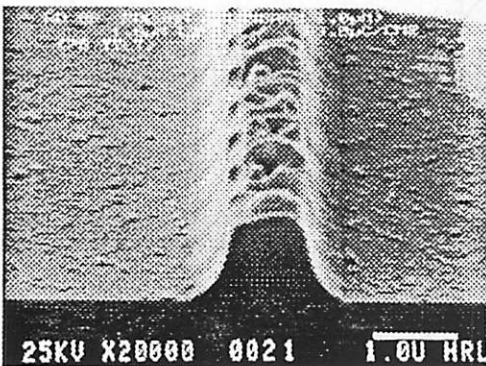
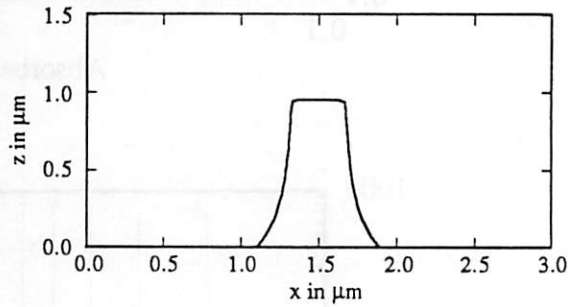


(a)

### Simulation



(b)



(c)

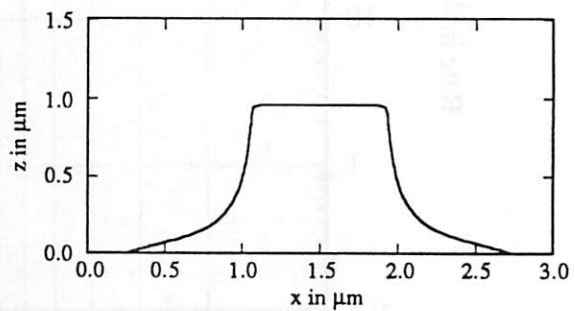
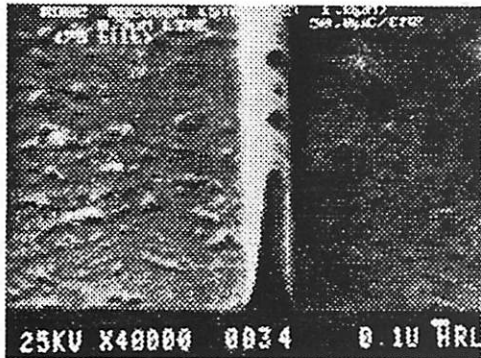


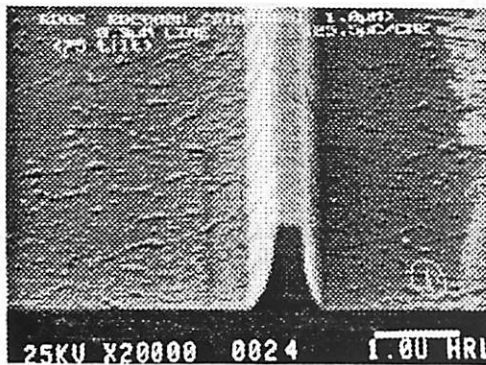
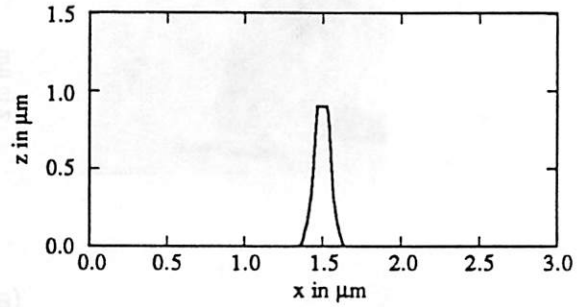
Figure 3.5. Experimental and simulated resist line-edge profiles for an isolated line exposed in 1.0 μm of RD-2000N at doses of 63 μC/cm<sup>2</sup> with linewidth of (a) 0.3 μm (b) 0.5 μm, and (c) 1.0 μm using 2 min development.

## Experimental

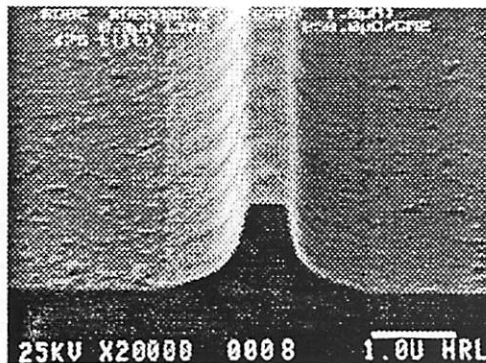
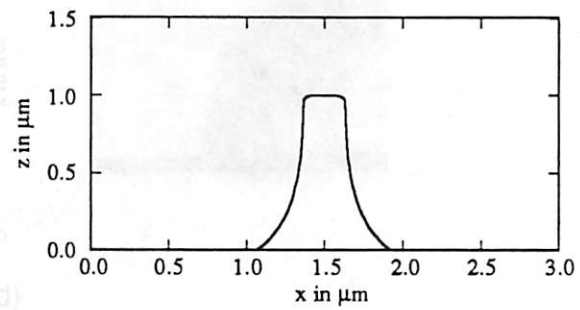


(a)

## Simulation



(b)



(c)

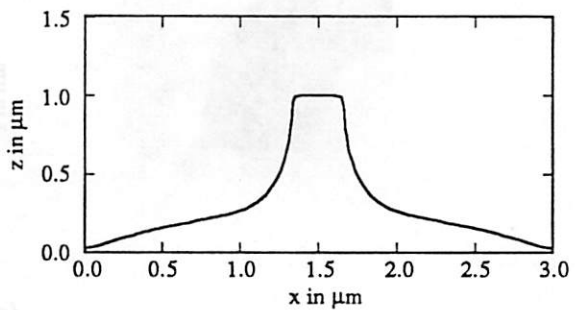
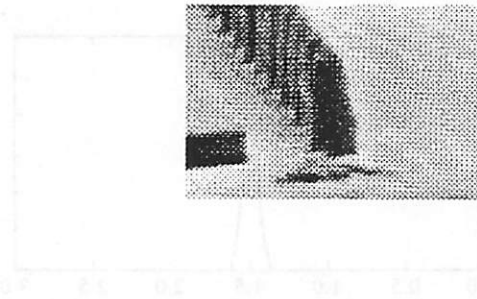


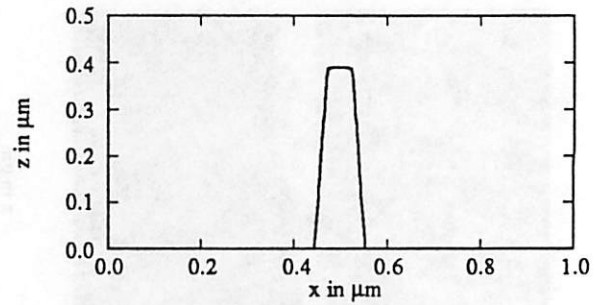
Figure 3.6. Experimental and simulated resist line-edge profiles for a 0.3 μm isolated line exposed in 1.0 μm of RD-2000N at doses of (a) 50 μC/cm<sup>2</sup>, (b) 125 μC/cm<sup>2</sup>, and (c) 250 μC/cm<sup>2</sup> using 2 min development.

## Experimental



(a)

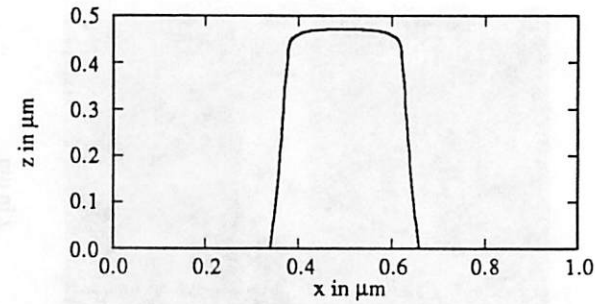
## Simulation



(b)



(b)



(c)

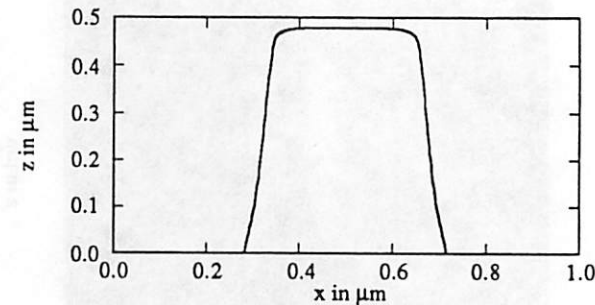
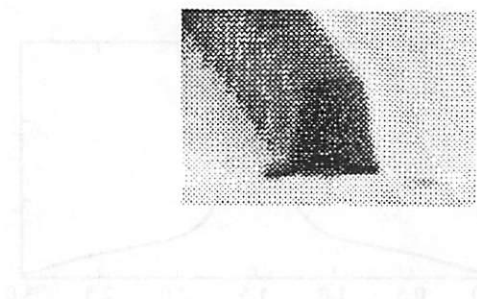


Figure 3.7. Experimental and simulated resist line-edge profiles for a 0.3 μm isolated line exposed in 0.5 μm of ECX-1033 at doses of (a) 10.0 μC/cm<sup>2</sup>, (b) 20.0 μC/cm<sup>2</sup>, and (c) 31.6 μC/cm<sup>2</sup> using 2 min development.

sectional SEM micrographs and simulated resist line-edge profiles for 0.3, 0.5, and 1.0  $\mu\text{m}$  isolated lines, exposed with  $63 \mu\text{C}/\text{cm}^2$  and developed in RD-2000N developer for 2 min. Figure 3.6 shows the variations of the linewidth due to over-exposure, as three 0.3  $\mu\text{m}$  isolated lines were exposed with 50, 125, and 250  $\mu\text{C}/\text{cm}^2$ . Generally, good agreement is obtained between the simulation and the experiment, especially considering the large range of doses used. The advantage of ECX-1033 is demonstrated in Figure 3.7, where experimental and simulated 0.3  $\mu\text{m}$  lines of ECX-1033, with similar dimensions to the ones for RD-2000N in Figure 3.6, are shown. For a 2 minute development in MF-312, the doses required are reduced by a factor of 5 to 8. In addition, there are no pedestals in the ECX-1033 line-edge profiles due to the high contrast of this resist.

### **3.3.4 Interrupt Effect in the Development of a DNQ Resist**

The effect of interrupted development on the dissolution of the IBM DQN resist can be observed by monitoring the resist film thickness remaining as a function of development time under different exposures. Figures 3.8a and 3.8b compare the resist film thickness versus development time curves with straight development and interrupted development for doses ranging from 0 to 70  $\mu\text{C}/\text{cm}^2$ . The curve with straight development was measured with the DRM. On the other hand, resist film thickness data for interrupted development were measured at the end of each interrupt with a Nanospec. The interrupt schedule used consisted of 60, 30, ..., 30 second development intervals with a total development time of 5 minutes. As a result, data were obtained for 60, 90, 120, 150, 210, 240, 270, and 300 second development times.

The two sets of thickness curves are considerably different. The time difference of 50 seconds versus 2 minutes for the 60  $\mu\text{C}/\text{cm}^2$  curves to reach zero thickness is likely due

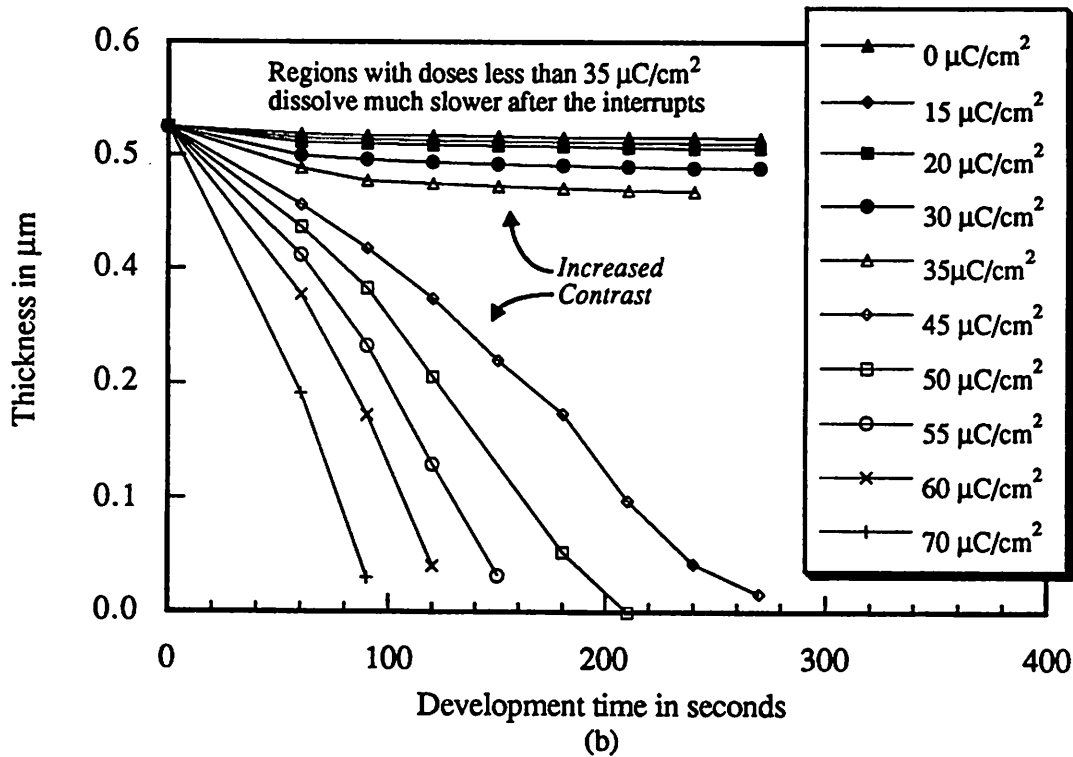
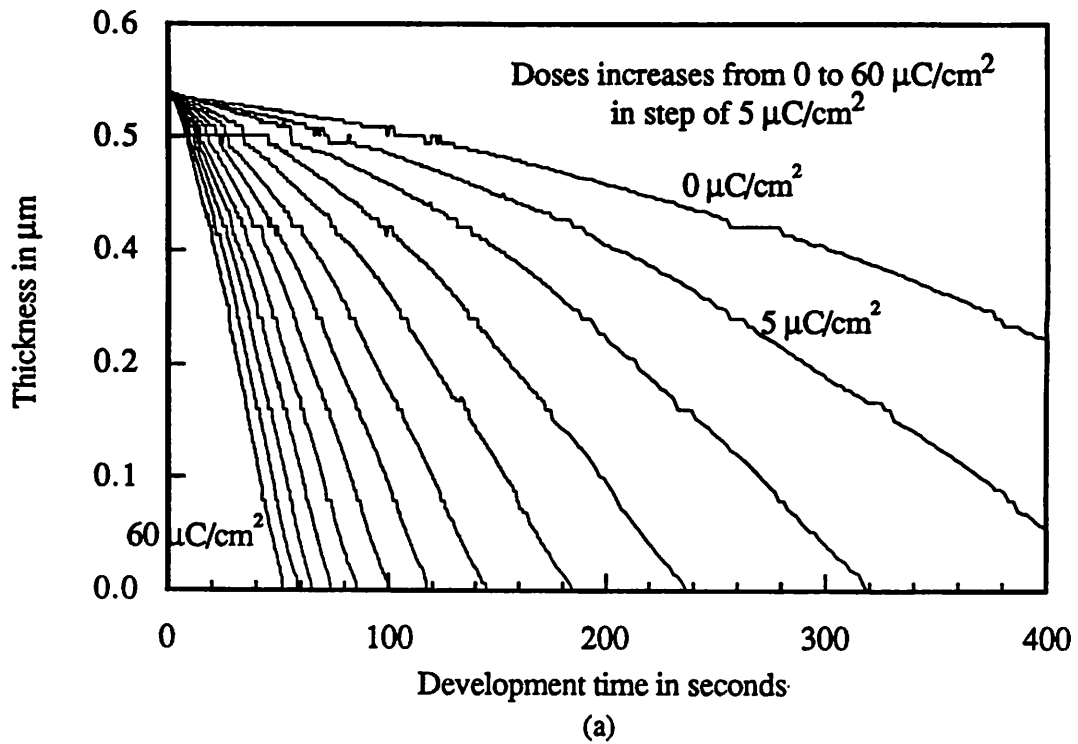


**Figure 3.8.** Comparison of resist film thickness versus development time curves of an IBM DNQ/Novolak resist with (a) straight development in a DRM and (b) thickness measured at the end of each interrupt using a 60, 30, ..., 30 sec interrupted development.

to a different lot of developer and the absence of agitation in the tank development for the interrupted case. Nonetheless, there is a significant increase in the contrast of the resist with interrupted development. In straight development, the dissolution rate of the resist increases gradually with exposure dose. However, in interrupted development, there is very little development for resists with exposure doses less than or equal to  $35 \mu\text{C}/\text{cm}^2$  after the first interrupt. When the dose exceeds  $40 \mu\text{C}/\text{cm}^2$ , the dissolution rate of the resist does not appear to be affected by the interrupt. As a result, the contrast of the resist is improved. Furthermore, since all the features delineated in the resist near the endpoint of the development receive very little dose, their near-zero dissolution rates significantly minimize the changes in linewidth due to over-development. Therefore, interrupted development improves both the contrast and the process latitude.

#### **3.3.4.1 Rate Dependence on Deposited Energy and Interrupt**

In order to gain a deeper understanding of the interrupted development, the development rate as a function of deposited energy for each development interval was compared. These dissolution rate data were estimated from the thickness versus development time curves using linear extrapolation. Therefore, they can be considered as an average development rate in that development interval. The average dissolution rate versus deposited energy data for all the development intervals are plotted in Figure 3.9. In the first development cycle, the average dissolution rate is a straight line on a log rate versus energy plot, indicating an exponential dependence on deposited energy. However, after the first interrupt there is a critical energy around  $410 \text{ J}/\text{cm}^3$ , below which the dissolution rate decreased by more than a factor of 5. As more interrupts were applied, the decrease in the rate continued until it reached around  $0.1 \text{ \AA}/\text{sec}$ . Above the critical energy, the average dissolution rates were not affected by the interrupts. These rate data indicate that the improved performance

of the DNQ resist with interrupted development is due to the introduction of additional rate retardation after the interrupt in the low exposure dose regions.

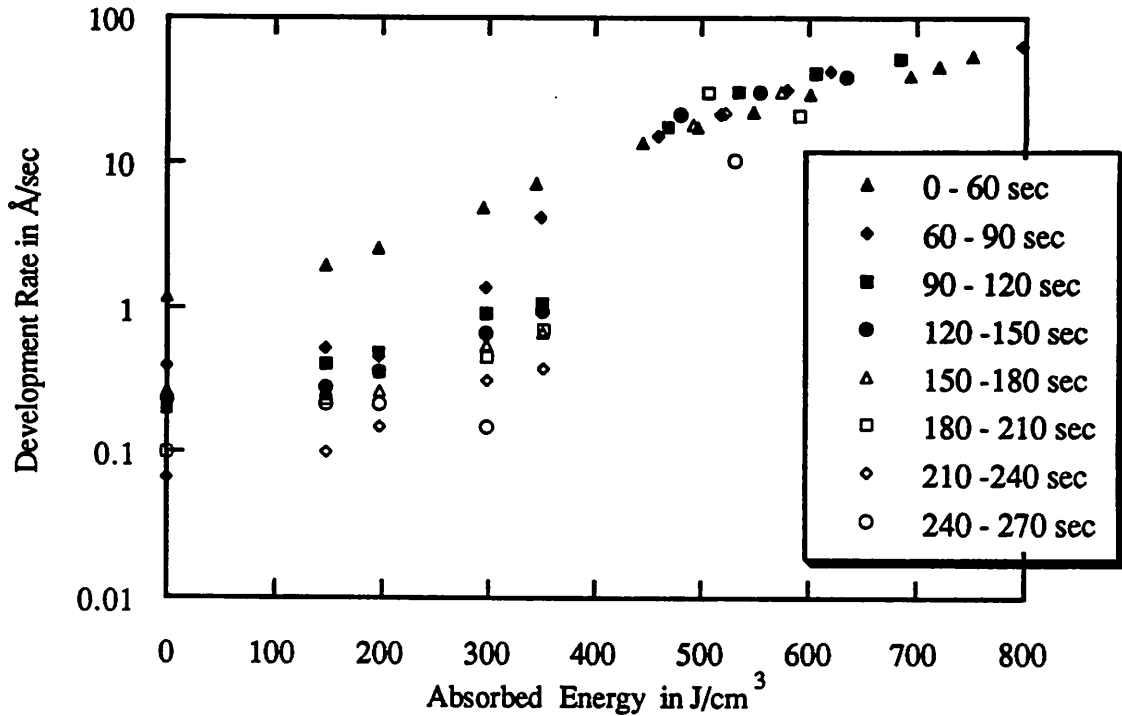


Figure 3.9. Dissolution rate as a function of deposited energy for the different development intervals used in obtaining the thickness versus development time data shown in Figure 3.8b.

### 3.3.4.2 Modeling the Rate Data of Interrupted Development

To test the validity of the dissolution rate data, a semi-empirical equation was developed to model the data and to simulate the interrupted development process:

$$\log R(E) = F_1 + F_2 (F_5 (F_3 E - F_4) + \tanh (F_3 E - F_4)) \quad (\text{EQ 3.2})$$

In Equation (3.2), all the fitting parameters can be estimated from the data and thus good initial guesses can be obtained for the nonlinear regression. The hyperbolic tangent function was chosen to fit the abrupt jump of the dissolution rate when the deposited energy changes from 300 to 500 J/cm<sup>3</sup>. Therefore,  $F_3$  and  $F_4$  correspond to the horizontal translation of the

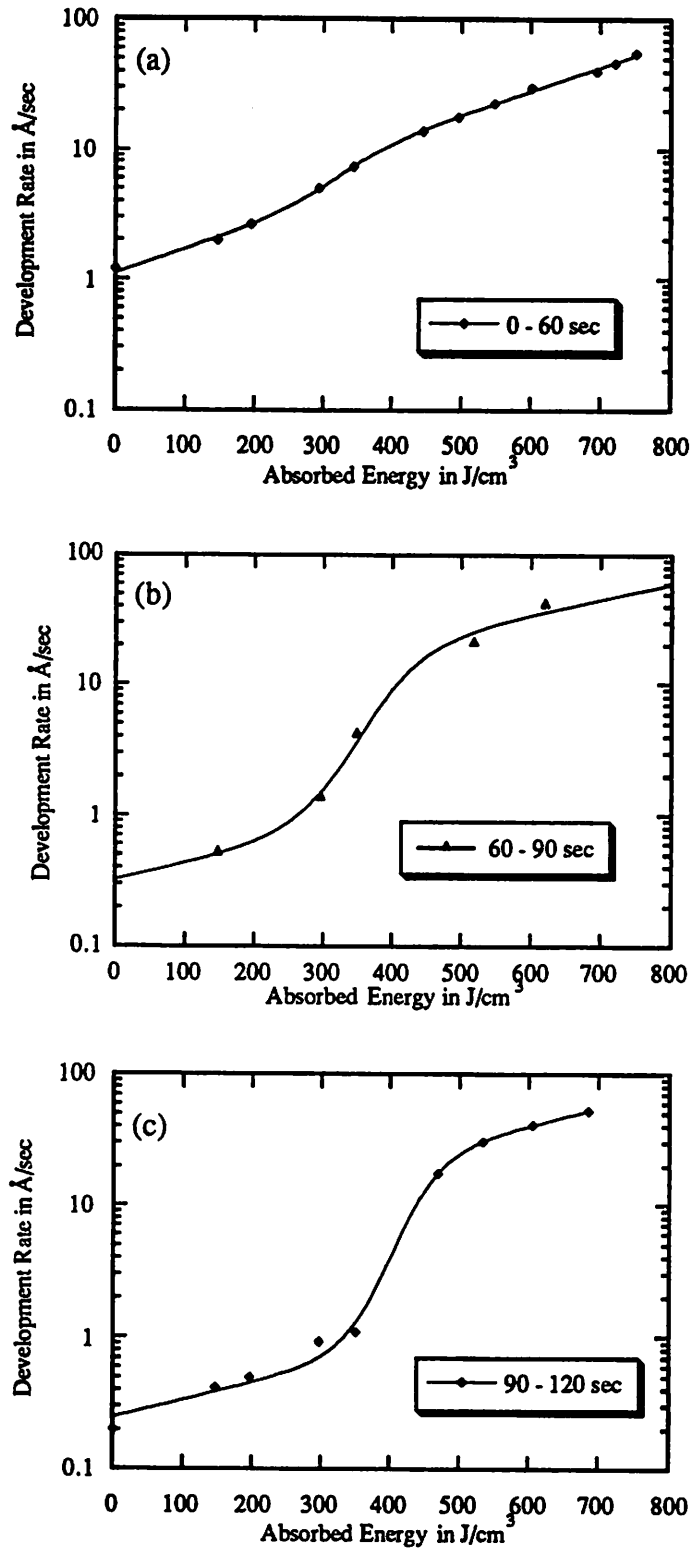


Figure 3.10. Dissolution rate data and the fitted curves of Equation 2.4 for the first three development intervals: (a) 60 - 90 sec, (b) 90 - 120 sec, and (c) 90 - 120 sec.

hyperbolic tangent function from the origin to the point near the critical energy.  $F_1$  is used to shift the curve up from the abscissa to the rate near the critical energy.  $F_2$  is the scaling factor for the range of dissolution rate in the data. Finally, the term involving  $F_5$  is added to describe the sloping of the rate data outside the critical energy regions. The function is very stable and the fitted curves for the first three intervals are plotted in Figure 3.10. The fitting parameters for equations of the first seven development intervals are listed in Table 3.4. However, after 210 sec of development, there was insufficient data to continue the curve fitting with Equation (3.2).

TABLE 3.4. Fitted Parameters of the Different Development Interval Rate Equations

Dev. Time.	$F_1$	$F_2$	$F_3$	$F_4$	$F_5$
0 - 60 sec	0.7817	0.1491	0.01091	3.482	1.131
90 - 60 sec	0.5848	0.6566	0.01064	3.731	0.1706
90 - 120 sec	0.6382	0.7156	0.01408	5.679	0.1299
120 - 150 sec	0.5834	0.7167	0.01903	7.621	0.09073
150 - 180 sec	0.5753	0.7055	0.01878	8.005	0.1075
180 - 210 sec	0.4952	0.7451	0.01837	8.117	0.1613

### 3.3.4.3 Comparison of Experiment and Simulation

Once the rate equations are determined, they can be implemented in *SAMPLE* to simulate interrupted development. For the first development cycle, the parameters from the first 60 second development interval are used in the rate equation. After the development time reaches 60 seconds, the rate parameters are changed to the second set of parameters. For development longer than 210 seconds, the parameters from the sixth interval are used. Figure 3.11 shows the *SAMPLE* calculations of resist film thickness remaining as a function of development time and they match the experimental data very well. The predictions of resist line-edge profiles with this time-varying rate equation approach are also quite good.

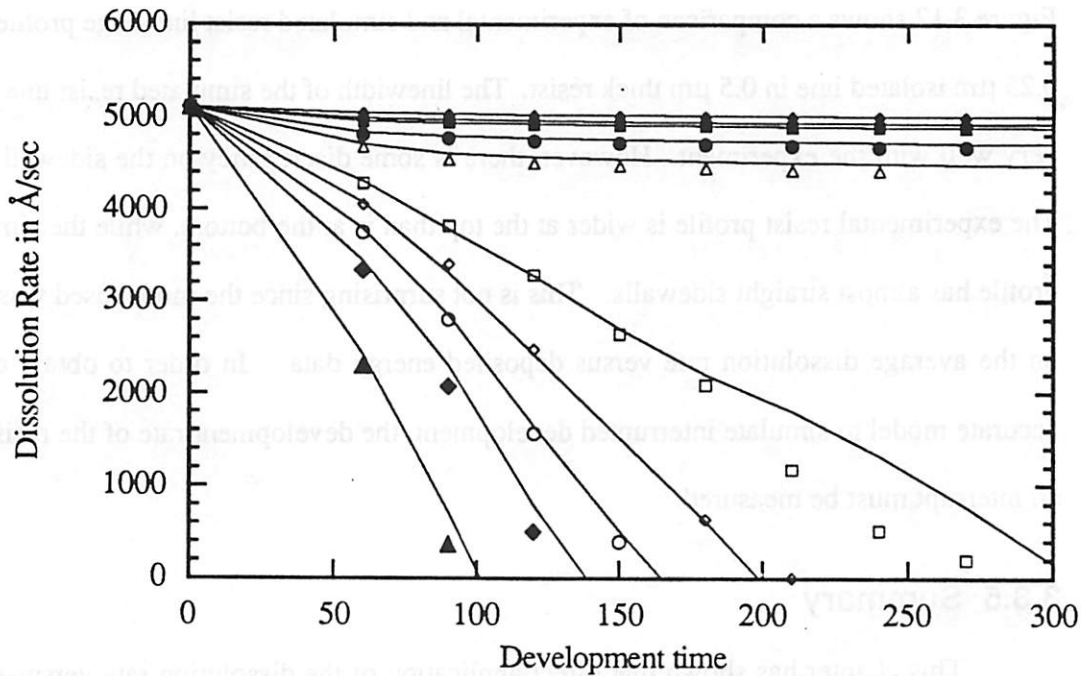


Figure 3.11. Comparison of experimental and simulated resist film thickness remaining as function of development time. Solid lines are simulation results.

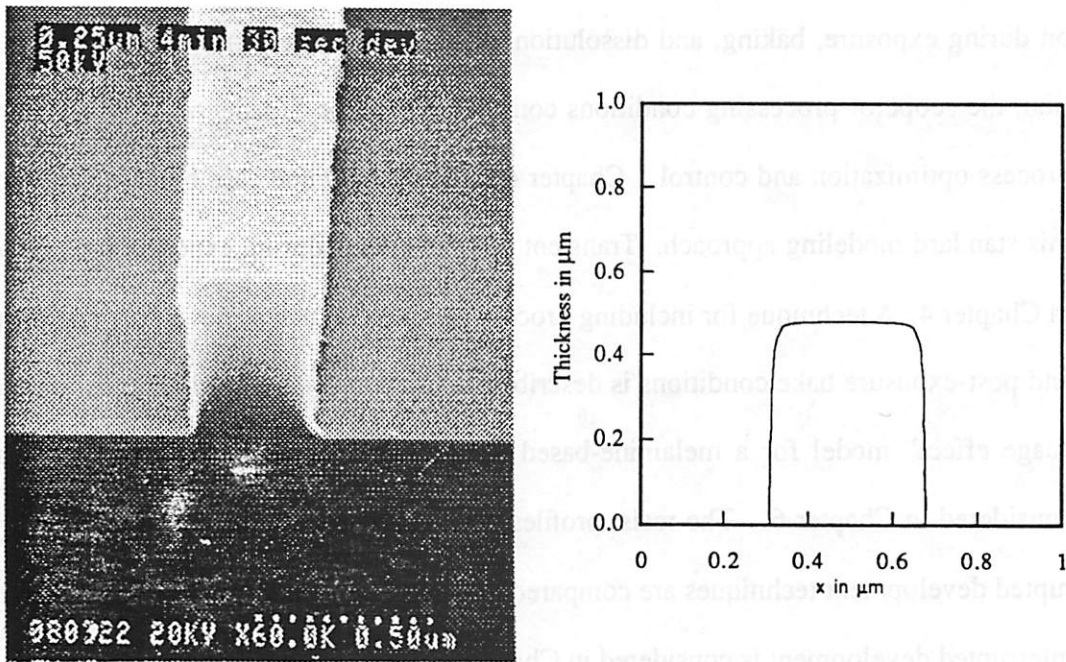


Figure 3.12. Comparison of experimental and simulated resist line-edge profiles for a  $0.25 \mu\text{m}$  isolated line. The exposure dose is  $45 \mu\text{C}/\text{cm}^2$  and the resist was developed with a 60,30,...,30 sec interrupted development for 4 min 30 sec. The simulation cannot reproduce the greater than  $90^\circ$  sidewall angle in the experimental resist profiles.

Figure 3.12 shows a comparison of experimental and simulated resist line-edge profiles for a 0.25  $\mu\text{m}$  isolated line in 0.5  $\mu\text{m}$  thick resist. The linewidth of the simulated resist line agrees very well with the experiment. However, there is some discrepancy on the sidewall angle. The experimental resist profile is wider at the top than is at the bottom, while the simulated profile has almost straight sidewalls. This is not surprising since the model used was based on the average dissolution rate versus deposited energy data. In order to obtain a more accurate model to simulate interrupted development, the development rate of the resist after an interrupt must be measured.

### 3.3.5 Summary

This chapter has shown that direct application of the dissolution rate versus energy model under a specific set of process conditions gives a model which can be used to predict resist profiles. However, from these case studies it is clear that there are phenomena that go on during exposure, baking, and dissolution which are not adequately described. In addition, the scope of processing conditions considered must be broadened to be of interest in process optimization and control. Chapter 4 to 8 now examine case by case extensions of this standard modeling approach. Transient thermal effects during exposure are considered in Chapter 4. A technique for including process parameters such as developer concentration and post-exposure bake conditions is described in Chapter 5. A closed-form solution of the “cage effect” model for a melamine-based acid-hardening chemically-amplified resist is considered in Chapter 6. The resist profiles obtained with variations of the original interrupted development techniques are compared in Chapter 7. Finally, a time-delay model for interrupted development is considered in Chapter 8.

## References

- [1] I. Adesida, "Electron Energy Dissipation in Layered Media," *Ph.D. Dissertation*, Department of Electrical Engineering and Computer Sciences, University of California, Berkeley, 1979.
- [2] E. J. Dudewicz, *The Handbook of Random Number Generation and Testing with TESTRAND Computer Code*, American Sciences Press, Columbus, Ohio, 1981.
- [3] W. Bell II, P. Flanner III, C. Zee, N. Tam, and A. Neureuther, "Resist Characterization Using a Multichannel Development Rate Monitor," *Proceedings SPIE: Advances in Resist Technology and Processing V*, vol. 920, pp. 382-389, 1988.
- [4] T. E. Everhart and P. H. Hoff, "Determination of Kilovolt Electron Energy Dissipation vs. Penetration Distance in Solid Materials," *J. Appl. Phys.*, vol. 42, no. 13, pp. 5837-5846, 1971.

## **Chapter 4**

# **Thermal Effects of Electron-Beam Exposure**

During the course of systematic measurements of dissolution rate of the Hitachi RD-2000N resist, it was discovered that exposures on the AEBLE-150 at  $25 \text{ A/cm}^2$  affect the sensitivity of the resist and produce deformation in the resist when the doses were above  $30 \mu\text{C/cm}^2$ . These effects were then examined carefully and were determined to be caused by the thermal heating of the resist during exposure. A new massively-parallel modeling approach was then developed to estimate the temperature rise and to examine the role of exposure pixel placement in the localized heating of the resist during exposure. This chapter presents the experimental results in the identification of the thermal effects and describes the temperature rise estimations with the simulation model.

### **4.1 Introduction**

Beam-induced heating is a major concern in e-beam lithography because excessive temperature rise can cause pattern variations.[1]-[3] With gaussian-beam raster scanning machines, thermal effects mostly occur in mask writing where the quartz substrates are not thermally conductive.[4] As the demands for higher throughput continue, however, variable shape-beam exposure systems with high current capability are becoming the dominant exposure tools in direct silicon write.[6][7] This class of exposure machines can decrease the writing time of a wafer by reducing the number of flashes required in a pattern and minimizing the dwell time for each flash. As the size of the beam increases further with cell projection lithography [8], transient temperature rise becomes more severe.

In direct writing on silicon wafers, the wafer generally provides a good heat sink so that the primary concern is one of local heating in the resist. Chemical changes in the resist

can be expected with moderate temperature rise. If the temperature rises above the glass transition or ceiling temperature of the resist during exposure, it could cause both chemical and physical changes to the resist, such as diffusion reactions and violent outgassing of volatile components [9]. These thermal effects are undesirable because they can alter the linewidth or contaminate the e-beam column. The Hitachi RD-2000N is a prime example of resist affected by beam-induced heating when it is exposed in the Etec AEBLE-150. Similar resist heating problems also have been observed by van der Drift *et al.* [4] and Veneklasen [5]. The following sections will show that although the AEBLE-150 can deliver up to  $100 \text{ A/cm}^2$ , the maximum current density that can be used should not exceed  $25 \text{ A/cm}^2$  because exposure with beam current density at or above that would deform the resist pattern. As a result, thermal effects can severely limit the throughput of the exposure system.

In order to reduce these effects, excess temperature rise during exposure must be prevented. The knowledge of rise in temperature in the resist and its dependence on the exposure parameters is essential in determining the safe operating condition. Since there is currently no practical way to measure the temperature in the resist during exposure, the temperature rise has to be estimated by solving the heat diffusion equation. Previous work in the literature has focused on calculating temperature rise in the substrates of the resist under the e-beam. Murai *et al.* calculated the temperature rise in quartz substrate (with no resist) by solving the standard three-dimensional differential equation for heat diffusion [10]. In their calculation, the maximum temperature reached  $480^\circ\text{C}$  when the substrate was exposed with  $4 \mu\text{m}^2$  beam for  $2 \mu\text{s}$  ( $10 \mu\text{C/cm}^2$  at  $5 \text{ A/cm}^2$  and  $30 \text{ kV}$ ). In the work by Ralph *et al.*, [11] the temperature rises in Si and quartz substrates were calculated using the Green's function method. In their analysis, Si substrate temperature under an e-beam becomes critical (over  $100^\circ\text{C}$ ) only for cases with large exposure area ( $5 \times 5 \mu\text{m}^2$ ), high current density

(over  $50\text{A}/\text{cm}^2$ ) and high accelerating voltage (40 keV). In both cases, the calculations neglected the temperature rise in the resist and thus are not realistic estimation of the threshold of thermal effects in resist on Si substrate.

## 4.2 Thermal Effects on the Hitachi RD-2000N Resist

### 4.2.1 Beam Current Effects

In Chapter 2, a quantitative model of dissolution rate versus absorbed energy for RD-2000N has been shown to give good agreement between simulated and experimental resist profiles. However, at beam-current density of  $25\text{ A}/\text{cm}^2$  and high exposure doses, deviations from this model occur. The experimental results and the fitted dissolution rate obtained from RD-2000N exposed at  $25\text{ A}/\text{cm}^2$  at 20 keV are plotted in Figure 4.1. To illustrate the depth dependence of the dissolution rate, the points from the top most  $0.1\text{ }\mu\text{m}$  are

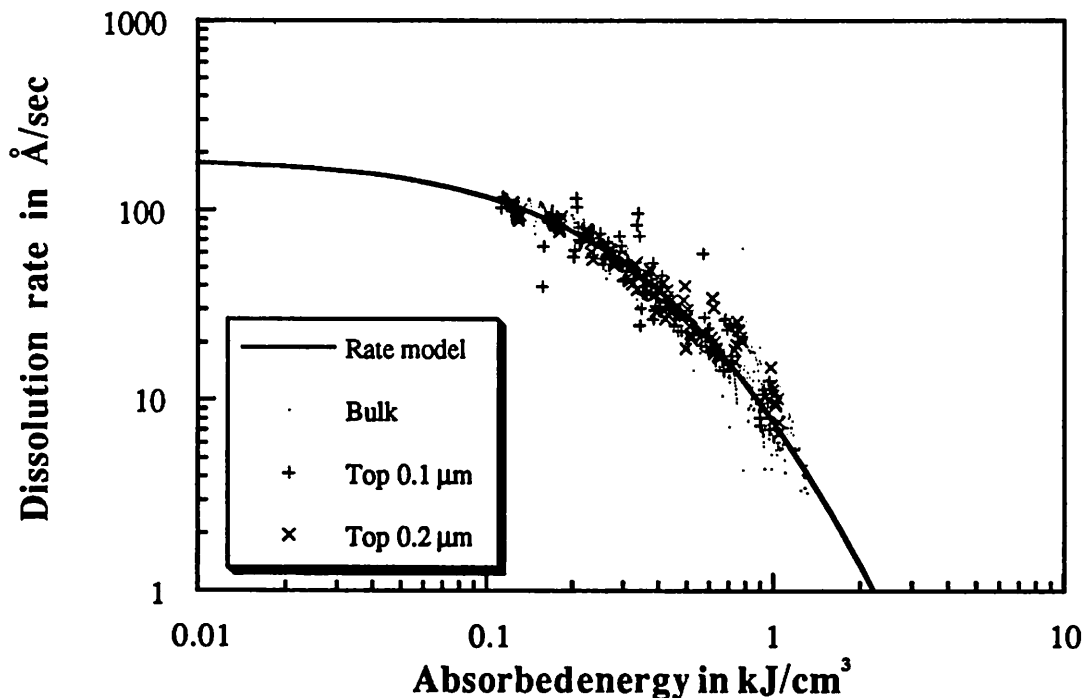
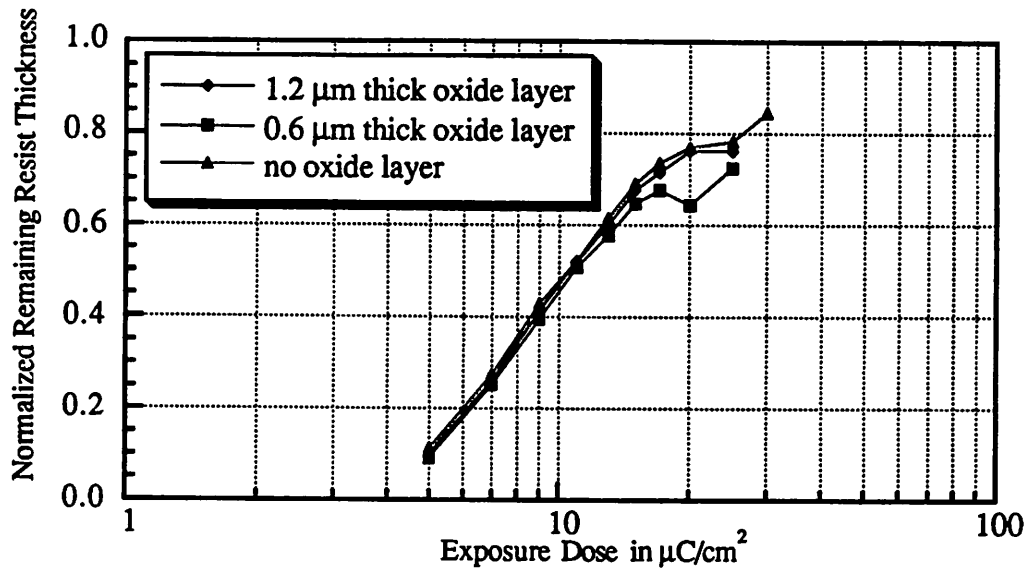


Figure 4.1. Dissolution rate as a function of absorbed energy for RD-2000N exposed at  $25\text{ A}/\text{cm}^2$  at 20 keV. Points from the top most  $0.1\text{ }\mu\text{m}$  are shown as + and those from the second  $0.1\text{ }\mu\text{m}$  are shown as x.



**Figure 4.3.** Normalized thickness remaining versus log dose curves for RD-2000N for 120 sec development with 0.0, 0.6  $\mu\text{m}$ , and 1.2  $\mu\text{m}$  thick oxide layers on Si substrate with exposure at 25  $\text{A}/\text{cm}^2$ .

#### 4.2.2 Oxide Thickness

To explore the effect of thermal impedance of underlying layers on potential thermal effects, a series of DRM resist thickness measurements were carried out using oxide substrate with exposure at 25  $\text{A}/\text{cm}^2$ . An oxide thickness of 1.2  $\mu\text{m}$  has a thermal impedance equivalent of 120  $\mu\text{m}$  of silicon. The resulting curves of resist thickness are shown in Figure 4.3 as a function of exposure dose for a development of 120 seconds. Little difference is observed for doses below 15  $\mu\text{C}/\text{cm}^2$ . However, at higher doses the behavior of the curves becomes very irregular. This irregularity is associated with the difficulty of the DRM due to reflectivity versus time data deteriorating in quality in this region. Difficulty in obtaining over 80% of the thickness remaining is also observed. This behavior is not markedly different from that observed on bare silicon indicating that the presence of oxide does not present a significant thermal problem. It is also an indication that the thermal conductivity of oxide is likely higher than that of the resist.

plotted in + and those from the second 0.1  $\mu\text{m}$  are plotted in x. For low deposited energy, the surface rates are indistinguishable from the bulk values and are described by Equation (2.5) with  $185\text{\AA}/\text{sec}$  for  $R_0$ ,  $812\text{ J}/\text{cm}^3$  for  $E_0$ , and 3.97 for  $\alpha$ . The dissolution rates in the surface region are more irregular than the rates in the bulk and at high doses, all the + and x are very close to or above the curve.

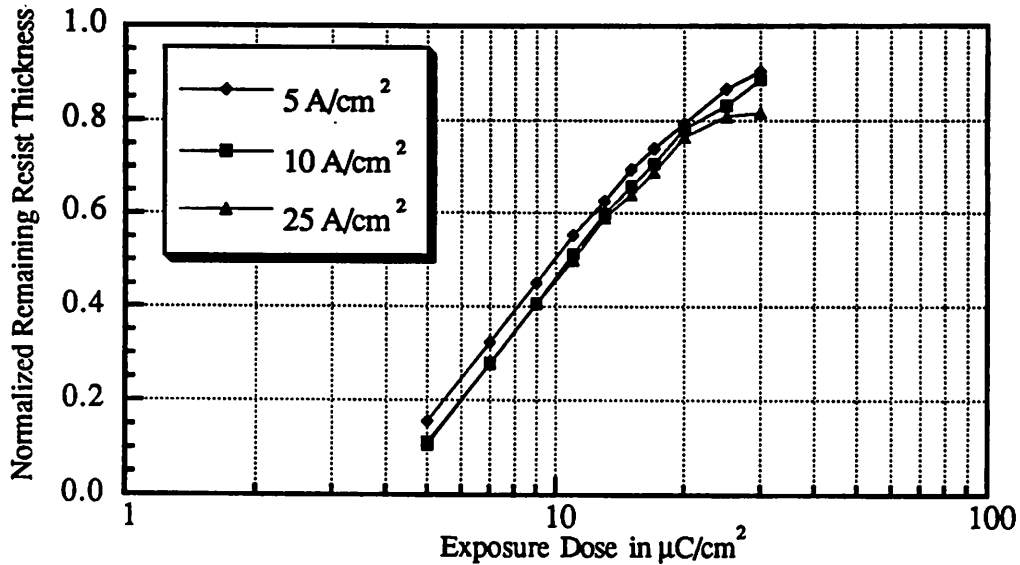


**Figure 4.2.** Normalized thickness remaining versus log dose curves for RD-2000N for 90 seconds development with exposure at beam-current densities of 5, 10, and 25  $\text{A}/\text{cm}^2$ .

This unusual behavior at high beam-current densities can be seen in the characteristic curves of RD-2000N, which are shown in Figure 4.2. These curves are for resists exposed with beam-current densities of 5, 10, and 25  $\text{A}/\text{cm}^2$ , and a development of 90 seconds in the RD-2000N developer. The 5  $\text{A}/\text{cm}^2$  data show a slight lateral shift but this may be due to dose calibration inaccuracy at short dwell time. The more important aspect is the bending down of the 25  $\text{A}/\text{cm}^2$  curve at high dose. This prompted us to devise further high beam current exposure experiments.

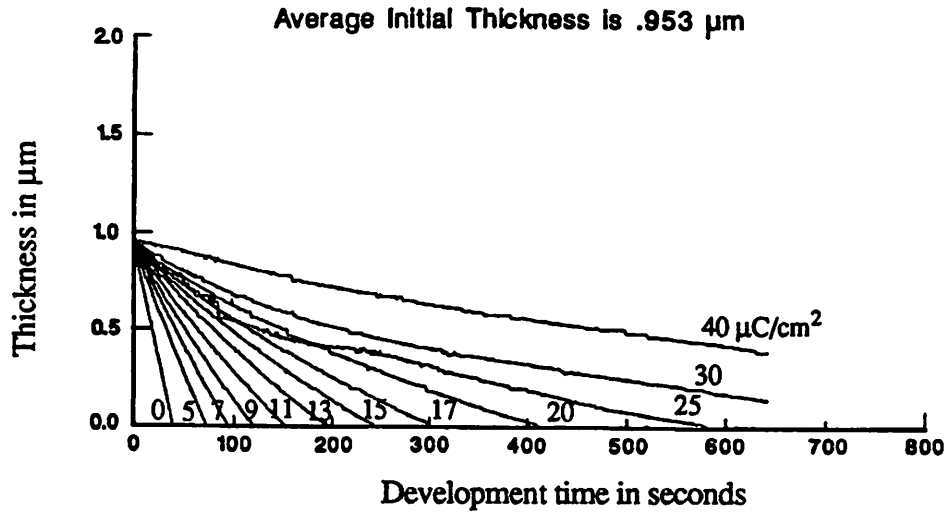


**Figure 4.4.** Thickness versus development times curves for different doses at  $25 \text{ A/cm}^2$  for a  $1.65 \mu\text{m}$  resist.

### 4.2.3 Resist Thickness

Assuming the thermal conductivity limitation is due to resist, thicker resist should show a stronger thermal effect than thick oxide substrate. This hypothesis was verified from DRM measurements on thick resist samples ranging from  $1 \mu\text{m}$  to  $2 \mu\text{m}$  and visual examination of the resist after exposure.

The resist film thickness remaining versus development time curves for  $0.95 \mu\text{m}$  and  $1.65 \mu\text{m}$  thick resists are shown in Figures 4.4 and 4.5 respectively. Note that the  $25 \mu\text{C/cm}^2$

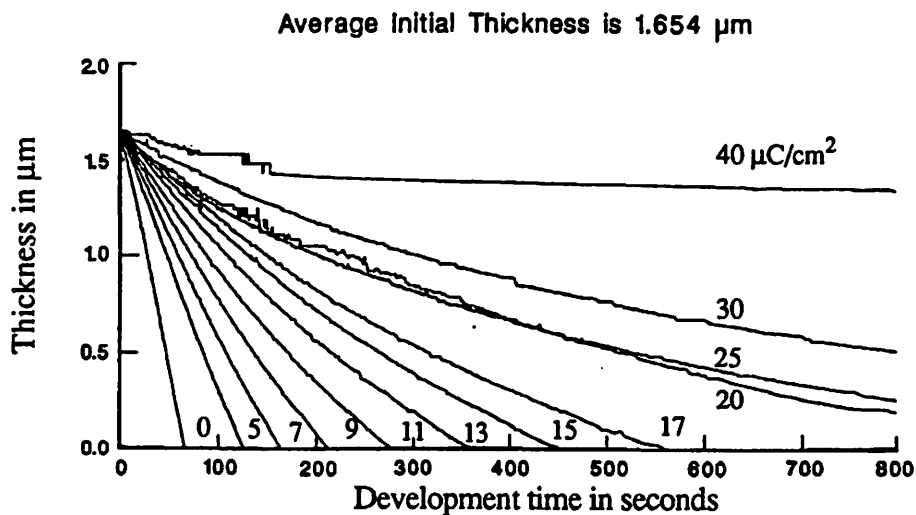
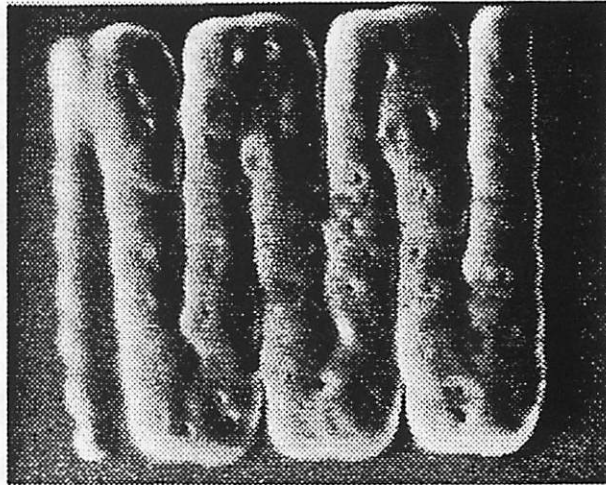


**Figure 4.5.** Thickness versus development time curves for different doses at  $25 \text{ A/cm}^2$  for a  $0.95 \mu\text{m}$  resist.

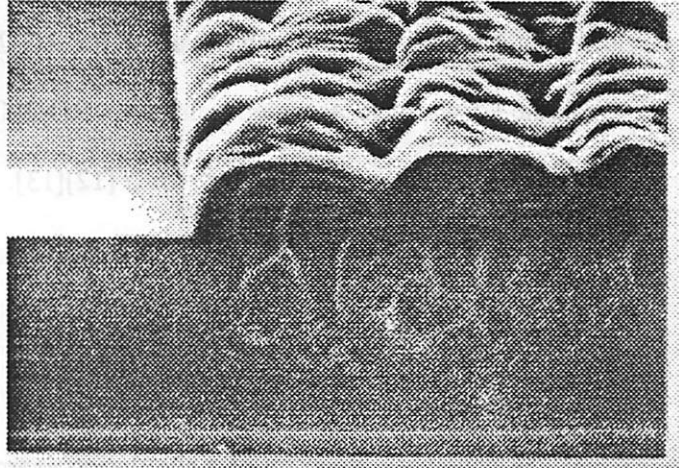
curve for the 0.95  $\mu\text{m}$  resist and the 20  $\mu\text{C}/\text{cm}^2$  curve for 1.65  $\mu\text{m}$  thick resist cross over to adjacent curves. These erratic thickness curves would not occur if the dissolution rate were a monotonic decreasing function of dose. The fact that the dose at which the crossover is lower for thicker resist is a clear indication of a heating effect.

**Figure 4.6.** SEM micrograph of a 10  $\mu\text{m}$  x 10  $\mu\text{m}$  square filled by a serpentine pattern exposed on 1.5  $\mu\text{m}$  resist.



Direct evidence of heating effects can be observed from the frosty latent images of the large DRM exposure patterns which appeared in the thicker resist at a dose of 40 versus 60  $\mu\text{C}/\text{cm}^2$  for thin resist. SEM of the exposed resists showed very interesting features in the high dose areas. For example, a 100  $\mu\text{m}^2$  square written with a serpentine pattern after exposure is shown in Figure 4.6. From this picture, the frosty latent images of the resist can now be understood as local surface roughness phenomenon. Figure 4.7 depicted the SEM cross-section of the surface features in a 1.5  $\mu\text{m}$  thick resist exposed at a dose of 60  $\mu\text{C}/\text{cm}^2$ . The resist can be seen to expand several tenths of  $\mu\text{m}$  above the surface and many cavities can be found down to about 0.5  $\mu\text{m}$  into the resist. These cavities were also observed in resist receiving lower doses. The expanded resist was highly porous and thus allowed easy penetration by the developer. The erratic behavior of the resist at about 25  $\mu\text{C}/\text{cm}^2$  can now be explained by this channeling effect. At higher doses, the resist was rendered insoluble and therefore its dissolution was not affected by the cavities.

**Figure 4.7.** SEM of cross-section of 1.65  $\mu\text{m}$  resist exposed with a dose of 60  $\mu\text{C}/\text{cm}^2$ .



### 4.3 Temperature Rise Simulation

In the previous sections, the thermal effects were shown to depend strongly on a number of important processing parameters such as resist thickness, exposure dose, and beam-current density. In addition, these effects are most severe when the beam reverses its direction in a serpentine manner as in the case of writing a large pattern where the beam has to make several passes to complete it. In order to estimate the transient temperature rise in the resist during exposure, a computer program is developed which can solve the heat diffusion equation in three dimensions with the resist as the domain. The program is implemented on a massively-parallel Connection Machine CM-2 and it solves the heat diffusion equation, Equation (4.1), using the explicit Euler method.

$$\rho \hat{C}_p \left( \frac{\partial T}{\partial t} \right) = (\nabla k) \nabla T + E(t, x, y, z) \quad (\text{EQ 4.1})$$

In the above equation,  $\rho$  is the density,  $\hat{C}_p$  is the heat capacity, and  $k$  is the thermal conductivity of the resist. Based on the physical changes observed in RD-2000N, the temperature rise is believed to be above the glass transition temperature. It is known that the heat capacity and thermal conductivity depend on temperature. Here we consider the mate-

rial to be below the glass transition temperature and approximate its thermal conductivity and heat capacity as constants. Values for RD-2000N and other resists are currently not available so we have assumed values for RD-2000N which are  $2.09 \times 10^{-3}$  J/cm-s-K for  $k$ , 1.47 J/g-K for  $\hat{C}_p$ , and  $1.2$  g/cm<sup>3</sup> for  $\rho$  [12][13]. Under this assumption, Equation (4.1) can be simplified to,

$$\rho \hat{C}_p \frac{\partial T}{\partial t} = k \nabla^2 T + E(t, x, y, z) \quad (\text{EQ 4.2})$$

A schematic diagram of a simulation example is shown in Figure 4.8 In this example, the simulation domain consists of a  $1.5 \mu\text{m} \times 6 \mu\text{m} \times 6 \mu\text{m}$  block of resist. The initial and boundary conditions used are as follows:

$$T(0, x, y, z) = T_{\text{Ambient}} \quad (\text{EQ 4.3})$$

$$T(t, x, y, h) = T_{\text{Substrate}} \quad (\text{EQ 4.4})$$

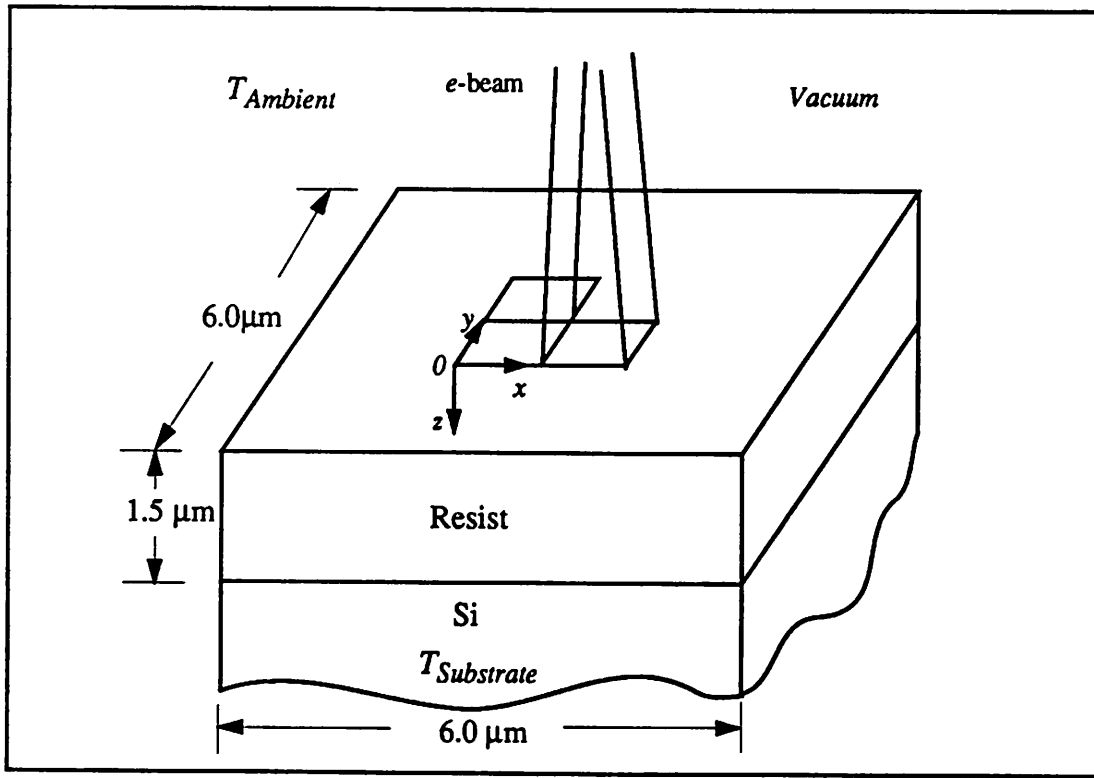


Figure 4.8. Schematic diagram of simulation domain for the temperature calculation.

$$\frac{\partial T}{\partial z}(t, x, y, 0) = 0 \quad (\text{EQ 4.5})$$

$$\left. \frac{\partial T}{\partial y} \right|_{y=\infty} = \left. \frac{\partial T}{\partial x} \right|_{x=\infty} = 0 \quad (\text{EQ 4.6})$$

Equation (4.3) is the initial condition. The boundary condition on the resist/Si interface, Equation (4.4), is based on the assumption that the conductivity of the substrate is sufficiently high and the amount of energy deposited in the substrate is low enough that there is negligible change in the substrate temperature. This assumption is supported by Figure 4.7 in which the foaming of the resist was found to be most severe near the top of the resist and abruptly stopped at about 0.5  $\mu\text{m}$  from the resist/Si interface. This distribution of cavities proved that the interface was cooler than the surface and the bulk of the resist during exposure. Since the resist was exposed under low pressure and heat loss via radiation is negligible, no heat transfer should occur on the top surface of the resist. As a result, the temperature gradient in the  $z$  direction is zero in Equation (4.5). The final boundary conditions in Equation (4.6) is based on the fact that the temperatures very far away from the source should be constant. In this case, it is safe to assume that this condition is met at about 2  $\mu\text{m}$  away from the exposed region due to the small heat diffusion length of the resist during the exposure.

The energy deposited by the electron beam is represented by  $E$  in Equation (4.2). In order to simplified the computation of the energy deposition, it is approximated with the following equation,

$$E(x, y, z, t) = f(x, y, t) \cdot e(z) \quad (\text{EQ 4.7})$$

where  $e(z)$  is the Everhart and Hoff equation [14] and  $f$  is the beam shape factor. This  $f$  factor is used to describe the lateral distribution of the energy deposition as well as the time

sequence of the exposure flashes. For the square beam used in the simulation,  $f$  is 1 in the center of the beam and the edge slopes are approximated with a gaussian function. When the beam is off,  $f$  is then set to zero. Thus, the size, location, dwell time, and blank time for the electron beam in the simulation are specified through this  $f$  function. For a more detailed examination of electron energy deposition effects, the energy per unit volume from Monte Carlo simulation could be included.

## 4.4 Simulation Results

In this section, the results of the simulation of temperature rise from several examples are presented. These examples are set up to investigate the differences in transient temperature rise within the resist under various beam-current densities, resist thicknesses, beam sizes, and pixel placement patterns.

### 4.4.1 Beam Current Density, Resist Thickness, and Flash Size

In a single exposure flash, the maximum temperature rise is undoubtedly located in the center of the exposure. Therefore, to find the hottest spot in the resist during exposure, the temperatures along the z-axis at the center of  $1 \times 1 \mu\text{m}^2$  and  $2 \times 2 \mu\text{m}^2$  exposure flashes for 0.5 and 1.5  $\mu\text{m}$  thick resists are calculated. The resulting temperatures can be plotted as three-dimensional surfaces with depth into the resist and exposure dose as the independent variables. Separate surfaces are shown for beam-current densities of 5, 10, and 25 A/cm<sup>2</sup> in Figure 4.9. In Figure 4.9 (a) and (b), the temperatures at the center of a  $1 \times 1 \mu\text{m}^2$  exposure flash are plotted and in Figure 4.9 (c) and (d), the temperatures at the center of a  $2 \times 2 \mu\text{m}^2$  exposure flash are plotted.

The temperature rise in thin resist is very different from thick resist. In the 0.5  $\mu\text{m}$  resist simulations, the temperature in the resist reaches a plateau as the dose increases and

the height of this plateau is nearly proportional to beam current density. The maximum temperatures are at zero depth of at the resist surface. This indicates a steady state situation where the rate of energy deposited is equal to rate of energy dissipated by heat transfer from resist to the Si substrate. The saturation dose and the maximum temperature depended on the beam-current density and to a somewhat lesser degree, the exposure flash size. For examples, in Figure 4.9 (a) and 4.9 (b), the maximum temperatures for  $5 \text{ A/cm}^2$  exposure are

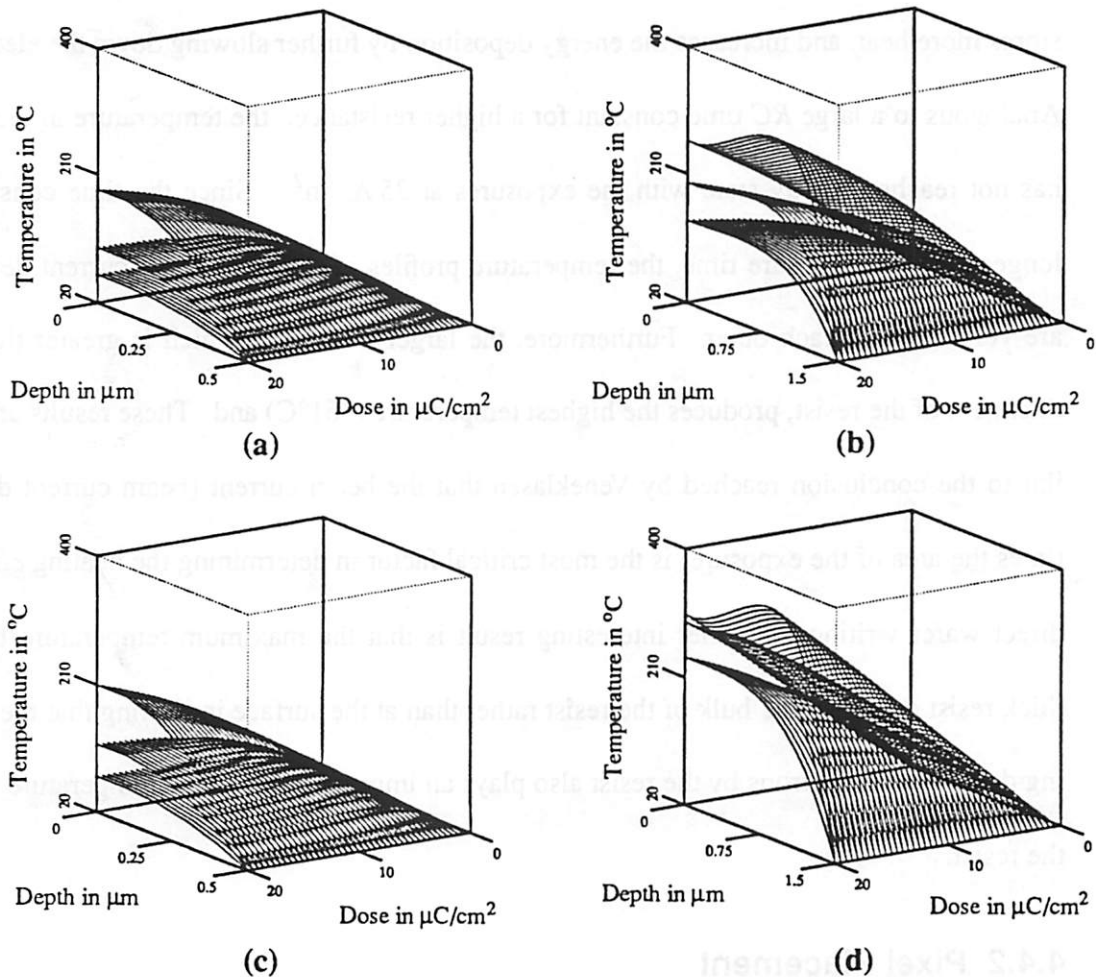


**Figure 4.9.** Simulated temperature in the resist at the center of an exposure flash for beam-current densities of 5, 10, and  $25 \text{ A/cm}^2$ . The higher the beam-current density, the higher is the temperature in the resist. (a)  $1 \times 1 \mu\text{m}^2$  in  $0.5 \mu\text{m}$  thick resist, (b)  $1 \times 1 \mu\text{m}^2$  in  $1.5 \mu\text{m}$  thick resist, (c)  $2 \times 2 \mu\text{m}^2$  in  $0.5 \mu\text{m}$  thick resist, and (d)  $2 \times 2 \mu\text{m}^2$  in  $1.5 \mu\text{m}$  thick resist.

reached after approximately  $10 \mu\text{C}/\text{cm}^2$  and the difference between the two flash sizes is only  $11^\circ\text{C}$  ( $62^\circ\text{C}$  for the  $1 \times 1 \mu\text{m}^2$  flash and  $73^\circ\text{C}$  for the  $2 \times 2 \mu\text{m}^2$  flash). But for both cases, the maximum temperatures increase by a factor of 3 when the beam-current density is increased from 5 to  $25 \text{ A}/\text{cm}^2$  ( $188^\circ\text{C}$  and  $210^\circ\text{C}$  respectively).

In the cases of the thicker  $1.5 \mu\text{m}$  resist, the temperature profiles are very different from those of the thinner resist because the thicker resist increases the thermal impedance, stores more heat, and increases the energy deposition by further slowing down the electrons. Analogous to a large  $RC$  time constant for a higher resistance, the temperature in the resist has not reached steady state with the exposures at  $25 \text{ A}/\text{cm}^2$ . Since the time constant is longer than the exposure time, the temperature profiles of different beam current densities are very close to each other. Furthermore, the larger flash size, which is greater than the thickness of the resist, produces the highest temperature ( $361^\circ\text{C}$ ) and These results are similar to the conclusion reached by Veneklasen that the beam current (beam current density times the area of the exposure) is the most critical factor in determining the heating effect in direct wafer writing. Another interesting result is that the maximum temperature for the thick resist occurs in the bulk of the resist rather than at the surface indicating that the slowing down of the electrons by the resist also plays an important role in the temperature rise in the resist.

#### **4.4.2 Pixel Placement**

In this section, the effects of adjacent pixels on the temperature rise during exposure are investigated. Four exposure flashes are simulated which are exposed sequentially near the center of a  $1.5 \mu\text{m}$  resist to form a  $2 \mu\text{m} \times 2\mu\text{m}$  square. In the simulation,  $1 \mu\text{m} \times 1 \mu\text{m}$

square beam at 20 keV with a current density of  $10\text{A}/\text{cm}^2$  is used to write each pixel. The resulting contours of constant temperature at the end of each flash are shown in Figure 4.10 for an exposure dose of  $10\ \mu\text{C}/\text{cm}^2$ , which corresponds to a dwell time of 100 ns. The temperatures in the hottest layer in the resist, which is at  $0.4\ \mu\text{m}$  from the substrate, are plotted. The peak temperature after writing the fourth pixel is  $40^\circ\text{C}$  higher than that of the first pixel,

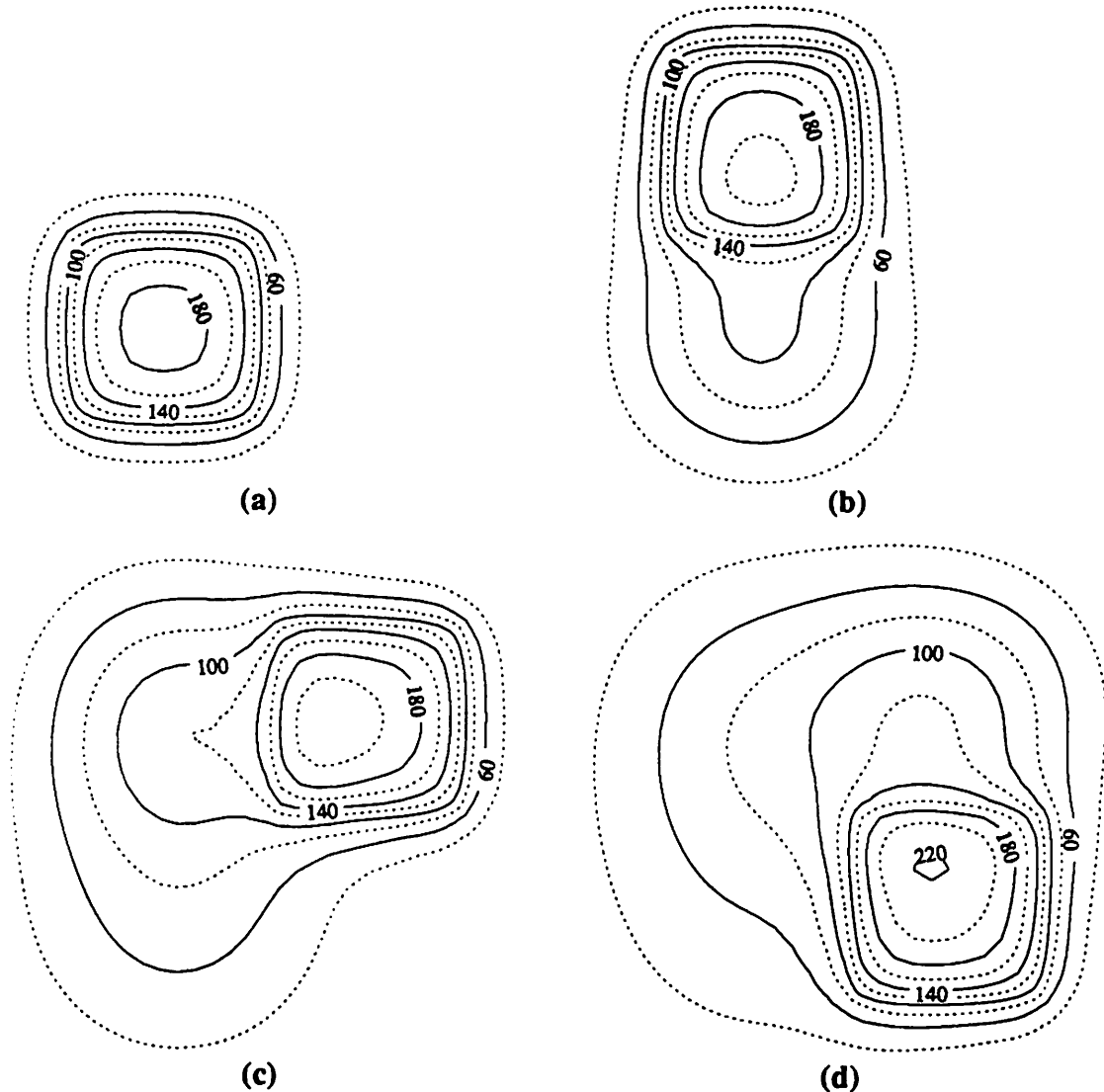


**Figure 4.10.** Contours of temperature for a sequence of four exposure pixels at the end of each exposure for a  $1.5\ \mu\text{m}$  thick resist at a depth of  $1.1\ \mu\text{m}$ . The beam current density is  $10\ \text{A}/\text{cm}^2$  and the dose is  $10\ \mu\text{C}/\text{cm}^2$ . The blank time between flash is 100 ns. (a) First pixel, (b) second pixel, (c) third pixel, and (d) fourth pixel.

and the area of the 180°C contour is about three times larger. The simulation results indicate that the heat contributed from the surrounding pixels can increase the temperature rise by more than 20% and will be important for pixels smaller than the resist thickness.

## 4.5 Conclusion

Exposure of Hitachi RD-2000N resist at a beam-current density of 25 A/cm<sup>2</sup> on the AEBLE-150 produced noticeable changes in dissolution which were caused by beam-induced heating. For a thickness of 1 μm, the effect is directly observable as a latent image on the surface of large exposed area at a dose of 40 μC/cm<sup>2</sup>. SEM micrographs of resist cross-section showed that the latent images on the surface were caused by the rough resist surfaces. The rough topography appeared as a consequence of the expansion and cavity formation in over-heated areas. Although with less intensity, these cavities were also found to occur at lower doses. Furthermore, cavities formed in resist received doses near 25 μC/cm<sup>2</sup> appeared to have increased the dissolution rate near the surface by channelling the developer into the bulk of the resist. At higher doses, the resist becomes insoluble, and therefore, there was no increase in dissolution rate. These effects were not noticeably influenced by the substrate material but rather depended strongly on the resist thickness indicating that the thermal conductivity of the resist is much lower than that of the substrate.

A massively-parallel computer program was developed to analyze the transient electron-beam-induced heating of the resist. Simulation results indicate that the highest temperature occurs near the surface of the resist when the beam-current density is below 10 A/cm<sup>2</sup>. However, when a 25 A/cm<sup>2</sup> beam is used to expose 1.5 μm thick resist, the peak temperature occurs in the bulk of the resist due to the increase in the thermal impedance as well as slowing down of the electrons. With the exposure size greater than the thickness of the

resist, the temperature rise seems to be less dependent on the beam current density. The heat capacity of the resist also plays an important role in the contribution of heating to adjacent pixels. In these simulations, the temperature rises is quite significant and will likely reach the glass transition temperature.

With the advent of chemically-amplified resist, the dose requirement is lowered by a factor of 5 or more and thus, the problems of resist heating during exposure seem to be alleviated. However, these resists are very temperature sensitive as their development behaviors are controlled by thermal-driven catalytic reactions after exposure. In Chapter 6, it will be shown that the bake reaction is limited by a factor

$$k_1 e^{-mk_2 t} \quad (\text{EQ 4.8})$$

The values for the above parameters are in Table 6.1. Assuming a temperature rise of 200°C for 200 ns during a 10  $\mu\text{C}/\text{cm}^2$  exposure at 10  $\text{A}/\text{cm}^2$ , the crosslinking reaction rate limiting factor is approximately 0.1. Since this factor is an indirect measure of the extent of the crosslinking reaction, this small value indicates that less than 1% of the possible crosslinking is produced directly via thermal effects. Direct e-beam induced crosslinking of the resin and the crosslinker is more likely to occur.

## References

- [1] N. K. Eib and R. J. Kvitek, "Thermal distribution and the effect on resist sensitivity in electron-beam direct write," *J. Vac. Sci. Technol.*, B7 (6), pp. 1502-1506, Nov/Dec 1989.
- [2] K. Nakajima, T. Honda, and H. Matsumoto, "New Compensation Method for Avoiding Proximity Resist Heating in Variably Shaped Electron Beam Lithography," *J. Vac. Sci. Technol.*, B8 (6), pp. 1437-1440, Nov/Dec 1990.
- [3] K. Saito and T. Sakai, "A Criterion to Judge Whether the Resist Heating Effect will Occur", *Proceedings of the 35th International Symposium on Electron, Ion, and Photon Beams*, May 1991.
- [4] E. van der Drift, A. C. Enters, and S. Radelaar, "Thermal Effects in High Voltage E-beam Lithography," *Proceedings of the 35th International Symposium on Electron, Ion, and Photon Beams*, May 1991.
- [5] L. H. Veneklasen, "Optimizing EBL Writing Strategies Subject to Electron Optical, Pattern, and Resist Constraints," *Proceedings of the 35th International Symposium on Electron, Ion, and Photon Beams*, May 1991.
- [6] H. C. Pfeiffer, T. R. Groves, and T. H. Newman, "High-throughput, high-resolution electron-beam lithography," *IBM J. Res. Develop.*, vol. 32, no. 4, pp. 495-501, July 1988.

- [7] M. Fujinami, N. Shimazu, T. Hosokawa, and A. Shibayama, "EB60: An advanced direct wafer exposure electron-beam lithography system for high-throughput, high-precision, submicron pattern writing," *J. Vac. Sci. Technol.*, B 5(1), pp. 61-65, Jan/Feb 1987.
- [8] Y. Nakayama, S. Okazaki, N. Saitou, and H. Wakabayashi, "Electron-beam Cell Projection Lithography: A New High-throughput Electron-beam Direct-writing Technology Using A Specially Tailored Si Aperture," *J. Vac. Sci. Technol. B*, vol. 8, no. 6, pp. 1836-1840, Nov/Dec 1990.
- [9] Wayne M. Moreau, *Semiconductor Lithography*, pp. 432-433, Plenum Press, New York, 1988.
- [10] F. Murai, S. Okazaki, N. Saito, and M. Dan, "The effect of acceleration voltage on linewidth control with a variable-shaped electron beam system," *J. Vac. Sci. Technol.*, B 5(1), pp. 105-109, Jan/Feb 1987.
- [11] H.I. Ralph, G. Duggan, and R.J. Elliott, "Resist Heating in High Speed Electron Beam Pattern Generators," *Proceedings of Symposium on Electron, Photon, and Ion Beam Science and Technology, Tenth International Conference*, pp. 219-230, 1982.
- [12] D. R. Anderson, "Thermal Conductivity of Polymers," *Chem. Rev.*, vol. 66, no. 6, pp. 677-690, 1966.
- [13] K. Eiermann and K.-H. Hellwege, "Thermal Conductivity of High Polymers from -180°C. to 90°C.," *Journal of Polymer Science*, vol. 57, pp. 99-106, 1962.

- [14] T. E. Everhart and P. H. Hoff, "Determination of Kilovolt Electron Energy Dissipation vs. Penetration Distance in Solid Materials," *J. Appl. Phys.*, vol. 42, no. 13, pp. 5837-5846, 1971.

## **Chapter 5**

# **Empirical Extensions to Dissolution Rate Model for Chemically-Amplified Resists**

The range of resist profile modeling is extended to include additional processing variables by utilizing a novel approach of empirical extensions to the mechanism-based (EEMB) dissolution rate model. The technique consists of using a central composite design experiment of dissolution rate measurements to study the effects of processing variables on the parameters in the dissolution rate function. Simple empirical functions relating these parameters to the processing variables were then obtained with linear regression. These empirical functions in conjunction with the mechanism-based rate model extends the use of the dissolution rate function of absorbed energy density to include developer concentration and post-exposure bake over a wide range of processing conditions. This enables resist profile simulation for the optimization of post-exposure bake and developer concentration in the processing of chemically-amplified resists.

### **5.1 Empirical Extension of Mechanism-based Resist Model**

Ideally, a dissolution rate model should give an accurate prediction of resist profiles for a wide range of processing conditions. The dissolution rate versus absorbed energy functions discussed in Chapter 2 have been shown to provide good agreement to experiment with a variety of resist patterns, development times, and exposure doses for typical electron-beam resists. However, if the developer concentration is changed, a new development rate measurement experiment is needed to determine the rate equation for that developer concentration. This limited capability of the rate function is further exemplified in the modeling of chemically-amplified resists. The dissolution rate of these resists is controlled by thermal driven catalytic reactions during the post-exposure bake (PEB). As a result, in addition to

the developer concentration, the behavior of the resists also depends strongly on the temperature and duration of the PEB. Therefore, simulation using the dissolution rate function of absorbed energy cannot be used to predict the optimal PEB condition and developer concentration without performing a large number of experiments.

A mechanistic approach has also been developed to model the chemical amplified resists with optical exposure. Ferguson *et al.* used reaction kinetics to describe the exposure and the post-exposure bake of these systems [1]. The disadvantage of this technique is that extensive experimental work is needed to characterize the chemical reactions with special techniques such as Fourier Transform IR spectroscopy. In addition, the chemical changes of some resists have very weak spectral changes and are almost impossible to measure. To date, this approach has been limited to PEB effects and is most useful in characterizing effects in the design of resists such as those of sensitizer types and loading. The mechanisms of dissolution and the role of developer concentration have been discussed by Hinsberg *et al.* [2]. To date mechanistic models of resist dissolution have not been developed. Top-down factorial experiments have been used by Blum *et al.* to study the effects of post-exposure bake and developer concentration on performance measures such as sensitivity and contrast in chemically-amplified resists [3]. Although their results can be used to choose an optimal process based on contrast and sensitivity, dose calibration using SEM inspection of resist profiles are still needed due to the lack of model for simulation. While mechanism-based studies have the advantage of providing direct understanding and efficient parameterization, they do not have the scope of multiple parameters and ability to assist in process optimization.

In order to efficiently model the processing of chemically-amplified resist, a new approach is developed which utilizes the power of factorial experiment to systematically

track the variations of the parameters in the dissolution rate functions as the processing conditions change. Once the effects of the key processing factors on the parameters of the rate model are identified, they can be modeled with empirically-fitted functions using linear regression. By using these empirical extensions to the mechanism-based (EEMB) dissolution rate model, the processing of chemically-amplified resists can then be simulated for any post-exposure bake and developer concentration. This novel approach is illustrated in Fig-

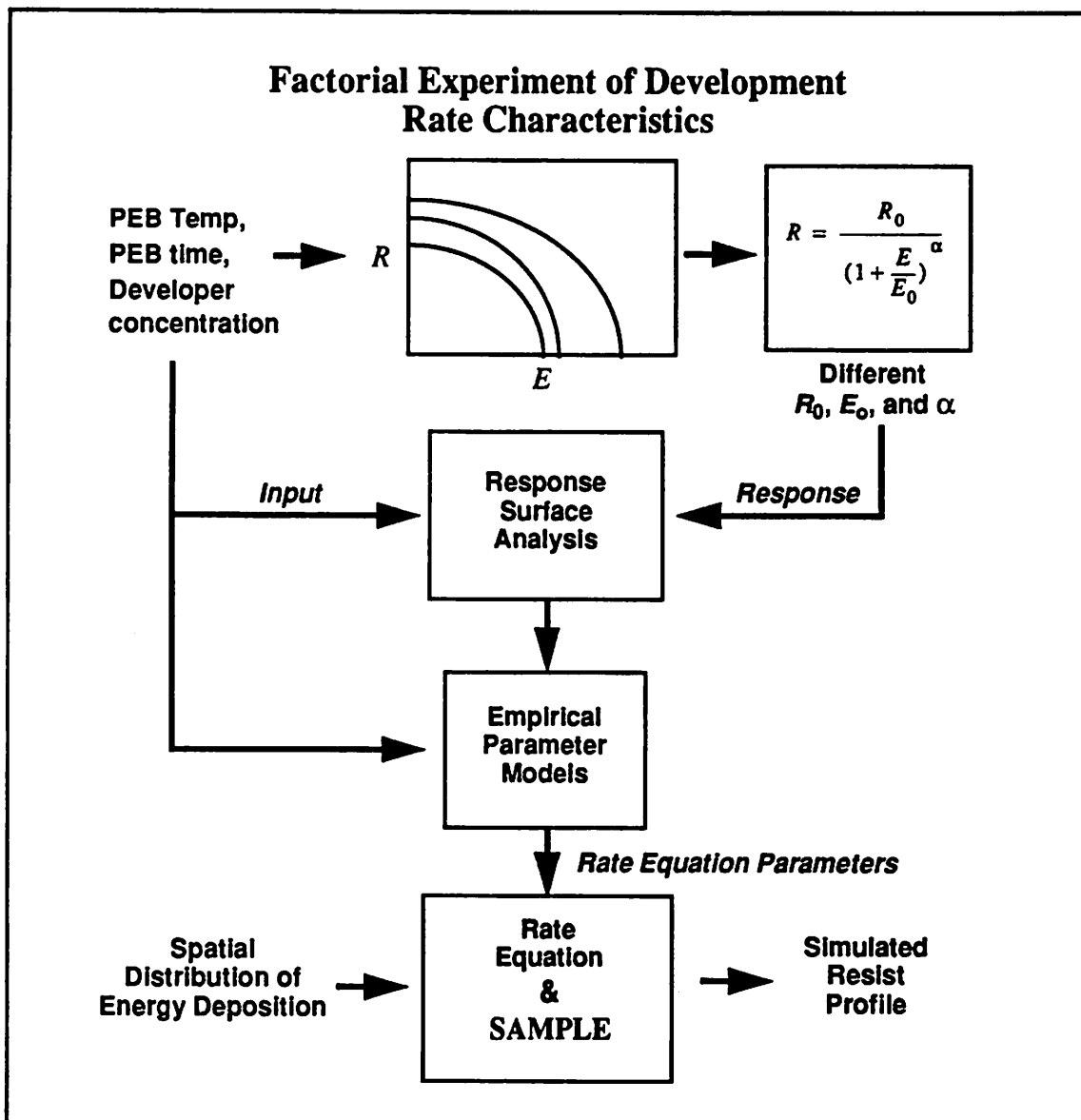


Figure 5.1. Schematic diagram of the empirical extension of the mechanism-based model of chemically-amplified resists for effects of post-exposure bake temperature, time, and developer concentration.

ure 5.1 and it assumes that the dissolution rate function is a physically-based model which is well suited for use in process simulation program such as *SAMPLE*. For the case which will be studied, a power law relationship between the log of dissolution rate and the molecular weight of the resist after exposure is used. The experimental design of the development rate measurements, the statistical analysis of the dissolution rate data, and the determination of the EEMB model will now be presented. Resist profiles simulated with the EEMB rate model are then compared to experiment to determine the validity of the model. Process optimization criteria are also derived from the EEMB model.

## 5.2 Factorial Experiment Design

To maximize the range of the processing factors studied and to obtain estimates of the curvature of the response surfaces, three or more levels of factor have to be used in the factorial experiment. Since there are three key factors involved in the processing of chemically-amplified resists, if we are to use a full factorial design to fit the response surfaces, 27 DRM experiments would be needed. The number of experiments would become prohibitively large, if the experiments have to be repeated to determine the experimental errors. Fortunately, the number of experiments required can be substantially reduced with a central composite design [4][5]. Figure 5.2 illustrates this composite design. In this design, the experiment can be performed in two stages. The first stage of experiments follows a  $2^3$  factorial design, enhanced with center point replications. These initial experiments can be used to check for curvature in the surface and estimate the experimental errors. If significant curvature is found to exist, a second stage of experiments can be performed. This second stage of experiments have 2 points along each of the three axes extending beyond the face of the cube, making five levels for each factor. Additional center points can also be included as a check for experimental error and blocking effect if the two stages are performed at dif-

ferent times. The set up of these two blocks of experiments ensures that no confounding will occur in estimates of the quadratic and linear effects. If three center points are used in each stage, only 20 experiments is needed.

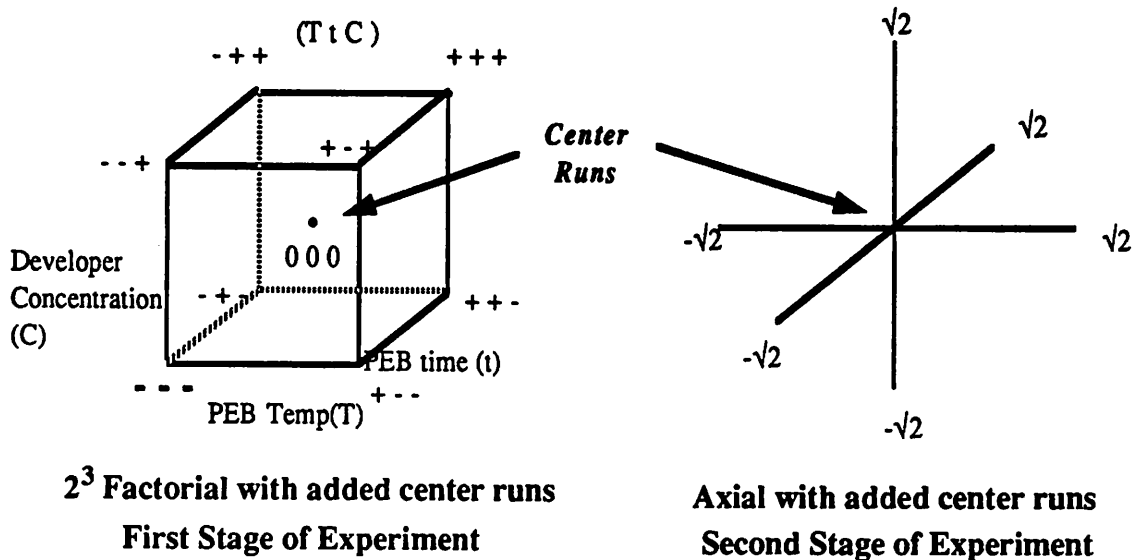


Figure 5.2. The central composite design with the three key processing parameters.

## 5.3 Factorial Experiment

### 5.3.1 Resist Preparation

The resist used in this study was Shipley SAL-601-ER7 negative electron-beam resist. We used 4 inch wafers spin coated with resist at 4500 rpm for 45 seconds to a thickness of about 0.6  $\mu\text{m}$ . The wafers were then soft-baked in an oven at 80°C for 30 seconds. Subsequently, the wafers were exposed with exposure pattern containing 12, 2 x 8  $\text{mm}^2$  rectangles on a JEOL system at Hwelett Packard in Palo Alto with 20 keV accelerating voltage and 0.25  $\text{A}/\text{cm}^2$  current density. Each rectangle received a different exposure dose ranging from 0.3 to 3.5  $\mu\text{C}/\text{cm}^2$ . After the post-exposure bake, the resists were developed in the Perkin Elmer Development Rate Monitor (DRM) for 10 minutes as the dissolution rates of the exposed areas were being measured. The developer used was the MF-312 developer from

Shipley diluted with DI water and the developer temperature was set at 21°C for all the runs. The post-exposure bake conditions and the developer concentration used are discussed in the next section.

### 5.3.2 Levels of the Factors

The experiments were conducted in two stages following the central composite design. In the first stage of experiments, three replicated center points were included. After the completion of the first stage, significant curvature was observed in both of the parameter models. Therefore, the second stage of experiments was performed with 2 replicated center points. The three factors and their levels used in the two stages of experiments are listed in Table 5.1. The order of the runs was randomized to prevent introduction of systematic errors. Nonetheless, the two stages of experiments were performed two weeks apart, increasing the odds that some changes in the resist materials or processing conditions might occur. After the experiment was completed, a blocking effect between the two stages was indeed observed and it will be discussed in section 5.6.1.

**Table 5.1: Factors and levels in the two stages of the design experiment. Actual levels used are in parentheses.**

Level	Bake Temperature	Bake Time	Developer Concentration
-1.4	108°C	60 sec (-2)	0.229N (-1.6)
-1	110°C	75 sec	0.257N
Center	115°C	90 sec	0.297N
+1	120°C	105 sec	0.351N
+1.4	122°C	150 sec (4)	0.370N

## 5.4 Dissolution Rate Data

The high contrast and sensitivity of SAL-601-ER7 are illustrated in Figure 5.3 as the fitted dissolution rate function obtained from run #5 of the factorial experiments is plot-

ted with the experimental data. The dissolution rate data were highly non-linear due to the chemical amplification of the exposure energy. There was very little change in the dissolution rate below an energy density of 0.01 kJ/cm<sup>3</sup>. However, as the energy density increased toward 0.1 kJ/cm<sup>3</sup>, the dissolution rate decreased by nearly 3 orders of magnitude. For the 20 keV exposure used, this energy deposition corresponds to a sensitivity of 3-4 μC/cm<sup>2</sup>.

The dissolution rate equation discussed in Chapter 3, Equation (3.1), was found to be inadequate in describing the dissolution rate of chemically-amplified resist due to its high contrast. In order to improve the fit of the rate function to the dissolution rate data, Equation (3.1) is modified by adding a parameter,  $\beta$ , which can increase the ability for the curve to “bent downward,”

$$R = \frac{R_0}{\left[ 1 + \left( \frac{E}{E_0} \right)^\beta \right]^\alpha} \quad (\text{EQ 5.1})$$

Although all four parameters in Equation (5.1) could be determined by direct fitting, an alternative fitting strategy was adopted. This strategy was prompted by the observation that multiple solutions for the same least square residual would occur which would make it difficult to systematically correlate the fitting parameters among the runs. Of the four parameters in the rate function, only  $R_0$ , the dissolution rate of unexposed resist, can be verified by independent measurement ( $R_0 = \text{Resist thickness divided by time to clear}$ ). On the other hand,  $E_0$ ,  $\beta$ , and  $\alpha$  had to be determined from non-linear regression. In negative resists with no chemical amplification,  $\beta$  is usually found to be 1 and  $\alpha$  is usually between 2 to 10. However, SAL-601-ER7 has a much higher contrast than conventional negative resists and very different values of  $\beta$  and  $\alpha$  had to be tried in fitting the rate equation. Since there was

considerable amount of noise in the data, there were many combinations of  $R_o$ ,  $E_o$ ,  $\beta$ , and  $\alpha$  which can be judged as good fit. Fortunately, in trying different values of  $\beta$  and  $\alpha$ , it was found that  $\beta$  equal to 1.5 and  $\alpha$  equal to 31 could be used to give a very good fit of the rate equations for almost all the runs. In the cases where different values of  $\beta$  and  $\alpha$  were extracted, the differences were only a few percent. Therefore, in order to have consistency in extracting the parameters for the dissolution rate functions from all the runs, we set  $\beta$  to 1.5 and  $\alpha$  to 31. Once  $\beta$  and  $\alpha$  were set,  $E_o$  and  $R_o$  were extracted automatically by minimizing the ratio of the predicted to the experimental sum of squares for the residuals. Their dependence on the three processing parameters could then be studied.

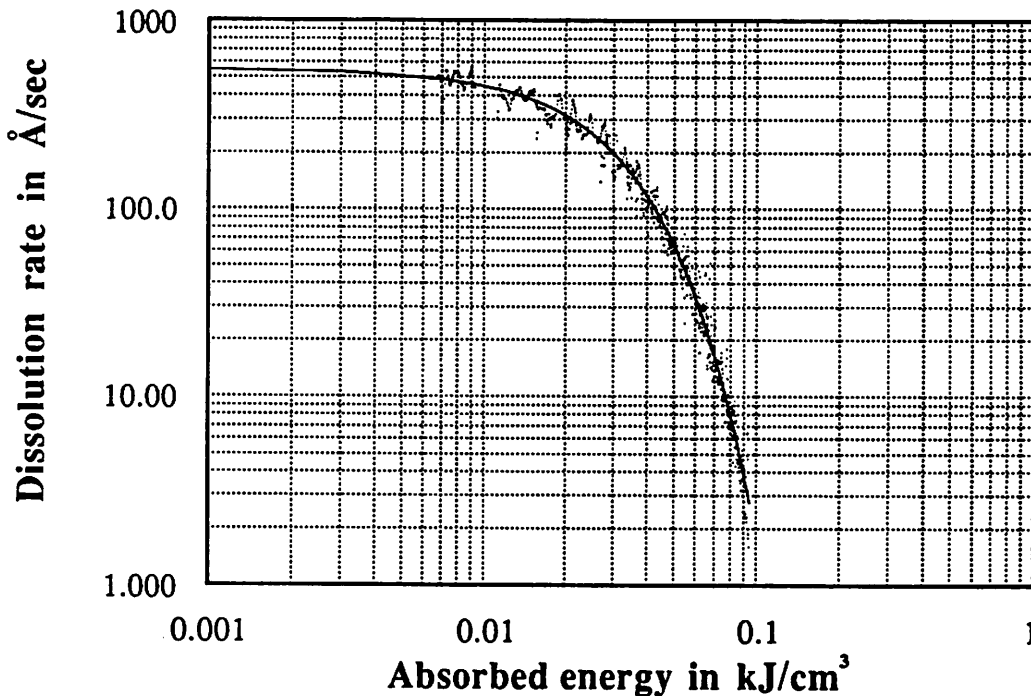


Figure 5.3. Dissolution rate versus absorbed energy of SAL-601-ER7 from run #5.

## 5.5 First Experimental Stage and Linear Effects

The first step in determining the models for  $E_o$  and  $R_o$  was to identify the significant effects. The experimental averages and effects of  $E_o$  and  $R_o$  were first calculated with data

from the  $2^3$  factorial experiments of the first stage of the composite design using Yate's algorithm [6]. Then the standard errors ( $\sigma$ ) for the effects were calculated from the estimates of the experimental errors in the 5 replicated center runs of both stages. Any effect within  $\pm 2\sigma$  was considered to be significant.

### 5.5.1 Effect Calculation for $E_o$

The extracted values for  $E_o$  and the effects are listed in Table 5.2. The average value of  
namely, PEB Temperature (T), PEB time (t), and developer concentration (C), were significant.

**TABLE 5.2: Extracted  $E_o$  and its effect using Yate's algorithm. Significant effects are in bold face.**

Run	T	t	C	$E_o(\text{J/cm}^3)$	<i>1</i>	<i>2</i>	<i>3</i>	<i>D.F.</i>	$E_o$ Effect	Type
1	-	-	-	253	427	817	1749	8	218.6	AVG
2	+	-	-	174	390	932	-305	4	<b>-76.3</b>	T
3	-	+	-	224	490	-157	-85	4	<b>-21.3</b>	t
4	+	+	-	166	442	-168	25	4	6.3	Tt
5	-	-	+	288	-79	-37	115	4	<b>28.8</b>	C
6	+	-	+	202	-58	-48	-31	4	-7.8	TC
7	-	+	+	262	-86	21	-11	4	-2.8	tC
8	+	+	+	180	-82	4	-17	4	-4.3	TtC

Standard Error =  $\pm 4.1$

### 5.5.2 Effect Calculation for $R_o$

The extracted values for  $R_o$  and the effects are listed in Table 5.3. The average value of  $R_o$  was 294.8 Å/sec and  $\sigma$  was 6.8 Å/sec. Due to the relatively small  $\sigma$ , all the effects had to be considered significant except the three-factor interaction effect. In order to obtain

a simpler model for  $R_o$ , several data transformations were tried. The square root transformation, for example, was found to lead to a simpler model. This square root transformation was adopted and the effects on  $\sqrt{R_o}$  are listed in Table 5.4. After the transformation, the number of significant effects was reduced from 6 to 3. They were the PEB temperature (T), PEB time (t), developer concentration (C), and temperature-time interaction (Tt).

**TABLE 5.3: Extracted  $R_o$  and its effect using Yate's algorithm. Significant effects are in bold face.**

Run	T	t	C	$R_o(\text{\AA}/\text{sec})$	1	2	3	D.F.	$R_o$ Effect	Type
1	-	-	-	77	158	305	2359	8	294.8	AVG
2	+	-	-	81	147	2054	-121	4	<b>-30.4</b>	T
3	-	+	-	86	1073	-21	-103	4	<b>-25.8</b>	t
4	+	+	-	61	981	-100	-66	4	<b>-16.5</b>	Tt
5	-	-	+	552	4	-11	1749	4	<b>437.5</b>	C
6	+	-	+	521	-25	-92	-79	4	<b>-19.7</b>	TC
7	-	+	+	525	-31	-29	-81	4	<b>-20.2</b>	tC
8	+	+	+	456	-69	-38	-11	4	<b>-2.5</b>	TtC

Standard Error =  $\pm 6.8$

**TABLE 5.4: Effects of square root of  $R_o$ .**

Run	T	t	C	$\sqrt{R_o} (\text{\AA}/\text{sec})^{1/2}$	1	2	3	D.F.	$\sqrt{R_o}$ Effect	Type
1	-	-	-	8.79	17.76	34.80	125.39	8	15.67	AVG
2	+	-	-	8.97	17.04	90.59	-3.49	4	<b>-0.87</b>	T
3	-	+	-	9.25	46.32	-1.26	-2.77	4	<b>-0.69</b>	t
4	+	+	-	7.80	44.27	-2.23	-2.52	4	<b>-0.63</b>	Tt
5	-	-	+	23.49	0.19	-0.71	55.78	4	<b>13.95</b>	C
6	+	-	+	22.83	-1.45	-2.05	-0.96	4	<b>-0.24</b>	TC
7	-	+	+	22.91	-0.67	-1.64	-1.34	4	<b>-0.33</b>	tC
8	+	+	+	21.35	-1.56	-0.89	-0.75	4	<b>0.19</b>	TtC

Standard Error =  $\pm 0.26$

## 5.6 Second Experimental Stage and Quadratic Effects

Although simple linear models can be constructed after the significant effects were identified, several tests had to be performed to ensure the models were adequate. If the response surfaces of  $E_o$  and  $\sqrt{R_o}$  had significant curvature, they would have to be approximated with quadratic functions instead. One of the curvature tests was the comparison of the average values of both parameters to that of the replicated center runs. If the response surfaces were linear, then the average and the center points should have similar values. This test was carried out and it was found that significant curvature existed in both response surfaces. Therefore, the second stage of the experiments was performed to provide data for the estimates of higher order terms for the parameter functions. The results from the second experimental stage and all the center runs are listed in Table 5.5.

**TABLE 5.5: Results from the second stage of the experiment and the center runs.**

Stage	Run	T	t	C	$\sqrt{R_o}(\text{\AA}/\text{sec})^{1/2}$	Avg.	$E_o(\text{J}/\text{cm}^3)$	Avg.
1	9	c	c	c	14.87		206	
1	10	c	c	c	14.97	<b>14.74</b>	196	<b>199</b>
1	11	c	c	c	14.39		195	
2	7	c	c	c	17.44		185	
2	8	c	c	c	17.00	<b>17.22</b>	178	<b>181.5</b>
2	1	-1.4	c	c	17.80		241	
2	2	1.4	c	c	16.43		157	
2	3	c	-2	c	18.52		202	
2	4	c	4	c	16.49		161	
2	5	c	c	-1.6	6.09		177	
2	6	c	c	1.4	28.09		209	

### 5.6.1 Effect between First and Second Experimental Stage

Despite all efforts in keeping the other non-significant processing factors under control, there was substantial discrepancy in  $\sqrt{R_o}$  and  $E_o$  between the two stages. A linear model for  $\sqrt{R_o}$  derived from the first stage of experiments was used to predict the result from

the second stage of experiments. The plots of residuals for that model are shown in Figure 5.4 and a constant shift was observed. Though not as obvious as the case for  $\sqrt{R_o}$ , the plots of residuals for  $E_o$  (Figure 5.5) also displayed similar shift, but in the opposite direction. In addition, residuals from the two stages of experiment had similar curvilinear relationships with the predicted  $E_o$ , further illustrating the inadequacy of the linear model.

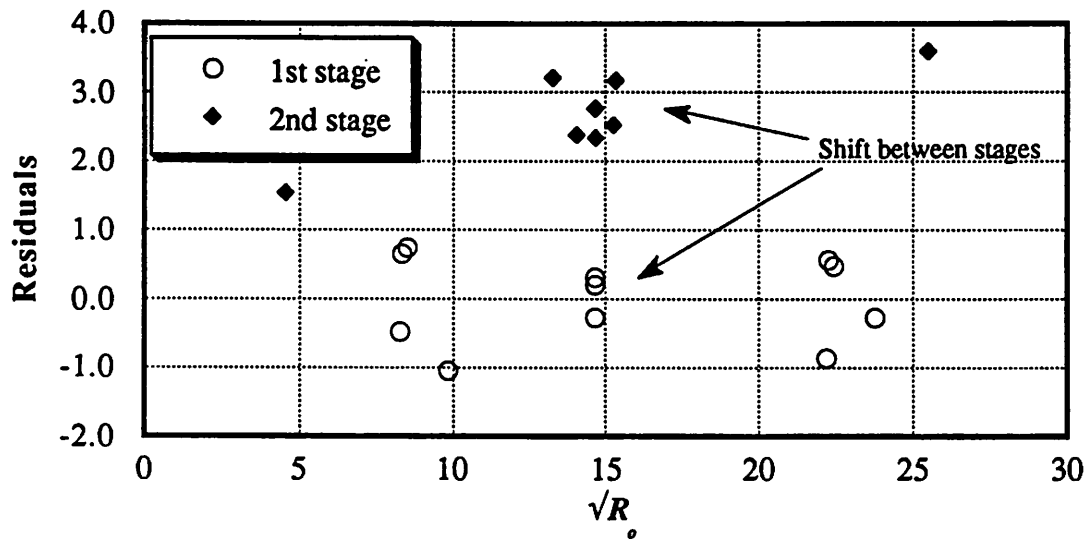


Figure 5.4. Plots of residuals for linear  $R_o$  model.

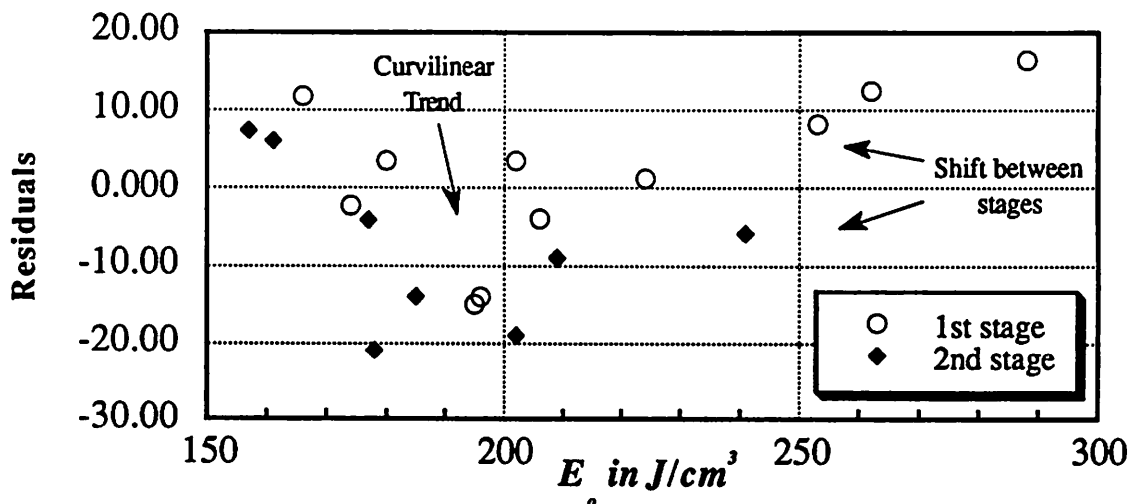


Figure 5.5. Plots of residuals for linear  $E_o$  model.

There were only a few possible sources of variations in the processing that could have contributed to this blocking effect. The most likely ones were aging of the resist and/or the developer because of the uniformity of the shift in the observed  $R_o$ 's. On the other hand, since all but two of the runs in the second stage had the same bake temperature, drift in the oven temperature could also be responsible for this discrepancy. After further investigation, it was discovered that a new bottle of resist was used in the second stage of experiments. Therefore, the most likely reason was that either the resist in the first stage of experiments aged or the new resist had a slightly different formulation. Nonetheless, the overall experimental design was such, that despite the blocking effect, significant quadratic models of the process can be derived without serious confounding with the blocking effect. These derivations are described next.

## 5.7 Quadratic Models for $\sqrt{R_o}$ and $E_o$

Based on the curvature check and the analysis of residual of the simple linear models, it was concluded that quadratic models were required to describe  $\sqrt{R_o}$  and  $E_o$  accurately. Moreover, an extra linear term was added to each model to account for the blocking effect. The coefficients for the two models were then determined using least squares technique with all the runs included. The models for  $\sqrt{R_o}$  and  $E_o$  are as follows:

$$\sqrt{R_o} = 15.913 - 0.454T - 0.307t + 7.086C - 0.279C^2 - 0.316Tt + 2.520B \quad (\text{EQ 5.2})$$

$$E_o = 207.2 - 35.4T + 9.0T^2 - 7.7t + 13.3C - 19.2B \quad (\text{EQ 5.3})$$

In the above equations,  $T$ ,  $t$ , and  $C$  are normalized processing parameters with respect to the levels used in the factorial experiments.  $B$  is the blocking effect parameter which has value of either 0 or 1 corresponding to the first and the second stage.

## 5.8 Analysis of the Residuals

Before the goodness of the fit can be determined, it is necessary to inspect the residuals for the possible indications of model inadequacy. The residuals for the quadratic models of  $\sqrt{R_o}$  and  $E_o$  were calculated and are plotted in Figures 5.6 and 5.7 respectively. For  $\sqrt{R_o}$ , the plots of residuals did not show any trend and the residuals appeared to be randomly distributed. So the model for  $\sqrt{R_o}$  appeared to be quite good. But the plot of residuals versus the predicted values for  $E_o$  still showed a slight curvilinear trend. Moreover, the range of the residuals, on the order of a few percent of the predicted  $E_o$ , were also quite large.

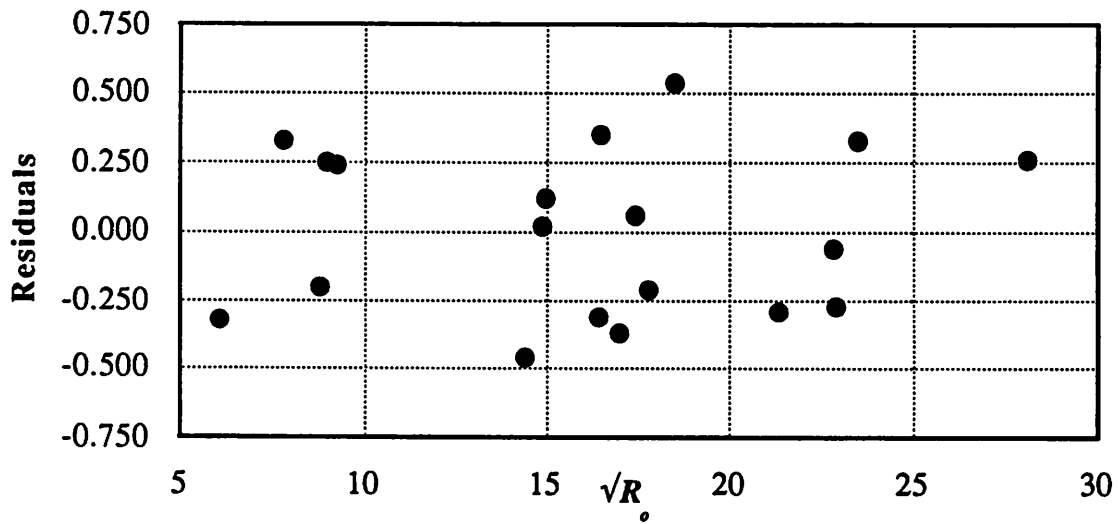


Figure 5.6. Plots of residuals for  $\sqrt{R_o}$  quadratic model.

From the plots of residuals, we can see that the model for  $\sqrt{R_o}$  are more accurate than the model for  $E_o$ . This difference in the accuracy of the models perhaps can be explained by the fact that  $R_o$  is a physical parameter (dissolution rate of unexposed resist), whereas  $E_o$  is a parameter extracted with nonlinear regression. In the parameter extraction procedure for the dissolution rate model, the values of  $\alpha$  and  $\beta$  had no influence on the determination of  $R_o$ . On the other hand, the best value for  $E_o$  depended strongly on both  $\alpha$  and  $\beta$ .

The unknown blocking effect could have also interfered with the assumption that  $\alpha$  and  $\beta$  were constants. Nonetheless, the resulting model still matched most of the runs, and only in with a few cases was the discrepancy more than a few percent. The final test for the models was to inspect the correlations between the two residuals. Figure 5.8 shows no evidence of such correlations.

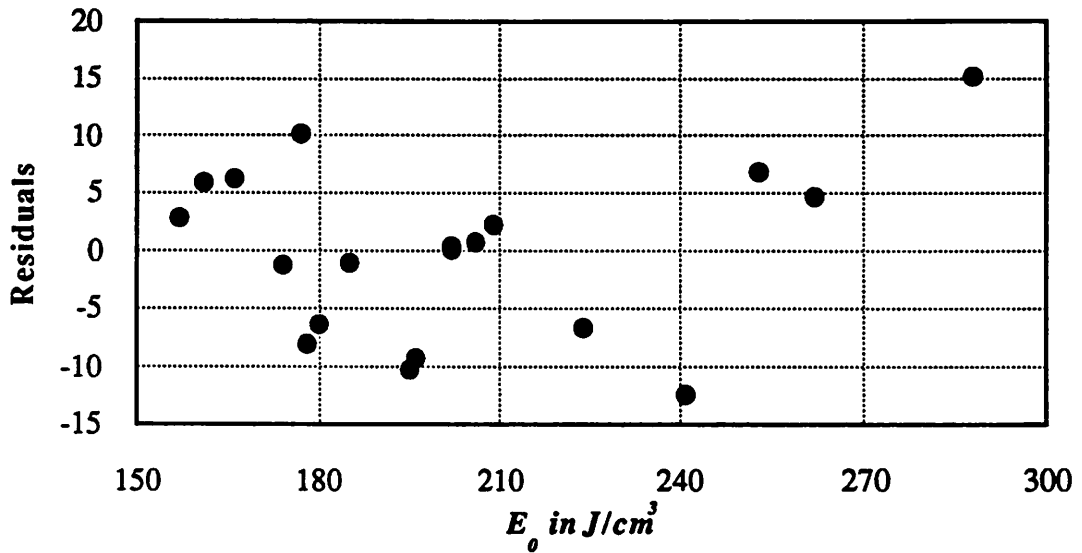


Figure 5.7. Plots of residuals for  $E_0$  quadratic model.

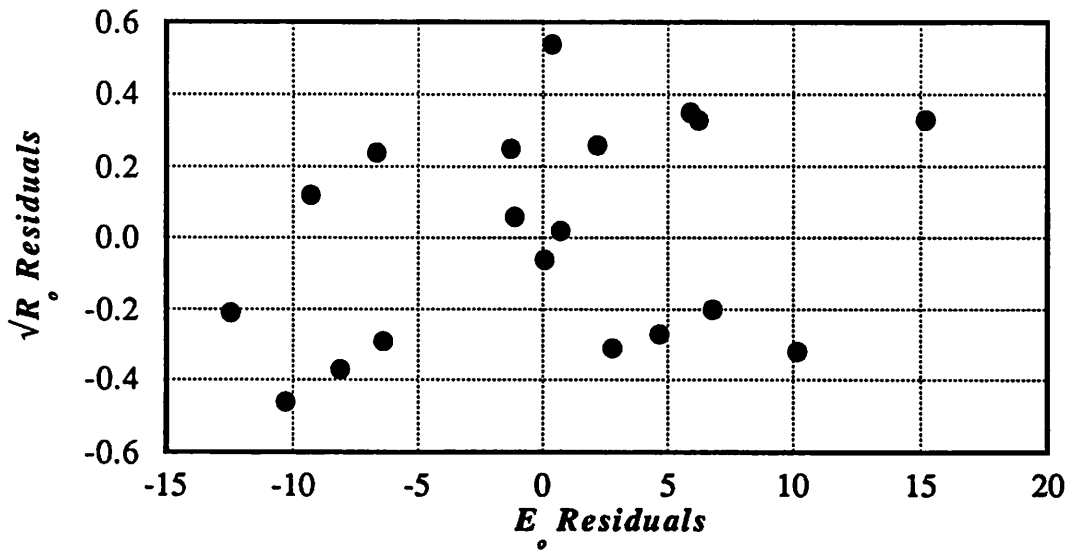


Figure 5.8. Plots of residual correlation.

## 5.9 Analysis of Variance

Since the two models did not show inadequacy, their goodness of fit can be determined by the analysis of variance. In Tables 5.6 and 5.7, the sums of squares for the observed, estimated and residuals of  $\sqrt{R_o}$  and  $E_o$  are shown. The sums of squares for the residuals are further broken down into a lack of fit part and a pure error part. The ratio of the lack of fit to pure error indicated whether the sum of squares for the residuals are caused by the lack of fit or pure error. In both cases, these ratios were very small suggesting there was no reason to suspect lack of fit. To formally determined the significance level, the F-distribution was used. Ratio for  $\sqrt{R_o}$  as great or greater than 0.23 can be expected about 96% of the time. The larger experimental errors in the  $E_o$  data push confidence level even higher (99% of the time).

TABLE 5.6. Analysis of variance for  $\sqrt{R_o}$  data.

source	sum of squares	degrees of freedom	mean square
model	$S_M = 5629.4$	7	
residual	lack of fit	$S_L = 0.36$	0.0514
	pure error	$S_E = 1.14$	0.228
	$S_R = 1.5$	12	0.125
		7	
		5	
total	$S_T = 5630.9$	19	ratio = 0.23

TABLE 5.7. Analysis of variance for  $E_o$  data

source	sum of squares	degrees of freedom	mean square
model	$S_M = 805070$	6	
residual	lack of fit	$S_L = 194$	24.3
	pure error	$S_E = 796$	159
	$S_R = 990$	13	76.2
		8	
		5	
total	$S_T = 806060$	19	ratio = 0.15

## 5.10 Estimation of Confidence Interval for the Main Model

### 5.10.1 Variance of fitted $\sqrt{R_o}$ and $E_o$

Since direct calculation of the variance of the fitted parameters was very complicated, an average variance was computed instead using Equation (5.4)[7]:

$$\bar{V}(\hat{y}) = \frac{1}{n} \sum_{i=1}^n V(\hat{y}_i) = \frac{p\sigma^2}{n} \quad (\text{EQ 5.4})$$

On the assumption that the model was adequate, an estimate of the error variance  $\sigma^2$  for  $\sqrt{R_o}$  were

$$s^2 = \frac{S_R}{n-p} = \frac{1.5}{19-7} = 0.125 \quad (\text{EQ 5.5})$$

and for  $E_o$ ,

$$s^2 = \frac{S_R}{n-p} = \frac{990.2}{19-6} = 76.2 \quad (\text{EQ 5.6})$$

Substituting the result from Equation (5.5) and (5.6) into Equation (5.4), we found  $\bar{V}(\sqrt{R_o}) = 0.046$  and  $\bar{V}(E_o) = 24.1$ . The confidence limits for the two estimates can be easily calculated from the student  $t$ -distribution with their respective degrees of freedom. For example, an extra wafer (wafer #20) was included in the second batch of wafer with post-exposure bake at 115°C for 60 sec and developer concentration of 0.27N. The observed and estimated values from the quadratic models are compared in Table 5.8 along with the 95% confidence limits.

**TABLE 5.8.** Comparison of observed and estimated  $\sqrt{R_o}$  and  $E_o$  for wafer #20.

Parameter	Observed	Quadratic model	95% Confidence limits
$\sqrt{R_o}$	13.67	13.77	$\pm 0.47$
$E_o$	185	194	$\pm 10.6$

The results in Table 5.8 indicate there was good agreement between the estimated and observed values. However, the credibility of a hypothesized pair of values for  $(\sqrt{R_o}, E_o)$ , with the joint confidence regions formed by the two limits, is questionable. In Figure 5.9 we show the contours of the sum of squares surface calculated from the ratios of estimated to experimental dissolution rate values for wafer #20. The values of the surface were indicators to the goodness of fit of the rate model, and the smaller the value, the better is the fit. The point with coordinates [13.77, 194] lies well within the region with the minimum value. However, consider another point with coordinates [13.45, 188]; although it is within the individual limits of joint confidence region, it has a larger sum of squares ratio. As a result, any estimated values should be checked by referring to the contours of sum of squares.

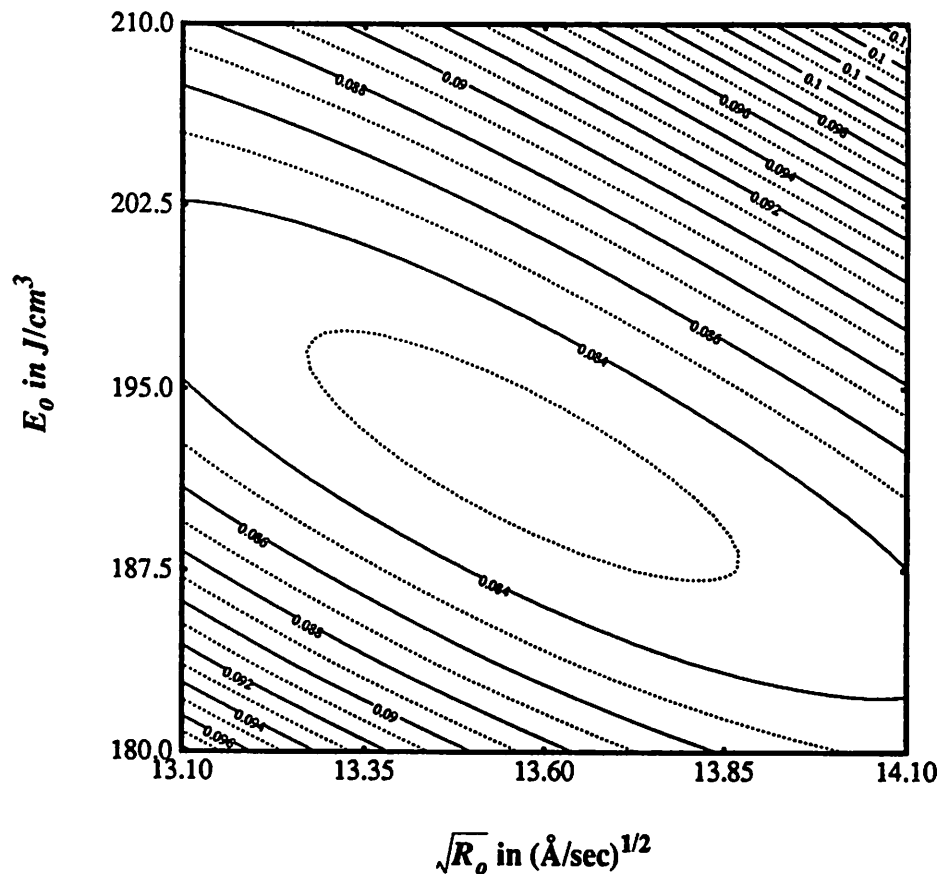


Figure 5.9. Contours of ratio of sum of squares surface, wafer #20 with post-exposure bake at 115°C for 60 sec and development in 0.27N MF-312 developer.

## 5.11 Comparison of Simulated and Experimental Resist Profiles

In this section, the validity of the extended model is verified by demonstrating the good agreement between the simulated and the experimental resist profiles over a wide range of processing conditions. In the following examples, 0.5  $\mu\text{m}$  line/space and isolated space resist profiles on SEM micrographs are compared to simulation. The SEM micrographs of resist profiles were obtained from dose-matrix experiments. These experiments were designed to determine the doses which produce the correct linewidth for a given pattern and process. As preliminary process evaluation tests, these patterns were not proximity corrected. Resist profiles were inspected by SEM and the doses which produced the satisfactory profiles were recorded.

In the simulation, the resist profiles were generated with the same processing conditions as in the experiments. First, the electron energy deposition was obtained from Monte Carlo simulation with the resist atomic composition of SAL-601-ER7, the thickness of the resist, and the accelerating voltage as input. Then the parameters for the dissolution rate functions were calculated for the specific PEB temperature, PEB time, and the developer concentration. Since the wafers for the resist profile study were processed after the second stage of the statistical experiments, the blocking terms in Equation (5.2) and Equation (5.3) were set to 1 in the calculation. Finally, the rate functions were entered into SAMPLE to simulate the resist profiles.

Simulated and experimental resist profiles are compared in two cases. The first case had the same post-exposure bake and developer concentration as in wafer #20 described in the previous section. The second case was a more ambitious test, as processing condition outside the parameter spaces studied was used.

### 5.11.1 Samples within the Parameter Space

For the first case of wafer #20, the resist was baked at 115°C for 60 sec after exposure and was developed in 0.27N MF-312 developer for 5 min. For a 0.5  $\mu\text{m}$  line/space pattern, 3.5  $\mu\text{C}/\text{cm}^2$  and 3.83  $\mu\text{C}/\text{cm}^2$  produce linewidth close to the desire value. The SEM micrographs of the resist profiles and the simulations are shown in Figure 5.10. The SEM micrographs were taken from 70° tilt samples. The profiles from simulation match very well to the ones from experiment in terms of linewidth and sidewall angle. However, the simulated profiles appear to be slightly taller than the actual resist profiles even with the 70° tilt in the samples in the SEM micrographs taken into account. Another example is shown in Figure 5.11 where the profiles for a 0.5  $\mu\text{m}$  isolated space are compared. Again, the simula-

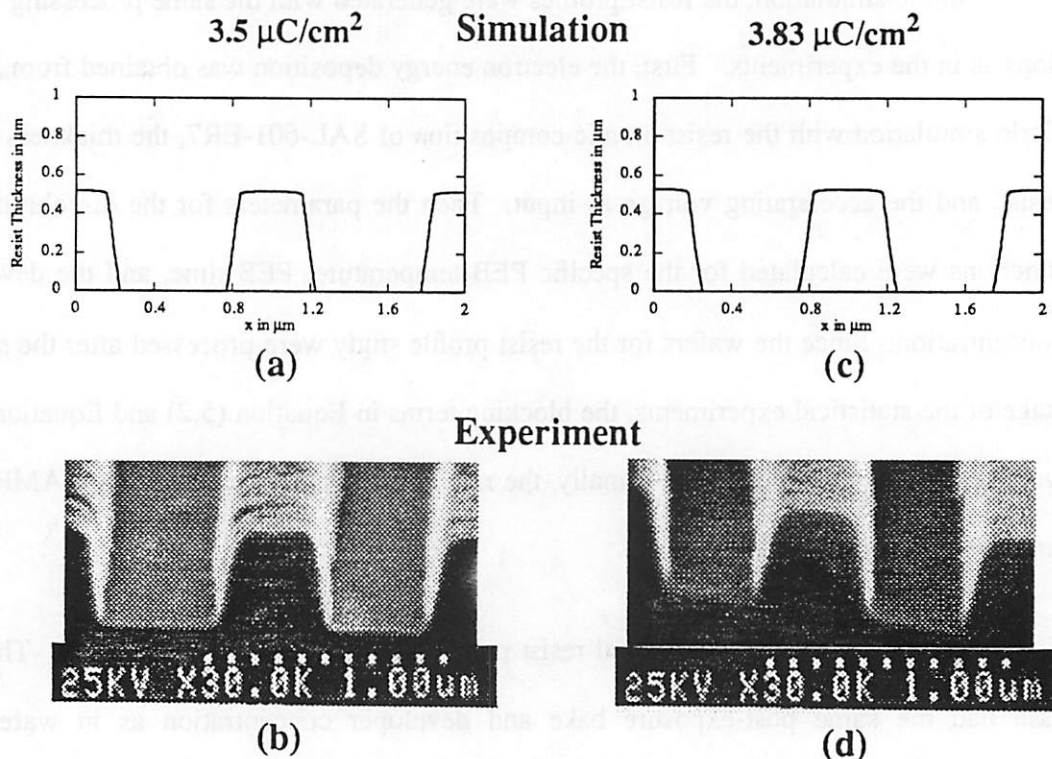


Figure 5.10. Comparison of simulated and experimental resist profiles for 0.5  $\mu\text{m}$  line and space pattern. Processing conditions are PEB at 115°C for 60 sec and development in 0.27N MF-312 for 5 min. (a) 3.5  $\mu\text{C}/\text{cm}^2$  simulated, (b) experiment; (c) 3.83  $\mu\text{C}/\text{cm}^2$  simulated, (d) experiment.

tion is very similar to the experiment except a small discrepancy in the thickness of the resist after development indicating the predicted dissolution rate at the high dose region is too slow. This underestimation of the dissolution rate for the high dose regions by the rate function can be attributed to the errors in the measurements of slow dissolution rate by the DRM. When the rate is slow enough such that the thickness of resist removed is less than  $\lambda/2n$  of the measuring wavelength, the DRM cannot calculate the thickness removed due to the lack of information. Thus the DRM will mistakenly produce a zero dissolution rate. These errors are inherited by the dissolution rate function and are sometimes reflected in the discrepancy of the top-loss between simulated and experimental resist profiles.

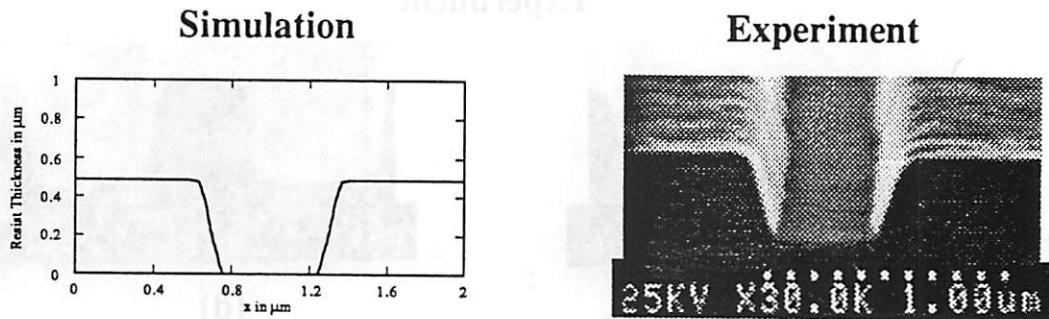


Figure 5.11. Comparison of simulated and experimental resist profiles of a  $0.5 \mu\text{m}$  isolated space with  $2.6 \mu\text{C}/\text{cm}^2$ . Processing conditions are PEB at  $115^\circ\text{C}$  for 60 sec and development in 0.27N MF-312 for 5 min.

### 5.11.2 Samples outside the Parameter Space

The resist for the second case was baked at  $115^\circ\text{C}$  for 90 seconds after exposure. Although the post-exposure bake was the same as level zero of the factorial experiment, the developer used was 0.38N, which was higher than the highest level used previously. Based on these conditions, the rate parameter functions yielded  $209 \text{ J}/\text{cm}^3$  for  $E_o$  and  $850 \text{ \AA}/\text{sec}$  for  $R_o$ . Once these parameters were determined, the same comparisons were made and the resulting profiles are shown in Figure 5.12 and Figure 5.13 for the  $0.5 \mu\text{m}$  line/space and isolated space patterns respectively. The agreement between simulation and experiment was

excellent, because this process has higher contrast than the previous case, a fact that tends to minimize the zero rate error in the rate function.

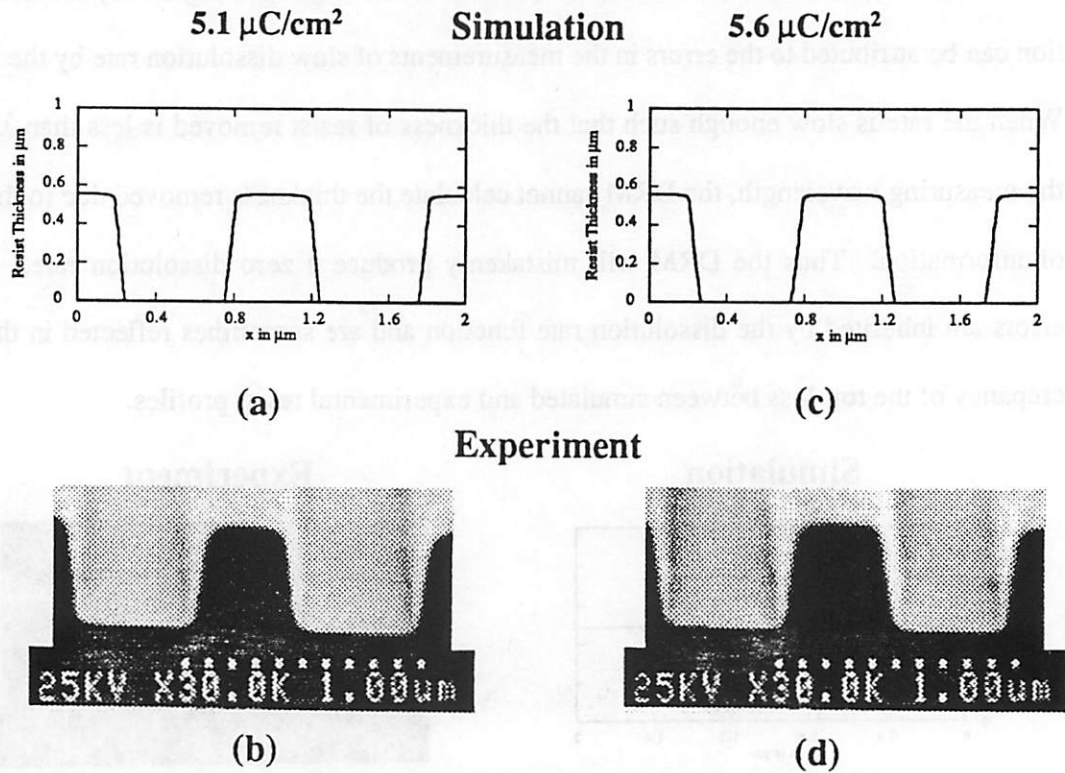


Figure 5.12. Comparison of simulated and experimental resist profiles for  $0.5 \mu\text{m}$  line and space pattern. Processing conditions are PEB at  $115^\circ\text{C}$  for 90 sec and development in 0.38N MF-312 for 5 min. (a)  $5.1 \mu\text{C}/\text{cm}^2$  simulated, (b) experiment; (c)  $5.6 \mu\text{C}/\text{cm}^2$  simulated, (d) experiment.

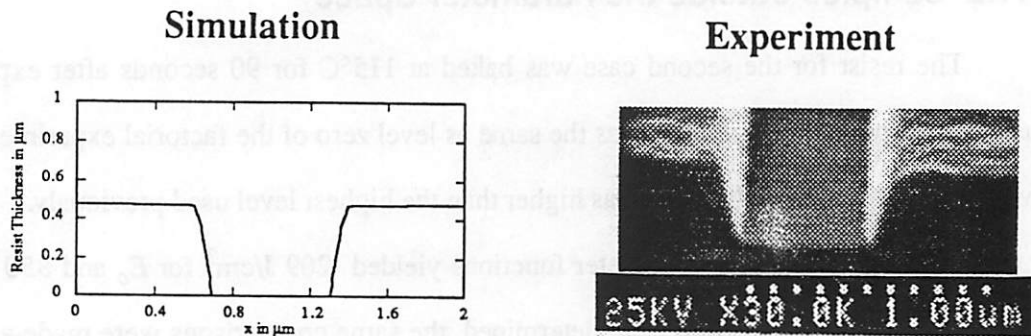


Figure 5.13. Comparison of simulated and experimental resist profiles of a  $0.5 \mu\text{m}$  isolated space with  $3.2 \mu\text{C}/\text{cm}^2$ . Processing conditions are PEB at  $115^\circ\text{C}$  for 90 sec and development in 0.38N MF-312 for 5 min.

## 5.12 Process Optimization

Besides resist profile simulation, the semi-empirical dissolution model can also be used to derive other resist characteristics such as contrast and sensitivity. These characteristics can be related to the processing conditions with the empirical rate parameter model to help determine the optimal processing conditions. For simplicity, assuming the resist received ideal exposure (uniform energy deposition in the resist), the dissolution rate is then only a function of exposure dose and the amount of thickness removed is equal to the rate times the development time. After normalized to the initial resist thickness, the thickness retention  $\Gamma$  is given by:

$$\Gamma = 1 - \frac{\tau}{\left[1 + \left(\frac{kD}{E_o}\right)^\beta\right]^\alpha} \quad (\text{EQ 5.7})$$

Here  $\tau$  is the normalized development time,

$$\tau = \frac{R_o t_D}{T_o} \quad (\text{EQ 5.8})$$

where  $t_D$  is the development time and  $T_o$  is the resist thickness. For a 50% thickness retention, we set  $\Gamma$  equal to 0.5 and solve for  $D_{0.5}$

$$D_{0.5} = \frac{E_o}{k} \left[ (2\tau)^{1/\alpha} - 1 \right]^{1/\beta} \quad (\text{EQ 5.9})$$

To calculate the contrast ( $\gamma$ ), we first have to obtain thickness retention as a function of exposure dose. Rearranging Equation (5.9),  $E_o$  can be expressed in term of  $D_{0.5}$ :

$$E_o = \frac{kD_{0.5}}{\left[ (2\tau)^{1/\alpha} - 1 \right]^{1/\beta}} \quad (\text{EQ 5.10})$$

Substituting Equation (5.7) in (5.10) and letting  $x = \log_{10}D$ , we obtain the contrast curve,

$$\Gamma = 1 - \frac{\tau}{\{1 + [(2\tau)^{1/\alpha} - 1] \left(\frac{10^x}{D_{0.5}}\right)^\beta\}^\alpha} \quad (\text{EQ 5.11})$$

Taking advantage of the fact that the contrast curve at 50% thickness retention is almost linear to the log of the exposure dose,  $\gamma$  is obtained by taking the derivative of  $\Gamma$  with respect to  $x$  on the first order term of the Taylor expansion of Equation (5.11) around  $x = \log_{10}D_{0.5}$

$$\gamma = \frac{\ln 10}{2} \alpha \beta \left[ 1 - \frac{1}{(2\tau)^{1/\alpha}} \right] \quad (\text{EQ 5.12})$$

Equation (5.12) shows that the resist contrast depends strongly on  $\alpha$ ,  $\beta$ , and  $\tau$ . However, for  $\alpha > 1$  and  $\tau > 1$ ,  $(2\tau)^{1/\alpha} \approx 1$ , and the second term in Equation (5.12) can be approximated by  $\ln(2\tau)^{1/\alpha}$ . Equation (5.12) can then be simplified to

$$\gamma \approx \frac{1}{2} \beta \ln 10 \cdot \ln (2\tau) \quad (\text{EQ 5.13})$$

Therefore, the dependence of  $\gamma$  on  $\alpha$  is negligible. Since  $\beta$  appeared to be constant for SAL-601-ER7, to improve the contrast,  $\tau$  has to be increased at the expense of sensitivity by either using a longer development time or a more concentrated developer, or both. Substituting Equation (5.2) and (5.3) in (5.12) and (5.9), we can determine quantitatively, the dependence of  $\gamma$  and  $D_{0.5}$  on the processing conditions. For example,  $\gamma$  and  $D_{0.5}$  as a function of PEB temperature and developer concentration for a 90 seconds PEB and 10 minute development, are plotted in Figure 5.13 and 5.14 respectively. Since higher con-

trast can reduce proximity effects, a good process window is in the upper right-hand quadrant of the contour plots corresponding to using high PEB temperatures and high developer concentrations. In that region, the contrast of the resist is around 6 and the sensitivity is about  $2 \mu\text{C}/\text{cm}^2$ . Although the trend suggests using even higher temperatures and concen-

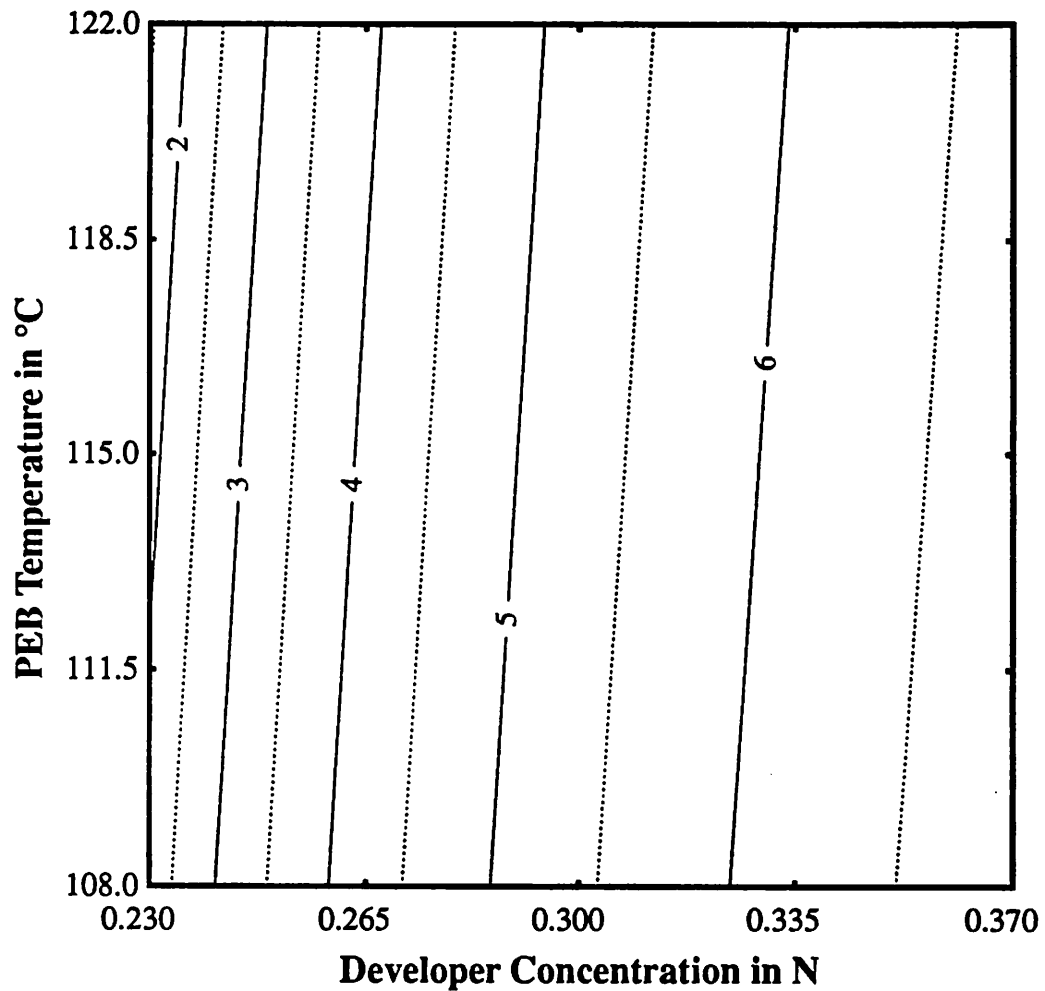


**Figure 5.14.** Contours of constant contrast for SAL-6010-E7 under ideal exposure for 90 sec post-exposure bake with different temperatures and 10 min development with various developer concentration. Contrast increases with higher developer concentration and to a much lesser degree, the PEB temperature.

tations, there are physical limits on both processing parameters. Too high a PEB temperature would degrade the contrast as the novolak resin in the resist will become unstable above 125°C and will start to crosslink in the unexposed areas. Too strong a developer will decrease the sensitivity of the resist and in the extreme case, make the resist swell after development. As for PEB time and development time, their effects are not as significant as

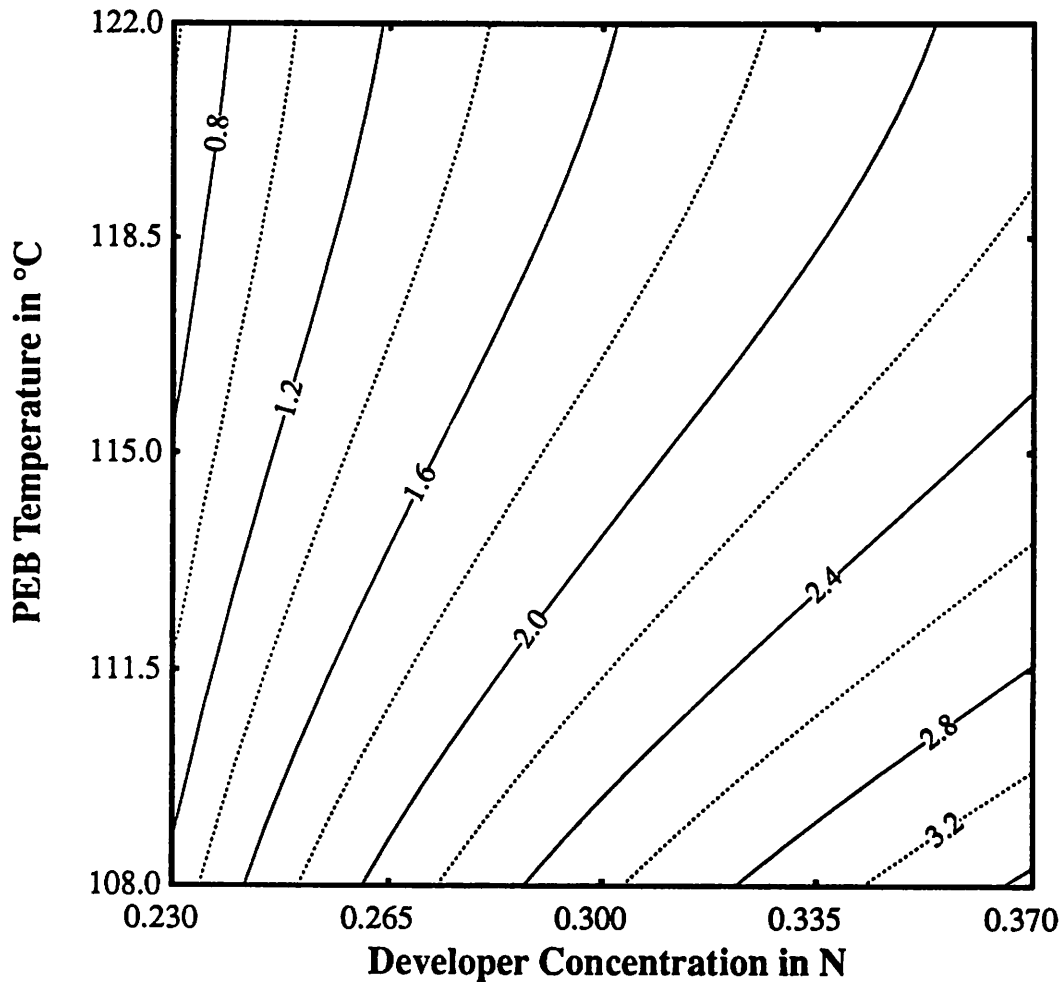


Figure 5.15. Contour of constant sensitivity (in  $\mu\text{C}/\text{cm}^2$ ) for SAL-6010-E7 under ideal exposure for 90 sec post-exposure bake with different temperatures and 10 min development with various developer concentration. Developer concentration and PEB temperature have opposite effects on sensitivity.

the other factors. In general, a PEB of about 90 seconds should be sufficient and a long development time is also desirable as it will improve the contrast.

### 5.13 Summary

A methodology based on empirical extensions to the mechanism-based dissolution rate function of absorbed energy was developed to extend the range of profile modeling for advanced electron-beam resists. By combining mechanism-based dissolution rate model with empirical-fitted parameter functions of processing conditions, the effects of the post-exposure bake and the developer concentration can be included for chemically-amplified resists. The combined model consists of a dissolution rate function of absorbed energy and simple functions relating the parameters in the rate function to the processing conditions. Thus, once these rate-model parameter functions are determined, a rate equation can be obtained for any processing conditions. These simple rate-model parameter functions are obtained from statistically design experiment and response surface analysis. With a central composite design experiment of dissolution rate measurements, the number of runs required is minimized.

This technique of using empirically fitted parameter functions to enhance the mechanism-based rate model was applied to Shipley SAL-601-ER7 negative resist. An experiment using a central composite design was performed with the PEB temperature, PEB time, and developer concentration as the factors. Of the four parameters in the rate function, only  $E_o$  and  $R_o$  are found to be affected by the processing factors.  $\beta$  and  $\alpha$  appeared to be independent of processing conditions and they have values of 1.5 and 31 respectively. For  $E_o$ , only the major effects were significant. On the other hand, a square root transformation was needed to reduce the number of significant effects in  $R_o$ . In addition to the main effects, the

interaction of PEB temperature and PEB time was also significant. Based on the curvature of the response surfaces and the analysis of residuals, it was found that quadratic functions are needed to describe  $E_o$  and  $R_o$  accurately. In the function for  $E_o$ , the square term was the PEB temperature, and in the function for  $R_o$ , the square term was in the developer concentration. Finally, a blocking term was added to each function to account for the discrepancy observed between the first and second stages of the experiments.

The extended model for SAL-601-ER7 agreed very well with experiment. First,  $E_o$  and  $R_o$  predicted by the two parameter functions were found to be within the 95% confidence limit of the experiment. Resist profile simulations using these parameters look almost identical to the SEM micrographs of the experimental resist profiles. Moreover, important performance indicators such as contrast and sensitivity can also be derived from the combined model, which can be used to optimize the processing of the resist. A post-exposure bake of  $118\pm 4^\circ\text{C}$  for 90 seconds and development in  $0.34\pm 0.03\text{N}$  developer, from 3 to 10 minutes result in a contrast around 6 and sensitivity\* around  $2.5 \mu\text{C}/\text{cm}^2$  for the SAL-601-ER7 resist.

However, the use of the empirical extension to the mechanism-based resist model does not directly explore the mechanisms involved in the post-exposure bake and the development process. Therefore, it cannot help in the understanding of the chemical and physical processes which govern the resist's behavior. For example, in the optically exposed SNR-248 chemically-amplified resist, the diffusion of the acid catalysts affects resist profiles significantly. Since the chemistry of SAL-601-ER7 is very similar to that resist, it is not clear that if the diffusion of the acid can be ignored in the modeling of the e-beam resist.

---

\*. Sensitivity extrapolated from  $D_{0.5}$  to 100% resist thickness retention.

Furthermore, since the dissolution rates of these resists are governed by the acid-catalyzed crosslinking reaction, the dissolution rate should be a function of the extent of crosslinking reaction, rather than a function of absorbed energy density. In next chapter, optical and e-beam exposed chemically-amplified resists are compared to elucidate the mechanisms of the post-exposure bake and development processes.

## References

- [1] R. A. Ferguson, Y. Shacham-Diamand, C. A. Spence, and A. R. Neureuther, "Modeling and Simulating of Multiple Chemical States in Photoresist Materials," *Proceedings of SPIE, Advances in Resist Technology and Processing VI*, vol. 1086, pp. 262-273, 1989.
- [2] W. D. Hinsberg and M. L. Gutierrez, "Effect of Developer Composition on Photoresist Performance," *Proceedings of Kodak Microelectronics Seminar*, pp. 52-56, (1983).
- [3] A L. Blum, M.E. Perkins and H.-Y. Liu, "A Study of the Effect of Key Processing Variables on the Lithographic Performance of Microposit SAL601-ER7 Resist," *J. Vac. Sci. Technol.*, B6, pp. 2280, 1988.
- [4] G. P. E. Box, W. G. Hunter, and J. S. Hunter, *Statistics for Experimenters*, John Wiley & Sons, pp. 524, New York, 1978.
- [5] G. R. Bryce and D. R. Collette, "Process Characterization and Optimization using Statistical Design Techniques," *Proceedings of the Kodak Microelectronics Seminar*, pp. 134-142, November 14-15, 1983.
- [6] G.P.E. Box, W. G. Hunter, and J. S. Hunter, *Statistics for Experimenters*, John Wiley & Sons, pp. 323, New York, 1978.

## **Chapter 6**

# **Mechanism and Model of the Crosslinking Reaction in Acid-Hardening Chemically-amplified Resists**

A practical model based on a linear approximation of the “cage effect” in the crosslinking reaction of the melamine-based acid-hardening chemically-amplified resist is presented, which is explicitly characterized in terms of the dose-dependent saturation of the reaction. This model is derived from measurements of the extent of reaction obtained with Fourier-transform infrared (FTIR) spectrometry. The level of saturation is an explicit parameter characterized through the maximum conversion of the melamine crosslinking sites measured by FTIR for different PEB temperatures and exposure doses. In this model, the dose-dependent saturation of the acid-catalyzed crosslinking reaction during the post-exposure bake is assumed to be caused by a “cage effect” mechanism [1]. This new model not only provides a closed-form solution to the reaction rate equation, but it also enables the systematical determination of kinetic parameters from the extent of reaction measurements with a simple least squares technique. When this model is combined with the characteristic dissolution rate curve as a function of the extent of reaction, it can be used to determine the lithographic behavior of the resist during exposure, post-exposure bake, and development.

### **6.1 Introduction**

The concept of chemical amplification was conceived to improve the quantum efficiency of resist systems used in advanced lithographic processes such as deep-UV and X-ray lithography.[2]-[3] In chemically-amplified resists, the photo-active compounds do not directly control the resists' behaviors. Instead, upon radiation, they will release catalysts in the resist, which are usually either acid or base moieties. These moieties will then catalyze the thermodynamical reactions which govern the resists' solubilities. Thus these resist sys-

tems can circumvent the intrinsic sensitivity limitation that quantum efficiency imposes on conventional resist systems. Unlike the conventional resist systems, which consume at least one photon for every productive chemical transformation, a single catalytic moiety can now initiate multiple chemical events. An excellent example is the family of acid-hardening resists, including the Shipley SAL-601-ER7 and the SNR-248 resists, which uses a melamine-based crosslinking agent. These resists have made strong impact in both optical and electron-beam lithography [4].

Mechanistic approaches to the modeling of the family of melamine-based acid-hardening resists have demonstrated promise in understanding the mechanism of the crosslinking reaction. Detailed studies of the resists based upon the chemical reaction kinetics and physical mechanisms of the exposure, bake, and development steps can lead to an improved understanding of these mechanisms and to resist models which can address important issues that the phenomenological approach fails to address. For example, according to the EEMB model discussed in Chapter 5, the longer the baking time, the higher is the contrast for SAL-601-ER7 resist. But does longer baking time increase the amount of acid diffusion\*, leading to a change in the linewidth? To answer questions like this, we need to develop mechanism-based models so that rigorous simulation can be used.

Most researchers have used dissolution measurement to indirectly deduce models for the PEB and the development processing of the resist. Ziger *et al.* [6] have examined data on thickness versus development time data of SNR-248 under various PEB and development conditions and extracted kinetic parameters from a simplified dissolution model using two lumped parameters:  $E_0$  and  $\alpha_p n$ . The former is the maximum dose to clear which is a sensitivity parameter, and the latter represents the combined effects of PEB and develop-

---

\*. Acid diffusion is believed to cause the disappearance of standing wave pattern in the deep-UV exposed SNR-248 resist, which is another member of the acid-hardening resists.

ment on the contrast of the resist. In their derivation, both parameters' temperature behaviors were assumed to be Arrhenius type. The dependence of  $E_0$  on the bake process and the development time was measured and successfully correlated. An activation energy for  $E_0$  was obtained. However, the other lumped parameter,  $\alpha_n n$ , had an abrupt change in the slope of the Arrhenius plot. This discrepancy is believed to be due to the saturation of the crosslinking reaction at high conversion of the melamine crosslinking sites which is not included directly in the model.

In the study of KrF excimer laser exposure on SAL-601-ER7, Fukuda and Okazaki [7] proposed a kinetic model which takes into account both exposure-induced and thermal-driven crosslinking reactions of the melamine. However, the extent of crosslinking reaction was indirectly deduced from dissolution rate of the resist. Furthermore, the data presented in their work used extremely long baking times. As a result, their estimation of the consumed crosslinker did not reflect the rate of the reaction, but rather, the equilibrium conversion of the reaction as a function of exposure dose.

Seligson *et al.*[1] looked at the curves of resist film thickness remaining versus exposure dose under different PEB conditions for SAL-601-ER7 and observed a reciprocal relationship between dose and bake time. They postulated a "cage effect" model in which the crosslinking restricts the movements of the reactants as the reaction proceeded. From the form of their reaction rate equation, they deduced a mathematical expression for an equivalent dose,  $D_{eff}$  which incorporated the effects of the PEB processing variables, time and temperature. The PEB temperature and time behavior of  $D_{eff}$  is characterized by an activation energy and an experimental determined order of the acid catalyst in the crosslinking reaction.

While the above modeling approaches use mechanistic models to account for the changes that occur within the resist during processing, they are not based on direct measurement of the changes during the individual processing steps. Recently, Ferguson *et al.* [8] used FTIR and careful curve fitting to establish a kinetic model for the optical exposure and baking of the SNR-248 resist. The rate of the crosslinking reaction was found to be dependent on the concentration of the acid catalyst to the 1.42 power. In addition, an acid-loss reaction was introduced to explain the dose-dependent saturation of the acid-catalyzed crosslinking reaction during the post-exposure bake.

In this chapter, we first develop a practical model which is based on a linear approximation of the “cage effect” for evaluating bake kinetics. Based on this model, a closed-form solution is derived for the reaction rate equation and the kinetic parameters are extracted with a linear least squares technique. The key to this model is the use of equilibrium conversions of the melamine crosslinking sites observed in FTIR measurements. This model is then used to compare the direct exposure changes and bake kinetics of e-beam versus optical exposure on the SNR-248 resist. Comparison of the correlations between dissolution rate and the extent of crosslinking reaction is also included. The experimental procedures for the FTIR and the development rate measurements in this study are provided in the appendix to this chapter.

## **6.2 Acid-Catalyzed Crosslinking Reaction**

### **6.2.1 Melamine-hydroxyl Crosslinking Reaction Mechanism**

The reaction mechanism of the melamine crosslinking agent with the hydroxy group on the resin polymer molecule have been studied by Blank [9] and the proposed mechanism of the reaction is illustrated in Figure 6.1. Upon exposure, the acid generator produces hydrobromic acid. The reaction after the acid generation by the photolysis (or radiolysis) of

the initiator can be described in four steps: i) Protonation of the melamine to form a carbonium ion. ii) Cleavage of a leaving group (alcohol, water) from the melamine. iii) O-alkylation or C-alkylation of the binding polymer resin by a carbonium ion. iv) Regeneration of the acid from the crosslinked resin group. Since all the reactions are reversible, the crosslinking usually reaches an equilibrium state. However, it is believed that the alcohol generated by the rate determining step evaporates during the PEB which drives the reaction to completion.

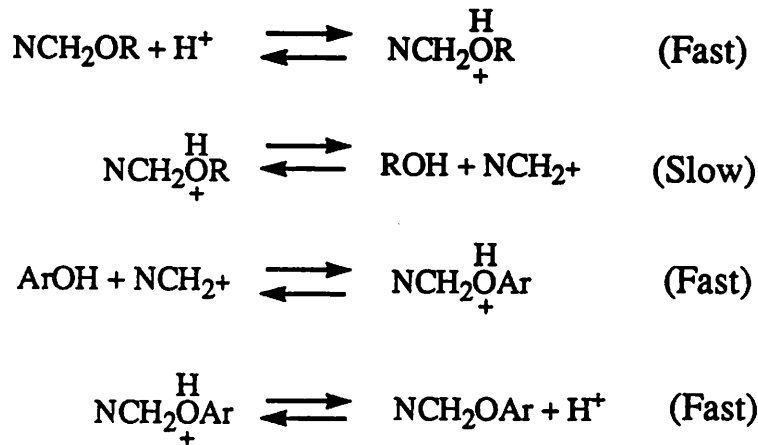


**Figure 6.1.** The sequential reaction of the resin polymer with HMMM during the post-exposure bake.

Since the rate determining step is the cleavage of the leaving group (ROH), the global rate of the crosslinking reaction can be modeled by:

$$\frac{\partial C_{AS}}{\partial t} = k_1 \cdot C_a^m \cdot C_{US} \quad (\text{EQ 6.1})$$

where  $C_{AS}$  is the normalized concentration of the crosslinked melamine sites,  $[\text{NCH}_2\text{OAr}]$ ;  $k_1$  is the global rate constant;  $C_a$  is the normalized concentration of the acid,  $[\text{H}^+]$ ;  $m$  is an unknown order of the reaction for the acid, and  $C_{US}$  is the normalized concentration of the melamine sites,  $[\text{NCH}_2\text{OR}]$ , which have not yet reacted.  $C_{US}$  is related to the  $C_{AS}$  by

$$C_{US} = 1 - C_{AS} \quad (\text{EQ 6.2})$$

Substituting Equation (6.2) to Equation (6.1), the rate of the crosslinking reaction can be solved in terms of the acid concentration and the global reaction rate constant.

However, the above equations describe only an idealized catalytic reaction sequence which may not be valid in a solid state polymer thin film. Direct measurements of the extent of crosslinking reaction by Ferguson *et al.* [8] and Tam *et al.* [10] have shown that the crosslinking reaction saturates at different values for different exposure doses and PEB temperatures. This is a clear evidence that the reaction is non-ideal because the acid produced which, to first order is proportional to the dose, should only affect the rate of reaction and not the equilibrium conversion. Therefore, a mechanism for the saturation of the crosslinking reaction is needed to fully explain the acid-catalyzed melamine-hydroxyl crosslinking reaction. Several mechanisms have been proposed and will now be discussed.

### 6.2.2 "Cage Effect" Model by Seligson *et al.*

Seligson *et al.* hypothesized that the formation of the crosslinked network might hinder the rate of the reaction. A schematic diagram of the HMMM crosslinked network with the phenolic resin is shown in Figure 6.2. In their hypothesis, the global rate constant of the rate determining step decreases as the crosslinking reaction progresses due to the restricted segmental diffusion of the resin chains. In addition, they decoupled the temperature dependence and concentration dependence in the description of the global rate constant. Based on the work of Meijer [11] on the melamine-hydroxyl crosslinking reaction, they proposed:

$$k_1(T, C_{AS}) = k'_1(C_{AS}) \cdot e^{-E_s/kT} \quad (\text{EQ 6.3})$$

where the temperature dependence of  $k_1$  is of Arrhenius type. When Equations (6.2) and (6.3) are substituted into Equation (6.1), the rate of reaction becomes

$$\frac{\partial C_{AS}}{\partial t} = k'_1 (C_{AS}) \cdot e^{\frac{-E_a}{kT}} \cdot D^m \cdot (1 - C_{AS}) \quad (\text{EQ 6.4})$$

Here, the concentration of acid is replaced with  $D$ , the exposure dose, which is a constant throughout the crosslinking reaction. Unfortunately, Equation (6.4) was not solved directly due to the lack of information on  $k'_1$ . Instead, an integral form of the solution was obtained which can relate the  $C_{AS}$  to a new variable through a function  $g[\ ]$ :

$$C_{AS} = g [D \cdot e^{-E_a/mkT} \cdot t^{1/m}] \quad (\text{EQ 6.5})$$

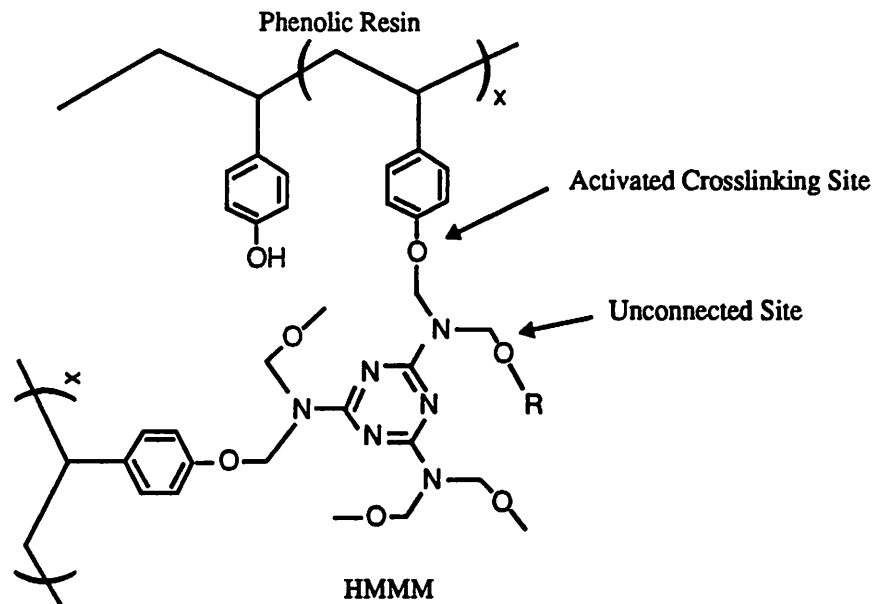


**Figure 6.2.** Two types of ether linkages could exit on the HMMM compound after the crosslinking reaction: the C-O-C-N structure on the site which hasn't reacted yet, and the C-O-C-Ar structure on the reacted site.

They further argued that the essential result is that any observable quantity of the resist which depends on  $C_{AS}$  is itself a function of the argument in  $g[]$ . Based on that assumption, they were able to evaluate effects of processing conditions on linewidth through  $g[]$ , in which the argument is designated as the effective dose,  $D_{eff}$ ,

$$D_{eff} = D \cdot e^{-E_a/mkT} \cdot t^{1/m} \quad (\text{EQ 6.6})$$

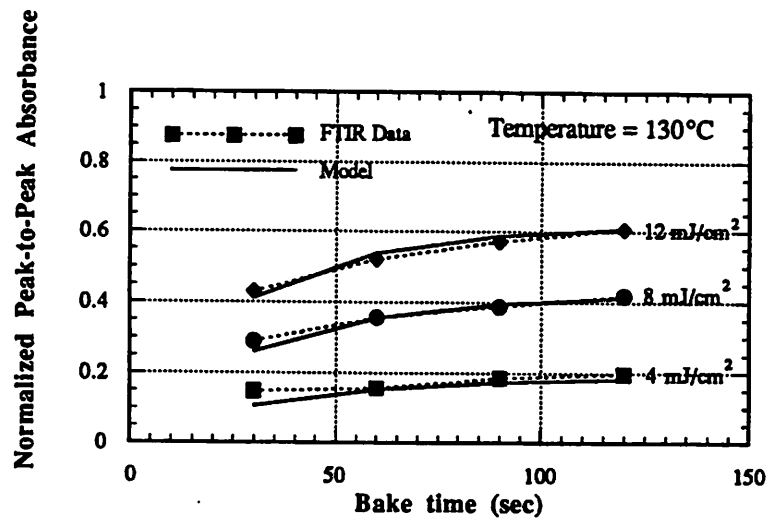
This  $D_{eff}$  model predicts that there exists a reciprocity between the process parameters and the extent of crosslinking. This interrelationship was confirmed and characterized by examining resist film thickness remaining versus exposure dose curves under various post-exposure baking conditions with PEB temperatures ranging from 88 to 140°C and PEB time ranging from 30 to 240 seconds. The activation energy of  $D_{eff}$  for SAL-601-ER7 was found to be 0.41 eV under deep-UV exposure and the order of the acid catalyst,  $m$ , was found to be 3. However, this model does not predict a saturation of the crosslinking reaction. For example, an arbitrarily large value of  $D_{eff}$  can be produced for any initial dose  $D$  provided a sufficiently long bake is applied. Evidence of the saturation of the crosslinking reaction under normal processing conditions has been seen with both e-beam and optical exposures (in the next section).

### 6.2.3 Acid Loss Mechanism by Ferguson *et al.*

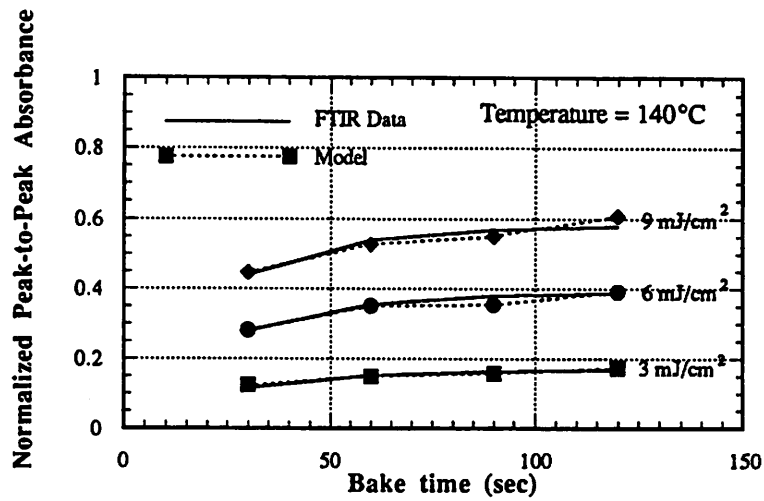
Ferguson *et al.* used FTIR to directly measure the extent of crosslinking reaction during the post-exposure bake in deep-UV exposed SNR-248 resist. Figure 6.3 shows the extent of the crosslinking reaction<sup>†</sup> as a function of PEB time for PEB temperatures of 130°C, 140°C, and 150°C. For different exposure doses, the extent of reaction saturates at

---

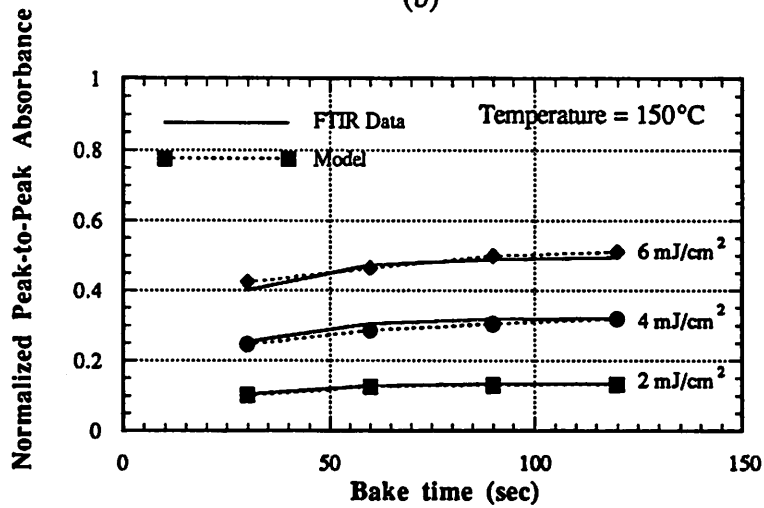
†. The extent of reaction is represented as  $\Delta$ -peak-to-peak absorbance between the peak at 990  $\text{cm}^{-1}$  and 1070  $\text{cm}^{-1}$ , corresponding to the resonant frequency in the ether bond of reacted melamine (product) and the unreacted melamine (reactant).



(a)



(b)



(c)

Figure 6.3. Normalized D-absorbance of deep-UV exposed SNR-248 as a function of PEB time at: (a) 120°C, (b) 130°C, and (c) 140°C.

different values for different baking temperature after about a 120 second bake. To model the quenching of the crosslinking reaction, Ferguson hypothesized that the reaction is stopped due to the consumption of the acid through a first-order side reaction given by:

$$\frac{\partial C_a}{\partial t} = -k_2 C_a \quad (\text{EQ 6.7})$$

where  $k_2$  is the rate constant for the acid loss reaction. Since this reaction is independent of Equation (6.1), the acid concentration can be solved in terms of  $k_2$ ,  $t$ , and  $C_{ao}$ , the initial acid concentration (or  $D$ , the exposure dose),

$$C_a = C_{ao} \cdot e^{-k_2 t} \quad (\text{EQ 6.8})$$

When the expression of the acid concentration is substituted in Equation (6.1), the rate of the crosslinking reaction is then given by,

$$\frac{\partial C_{AS}}{\partial t} = k_1 \cdot (1 - C_{AS}) \cdot C_{ao}^m \cdot e^{-mk_2 t} \quad (\text{EQ 6.9})$$

Equation (6.9) can be solved analytically to provide a closed-form solution of  $C_{AS}$  as a function of baking time and temperature.

Before we examine the solution of Equation (6.9), we can rearrange it to provide a different perspective on the reaction rate of crosslinking,

$$\frac{\partial C_{AS}}{\partial t} = (k_1 e^{-mk_2 t}) \cdot (1 - C_{AS}) \cdot C_{ao}^m \quad (\text{EQ 6.10})$$

When the rate coefficient  $k_1$  is combined with the exponential function, it in essence, represents an exponential decrease in the global rate constant with respect to PEB time. In Equation (6.10), the acid concentration is the initial acid concentration which is now a constant. As a result, this equation can be interpreted as a crude model of the “cage effect” in which

the quenching of the reaction is due to a reduction in the global rate constant as the crosslinking reaction proceeds. That is the disappearance of the acid catalyst is equivalent to a very specific type of “cage-effect”.

Returning to the analysis by Ferguson, Equation (6.9) was solved analytically, and  $C_{AS}$  is given by:

$$C_{AS} = 1 - \exp \left[ -C_{ao}^m \cdot \left( \frac{k_1}{mk_2} \right) \cdot (1 - e^{-mk_2t}) \right] \quad (\text{EQ 6.11})$$

A nonlinear regression technique was then used to extract the kinetic parameters  $k_1$ ,  $k_2$ , and  $m$  from the data plotted in Figure 6.3. The temperature behavior of the two rate coefficients were found to follow an Arrhenius behavior. Therefore, the rate coefficients were expressed as a pre-exponential term and an activation energy. The model fit shown in Figure 6.3 was obtained with the rate coefficients listed in Table 6.1. To fit the spread in the levels of saturation with doses, a non-integer power with a value of 1.42 has to be used for  $m$ .

**Table 6.1: Rate Coefficients of the Ferguson Model**

	$k_1$	$k_2$
Pre-exponential factor, sec <sup>-1</sup>	6.56 x 10 <sup>11</sup>	4600
Activation Energy, eV	0.88	0.43

Reexamining the model of Ferguson from the “cage-effect” point of view leads to further insight. The equilibrium conversion of melamine crosslinking sites alone can provide information on the order of acid in the rate equation. In Equation (6.11), as  $t \rightarrow \infty$ , the equilibrium conversion of  $C_{AS}$ , designated as  $\chi_e$ , is given by:

$$\chi_e = 1 - \exp \left[ -C_{ao}^m \cdot \left( \frac{k_1}{mk_2} \right) \right] \quad (\text{EQ 6.12})$$

This equation can be rearranged to give,

$$m \cdot \ln C_{ao} + \ln \left( \frac{k_1}{mk_2} \right) = \ln(-\ln(1 - \chi_e)) \quad (\text{EQ 6.13})$$

If the initial acid concentration is directly proportional to the exposure dose, then the order of acid concentration can be determined graphically from a log-log plot of  $-\ln(1 - \chi_e)$  versus exposure dose. These data are plotted in Figure 6.4 and a power law fits the data extremely well. The average of the extracted  $m$  values is 1.41, which is within 1% of the values obtained by Ferguson *et al.* In summary, using the saturated values of the extent of the reaction is a very effective means of determining  $m$ . However,  $k_1$  and  $k_2$  of the kinetic model of Ferguson still need to be determined with general nonlinear curve fitting of the FTIR data.

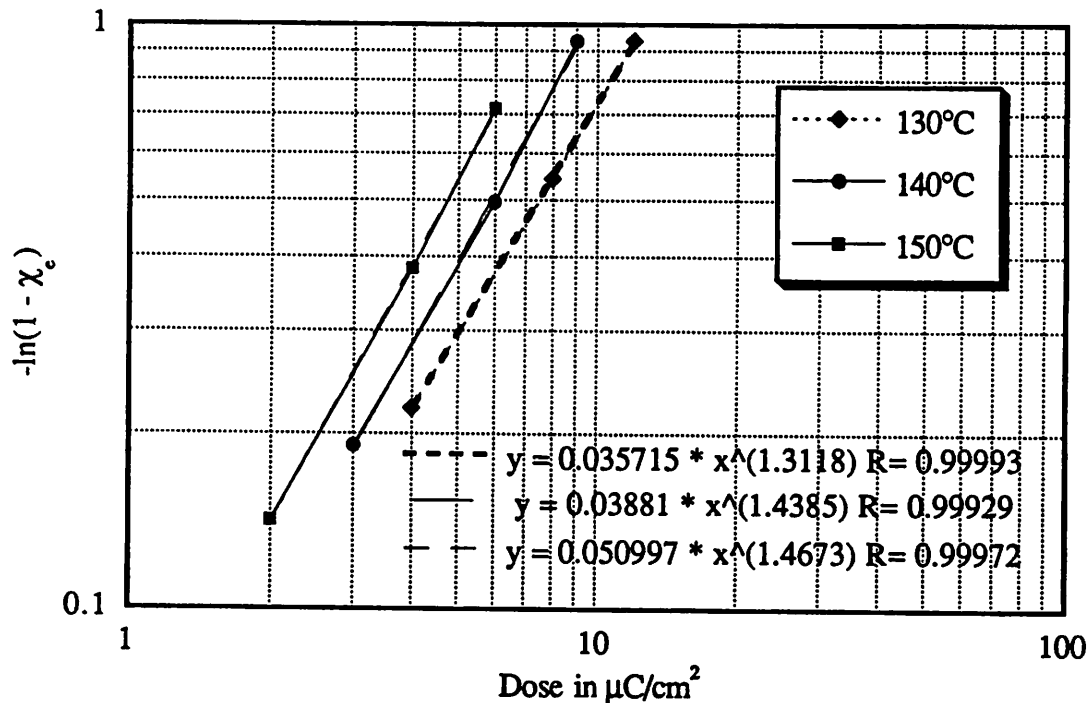


Figure 6.4. Log-log plots of  $-\ln(1 - \chi_e)$  versus exposure dose with data points at the end of the two minute PEB bake in Figure 6.3. The data fall on straight lines and the power law fits the data extremely well.

### 6.3 Novel Model of the “Cage Effect”

Based on the success of the new interpretation of the kinetic model of Ferguson, it is hypothesized that during the post-exposure bake, the global rate constant is a more general decreasing function of the extent of crosslinking due to the “cage effect”. Furthermore, the “cage effect” is decoupled from the rate coefficient by the introduction of a “cage effect” factor. Then the only constraints on this factor are that it should be unity when no activated site exists and approaching zero when the crosslinking reaction saturates. Accordingly, the reaction rate of crosslinking can be expressed as:

$$\frac{\partial C_{AS}}{\partial t} = k_1 \cdot f(C_{AS}, \chi_e) \cdot (1 - C_{AS}) \cdot C_{ao}^m \quad (\text{EQ 6.14})$$

where  $f$  is the “cage effect” factor and it is a function of  $C_{AS}$  and  $\chi_e$ . Here at  $C_{AS} = 0, f = 1$ , and at  $C_{AS} = \chi_e, f = 0$ .

This model is similar to the formulation of Seligson in Equation (6.4). However, we now go beyond the work of Seligson by finding a solution to this equation. Since two values of  $f$  are known, it is natural to start with the simple assumption of a linear variation given by:

$$f = 1 - \frac{C_{AS}}{\chi_e} \quad (\text{EQ 6.15})$$

Here  $\chi_e$  is the equilibrium conversion of melamine crosslinking sites which is a function of only the PBE temperature and the exposure dose. Thus, for a given post-exposure bake, the reaction rate of crosslinking becomes:

$$\frac{\partial C_{AS}}{\partial t} = k_1 \cdot \left(1 - \frac{C_{AS}}{\chi_e}\right) \cdot (1 - C_{AS}) \cdot C_{ao}^m \quad (\text{EQ 6.16})$$

This differential equation can be solved analytically and the solution is an expression for the normalized concentration of reacted melamine crosslinking sites:

$$C_{AS} = \frac{\exp\left[-\left(\frac{1-\chi_e}{\chi_e}\right) \cdot k_1 \cdot C_{ao}^m \cdot t\right] - 1}{\exp\left[-\left(\frac{1-\chi_e}{\chi_e}\right) \cdot k_1 \cdot C_{ao}^m \cdot t\right] - \frac{1}{\chi_e}} \quad (\text{EQ 6.17})$$

The above solution assumes that there is no reacted crosslinking sites before the post-exposure bake. Equation (6.17) indicates that as  $t \rightarrow \infty$ ,  $C_{AS} \rightarrow \chi_e$ . An advantage of this equation over Equation (6.9) is that for a particular resist processing condition with a specified dose and PEB temperature, there is only one fitting parameter to determine the extent of reaction versus PEB time data. This parameter is the combination of the multiplication factors for  $t$  in the exponential terms and is given by:

$$K = -\left(\frac{1-\chi_e}{\chi_e}\right) \cdot k_1 \cdot C_{ao}^m \quad (\text{EQ 6.18})$$

Moreover, the convergence of  $K$  with nonlinear least-squares fitting of Equation (6.17) is rapid and stable. Once the  $K$ 's are determined,  $k_1 C_{ao}^m$  for different PEB temperatures and exposure doses can be obtained since the  $\chi_e$ 's are already known from the FTIR measurements. For the data shown in Figure 6.3, there are three values for  $k_1 C_{ao}^m$  corresponding to the three exposure doses used in each PEB temperature. Thus, with two unknowns and three equations, the rate coefficient  $k_1$  and  $m$  can be determined for each PEB temperature.

Determination of  $K$  is straight forward and for each curve in Figure 6.3, a value for  $k_1 C_{ao}^m$  is obtained. At a given PEB temperature,  $k_1 C_{ao}^m$  is a function of exposure dose

only; therefore,  $k_1$  and  $m$  can be determined graphically from the log-log plots of  $k_1 C_{ao}^m$  versus exposure dose. These plots are shown in Figure 6.5 along with the parameters fitted to a power law in  $C_{ao}$ . The average value of  $m$  is 1.43 which is within 2% of the value determined by Ferguson *et al.* However, the range of  $m$  is about 0.3 and it is not clear if the trend of increasing  $m$  with PEB temperature is significant. The temperature behavior of the rate coefficient  $k_1$  follows Arrhenius behavior and the log  $k_1$  versus  $1/T$  plots are shown in Figure 6.6. From the slope of the fitted line, the activation energy  $E_a$  is found to be 0.334 eV and the pre-exponential constant (based on exposure dose) is  $19.67 \text{ sec}^{-1}$ .

To develop a complete model, the temperature and acid concentration effects on  $\chi_e$  also need to be characterized. Since  $\chi_e$  is the equilibrium conversion of melamine crosslinking sites, it is also expected to follow the Arrhenius behavior. Furthermore, it is postulated

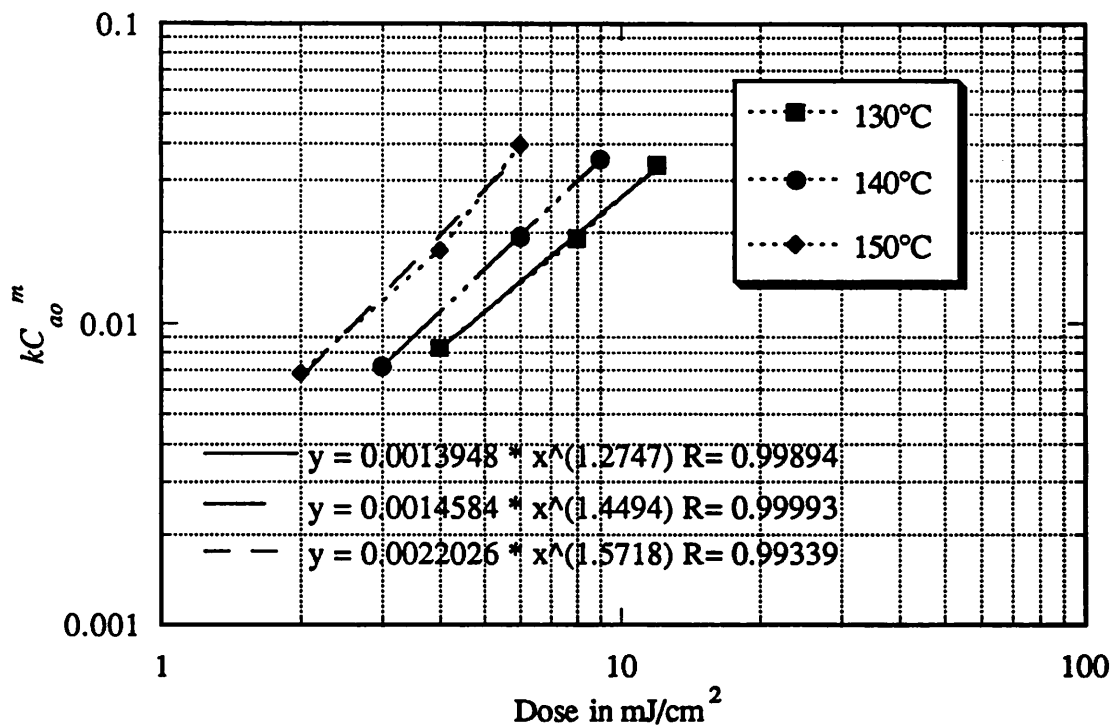


Figure 6.5. Log-log plots of  $k_1 C_{ao}^m$  versus exposure dose for the deep-UV exposed SNR-248 resists. The power law least-squares fits provide the values for  $m$  and  $k_1$ 's for different PEB temperatures.

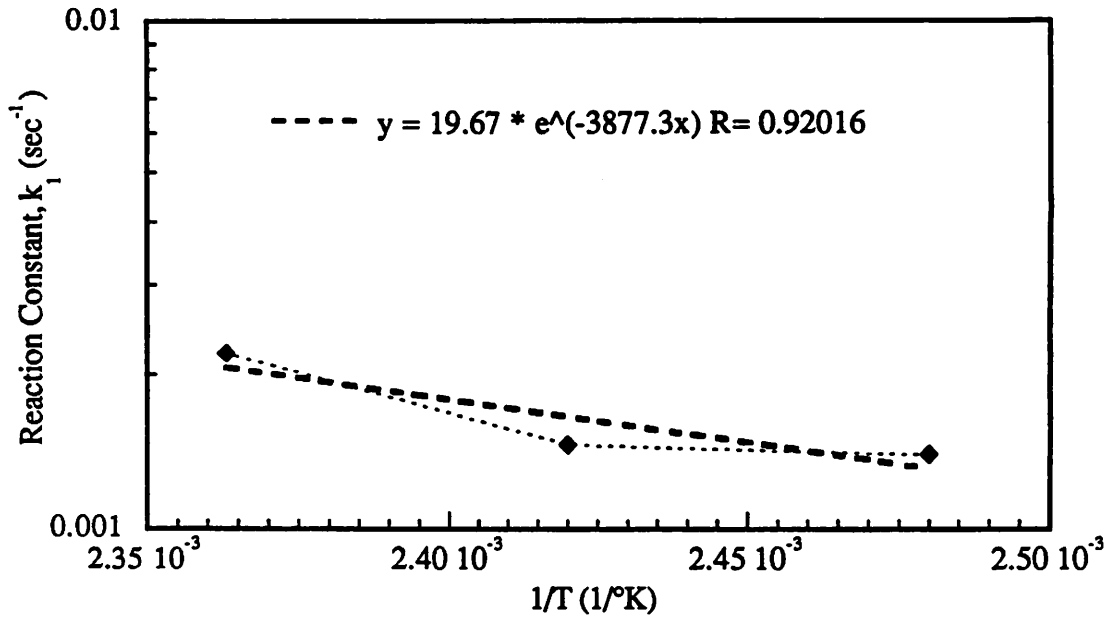


Figure 6.6. Arrhenius plot of  $k_1$  versus  $1/T$ .

that  $\chi_e$  should depend on  $C_{a0}^n$ . Thus,  $\chi_e$  is assumed to be:

$$\chi_e = K'_2 \cdot e^{-E_{a2}/kT} \cdot C_{a0}^n \quad (\text{EQ 6.19})$$

where  $K'_2$  is the pre-exponential factor, and  $E_{a2}$  is the activation energy for  $\chi_e$ . If the assumptions are correct, then the log-log plots of  $\chi_e$  versus exposure dose should be straight lines and  $n$  can be determined from the plots graphically. In addition, the Arrhenius plots of the intercept should give  $K'_2$  and  $E_{a2}$ . The log-log plot of  $\chi_e$  versus exposure dose is shown in Figure 6.7 and the Arrhenius plot is shown in Figure 6.8. From the log-log plot, the average value of  $n$  is 1.13. From the Arrhenius plot,  $K'_2$  is found to be 1.39 and  $E_{a2}$  is 0.117 eV.

Now that  $\chi_e$  is shown to be a function of the PEB temperature and the initial acid concentration, the extent of crosslinking can be fully expressed in terms of the exposure dose and the PEB condition as follows:

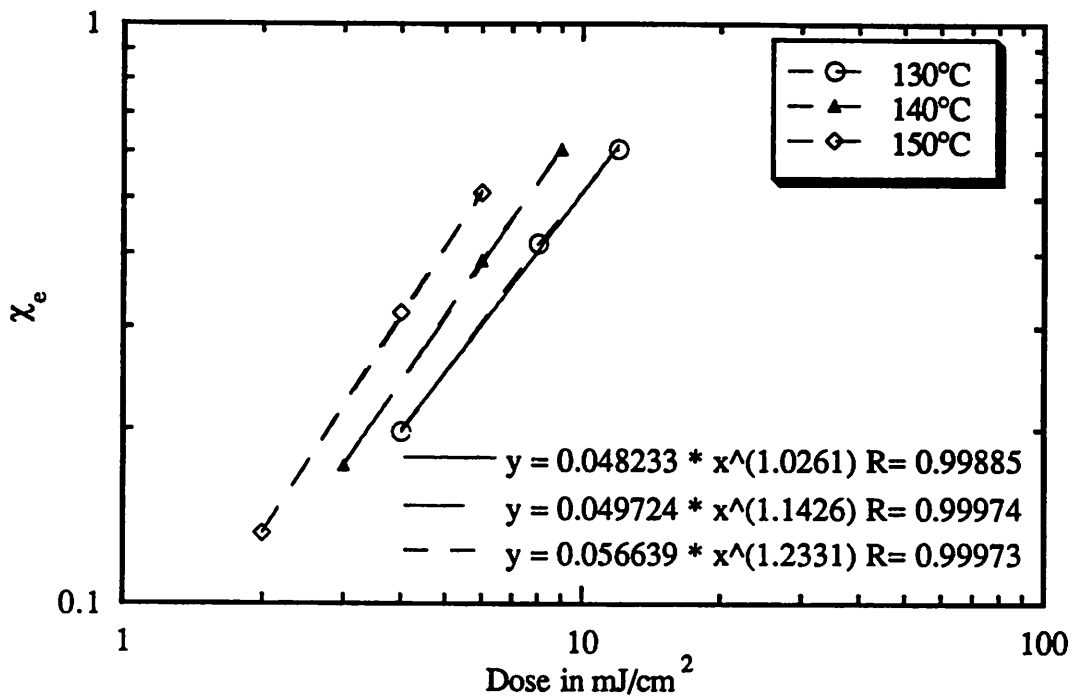


Figure 6.7. Log-log plot of  $\chi_e$  versus exposure dose for deep-UV exposed SNR-248 resist.

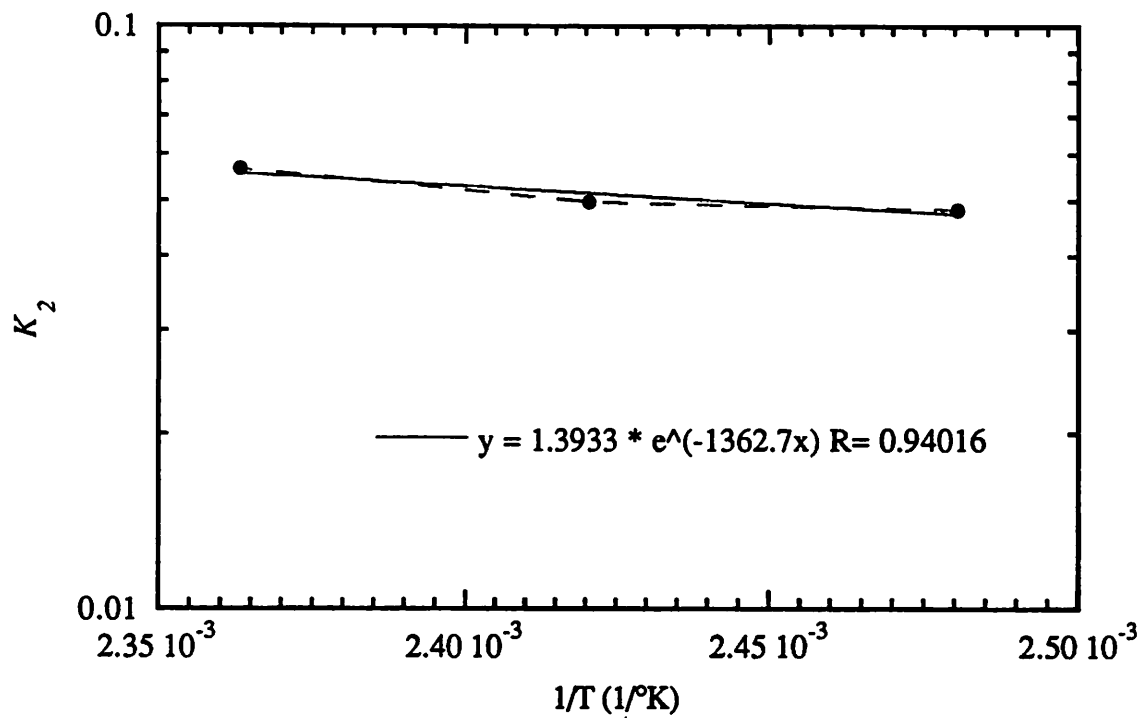


Figure 6.8. Arrhenius plot of  $k_2$  for deep-UV exposed SNR-248 resist.

$$C_{AS} = \frac{\exp\left[-\left(\frac{1}{K'_2 e^{-E_{a2}/kT} C_{ao}^n} - 1\right) k'_1 e^{-E_{a1}/kT} C_{ao}^m t\right] - 1}{\exp\left[-\left(\frac{1}{K'_2 e^{-E_{a2}/kT} C_{ao}^n} - 1\right) k'_1 e^{-E_{a1}/kT} D^m t\right] - \frac{1}{K'_2 e^{-E_{a2}/kT} C_{ao}^n}} \quad (\text{EQ 6.20})$$

Here  $T$  is the PEB temperature in °K,  $t$  is the PEB time in second, and  $C_{ao}$  is the initial acid concentration which can be calculated from the ABC parameters in Refs[8]. The various plots shown previously can be used to estimate the parameters graphically. For a composite model for all temperatures, the best fitted parameters can be determined formally with the linear least squares technique. For example, the  $\ln$  of  $k_1 C_{ao}^m$  can be linearized in terms of  $\ln C_{ao}$  and  $1/T$  to produce the following equation,

$$\ln(k_1 C_{ao}^m) = \ln k'_1 + \left(\frac{-E_{a1}}{k}\right) \cdot \frac{1}{T} + m \cdot \ln C_{ao} \quad (\text{EQ 6.21})$$

Similarly,  $\ln$  of  $\chi_e$  can also be linearized with the above method and its parameters can then be determined with the least squares technique. The best fit parameters for these procedures are summarized in Table 6.2. Notice the pre-exponential factors and the activation energies for the composite model differ substantially from the values obtained with the graphical technique for individual PEB temperature.

**Table 6.2: Parameters in the “Cage Effect” Model of the Crosslinking Reaction**

	Crosslinking Reaction	Equilibrium Conversion
Order in $C_{ao}$	$m = 1.423$	$n = 1.134$
Pre-exponential Factor	$k'_1 = 4.317 \times 10^9 \text{ sec}^{-1}$	$K'_2 = 1.725 \times 10^5$
Activation Energy	$E_{a1} = 0.694 \text{ eV}$	$E_{a2} = 0.370 \text{ eV}$

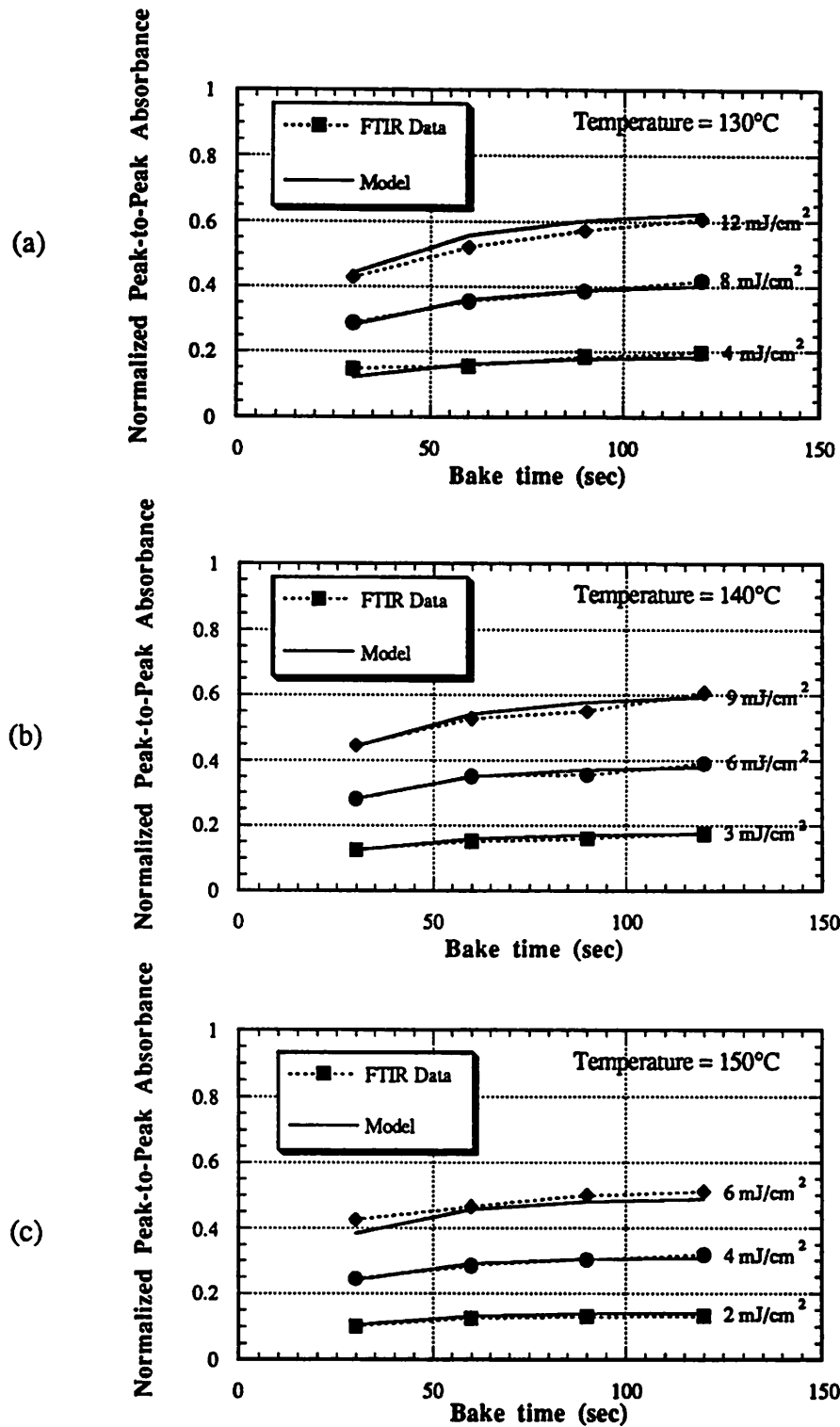
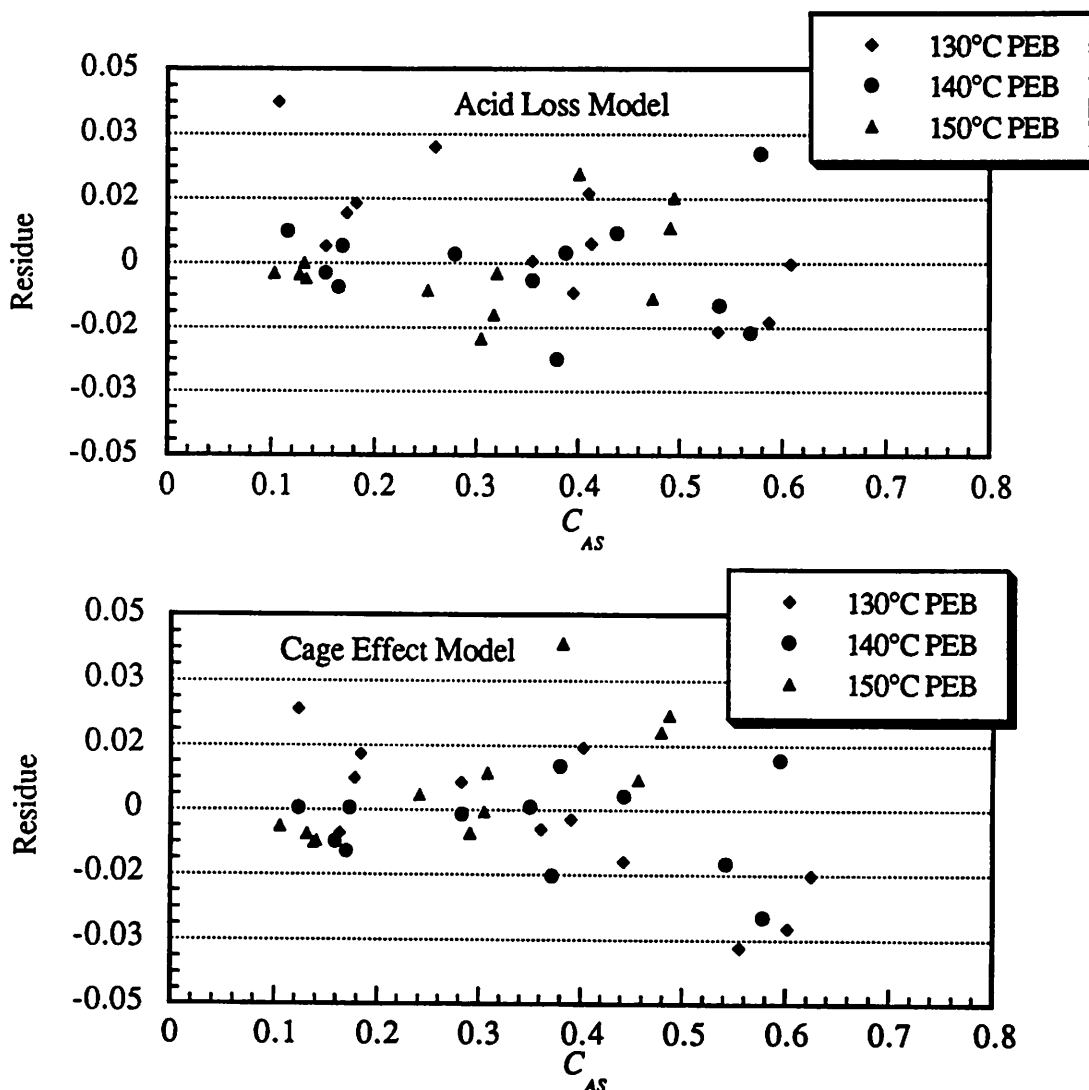


Figure 6.9. Comparison of experimental and theoretical calculations of  $C_{AS}$ , which are plotted as normalized peak-to-peak absorbance for three different PEB temperatures. The theoretical calculations is based on Equation 6.10 using the parameters in Table 6.2. The model fits the experimental data extremely well and is comparable to the Ferguson model in Figure 6.3.

To test the validity of this “cage effect” model, it is compared with the experimental data of Ferguson *et al.* presented earlier in Figure 6.3. The extent of crosslinking reaction predicted by this new model and the experimental data are plotted in Figure 6.9 and they show very good agreement. The goodness of fit of the new model is comparable to the acid-loss model as demonstrated by the plots of residues for the two models in Figure 6.10. The plots from both models are randomly distributed. The range of the residues in the acid-loss model is only slightly smaller than that of the “cage effect” model.



**Figure 6.10.** Comparison of residue plots between the Acid-Loss Model and the Cage Effect Model. The plots from the two models are randomly distributed. The range of the residues in the Acid-Loss Model is only slightly less than that of the Cage Effect Model.

Table 6.3 compares the parameters between the models based on the acid-loss and the “cage effect” mechanisms. The acid-loss model has one less parameter due to the assumption of a first order reaction in the acid-loss reaction rate equation. If the order of acid in the reaction is a not an integer in the acid-loss model, the solution of the reaction rate equation will be much more complicated. The data fit for both models give the order of acid in the crosslinking reaction as 1.42. However, the activation energies for the crosslinking reaction are different slightly. The “cage effect” model found  $E_{a1}$  to be 0.17 eV less than that of the acid-loss model. On the other hand, the activation energy of the acid-loss reaction is 0.06 eV less than the activation energy in the equilibrium conversion. These differences seems to cancel each other out in the overall reaction rate. For example, the extent of crosslinking and the reaction rate as a function of PEB time for a 6 mJ/cm<sup>2</sup> exposure dose calculated with the two models are plotted in Figure 6.12 for three different PEB temperatures. There is very little differences between the reaction rate of crosslinking. However, the extent of crosslinking reaction calculated by the “cage effect” model is slightly higher than that of the acid-loss model. This is probably due to the lower activation energy in  $k_1$  of the “cage effect” model.

**Table 6.3: Comparison of Kinetic Parameters between the Linear “Cage Effect” and the Acid-Loss Models**

	Linear “Cage Effect” Model		Acid-Loss Model
$k'_1$	$4.31 \times 10^9 \text{ sec}^{-1}$	$k'_1$	$6.56 \times 10^{11} \text{ sec}^{-1}$
$E_{a1}$	0.69 eV	$E_{a1}$	0.88 eV
$m$	1.42	$m$	1.42
$K'_2$	$1.73 \times 10^5$	$k'_2$	$4.60 \times 10^3 \text{ sec}^{-1}$
$E_{a2}$	0.37 eV	$E_{a2}$	0.43 eV
$n$	1.13	$n$	1

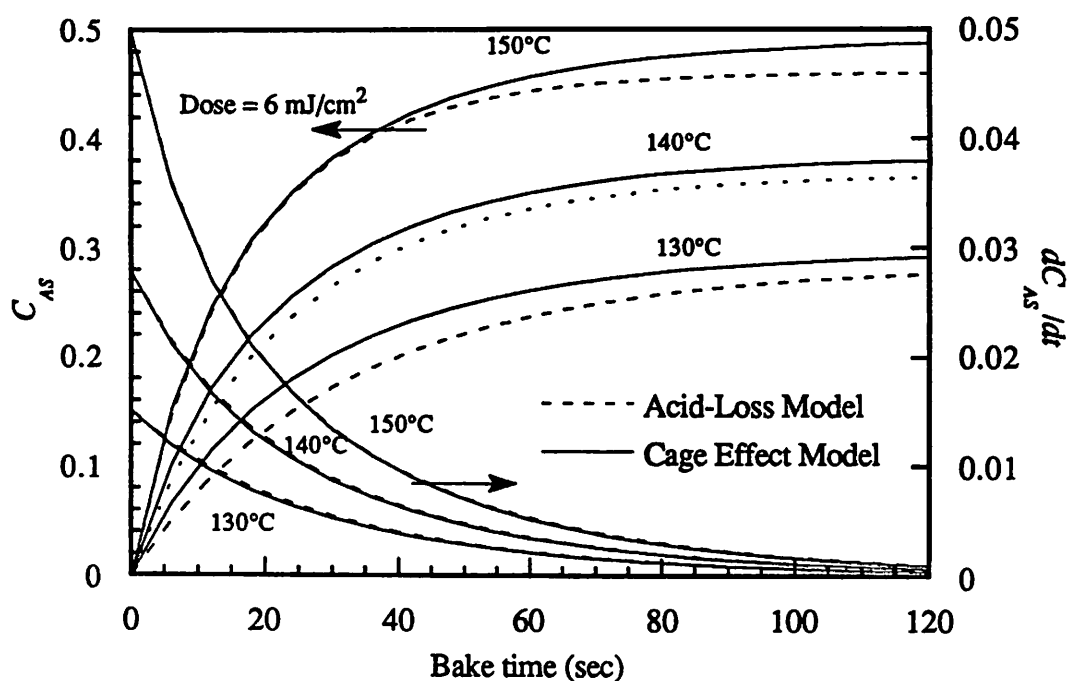


**Figure 6.11.** Comparisons of the extent and the rate of the crosslinking reaction between the acid-loss and the cage effect model for SNR-248 exposed with  $6 \text{ mJ/cm}^2$  under three different post-exposure bakes.

The “cage effect” model has several advantages over the acid-loss model. The “cage effect” mechanism can provide a more physical and more general model for the saturation of crosslinking reaction than the acid-loss mechanism. In the “cage effect” model, the saturation of crosslinking reaction can include the restricted movements of the resin side-chains, or the acid moieties, or both. The “cage effect” factor used in the new model is derived from a physically observable quantity  $\chi_e$ , which is the equilibrium conversion of the melamine crosslinking sites. However, in the acid-loss model, the rate coefficient has to be extracted indirectly with nonlinear regression based on the solution of the combined differential rate equation.

Another advantage of the “cage effect” model is the mathematical simplicity in the fitting of the FTIR data. Like the acid-loss model, it has an analytic formula relating the

extent of crosslinking reaction to the exposure dose and the post-exposure bake parameters. In addition, the convergence of the nonlinear regression in the determination of the term  $k_1 C_{ao}^m$  is rapid and stable. On the other hand, although the acid-loss model can be modified to incorporate  $\chi_e$  in the reaction rate equation by rearranging Equation (6.12) and substituting  $\chi_e$  for  $mk_2$  in Equation (6.11) to give

$$C_{AS} = 1 - (1 - \chi_e) \exp \left[ 1 - \exp \left( \frac{k_1 C_{ao}^m t}{\ln(1 - \chi_e)} \right) \right] \quad (\text{EQ 6.22})$$

the nonlinear regression convergence in the determination of the term  $k_1 C_{ao}^m$  is less certain. In the “cage effect” model, once  $k_1 C_{ao}^m$  and  $\chi_e$  are obtained, the order of acid in the reaction, and the kinetic and equilibrium constants can then be determined with a very simple linear least squares technique.

Once the parameters are determined, the “cage effect” model can be used to calculate the extent of crosslinking reaction for any PEB condition. These values can then be used to explore further the nature of the “cage effect” in the *SAMPLE-ARK* program. For example, if the saturation of the extent of crosslinking is due to restricted acid diffusion, then the “cage effect” factor can be applied to the diffusion constant of the acid in *SAMPLE-ARK*. If the “cage effect” is due to alcohol remaining in the immediate vicinity, this mechanism can also be modeled in *SAMPLE-ARK*. For the purpose of comparing the crosslinking reactions between deep-UV and e-beam exposed SNR-248 resists throughout this thesis, the closed-form solution of the “cage effect” model will be used due to its simplicity in the parameter extraction.

## 6.4 Comparison of Deep-UV and e-Beam Exposed SNR-248

The FTIR difference spectra before and after exposure ( $\Delta$ -absorbance) was used to compare exposure type effects. Details of this procedure and corrections for solvent bake-out effect are discussed in the appendix to this chapter. Direct comparison of the acid generation efficiency between optical and e-beam exposures with FTIR was not possible because no clear IR signals could be found for the chemical structures involved in the radiolysis of the acid generators. Nonetheless, there were dissimilarities in the before/after exposure difference spectra produced by e-beam and deep-UV exposures. Examples of the difference spectra are plotted in Figure 6.12 for optical and e-beam exposures. An absorption peak at  $990\text{ cm}^{-1}$  was observed after e-beam exposure. Since the raw  $\Delta$ -absorbance at  $990\text{ cm}^{-1}$  could represent the extent of reaction by the HMMM crosslinking agent, this observation suggested that the high energy electrons may have activated some of the HMMM compounds during exposure. The size of the peak increases as the exposure increases and for a dose of  $4\text{ }\mu\text{C}/\text{cm}^2$ , it reaches about 26% of the maximum measured value. As a result, these

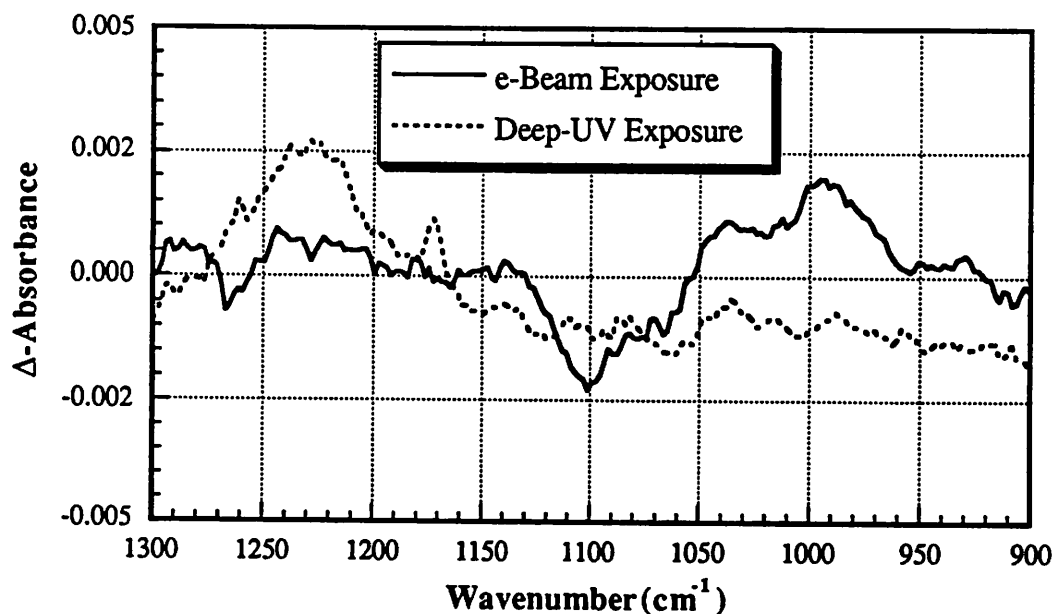


Figure 6.12. FTIR difference spectra of XP-8843 before/after exposure produced by deep-UV and e-beam exposures.

responses in the FTIR spectra are considered in the model to be caused by the initial- reacted melamine crosslinking sites. These data are plotted in Figure 6.13 within the range of typical lithographic doses. Since the FTIR measured values before the PEB saturated beyond a dose of  $4 \mu\text{C}/\text{cm}^2$ , exposure-induced changes were fit with a simple exponential response,

$$C_{ASo} = 0.25 (1 - \exp(-\frac{D}{0.95})) \quad (\text{EQ 6.23})$$

In the case of deep-UV exposure, a similar size of peak cannot be obtained unless hundreds of  $\text{mJ}/\text{cm}^2$  of exposure dose are applied.

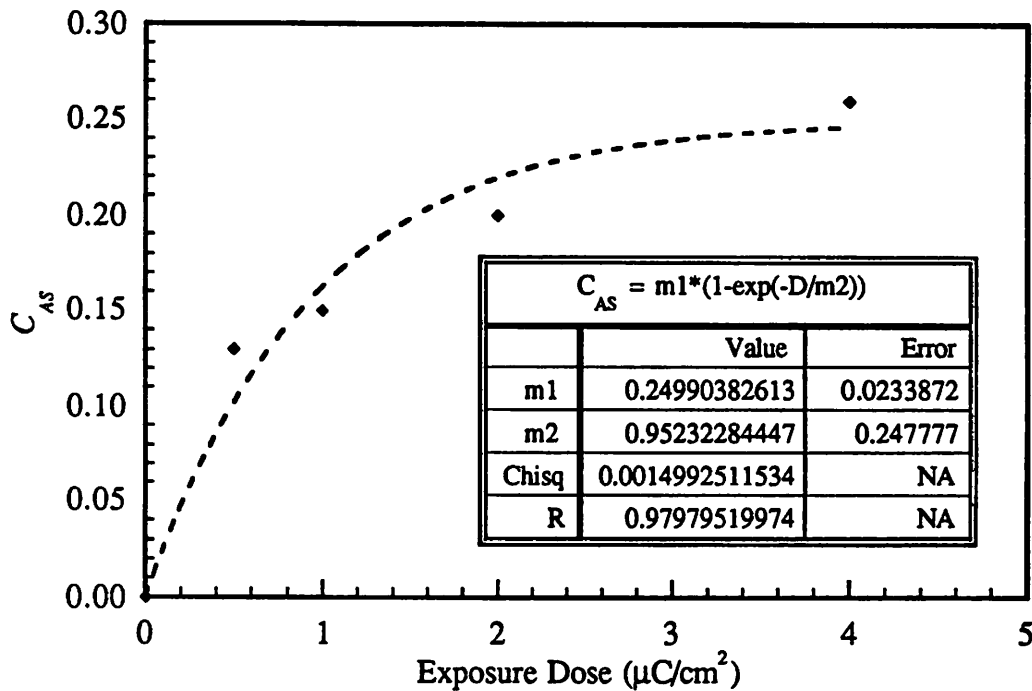


Figure 6.13. The normalized initial activated melamine crosslinking sites versus exposure dose up to  $4 \mu\text{C}/\text{cm}^2$ . The data are fitted with an exponential function.

#### 6.4.1 Post-Exposure Bake Effects

Although there are some differences in the post-exposure FTIR measurements between e-beam and optical exposed resists, the kinetics of their crosslinking reactions during the PEB are quite similar. Figure 6.14 shows the normalized  $\Delta$ -absorbance as a function of time for baking temperatures of 120, 130, and 140°C after e-beam exposures of 0.5, 1.0,

and  $1.5 \mu\text{C}/\text{cm}^2$ . Similar to the deep-UV data, the FTIR data obtained for e-beam exposure also exhibit saturation of the crosslinking reactions. However, the range of the PEB temperatures used were different from that of the deep-UV data. In addition, there appears to be more random fluctuations in the e-beam data. For example, one of the data point ( $t=120$  sec,  $D=1.5 \mu\text{C}/\text{cm}^2$ ) in the  $130^\circ\text{C}$  PEB data set was considered erroneous and had to be eliminated because its value was equal to the maximum value obtained in the experiment.

To compare the kinetics and the equilibrium of the crosslinking reaction under the two type of exposures, the kinetic parameters for the reaction rate have to be determined. However, unlike the deep-UV exposed SNR-248 resists, the e-beam exposed resists have some initial values of  $C_{AS}$  before the PEB; therefore, Equation (6.16) has to be solved with an initial condition such that at  $t = 0$ ,  $C_{AS} = C_{ASo}$ . The solution of Equation (6.16) then becomes:

$$C_{AS} = \frac{\exp\left[-\left(\frac{1-\chi_e}{\chi_e}\right) \cdot k_1 \cdot C_{ao}^m \cdot t\right] - \frac{1 - C_{ASo}}{1 - C_{ASo}/\chi_e}}{\exp\left[-\left(\frac{1-\chi_e}{\chi_e}\right) \cdot k_1 \cdot C_{ao}^m \cdot t\right] - \frac{1 - C_{ASo}}{\chi_e - C_{ASo}}} \quad (\text{EQ 6.24})$$

This equation is very similar to Equation (6.17) and it also has the same fitting parameter  $k_1 C_{ao}^m$  to determine the extent of reaction versus PEB time data. The extracted  $k_1 C_{ao}^m$  are plotted as a function of exposure dose in Figure 6.15. Both the  $130$  and  $140^\circ\text{C}$  data show good linearity in the log-log plot. However, the  $120^\circ\text{C}$  data shows some curvature and the slope ( $m$ ) of the power law fit is much larger than the ones from the other two temperatures. Unlike the data from deep-UV exposed resists in Figure 6.6, the  $m$  values do not show a clear trend with PEB temperature. This large range of observed  $m$  values is probably due to random errors in the FTIR measurements. Nonetheless, the average value of  $m$  is 1.37

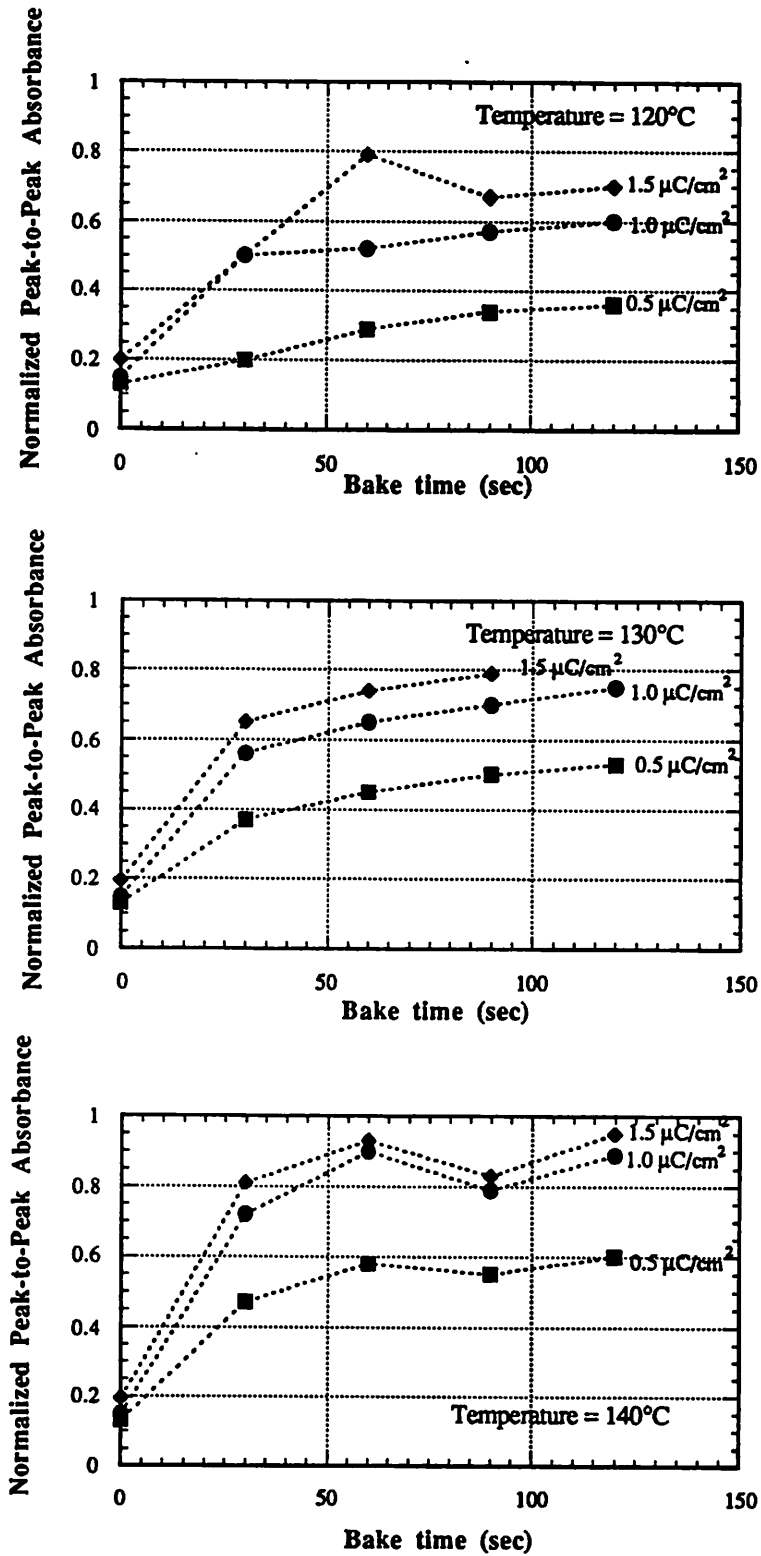


Figure 6.14. Extent of the crosslinking reaction plotted as the  $\Delta$ -absorbance versus PEB time for e-beam exposed SNR-248 resists with three different PEB temperatures.

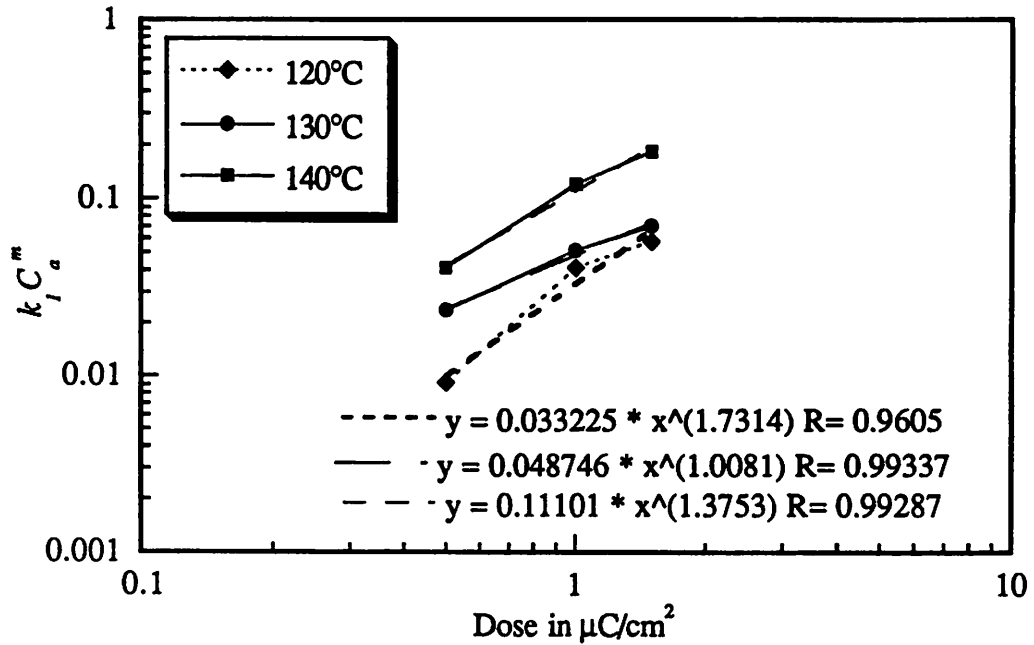


Figure 6.15. Log-log plots of  $k_1 C_{ao}^m$  versus exposure dose for the e-beam exposed SNR-248 resists. The power law least-squares fits provide the values for  $m$  and  $k_1$ 's for different PEB temperatures.

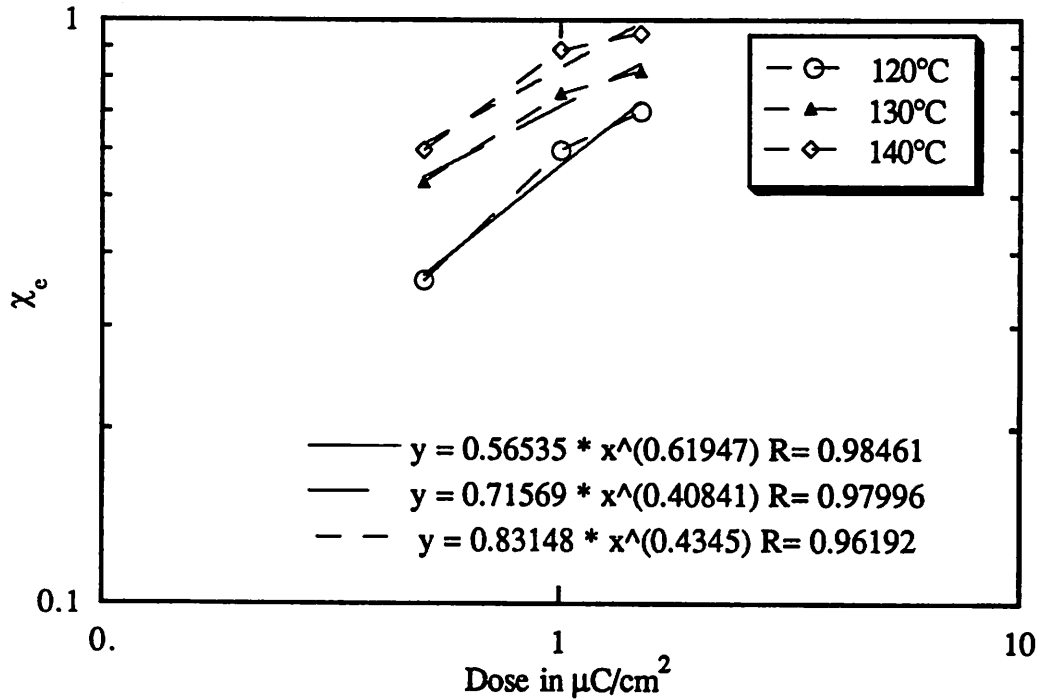


Figure 6.16. Log-log plots of  $\chi_e$  versus exposure dose for e-beam exposed SNR-248 resists under three different PEB temperatures.

with a standard deviation of 0.36. As a result, it can be concluded that the order of acid catalyst in the melamine crosslinking reaction does not differ significantly between deep-UV and e-beam exposures.

The temperature and exposure dose effects on the equilibrium conversion of the melamine crosslinking sites under e-beam exposure are also assumed to follow Equation (6.19). This hypothesis is tested by checking the linearity of  $\chi_e$  versus exposure dose in a log-log plot. These plots are shown in Figure 6.16. Some curvature in the  $\chi_e$  versus exposure dose data is observed. The data from all three temperatures seem to change slopes as the exposure dose changes from 1 to 2  $\mu\text{C}/\text{cm}^2$ . One possible explanation for this curvature in  $\chi_e$  is that the acid generation may not be proportional to exposure dose in the range of doses used in the experiment. Unfortunately, 0.5  $\mu\text{C}/\text{cm}^2$  is the lowest dose that could be generated on the AEBLE-150; therefore, data below 0.5  $\mu\text{C}/\text{cm}^2$  could not be obtained. To simplify the modeling of  $\chi_e$ , a power law is used to fit the data for each temperature and the results are included in Figure 6.16.

Contrary to the similarity of the  $m$ 's in the crosslinking reactions of optical and e-beam exposed resists, the orders of the acid catalyst in the equilibrium conversions are significantly different. In deep-UV exposed SNR-248, the average of  $n$  is 1.13, whereas in e-beam exposed SNR-248, the average of  $n$  is 0.48. The smaller  $n$  in the e-beam exposed resist implies that the increase in  $\chi_e$  with respect to the initial acid concentration is lower than that for deep-UV exposed resists. In other words,  $n$  can be considered as the factor that determines the spacing between the saturation levels in the extent of reaction versus PEB time data shown in Figures 6.3 and 6.14. For example, in Figure 6.3, when the doses are doubled,  $\chi_e$ 's are roughly doubled. On the other hand, in Figure 6.14,  $\chi_e$ 's only increases by a factor of approximately  $\sqrt{2}$  when the exposure dose is doubled. This discrepancy

could be due to the initial crosslinking induced by the e-beam exposure which may have reduced the effectiveness of the acid catalyst.

The temperature behaviors of  $k_1$  and  $K_2$  are assumed to follow Arrhenius type behavior and the Arrhenius plots for the two parameters are shown in Figure 6.17. Both curves show good linearity. The activation energies for  $k_1$  is 0.866 eV and for  $K_2$  is 0.271 eV as determined from the slopes of the semi-log plots of the kinetic and the equilibrium coefficients versus  $1/T$  curves. This activation energy is similar to the ones reported for SNR-284 resists with X-ray exposure by Seligson *et al.* [1] and Deep-UV exposure by Ferguson *et al.* using the acid-loss model [8]. However, it is slightly higher than one obtained with the new “cage effect” model. Thus, according to the “cage effect” model, the crosslinking reaction in deep-UV exposed SNR-248 resists has a lower energy barrier. The higher energy barrier in the crosslinking reaction of e-beam exposed resists is probably due to the

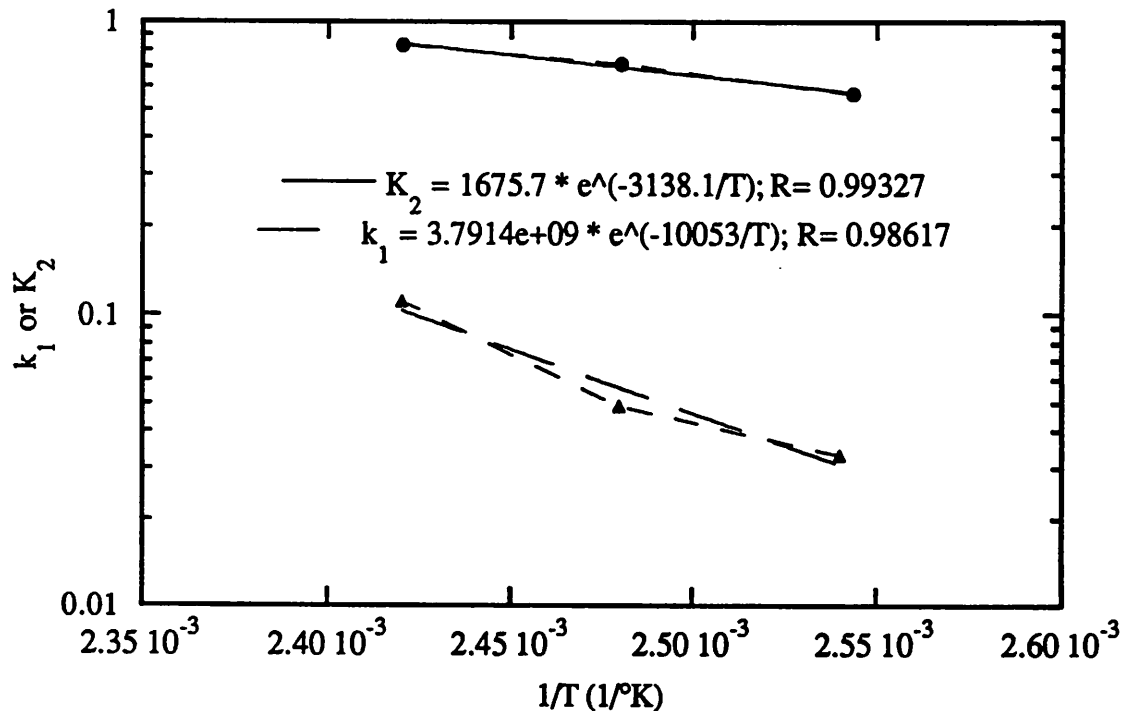


Figure 6.17. Arrhenius plots of  $k_1$  and  $K_2$  for e-beam exposed SNR-248 resist.

“cage effect” from the partial formation of the crosslinking network before the post-exposure bake. This result is consistent with the observation in  $n$ , in which the initial crosslinking in e-beam exposed SNR-248 resist reduces the effectiveness of the acid catalyst.

In the case of the equilibrium conversion,  $E_{a2}$  for e-beam exposed resists is smaller than that for deep-UV exposed resist. Again, this difference can be attributed to the “cage effect” from the initial crosslinking reaction induced by the e-beam exposures. Since the equilibrium constant usually consists of a ratio of the forward to the backward reaction, the lower  $E_{a2}$  implies that the “cage effect” is affecting the backward reaction more strongly than the forward reaction in the rate determining step.

**Table 6.4: Parameters in the “Cage Effect” Model for e-Beam Exposed SNR-248**

	Crosslinking Reaction	Equilibrium Conversion
Order in $C_{ao}$	$m = 1.37$	$n = 0.488$
Pre-exponential Factor	$k'_1 = 3.77 \times 10^9 \text{ sec}^{-1}$	$K'_2 = 2.39 \times 10^3$
Activation Energy	$E_{a1} = 0.866 \text{ eV}$	$E_{a2} = 0.283 \text{ eV}$

For a composite model for all PEB temperatures, a linear least squares technique is used to extract the kinetic and equilibrium parameters for e-beam exposed SNR-248 resists. The best fit parameters are summarized in Table 6.4. These parameters are then substituted into Equations (6.19), (6.23), and (6.24) to calculate the extent of crosslinking reaction. The comparison of the model to the experiment is shown in Figure 6.18. The fit of the data is not as good as in the case of the deep-UV exposed SNR-248 resists in Figure 6.9 due to the noises in the e-beam data. Nonetheless, the model is more than adequate to predict the extent of crosslinking reaction from the exposure and PEB conditions. If the dissolution rate of the resist is a function of the extent of crosslinking reaction, then this “cage effect” model can be used to predict the dissolution of the resist as well. This hypothesis is verified in the next section.

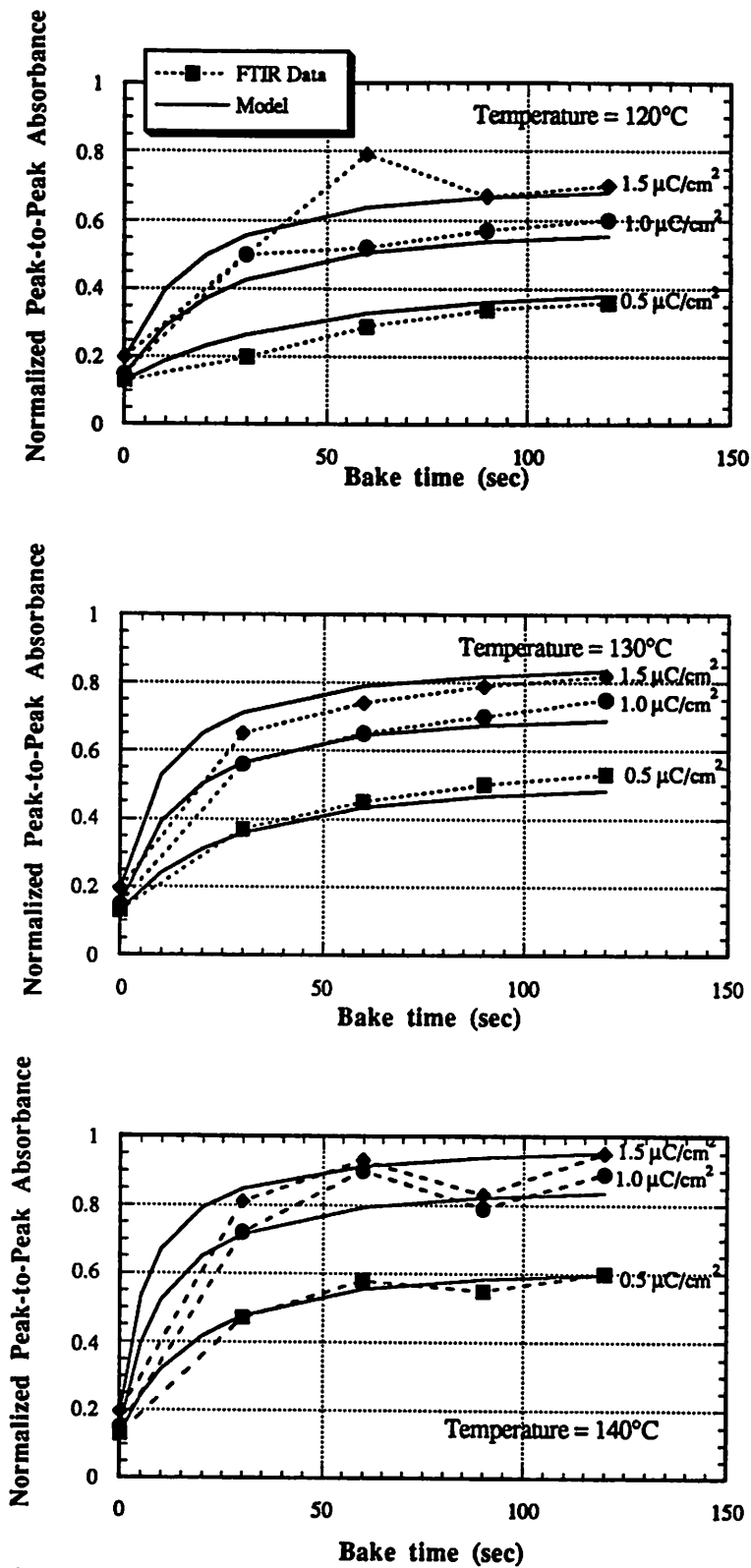


Figure 6.18. Comparison of the cage effect model with the least square fitted parameters and the experimental FTIR measured extent of crosslinking reaction.

## 6.5 Dissolution Rate as a Function of Extent of Crosslinking Reaction

The feasibility of developing a mechanism-based dissolution rate model which includes dose-bake tradeoffs is assessed by plotting the dissolution rate versus the extent of crosslinking reaction. Figure 6.19 shows the dissolution rate versus absorbed energy data for SNR-248 resist under two different PEB conditions. One PEB is at 120°C for 1 minute and the other is at 130°C for 30 seconds. Two distinct sets of dissolution rate versus absorbed energy density data can be observed. Although the 130°C bake is shorter, the resist shows higher sensitivity and contrast than the one with the longer but lower temperature PEB. These results show that temperature is more critical than time in the PEB as long as the PEB is longer than 30 seconds, which is approximately the time it takes for the crosslinking reaction to reach about 80% of the saturation level.

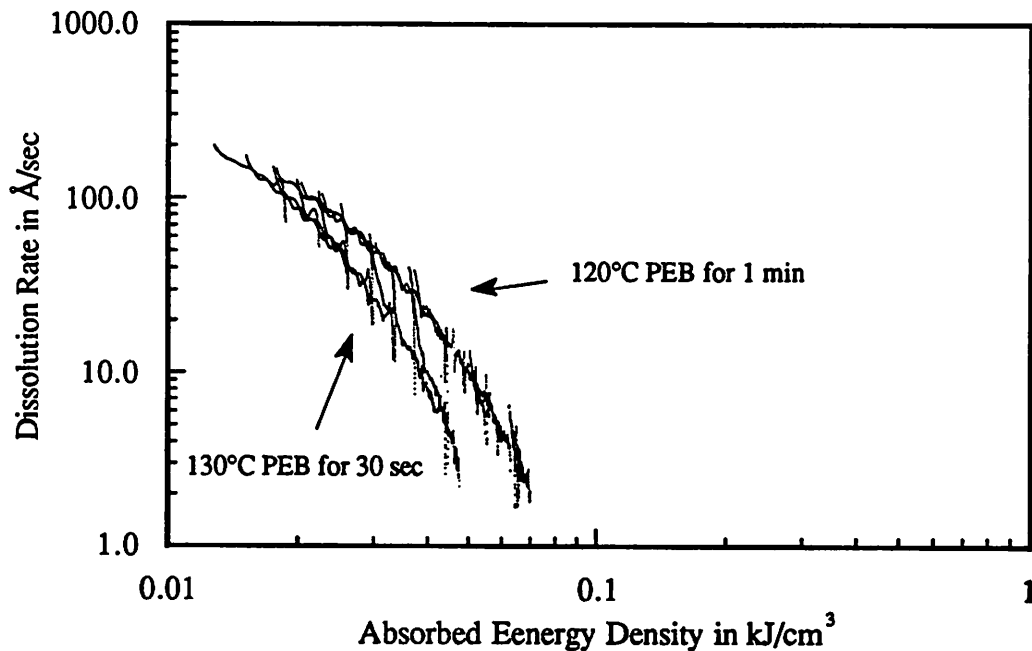
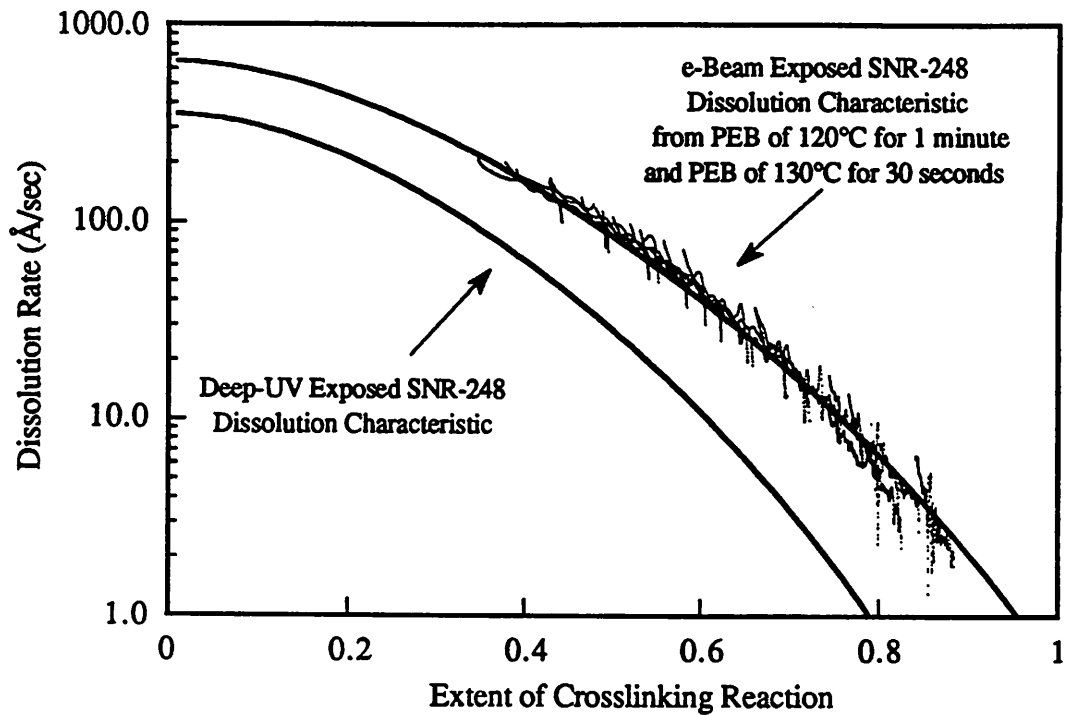


Figure 6.19. Dissolution rate versus absorbed energy density of e-beam exposed SNR-248. As the PEB conditions varies, the dissolution rate of absorbed energy characteristics also changes.



**Figure 6.20.** The dissolution rates obtained from e-beam exposed SNR-248 with two different PEB conditions are plotted against the extent of the crosslinking reaction. The plot is single-valued and tends to follow comparable data for deep-UV exposed SNR-248.

These two sets of data are then transformed to dissolution rate versus extent of crosslinking reaction using Equations (6.19), (6.23), and (6.24) and they are plotted in Figure 6.20. The fact that the dissolution rate is a single valued function with respect to the extent of crosslinking reaction for two separate PEB temperatures supports the validity of the “cage effect” model for different PEB conditions.

Ferguson *et al.* [8] showed that the dissolution rate could be related to the extent of crosslinking reaction by

$$Rate = R_o (1 - CE/C_o)^\alpha \quad (EQ 6.25)$$

where  $R_o$ ,  $C_o$ , and  $\alpha$  are fitting parameters and  $CE$  is the number of crosslinking events given by

$$CE = 15C_{AS}^2 - 20C_{AS}^3 + 15C_{AS}^4 - 6C_{AS}^5 + C_{AS}^6 \quad (\text{EQ 6.26})$$

The resulting dissolution models for both the deep-UV and e-beam exposed SNR-248 resists are plotted as solid lines in Figure 6.20. The fitted parameters for the two models are summarized Tables 6.5. The dissolution characteristics are very similar for the two exposure types. However, the dissolution of e-beam exposed SNR-248 resists is faster than that of the deep-UV exposed resists. This discrepancy is mostly likely caused by variations in the developer concentration used in the development rate measurements because the unexposed dissolution rate for e-beam exposed resists was 200 Å/sec faster than that of the deep-UV exposed resists.

**Table 6.5: Dissolution Rate Model Parameters**

Parameter	e-Beam	Deep-UV
$R_o$	550 Å/sec	350 Å/sec
$C_o$	7.5	6.3
$\alpha$	6.5	6.5

## 6.6 Summary

A complete model based on a linear approximation of the “cage effect” which occurs during the processing of Shipley SNR-248 resist has been developed. This model provides a closed-form solution relating the extent of crosslinking to the exposure and PEB conditions. Physical parameters can easily be extracted from the FTIR measurements of extent of crosslinking reaction due to the mathematical simplicity of this model. The behaviors of both optical and e-beam exposed resists have been examined using this model and are found to be comparable with interesting differences.

According to the “cage effect” model, the order of acid catalyst in the crosslinking reaction of e-beam exposed SNR-248 resists is similar to that of the deep-UV exposed resists. However, in e-beam exposed resists, some crosslinking is induced by the e-beam during exposure. As a result, this initial crosslinking might contribute to the slightly higher activation energy in the crosslinking reaction of e-beam exposed SNR-248 resists. The equilibrium conversions of the melamine crosslinking sites in e-beam exposed resists are also different from that of the deep-UV exposed resists. The power of acid concentration  $n$  in the expression for the equilibrium conversion for e-beam exposed resists is approximately 0.49 whereas in deep-UV exposed resists,  $n$  is 1.1. There is also a difference in the activation energies of the equilibrium constants which suggested the “cage effect” have a stronger influence on the backward reaction.

Dissolution characteristics between optical and e-beam exposed SNR-248 resists are very similar and they are both functions of extent of crosslinking reaction. However, in the development rate data, the e-beam exposed resists have faster dissolution rates than deep-UV exposed resists. This discrepancy is probably due to a difference in the concentration of developers used in the DRM experiments. Both sets of dissolution rate data can be fit with the dissolution rate model for deep-UV exposed resists. With the “cage effect” bake model and the dissolution rate model it is now possible to simulate the individual processing steps (exposure, PEB, and development) of acid-hardening SNR-248 resists for e-beam lithography. This can be done rapidly with the closed-form solution of the “cage effect” model or it can be done with more detailed attentions to the nature of the acid or alcohol diffusion using the *SAMPLE-ARK* program.

## **6.7 Appendix**

### **6.7.1 Fourier Transformed Infrared Spectrometry**

Using the naming convention by Ferguson *et al.*, the ethers on the HMMM are called unactivated crosslinking sites before they react and activated crosslinking sites after they are attached to the resin chain. Since the ether bond on the activated crosslinking site is adjacent to a benzene ring, the vibrational frequency of the C-O bond is different from that in the unactivated crosslinking site. As a result, the extent of the crosslinking reaction can be determined directly with FTIR by monitoring the changes in the IR bands corresponding to the two types of C-O bond during the post-exposure bake.

In FTIR spectrometry, the relative changes of the chemical structures in the resist after exposure and during the PEB are sought. In the melamine crosslinking reaction, the extent of the crosslinking reaction is tracked by monitoring the change in peak-to-peak absorbance of the IR spectrum at 990 to 1070  $\text{cm}^{-1}$ , corresponding to the vibrational frequencies of the ether bonds on the HMMM before and after the crosslinking reaction respectively.

### **6.7.2 Experimental**

The FTIR system used in this study is a transmission mode system scanning over a range of wavelengths from 2.5  $\mu\text{m}$  to 25  $\mu\text{m}$ . [12] The entire experimental system is enclosed in a plexiglass box to limit the atmospheric variation in the measurement environment. The resist sample are spin-coated on a Si wafer and placed on a computer controlled stage 45° normal to the IR beam. The Si wafers are polished on both sides to reduce the scattering associated with surface roughness.

The SNR-248 resist used in this study was 1  $\mu\text{m}$  thick and a prebake of 100°C for 90 sec was used in both the FTIR experiment and development rate measurements. Transmission mode FTIR spectra were taken from large area (1.6 x 1.6  $\text{cm}^2$ ) exposure patterns of the resist. In the e-beam exposure study, the resist was exposed on an Etec AEBLE-150 at 20 kV with beam current densities ranging from 5 to 40  $\text{A}/\text{cm}^2$ . In the deep-UV exposure study, the resist was exposed with a KrF ( $\lambda=248\text{nm}$ ) excimer laser. After the exposure, FTIR measurements were made on exposed resists which received different baking conditions with baking temperatures from 120°C to 140°C and baking times up to 30 minutes. Relative changes in the resist after each processing step were determined quantitatively from difference spectrum obtained by subtracting the FTIR spectra before and after the processing step.

The loss of casting solvent during the post-exposure bake must be accounted for when using difference spectra to obtain the relative concentration values. Solvent bake-out may produce significant peaks in an FTIR difference spectrum. The loss of solvent during the bake for XP-8843 can be easily observed by taking a difference spectrum for an unexposed region of the resist where no crosslinking occurs. The locations of these peaks are at 1240  $\text{cm}^{-1}$  and 1090  $\text{cm}^{-1}$ , which are very near to the characteristic peaks of the ether bonds on the HMMM, and thus could confound the estimation of the extent of the crosslinking reaction. To remove this solvent bake-out effect, the solvent loss spectra was subtracted from the measurements taken in the exposed regions of the resist where both crosslinking and solvent bake-out occur.

### 6.7.3 Extracting Data from FTIR Spectra

Typical FTIR difference spectra after the PEB are shown in Figure 6.21. The valley and the peak corresponding to the disappearance of the reactants and the generation of the products in the crosslinking reaction are easily identified. In the most rigorous approach to determine relative concentration of species in the resist, the area of the spectrum beneath the peak should be integrated. However, due to the small signal-to-noise ratio and the shift in the baseline of the difference spectra, a simpler approach is taken where the valley-to-peak magnitude between  $1070\text{ cm}^{-1}$  and  $990\text{ cm}^{-1}$  in the difference spectrum is used to represent the extent of the crosslinking reaction. A maximum value of 0.023 is observed on resists after a 30 minute bake corresponding to the consumption of all available HMMM sites. Subsequently, this number is used to normalized the extent of reaction for the rest of the measurements.

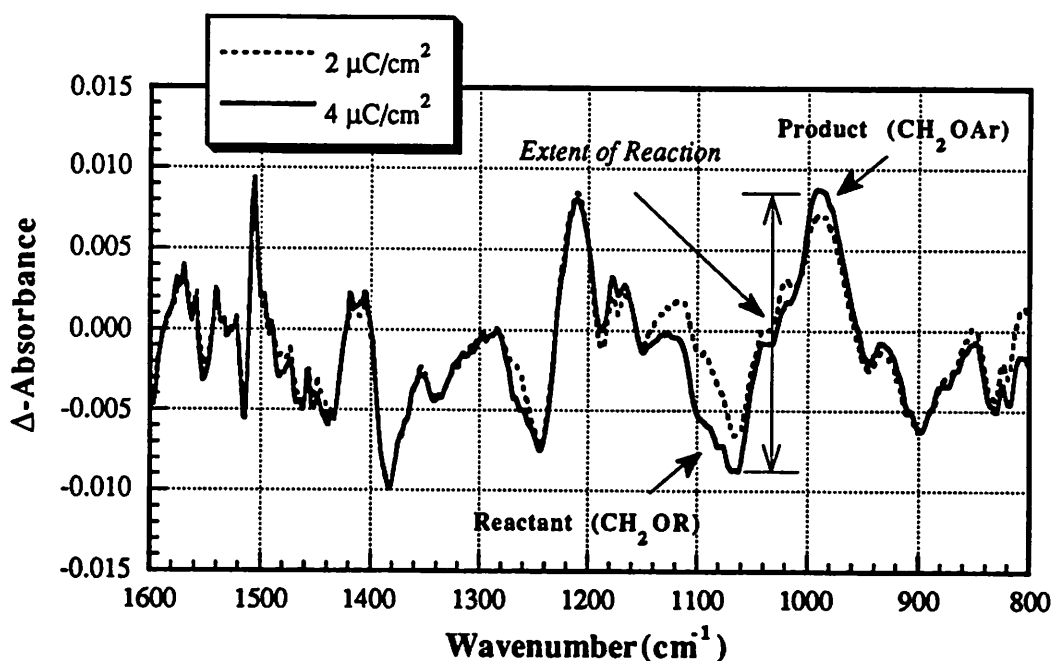


Figure 6.21. FTIR difference spectra of e-beam exposed XP-8843 after a PEB at  $130^{\circ}\text{C}$  for 30 seconds for exposure of  $2.0$  and  $4.0\ \mu\text{C}/\text{cm}^2$ .

## References

- [1] D. Seligson, S. Das, H. Gaw, and P. Pianetta, "Process Control with Chemically Amplification Resists Using Deep Ultraviolet and X-ray Radiation," *J. Vac. Sci. Technol.*, B6(6), pp. 2303-2307, Nov/Dec 1988.
- [2] C. G. Wilson and H. Ito, J. M. J. Fréchet, T. G. Tessier, and F. M. Houlihan, "Approaches to the Design of Radiation-Sensitive Polymeric Imaging Systems with Improved Sensitivity and Resolution," *J. Electrochem. Soc.*, vol. 133, vol. 1, pp. 181-187, Jan 1986.
- [3] R. Dammel, K. F. Dössel, J. Lingnau, J. Theis, H. L. Huber, and H. Oertel, "Photocatalytic Novolak-Based Positive Resist for X-ray Lithography — Kinetics and Simulation —," *Microelectronic Engineering*, vol. 6, pp. 503-509, 1987.
- [4] M. deGrandpre, K. Graziano, S. D. Thompson, H. Liu, and L. Blum, "High Resolution, Novolak based Negative Tone Electron Beam Resist," *Proceedings of SPIE, Electron-Beam, X-ray, and Ion-Beam Technology: Submicrometer Lithographies VII*, vol. 923, pp. 158-171, 1988.
- [5] A L. Blum, M.E. Perkins and H.-Y. Liu, "A Study of the Effect of Key Processing Variables on the Lithographic Performance of Microposit SAL601-ER7 Resist," *J. Vac. Sci. Technol.*, B6, pp. 2280, 1988.
- [6] D. Ziger, C. Mack, and R. Distasio, "The Generalized Characteristic Model for Lithography: Application to Negatively Chemically Amplified Resists," *Proceedings of SPIE, Advances in Resist Technology and Processing VIII*, vol. 1466, 1991.

- [7] H. Fukuda and S. Okazaki, "Kinetic Model and Simulation for Chemical Amplification Resists," *J. Electrochem. Soc.*, vol. 137, no. 2, pp.675-679, February 1990.
- [8] R. A. Ferguson, J. M. Hutchinson, C. A. Spence, and A. R. Neureuther, "Modeling and Simulation of a Deep-Ultraviolet Acid Hardening Resist," *J. Vac. Sci. and Technol. B*, vol. 8, no.6, pp. 1423-1427, Nov/Dec 1990.
- [9] W. Blank, "Reaction Mechanism of Melamine Resins," *Journal of Coatings Technology*, vol. 51, no. 656, pp. 61-70, September 1979.
- [10] N. N. Tam, R. A. Ferguson, A. Titus, J. M. Hutchinson, C. A. Spence, and A. R. Neureuther, "Comparison of Exposure, Bake, and Dissolution Characteristics of Electron-Beam and Optically Exposed Chemically Amplified Resists," *J. Vac. Sci. and Technol. B*, vol. 8, no.6, pp. 1470-1475, Nov/Dec 1990.
- [11] E. W. Meijer, "A Model Study for Coatings Containing Hexamethoxymethylmelamine," *Journal of Polymer Science: Part A: Polymer Chemistry*, vol. 24, pp. 2199-2208, 1986.
- [12] D. Drako, W. Partlo, W. Oldham, and A. Neureuther, "A Characterization System for Deep Ultra-Violet (UV) Resists," *SPIE Advances in Resist Technology and Processing VI*, Vol. 1086, 1989.

# **Chapter 7**

## **Effects of Interrupted Development on Resist Profiles**

In Chapters 2 and 3, interrupted development was shown to improve both the profile slope and linewidth control of features exposed in a positive DQN resist by retarding the dissolution rate of the lightly exposed regions. This chapter describes the experiments to investigate the roles of the rinsing, the drying, and the development steps in retarding the dissolution rate of the resist. Different interrupted development techniques such as interruption without a drying step, development with stagnant or flowing developer, and development with wetted resist are investigated. Scanning electron micrographs (SEM) of resist cross-section profiles delineated with these different techniques are compared. Since the changes in the bias of the resist profile with interrupted development is a manifestation of the rate retardation effect, the resist profile shape alone can be used to deduce the effectiveness of the technique.

### **7.1 Introduction**

The interruptions of the development process can be carried out several ways and varying the rinsing and drying techniques gives insight to the mechanism as well as helps to determine improved processing conditions. The interrupted development procedure described in Chapter 2 involves three steps: 1) interruption of the development with a rinse, 2) drying of the wafer with an air gun, and 3) submersion of the wafer in the developer for development (see Figure 2.6). In order to determine whether the drying step contributed to the improvement of the resist profiles, a new interrupted procedure was developed in which the drying step was skipped. However, in the course of repeating the experiment without the drying step, two other variables were introduced. One of the changes was the use of

spray development rather than immersion development in the a tank of stagnant developer. The other change was the existence of a pre-wetted resist surface. As a result, in addition to the standard interrupted development procedure, four different interrupted development schemes were performed to study the spray and the pre-wetting factors. In terms of bias, sidewall angle, and resist top-loss, the resist profiles generated with these processes were all superior to the ones obtained with straight development. An important implication of these results is that the rinsing of the resist is the most important step in interrupted development.

The comparison among different processing schemes were based on SEM micrographs of resist line-edge profiles. In particular, the effects of these interrupted development techniques on the half and subhalf micron features are presented. Before the details of the resist profiles are presented, the experimental conditions are described. The effects of the different development schemes on the resist profiles are then summarized.

## 7.2 Experimental

### 7.2.1 Exposure

The electron-beam exposure used in this study was done on the IBM EL-3 shape-beam machine at 50 keV on 0.5  $\mu\text{m}$  thick resists. The exposure patterns included isolated lines, isolated spaces, and line-and-space patterns with linewidths ranging from 0.15  $\mu\text{m}$  to 5.0  $\mu\text{m}$  with a pattern bias<sup>†</sup> of 0.1  $\mu\text{m}$ . These patterns were corrected for proximity effects using beam size and dose modulations. The resists were spin-coated on 3 inch wafers and were baked at 85°C for 15 minutes before exposure. Each wafer was divided into 4 quadrants and identical sets of patterns were exposed on each quadrant. Prior to development, the wafers were broken into 4 pieces and each piece was subjected to a different develop-

---

†. The pattern bias is directed so that the beamwidth would be narrower than the desired final image width. Thus, the 0.25  $\mu\text{m}$  image would be written with a 0.15  $\mu\text{m}$  beamwidth.

ment treatment. In all the experiments, one of the quadrants was used as the control experiment where the original interrupted development (OID) technique was applied.

## 7.2.2 Interrupted Development without the Drying Step

### 7.2.2.1 Interrupted Spray Development

Two ways to skip the drying step in the interrupted development were implemented. The first method was an interrupted spray development (ISD), in which the developer was continuously flowing across the surface of the wafer. When an interrupt was applied, the flow of developer was stopped abruptly and a rinse was applied with a spray gun. Figure 7.1 depicts the experimental set-up for this method. Since the time in switching between the flow of developer and the water rinse was kept very short, a film of either water or developer was always on the resist surface to ensure that the resist surface was never exposed to air.

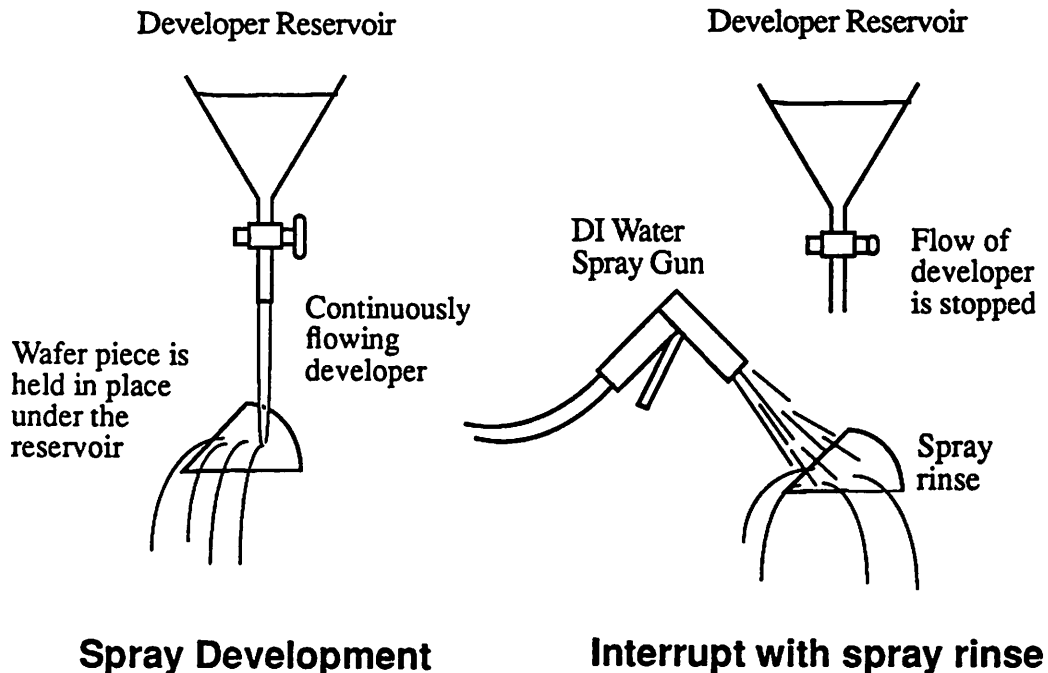


**Figure 7.1.** Experimental set-up of the interrupted spray development. At the end of the development interval, the flow of the developer is stopped and a spray rinse is applied immediately. No drying of the wafer is involved in this process.

Figure 7.2 shows the resist line-edge profiles of 0.25  $\mu\text{m}$  and 0.5  $\mu\text{m}$  isolated lines delineated in 0.5  $\mu\text{m}$  thick resists using straight, spray interrupted, and the original interrupted development. The resist profiles obtained with ISD showed improvement over straight development but to a lesser degree than OID. The development time for each process was chosen so that they were all stopped at the same endpoint<sup>‡</sup>. In straight develop-

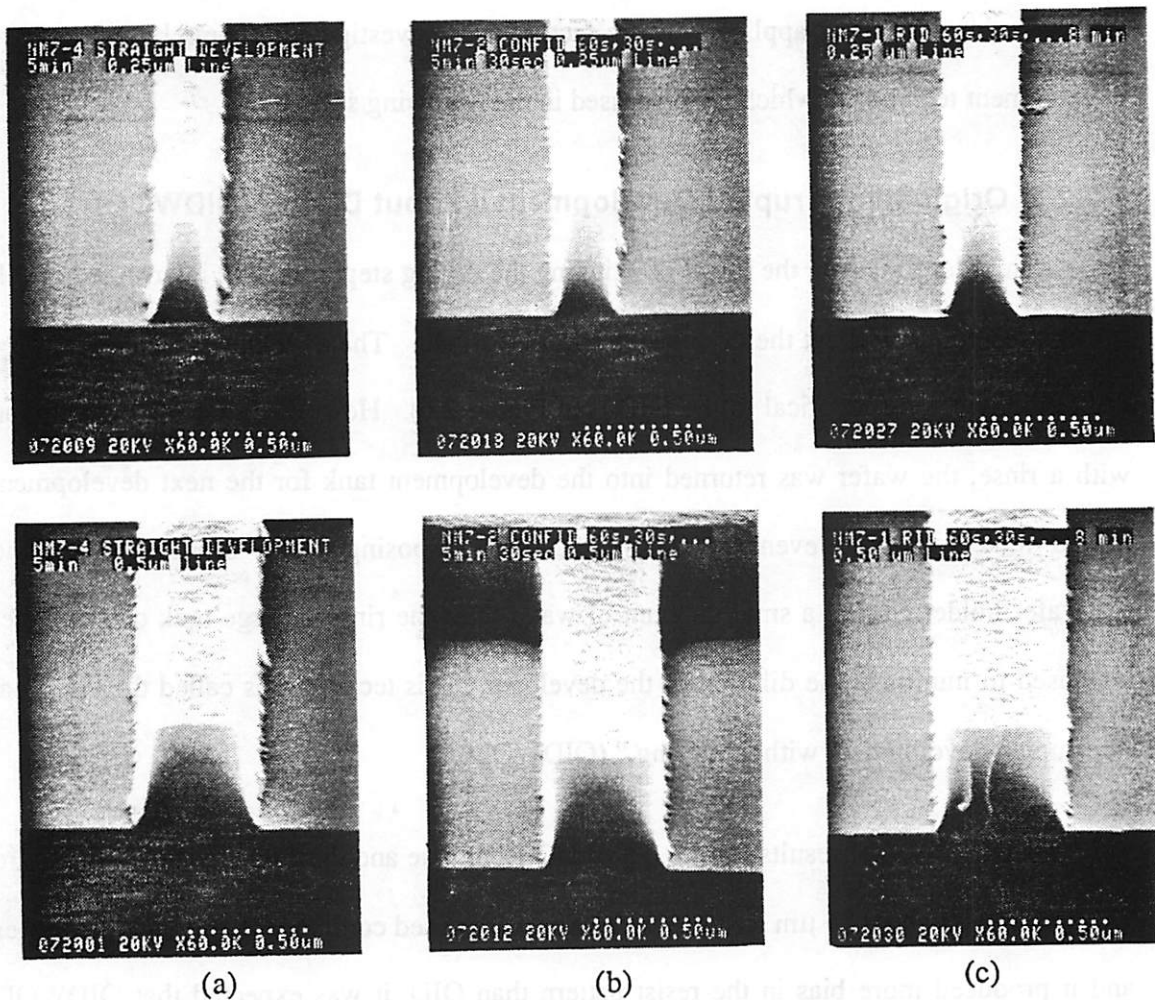


Figure 7.2. Resist line-edge profiles of 0.25  $\mu\text{m}$  and 0.5  $\mu\text{m}$  isolated lines on 0.5  $\mu\text{m}$  thick resist obtained with three different development techniques: (a) straight development, (b) spray interrupted development, and (c) standard interrupted development. Skipping the drying step works but gives more bias.

‡. The endpoint is defined by reaching the same dose-wedge positions on the resists and clearing all the residues near the edges and corners of large bright field areas.

ment, the resist profiles had taper sidewalls and the linewidths were the smallest among the three types of resist profiles. The ISD resist profiles had more vertical sidewall and less top-loss than the straight development. Therefore, interrupted development without the drying step can produce similar effects on the resist profiles. However, the ISD process gave more bias (narrower resist profiles) than the OID process. This difference in bias could be due to the skipping of the drying steps, the use of spray development, or the wetted resist surface when the developer was applied. These factors were investigated separately with special development techniques which are discussed in the following sections.

#### **7.2.2.2 Original Interrupted Development without Drying (OIDWOD)**

In order to isolate the effect of skipping the drying step, a second interrupted development technique without the drying step was performed. The development conditions for this technique were identical to the OID (see Figure 2.6). However, after the interruption with a rinse, the wafer was returned into the development tank for the next development period immediately to prevent the resist surface from exposing to air. Since the wafer and the wafer holder carried a small amount of water after the rinse, a large tank of developer was used to minimize the dilution of the developer. This technique is called the “original interrupted development without drying,” (OIDWOD).

Comparison of results for the OIDWOD technique and the ISD are shown in Figure 7.3 for 0.15  $\mu\text{m}$  and 0.25  $\mu\text{m}$  isolated lines. Since ISD used continuously flowing developer and it produced more bias in the resist pattern than OID, it was expected that OIDWOD would give less bias than ISD. However, contrary to intuition, the resist linewidths in the case of RIDWOD were slightly narrower than that of ISD. This difference in linewidth is most obvious in the 0.15  $\mu\text{m}$  isolated lines. The apparent faster dissolution of OIDWOD over ISD was probably due to the slightly longer time delay between development and rinse

in the OIDWOD. Another possible explanation could be that the stagnant water rinse in OIDWOD is less effective in establishing the rate retardation.

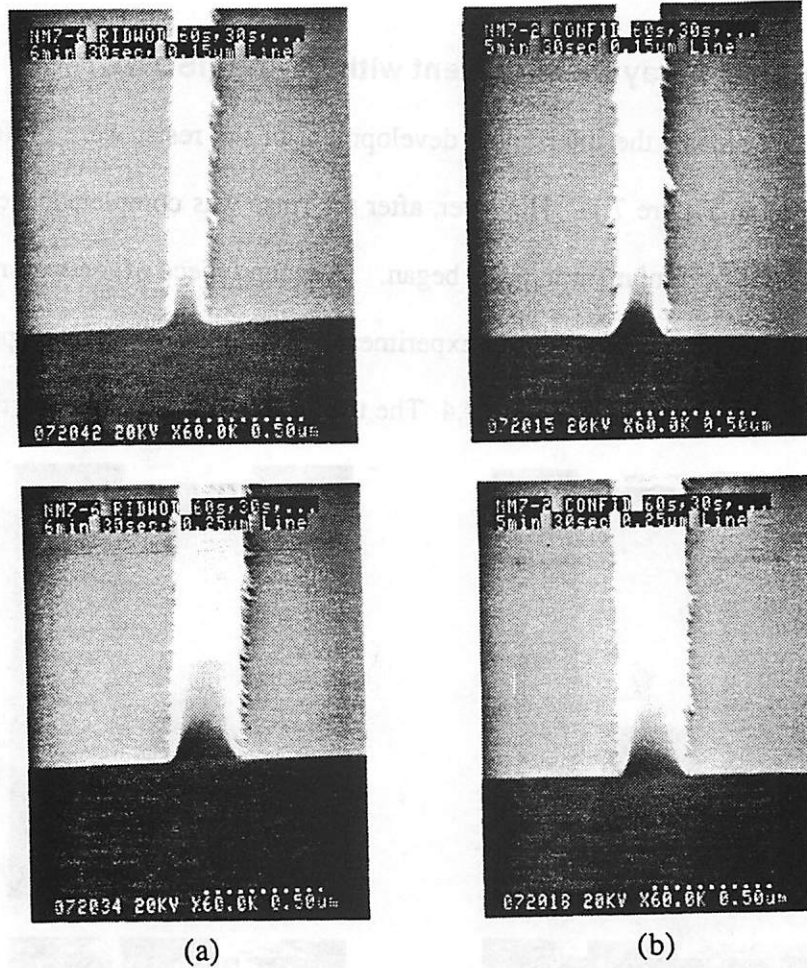


Figure 7.3. Resist line-edge profiles of 0.15  $\mu\text{m}$  and 0.25  $\mu\text{m}$  isolated lines on 0.5  $\mu\text{m}$  thick resists obtained with the two different interrupted development techniques that do not have the drying step: (a) spray interrupted development, and (b) original interrupted development without the drying step (OIDWOD). Development in stagnant developer gives more bias than in flowing developer.

### 7.2.3 Interrupted Development with Drying

The interesting results obtained with the interrupted spray development suggested that development with flowing developer could also affect the resist profiles even if the drying step was applied. On the other hand, the wetted resist surface could also be responsible

for the differences in the observed bias in the ISD resist profiles. To determine the significance of these two factors, they were added onto the original interrupted development process and their results are described next.

### 7.2.3.1 Interrupted Spray Development with Drying (ISDWD)

In this experiment, the interrupted development of the resist were performed with the set-up depicted in Figure 7.1. However, after the rinse was completed, the wafer was dried before the next development interval began. A second piece of the wafer was developed with the OID technique as a control experiment. Examples of the resist profiles from these two processes are shown in Figure 7.4. The use of flowing developer in the develop-

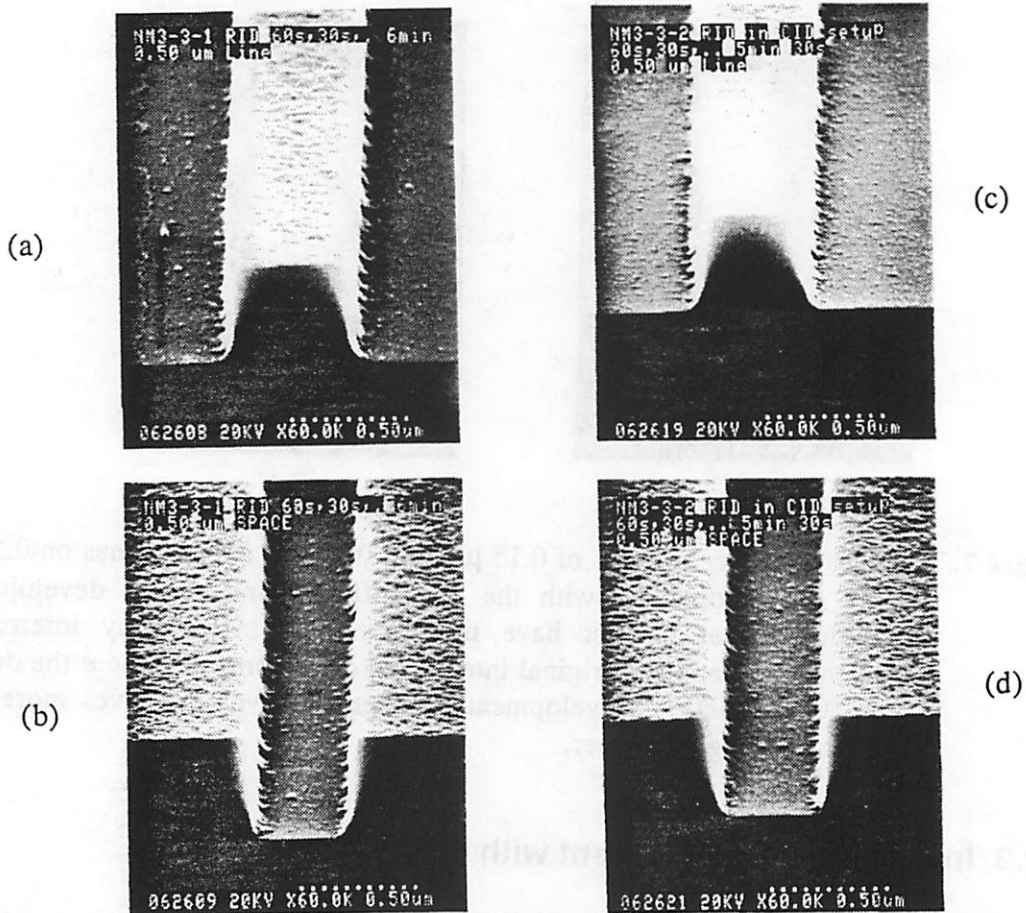


**Figure 7.4.** Comparisons of resist profiles obtained with OID and ISDWD. (a) 0.5 μm line, OID, (b) 0.5 μm line, ISDWD, (c) 0.5 μm gap, OID, and (d) 0.5 μm gap, ISDWD. Development in flowing developer gives more bias.

ment stage increased the bias of the process significantly. The linewidth of the isolated line in Figure 7.4b is narrower than the one in Figure 7.4a. In the isolated space, the gap delineated in Figure 6.4d is wider than the one in Figure 7.4c. These results indicate that the dissolution of the fully exposed resist is slightly faster in flowing developer than in stagnant developer.

### 7.2.3.2 Interrupted Development with Wetted Resist (RIDWDW)

To study the effect of a wetted resist surface in the development of the resist, resist line-edge profiles were obtained with DI water wetting technique. This technique was identi-

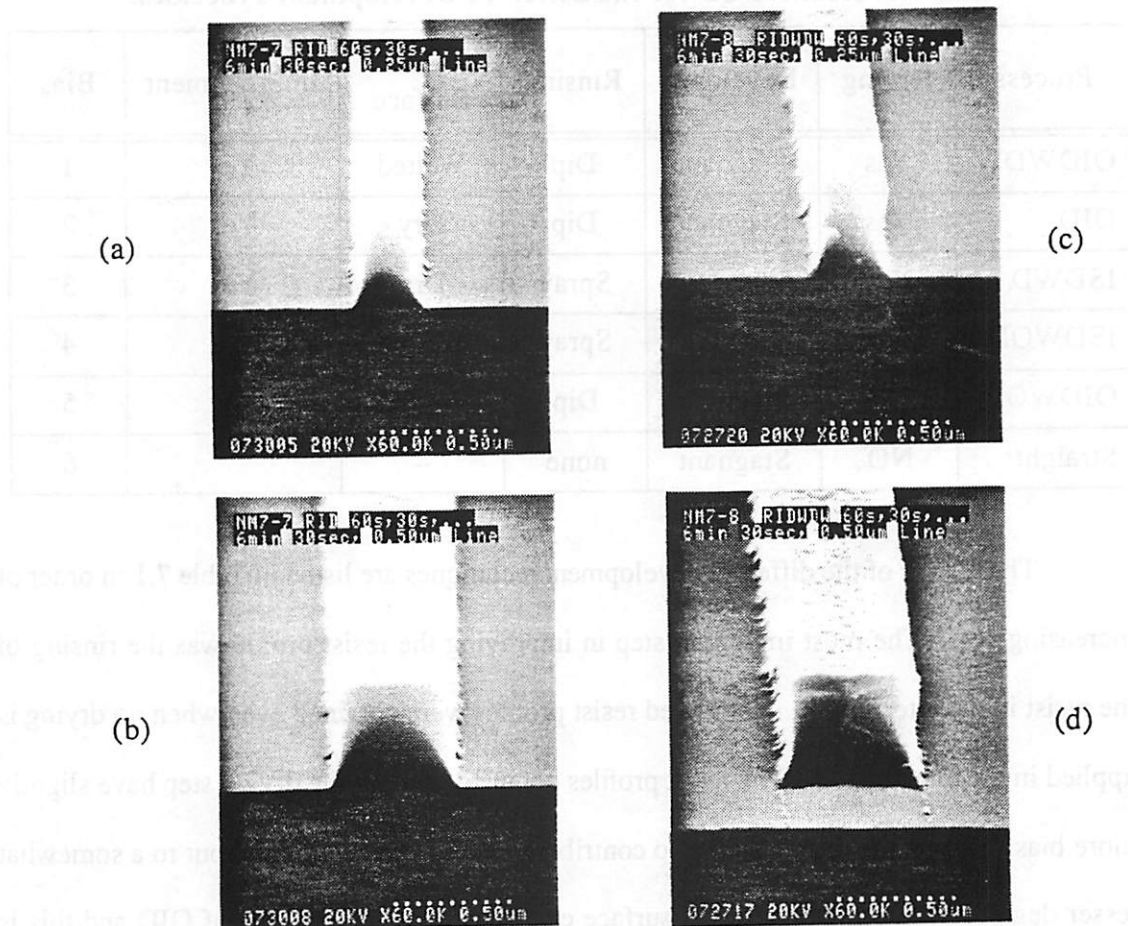


**Figure 7.5.** Comparison of the use of wet and dry resist surfaces prior to the development in the OID process. (a) 0.25 and (b) 0.5 μm lines with OID in which the resist was dry before dipping into the developer. (c) 0.25 and (d) 0.5 μm lines with RIDWDW in which the resist was wetted before dipping into the developer. The wetted surface gives less bias than OID.

cal to the OID except prior to the development of the resist, the wafer, which was blown dry with an air gun, was sprayed with DI water to create a wetted surface again. This procedure was applied at the beginning of every development interval. Figure 7.5 shows the resist profiles obtained with this process along with the profiles from a control experiment using the OID technique. The wetted resist surface produced less bias than the OID process. These results suggest that the wetted surface slows down the development of the resist which is probably due to local dilution of the developer near the surface of the resist.

### 7.3 Comparison of Techniques

**Table 7.1: Relative CD for the Different Development Processes.**

Process	Drying	Developer	Rinsing	Resist Surface	Improvement	Bias
OIDWDW	Yes	Stagnant	Dip	Wetted	Yes	1
OID	Yes	Stagnant	Dip	Dry	Yes	2
ISDWD	Yes	Flowing	Spray	Dry	Yes	3
ISDWOD	No	Flowing	Spray	Wetted	Yes	4
OIDWOD	No	Stagnant	Dip	Wetted	Yes	5
Straight	NO	Stagnant	none	--		6

The results of the different development techniques are listed in Table 7.1 in order of increasing bias. The most important step in improving the resist profile was the rinsing of the resist in the interruption. Improved resist profiles were obtained even when no drying is applied in the interruption. The resist profiles obtained without the drying step have slightly more bias. Hence, the drying step also contributed to the rate retardation but to a somewhat lesser degree. The pre-wetted resist surface can further reduce the bias of OID and this is probably due to the local dilution of developer near the surface of the resist at the beginning

of development. The use of spray development can overcome the dilution effect as in the case of ISDWD.

## 7.4 Summary

Although the mechanism of the rate retardation in interrupted development is not fully understood yet, it is believed to be a surface phenomenon involving some chemical reactions such as the AZ-coupling between the dissolution inhibitor and the resin.[1] These AZ-coupling reactions on the surface further reduce the dissolution rate of the resist in the low dose regions. However, the changes of the bias in the various interrupted development techniques suggest that transport phenomena during the development and rinse could also affect this surface layer.

Since the various interrupted development techniques used in this study can change the bias of the resist, they can be used to tailor resist profiles. For example, a 0.25  $\mu\text{m}$  line developed with RIDWOD is about 0.07  $\mu\text{m}$  smaller than the ones developed with RIDWDW. However, designing a suitable interrupted development schedule would require many characterization experiments. Simulations of interrupted development would significantly reduce the time and effort in optimizing the development schedule. These simulations require quantitative characterization of the surface rate retardation effects including the development rates of resists with and without interruption. The characterization experiments and the modeling approaches for these processes are described in Chapter 8.

## References

- [1] K. G. Chiong, K. Petrillo, F. J. Hohn, and A. D. Wilson, *J. Vac. Sci. Technol. B* **6**, 2238 (1988)
- [2] K. Honda, B. T. Beauchemin, Jr., R. J. Hurditch, and A. J. Blakeney, "Studies of The Molecular Mechanism of Dissolution Inhibition of Positive Photoresist Based on Novolak-DNQ," *Proceedings of SPIE, Advances in Resist Technology and Processing VII*, Vol. 1262, pp.493-500, 1990.
- [3] K. Honda, B. T. Beauchemin, Jr., E. A. Fitzgerald, A. T. Jeffries, III, S. P. Tadros, A. J. Blakeney, and R. J. Hurditch, "Studies of Dissolution Inhibition Mechanism of DNQ-Novolak Resist[II] Effect of Extended Ortho-Ortho Bond in Novolak," *Proceedings of SPIE, Advances in Resist Technology and Processing*, 1991.
- [4] S. Asaumi and H. Nakane, "Mechanism of Photoresist Resolution Improvement by Pre-exposure Treatment," *J. Electrochem. Soc.*, vol. 137, no. 8, pp. 2546-2549, 1990.

## Chapter 8

# Time-Delay Model of Interrupted Development

A time-delay model for the interrupted development of an IBM DQN resist is presented. This model is based on the time delays observed in the thickness versus development time measurements for resists which had received an interruption. The induction time is shown to be an exponentially decreasing function of absorbed energy density of the resist. Beyond the induction period, the dissolution of the resist is shown to revert to the normal dissolution without interruption. When this time-delay model is used in conjunction with the straight development rate equation of absorbed energy density in *SAMPLE*, it enables the simulation of the time-evolution of resist line-edge profiles with interrupted development for any interrupt schedule.

### 8.1 Introduction

The key to the simulation of interrupted development is the model for the development of the resist after interruption. In Chapter 3, the use of development-interval-specific rate equations based on the average dissolution rates for each development interval had only limited success. Although the data can be used to predict the resist thickness remaining at the end of each interrupt, simulated resist profiles based on these rate equations do not match the experimental profiles. In addition, the set of rate equations is good for only one particular interrupted development schedule. As a result, simulation based on this approach cannot be used to study the effects of development cycle variations unless a large number of characterization experiments are performed.

It is widely held that the improved wall angle and contrast with alkaline treatment and interrupted development are due to the formation of a surface induction layer after the

water rinse in the low dose regions. [1]-[4] This surface induction layer protects the surface of the resist from development and as the interruption treatment is repeated, the sidewalls of resist profiles are protected from further development. Consequently, steep and accurate resist patterns are obtained. Evidently, average development rates over the development cycle could not account for this surface effect. Therefore, in-situ development rate measurements of the resist after interruption are needed to characterize this surface induction layer.

In this chapter, the dissolution characteristics of the IBM DQN resist with and without interruption are compared. Then a practical model is developed to correlate the induction time to the absorbed energy density. This model and the development rate equation for the straight development of the resist are then implemented in *SAMPLE* to simulate the time-evolution of resist line-edge profiles. Comparison of simulated and experimental resist profiles are then used to validate this time-delay approach.

## 8.2 Dissolution Characteristics after Interruption Treatment

The major effect of the interruption treatment on the dissolution of the resist is the slowing down of the resist dissolution at the resist surface. Heretofore, it has not been known if this rate retardation occurs only on the top surface of the resist or extends to several thousand Å into the resist. Examples of this surface rate retardation are shown in Figure 8.1 where the film thickness versus development time curves of resists without and with an interruption treatment are compared for different exposure doses. In the curves obtained from straight development in Figure 8.1a, the slopes of the curve tend to increase with depth into the resist indicating that there is some depth dependence of the dissolution rate of the resist. Note that no initial delay or induction time is observed. On the other hand, in Figure 8.2b for development after an interruption treatment, induction periods or delays can be

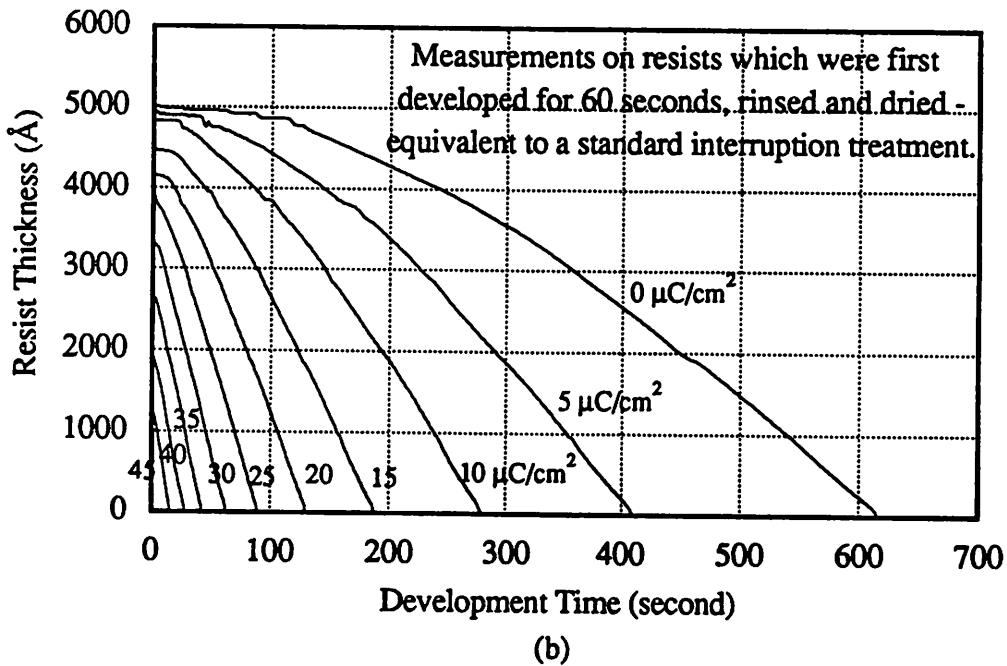
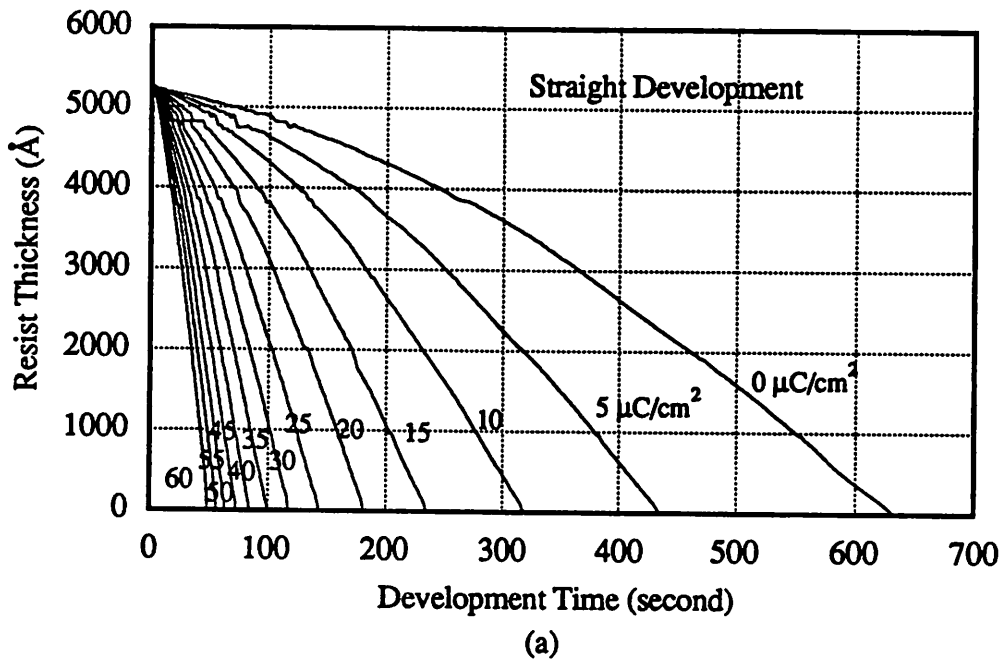


**Figure 8.1.** Thickness versus development time curves of the IBM DNQ/Novolak resists developed (a) without and (b) with a standard interruption treatment. After the interruption treatment, there is an obvious induction period before dissolution resumed. The duration of the induction period appeared to be a function of exposure dose.

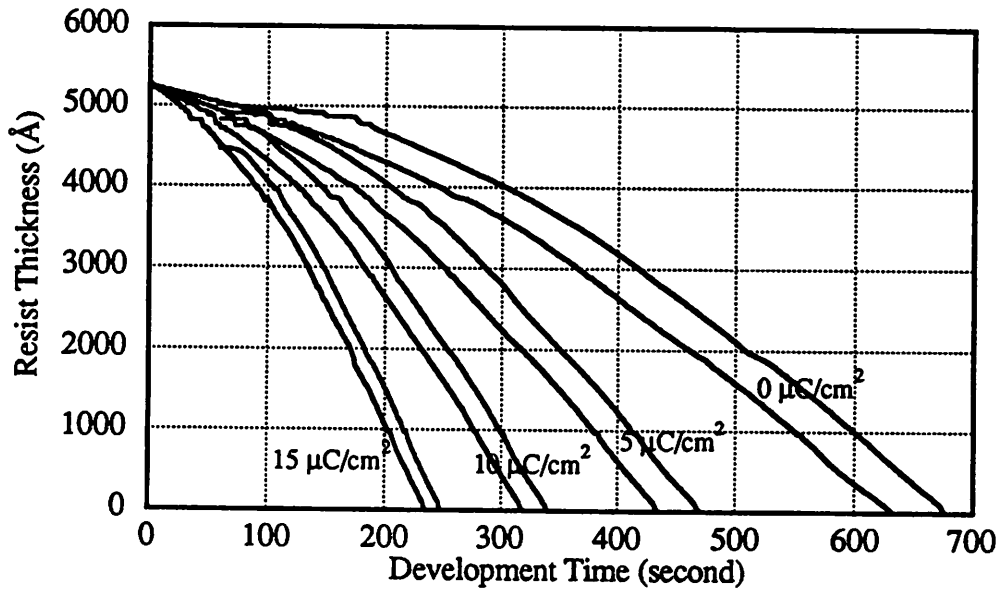
observed. These data are for an interruption after a 60 second development. The induction effect is especially strong in the low exposure regions. As the exposure dose increases, the induction time decreases.

To further compare the development characteristics of resist with and without an interruption treatment, the data in Figure 8.1b are shifted to show the total development time and then compared directly to the data in Figure 8.1a by plotting them on the same time scale in Figure 8.2. For all doses the starting points for the curves for interrupted development fall on a vertical line at 60 seconds with thicknesses nearly identical to that which would occur for normal development treatment at 60 seconds. Thus the interruption procedure does not appear to remove any significant amount of resist during the interruption.

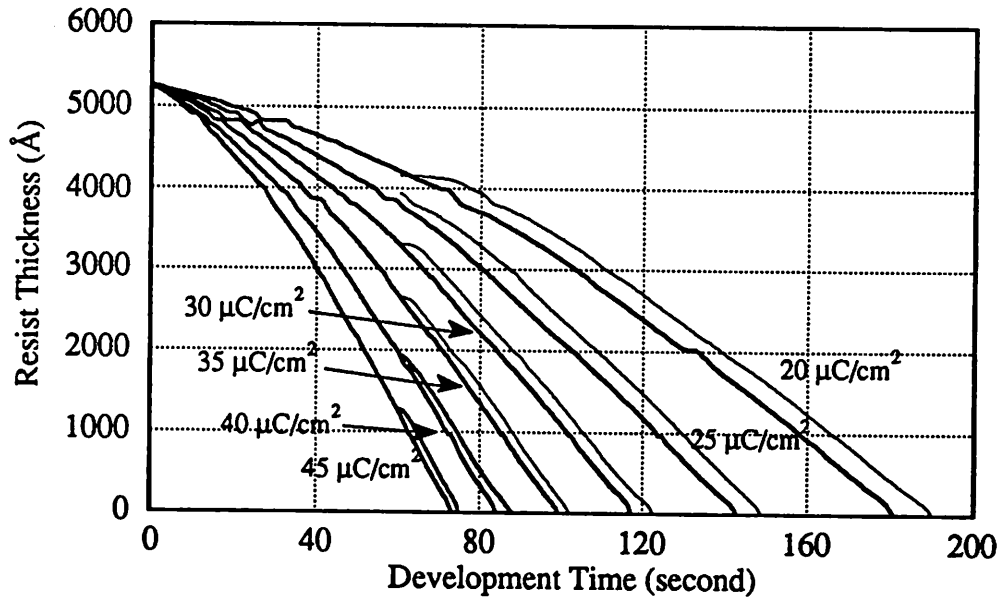
A second important observation is that the thickness versus development time curves for the resists are nearly parallel to each other once the induction layer is dissolved. This suggests that once the induction layer is dissolved, the resist dissolution behavior is identical to the original resist before the interruption.

In addition, for the resists with interrupted development, the depths over which their thickness versus development time curves are not parallel to the uninterrupted development ones are only on the order of 200 Å. That is the delay in development is confined to a very thin layer at the surface. A final observation is that the lateral shift of the parallel curves is a few seconds for high doses and tens of seconds for low doses. These four observations allow the overall effect of the interruption to be modeled as the introduction of a simple time delay,  $t_D$ , which decreases with increasing exposure dose.

Quantitative values for the time delay can be obtained easily from the difference in the development times at which the resists were completely clear. Using this approach the



(a)



(b)

**Figure 8.2.** Thickness versus total development time curves of the IBM DNQ/Novolak resists developed without and with a standard interruption treatment. (a) Low dose curves where the induction effect is more pronounced. (b) A small induction time exists even for very high dose regions. After the time delay, the curves are parallel to each other.

data in Figure 8.3 were determined. A simple exponential function can be used to accurately fit the time delay data. It is given by,

$$t_D = 37.7e^{-0.61E} \quad (\text{EQ 8.1})$$

where  $E$  is the absorbed energy density in  $\text{J}/\text{cm}^3$ .

The mechanism of contrast enhancement with interrupted development is now clear. Since the induction time is the longest for unexposed resist, its dissolution rate is reduced the most by interruptions. In fact, if the development interval is shorter than the induction time, the development rate is effectively zero. On the other hand, the induction times for highly exposed resists are much shorter than the development time used in a typical interrupted development cycle (e.g., 30 seconds). Therefore, the interruptions have very little effect on these resists. Since the ratio of the fastest and the slowest dissolution rate is one measure of contrast for positive resists, this near-zero dissolution rate for the unexposed resist greatly improves the contrast of the resist.

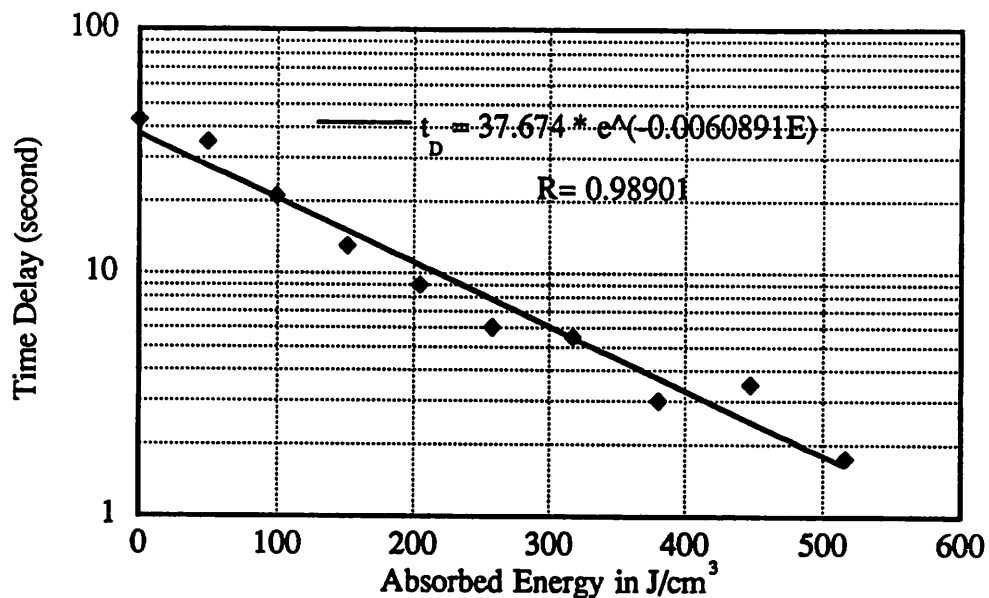


Figure 8.3. Time delay (induction time) versus absorbed energy density for the IBM DNQ/Novolak resist after interruption treatment. The data can be fitted with a simple exponential function.

Due to insufficient data from resists which were developed and interrupted more than once, it is yet not clear if this equation for the time delay will be valid for the subsequent interruptions. In order to verify this model for multiple interruptions, simulation of resist line-edge profiles with *SAMPLE* using this assumption will be compared to experimental profiles. It is anticipated that multiple interruptions will repeat this delay effect. Since the ultimate goal is to quantitatively predict resist line-edge profiles, we now undertake the simulations and will later use profile comparisons to determine if the repeated use of the single interruption is physically justified.

### 8.3 Input for Interrupted Development Simulation

*SAMPLE* is well suited for the implementation of this surface rate retardation model because its development simulation uses a surface advancing algorithm, called the string algorithm (see Chapter 2). The induction times on the surface after the interruption can easily be calculated from the absorbed energy density using Equation (8.1). For every advancement of the string, if the development time is less than the induction time, the rate is set to zero. When the development time for the interval becomes greater than the induction time of the point on the string, the advancement of that point is again carried out according to the distance determined by the normal dissolution rate.

To determine the true development time, *SAMPLE* has to keep track of the development time from the beginning of the development interval. Therefore, a new keyword “eblintdev” is added which is used to specify the schedule of the interrupts. The format of the new keyword is “eblintdev  $n$   $t_{indev}(1)$   $t_{indev}(2)$  ...” where  $n$  is number of interruption treatments and  $t_{indev}$ 's are the development times at which the interrupts are applied. For

example, for a 5 minute interrupted development with 60, 30, 30,..., 30 seconds development intervals, the input for the development simulation is:

```
eblintdev 8 60 90 120 150 180 210 240 270;
devtime 0 300 10;
ebldevelop;
```

Thus, the true development time at development interval  $i$  is given by:

$$t(i) = t_{Total} - t_{indev}(i-1) \quad (\text{EQ 8.2})$$

where  $t_{Total}$  is the total development time. However, before *SAMPLE* can be used to simulate interrupted development, a quantitative dissolution rate model for the normal development of the IBM DQN resist has to be obtained.

## 8.4 Dissolution Rate in Straight Development

The dissolution rate versus absorbed energy data are shown in Figure 8.4. They were obtained from combining the DRM measurements and the Monte Carlo simulation of electron energy deposition. In the DRM experiment, the development rate of a 0.5  $\mu\text{m}$  thick resist exposed at 50 keV with a dose matrix of 5 to 60  $\mu\text{C}/\text{cm}^2$  in 5  $\mu\text{C}/\text{cm}^2$  increments were measured. For positive DNQ resists, the dissolution rates have a strong dependence on the depth into the resists due to secondary surface rate retardation effects [5][6]. The dissolution rate for the IBM resist is no exception. The rate at the surface of the resist is about three times slower than the bulk rate. Surprisingly, the dissolution rate also decreases near the Si substrate. This effect has been confirmed by the SEM's of resist line-edge profiles. Simulations without this substrate effect could not reproduce the curved sidewalls near the bottom of the resist profile. In order to include the substrate effect, a rate equation, which is modified from the one proposed by Kyser and Pyle [7], is used. It is given by:

$$R(E, z) = R_o \left(1 + \frac{E}{E_o}\right)^\alpha \left(1 - A \exp\left(\frac{-z}{\lambda_1}\right) - B \exp\left(\frac{(z - z_{max})}{\lambda_2}\right)\right) \quad (\text{EQ 8.3})$$

where  $E$  is the deposited energy density in  $\text{kJ/cm}^3$ ,  $z$  is the depth into the resist in  $\mu\text{m}$ .  $R_o$ ,  $E_o$ ,  $\alpha$ ,  $A$ ,  $B$ ,  $\lambda_1$ , and  $\lambda_2$  are fitting parameters. The solid lines in Figure 8.4 are calculated using Equation (8.3) with the parameters listed in Table 8.2.

**Table 8.2: Rate Equation Parameters**

Parameter	$R_o$	$E_o$	$\alpha$	$A$	$\lambda_1$	$B$	$\lambda_2$
Values	$7.5 \text{ \AA/sec}$	$228 \text{ J/cm}^3$	2.27	0.8	$0.5 \mu\text{m}$	0.3	$0.05 \mu\text{m}$

## 8.5 Comparison of Simulation and Experiment for Straight Development

To verify the validity of the model for the straight development of the resist, Equation (8.3) is input into *SAMPLE* to simulate line-edge resist profiles. Figure 8.5 shows the

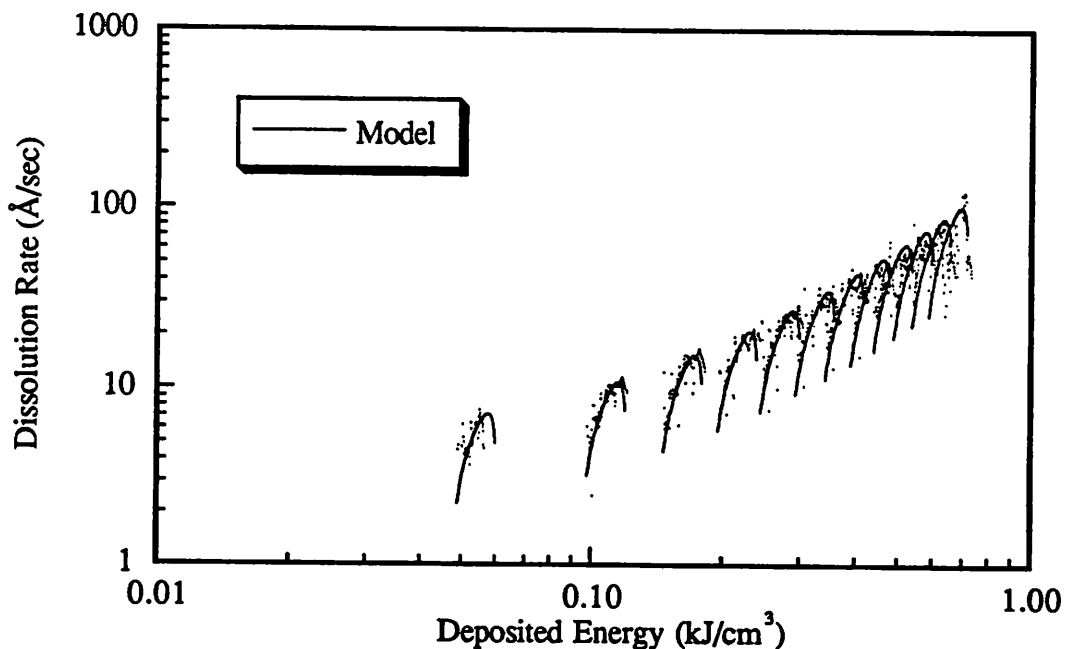


**Figure 8.4.** Dissolution rate versus deposited energy for the IBM DNQ/Novolak resist with straight development. Dissolution rate is also depended on the depth into the resist. The rate is lower both near the surface and at the substrate.

simulated and experimental 0.25  $\mu\text{m}$  features delineated in a 0.5  $\mu\text{m}$  thick resist with straight development. For these features, a pattern bias<sup>†</sup> of 0.1  $\mu\text{m}$  was applied. The patterns were corrected for the proximity effect using dose adjustments so that an isolated space, line, and line/space patterns would all come out on size. For example, the 0.25  $\mu\text{m}$  isolated space received 2.61 times the base dose, which is 45  $\mu\text{C}/\text{cm}^2$ . In the experiment, the endpoint was reached after 5 minutes of development.

In order to have good agreement between simulation and experiment, it was found necessary to reduce  $R_o$  from 7.5  $\text{\AA}/\text{sec}$  to 3.5  $\text{\AA}/\text{sec}$ . This result is not surprising since the development conditions in which the SEM micrographs of resist profiles were obtained were very different from the development conditions in the DRM. In the DRM experiment at Berkeley, there was continuous circulation of the developer whereas in the resist profile experiments made at IBM, Yorktown, the development was performed by immersion of the wafer in a stagnant tank of developer. In Chapter 7, it was shown that different techniques for applying the developer can affect the bias of the resist. It is also known that the development rate of unexposed resist varies from batch to batch of developer. It is highly likely that either the difference in the development conditions or the developer was responsible for the faster dissolution rate obtained on the DRM.

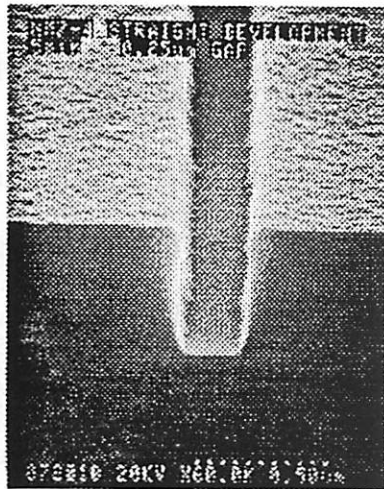
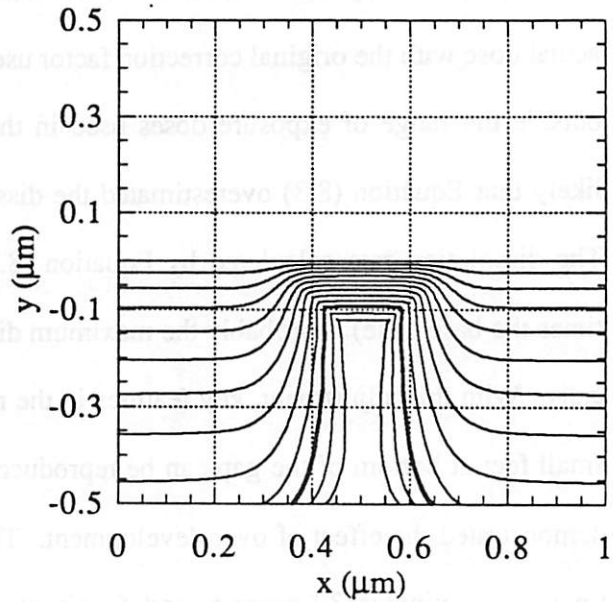
After the adjustment is made for  $R_o$ , there is very good agreement between simulation and experiment for the case of the isolated line. For the isolated line, the simulated profile for a 5 minute development displays a similar taper sidewall angle as in the SEM resist profile.

---

†. The pattern bias is directed so that the beamwidth would be narrower than the desired final image width. Thus, the 0.25  $\mu\text{m}$  image would be written with a 0.15  $\mu\text{m}$  beamwidth.



0.25  $\mu\text{m}$  line



0.25  $\mu\text{m}$  space

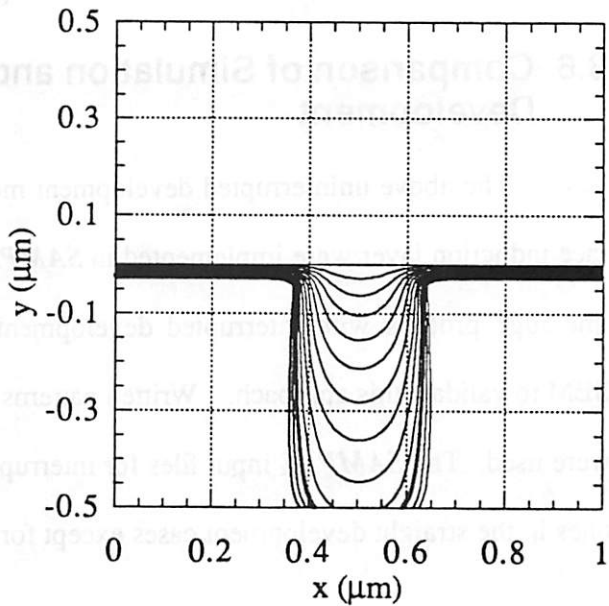


**Figure 8.5.** Comparison of simulated and experimental resist profiles with straight development. The development time for the experimental resist profiles was 5 minutes. In the simulation, the profiles from 0 to 6 minute of development in steps of 30 second are plotted. The profiles of 5 minute development is plotted using thicker line. Over-development significantly changes the resist profile of the isolated line.

However, in order to have the simulated isolated space profile agree with the experiment, the proximity effect correction factor<sup>‡</sup> has to be lowered from 2.61 to 2.00. Since the actual dose with the original correction factor used was in excess of  $100 \mu\text{C}/\text{cm}^2$ , which was outside the range of exposure doses used in the characterization experiment, it is highly likely that Equation (8.3) overestimated the dissolution rate of resist in the isolated space. The dissolution rate calculated by Equation (8.3) for resist exposed with  $90 \mu\text{C}/\text{cm}^2$  (2 times the base dose) is probably the maximum dissolution rate that could be obtained physically. With this adjustment, key features in the resist profiles such as pattern width and the small feet at bottom of the gap can be reproduced in the simulation. The simulations also demonstrated the effect of over development. The simulated resist profiles at development times of 5 minutes 30 seconds and 6 minutes showed significant additional dissolution resulting in a smaller isolated line and a wider isolated space.

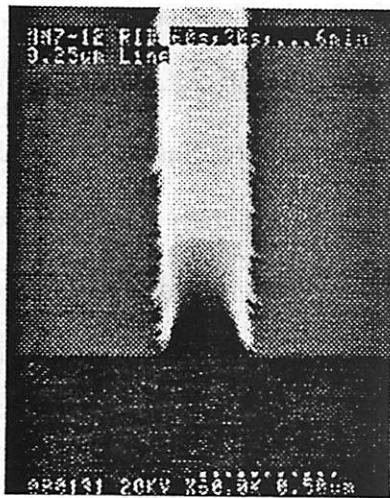
## 8.6 Comparison of Simulation and Experiment for Interrupted Development

The above uninterrupted development model and the time-delay model for the surface induction layer were implemented in *SAMPLE* to simulate the time-evolution of resist line-edge profiles with interrupted development. Simulated profiles are compared with SEM to validate this approach. Written patterns identical to the straight development cases were used. The *SAMPLE* input files for interrupted development were also identical to the ones in the straight development cases except for the `eblintdev` statement.

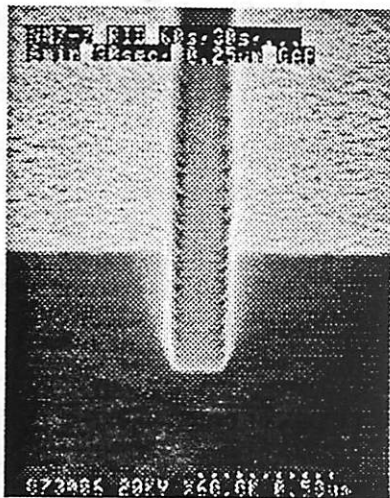
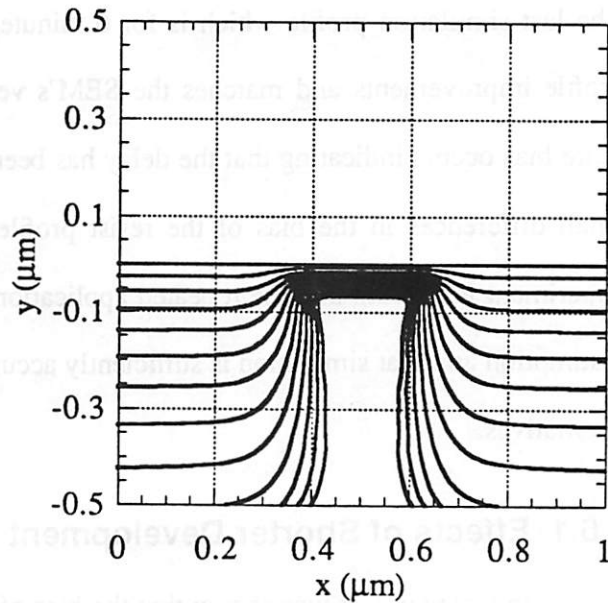
Figure 8.6 shows the simulated and experimental  $0.25 \mu\text{m}$  features delineated in a  $0.5 \mu\text{m}$  thick resist with interrupted development. The interrupted development schedule in

---

‡. Factor of dose increase from the base dose for proximity effect correction.



0.25  $\mu\text{m}$  line



0.25  $\mu\text{m}$  space

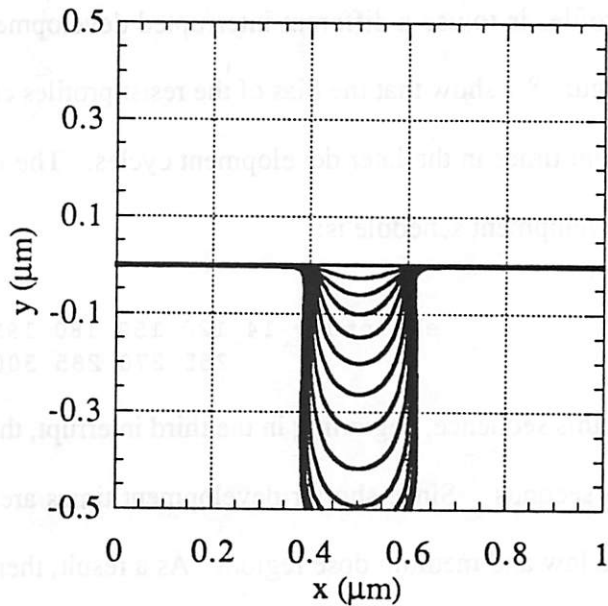


**Figure 8.6.** Comparison of experimental and simulated resist profiles for the interrupted development of the IBM DNQ/Novolak resist. The interrupted schedule is 60,30,30,...,30 for 6 minute. The shape of the profiles match very closely but the simulated profiles have more bias. This discrepancy indicates that the rate equation over estimated the dissolution rate of the resist.

this case was 60,30,30,...,30 seconds with a total development time of 6 minutes. The SEM's for resists with interrupted development show near vertical walls and less top loss. The last simulation profile which is for 6 minutes of total development time shows these profile improvements and matches the SEM's very well. In this case, however, slightly more bias occurs indicating that the delay has been slightly underestimated. Other than the small differences in the bias of the resist profiles, there is generally good agreement to experiment indicating that the repeated application of the interruption delay is a reasonable assumption and that simulation is sufficiently accurate to be used to investigate new process alternatives.

### 8.6.1 Effects of Shorter Development Cycle

In Chapter 7, it was shown that the bias of the resist profiles can be controlled with different interrupted development techniques. Another way to change the bias of the resist profiles is to use a different interrupted development schedule. Simulated resist profiles in Figure 8.7 show that the bias of the resist profiles can be reduced by decreasing the development times in the later development cycles. The `eblintdev` statement for this interrupted development schedule is:

```
eblintdev 14 120 150 180 195 210 225 240
          255 270 285 300 315 330 345;
```

In this sequence, beginning in the third interrupt, the development time of each cycle is only 15 seconds. Since shorter development times are used, there is even less development in the low and medium dose regions. As a result, there is a further reduction in pattern bias of the resist profile which made the isolated line wider and the isolated space narrower than the ones obtained with the original interrupted development schedule. In order to compensate

for the slower dissolution with the shorter development cycles, the first development cycle is 2 minute rather than the usual 1 minute development.

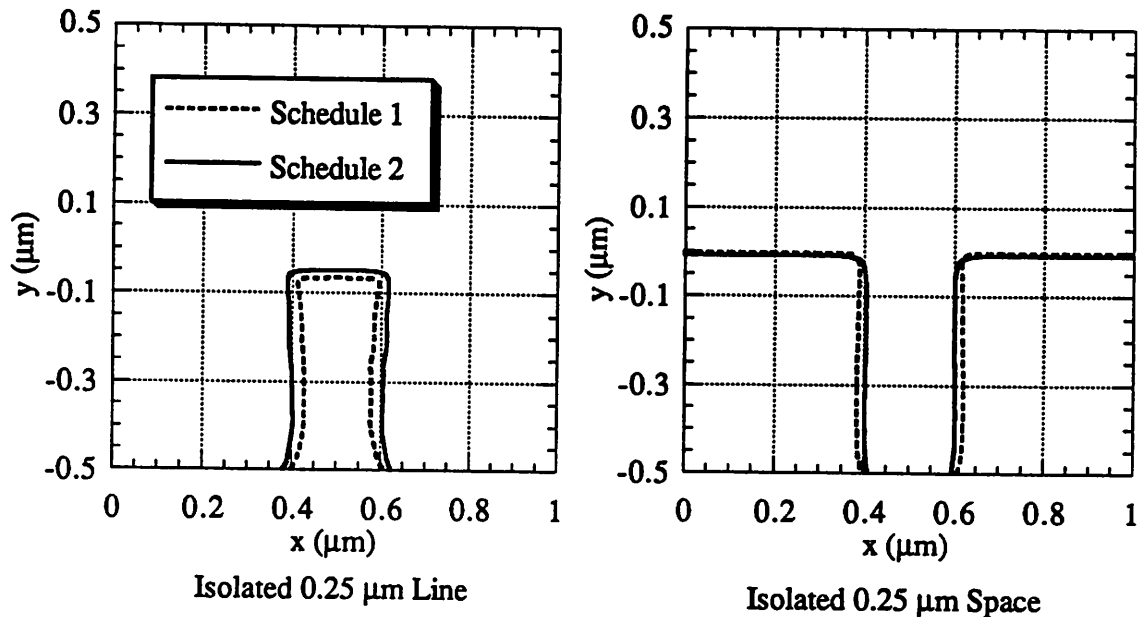


**Figure 8.7.** Comparison of simulated  $0.25\ \mu\text{m}$  features using two different interrupted development schedules. Schedule 1 is 60,30,30,...,30 seconds with 5.5 minute total development time and schedule 2 is 120,30,30,15,...,15 with 6.5 minute total development time. Schedule 2 produces resist profiles with less bias.

### 8.6.2 Effects of Additional Induction Time

Besides providing a capability for the simulation of interrupted development, the time-delay model and the rate equation also provide a means for investigating the mechanism of interrupted development. For example, it was shown in Chapter 7 that the effect of the drying step is to further decrease the bias of the resist profiles. One possible mechanism for this effect could be the introduction of some additional delay in the development due to the time it takes for the developer to establish proper contact with the resist surface. Figure 8.8 illustrates the effect of adding 3 seconds to the time-delay equation to account for wetting (Equation 8.1) on the  $0.25\ \mu\text{m}$  resist profiles. The added induction time decreases the pattern bias slightly and the effect is stronger for the isolated line. The additional time

delay effect could also be responsible for the smaller pattern bias observed in the RIDWDW experiment in Chapter 7 where the resist surface was pre-wet before development.

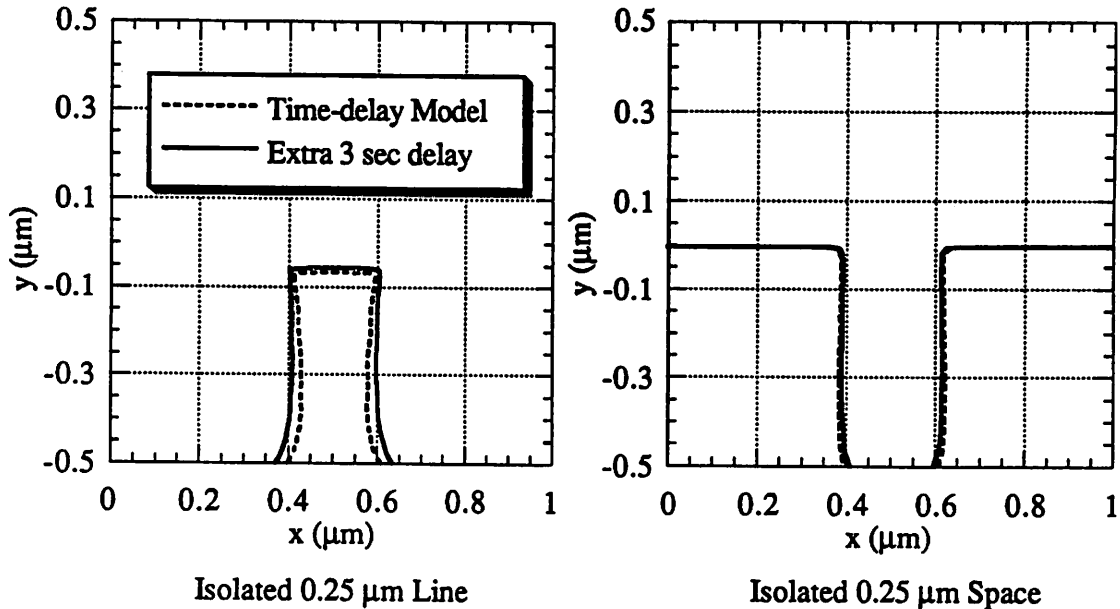


**Figure 8.8.** Effects of adding 3 extra seconds delay in the induction time on the resist profiles obtained with the 60,30,....,30 seconds interrupted development for 6 minute. The added induction time decreases the pattern bias slightly and the effect is stronger in the isolated line. This result could explain the decrease pattern bias observed in the RIDWDW experiment.

## 8.7 Summary

A time-delay model for the simulation of interrupted development of an IBM DNQ/Novolak resist has been developed which utilizes an induction time or delay as a function of absorbed energy density to model the effects of an interruption treatment. This induction time function is obtained from the thickness versus development time data of resist which was developed for 1 minute and received an interruption treatment prior to development measurement. This time delay is found to be an exponentially decreasing function of absorbed energy density. The induction effect is in essence a surface phenomenon because after the top 200 Å of resist is dissolved, the dissolution of the resist is the same for no inter-

ruption. This induction effect is in addition to a planar surface rate retardation where the rate near the surface and resist/substrate interface are slower than the bulk. This planar dissolution effect was fitted with a modified version of the rate equation for typical positive resists using two exponential factors to model the depth dependence at both the air and substrate interfaces.

The successful implementation of the time-delay models in *SAMPLE* has enabled the simulation interrupted development of the resist using any interrupt schedule including straight development. Excellent agreement between simulation and experiment has been demonstrated for a variety of resist patterns and development methods. Simulated resist profiles show that by shortening the times of the development cycles, the pattern bias can be increased. In addition, this model provides a foundation for the investigation of the effects of additional induction time on the resist profiles, which might be the mechanism responsible for the further reduction in the pattern bias with the drying or pre-wetting step. While induction effects are not as pronounced in other resist systems, the extended *SAMPLE* code should be suitable for differentiating developer-related induction effects and spin-cast-layer-related surface rate retardation effects.

## References

- [1] K. G. Chiong, K. Petrillo, F. J. Hohn, and A. D. Wilson, "Contrast and Sensitivity Enhancement of Resists for High-Resolution Lithography," *J. Vac. Sci. Technol.*, B6, pp. 2238-2244, Nov/Dec 1988.
- [2] T. Yoshimura, F. Murai, H. Shiraishi, and S. Okazaki, "PRISM: Process for Resist Profile Improvement with Surface Modification," *J. Vac. Sci. Technol.*, B6, pp. 2249-2253, Nov/Dec 1988.
- [3] S. Asaumi and H. Nakane, "Mechanism of Photoresist Resolution Improvement by Pre-exposure Treatment," *J. Electrochem. Soc.*, vol. 137, no. 8, pp. 2546-2549, 1990.
- [4] K. Itoh, K. Yamanaka, H. Nozue, and K. Kasama, "Dissolution Kinetics of High Resolution Novolac Resists," *Proceedings of SPIE: Advances in Resist Technology and Processing VIII*, vol. 1466, pp. 485-496, 1991.
- [5] D. Kim, W. Oldham, and A. Neureuther, "Development of Positive Photoresist," *IEEE Trans. on Electron Devices*, vol. ED-31, pp. 1730-1735, December 1984.
- [6] K. Honda, B. T. Beauchemin, Jr., R. J. Hurditch, and A. J. Blakeney, "Studies of the Molecular Mechanism of Dissolution Inhibition of Positive Photoresist Based on Novolak-DNQ," *SPIE Proceedings: Advances in Resist Technology and Processing VII*, vol. 1262, pp. 493-500, March 1990.
- [7] D. F. Kyser and R. Pyle, "Computer Simulation of Electron-Beam Resist Profiles," *IBM J. Res. Develop.*, vol. 24, no. 4, pp. 426-437, 1980.

## Chapter 9

# Conclusions and Future Research

### 9.1 Conclusions

An in-depth examination of chemical and physical mechanisms in resist materials has been made to support electron-beam lithography with high beam current exposure tools and advanced chemically-amplified resist systems. New models for resists and their associated quantitative parameters as well as a comprehensive set of extensions to the *SAMPLE* program have been developed for the characterization, modeling and simulation of advanced electron-beam lithography. These extensions include a simulator for electron-beam induced heating in the resist during exposure, empirical extensions to the mechanism-based dissolution rate function of absorbed energy to include additional processing variables, a model for the “cage-effect” in the acid-catalyzed crosslinking reaction of the melamine-based chemically-amplified resist, and a mechanistic model for the interrupted development of an IBM DQN resist.

Estimations of temperature rise in the resist during exposure have been obtained by solving the heating equation with a massively-parallel computer program which is based on the explicit Euler method. Simulation results indicate that electron-beam resists with low sensitivities (i.e.,  $> 30 \mu\text{C}/\text{cm}^2$  at 20 keV) will likely experience transient temperature rise above their glass transition temperatures when they are exposed with high beam current densities ( $> 25 \text{ A}/\text{cm}^2$ ). This electron-beam induced heating could lead to both physical and chemical changes in the resists. In the case of the Hitachi RD-2000N, when a beam current density higher than  $25 \text{ A}/\text{cm}^2$  is used, exposures from the AEBLE-150 caused expansion of the resist which leads to the formation of cavities in the resist. The increase in intensity of

these effects in thick resist indicates that the resist's thermal conductivity is even lower than that of the oxide. The transient time of the stored heat is on the order of 100 ns; and therefore, adjacent pixels can contribute to a higher temperature rise especially near the edge of a large pattern where the beam has to turn around.

A methodology based on empirical extensions to the mechanism-based (EEMB) dissolution rate function of absorbed energy has been developed to extend the range of profile modeling for advanced electron-beam resists. The application of this methodology to a negative chemically-amplified resist, SAL-601-ER7 has been successful in establishing a predictive model for the accurate simulation of the development of this resist under a variety of post-exposure bake conditions and developer concentrations. This model consists of a dissolution rate function of absorbed energy and empirical functions relating the parameters in the rate function to the three key processing variables. These empirical functions are determined from factorial experiments of dissolution rate measurements the using least squares technique. Important resist performance indicators such as contrast and sensitivity can also be derived from this model. Thus, this EEMB dissolution model can be used to choose an optimized processing condition as well as study dose-linewidth tradeoffs with simulation.

A practical model based on a linear approximation of the "cage effect" has been developed to describe the mechanism of the acid-catalyzed crosslinking reaction in the melamine-based negative chemically-amplified resist, SNR-248. This model is derived from measurements of the extent of the reaction obtained with FTIR. The "cage effect" is modeled by multiplying the global rate constant with a linear "cage effect" factor, which is a decreasing function of the extent of crosslinking reaction with values between 1 and 0. The slope of this linear function is explicitly characterized in term of the dose-dependent satura-

tion of the reaction. This model provides a closed-form solution relating the extent of the crosslinking to the exposure and PEB conditions. Due to the mathematical simplicity of this model, physical parameters can easily be extracted from log-linear plots of the FTIR measurements of the extent of the crosslinking reaction.

The power and flexibility of this “cage effect” model were demonstrated by applying it to and comparing results for both optical and e-beam exposures of SNR-248 resist. A complete model for the exposure, bake and dissolution has been based on this new “cage effect” model. While its characterization currently does not include process parameters such as developer concentration as in the EEMB approach, it can be used for direct resist line-edge profile simulation or for in-depth investigation of the causes of the “cage effect” in *SAMPLE-ARK*. The behavior of the dissolution characteristic curves for both exposure methods is quite similar. Certain quantitative parameters such as the order of the acid catalyst in the crosslinking reaction is nearly identical (1.37 for e-beam and 1.42 for optical). However, in e-beam exposed resist, some crosslinking is induced by the e-beam exposure. This initial crosslinking appears to contribute to the slightly higher activation energy in the crosslinking reaction of the e-beam exposed SNR-248 resist. The equilibrium conversion of the melamine crosslinking sites in the e-beam exposed resist is also larger than that of the deep-UV exposure. In the expression for the equilibrium conversion for the e-beam exposed resist, the power of the acid concentration  $n$ , is approximately 0.49, whereas for the deep-UV exposed resist  $n$  is 1.1. Difference also occurs in the activation energies of the equilibrium constants which suggests that the “cage effect” with e-beam exposure has a stronger hindrance on the backward reaction. For both exposure models, the dissolution rate of SNR-248 resist is a single valued function of the extent of the crosslinking reaction.

The unique chemistry of DQ and novolak resin has enabled the use of interrupted development to improve the contrast and process latitude of these resists. Various interrupted development techniques have been shown to affect the bias of the resist profiles. In all cases, improved profiles with straighter sidewalls and less top loss are obtained. This improvement results from the formation of an induction layer on the resist surface which is greatest in the areas that have received little or no exposure. The induction time of the surface layer is shown to be well-characterized by an exponentially decreasing function of exposure dose. A time-delay model has been developed which can be used to simulate interrupted development with any interruption schedule as well as provide a more fundamental understanding of the basic mechanisms which determine the shape of the resist profiles.

Some comments on the possible impact of combinations of the factors studied in separate chapters are appropriate. Heating effects considered in Chapter 4 were not seen in chemically-amplified resists exposed on the AEBLE-150 and from the model parameters in Chapter 6, heating is not apt to be important up to beam current densities of  $25 \text{ A/cm}^2$ . Developer concentration was found to be a significant factor in improving contrast in Chapter 5 and its effects could be approximately included in the "cage effect" model of Chapter 6 by utilizing parts of the  $R_0$  model. Resists other than the IBM DQN resist tend to show less dramatic surface-delay effects; however, where these effects are important, it is likely that they could be characterized with the model in Chapter 8 using different sets of parameters.

## 9.2 Future Work

The new extensions to the *SAMPLE* program described in this thesis are powerful tools for studying electron-beam lithography. Issues such as exposure induced heating, process optimization, and mechanisms of chemically-amplified resists, and modeling of the

interrupted development of an IBM DQN resist have been examined using the *SAMPLE* program and these extensions. Yet further improvement in the characterization, modeling approaches, and simulation can be suggested.

The applications of the transient temperature simulation program were only partially explored. Its accuracy as a modeling tool could also be improved. The heat source could be modeled more accurately by convolving an energy matrix of Monte Carlo spatial distribution with the exposure pattern. The domain of the simulation could be increased to include temperature calculation in the substrate especially for underlying high atomic weight materials. Important thermodynamic processes such as the increase in the thermal conductivity of the resist with increasing temperature and the uptake of energy during the phase transition of the resist should also be considered. New techniques should be developed to determine these parameters experimentally.

A more accurate development rate measurement technique for slowly developing resists could improve the accuracy of the dissolution rate model. The optical reflectivity measurement technique has a fundamental limitation such that a minimum of two extremes must be collected before any thickness calculation can be made. Consequently, resists with dissolution rates less than 1 Å/sec cannot be determined unless extremely long development times are used. Other development monitoring techniques such as the quartz crystal microbalance or the multiple wavelength interferometry can overcome this problem. In addition, these techniques require less data processing than the sinusoidal reflectivity measurements of DRM, and therefore, are less susceptible to the introduction of errors during the conversion of the raw reflectivity signals to thickness versus development time data.

With the variety of dissolution rate models needed to simulate the state-of-the-art resist technologies, a parser which can accept the dissolution rate equation as input should be implemented in *SAMPLE* to improve the flexibility of the program. For example, the EEMB dissolution rate model and DQN resist dissolution model differs substantially. With the current *SAMPLE* program, these functions have to be hard coded in the program and the parameters specified in the input for these functions seldom reflect the processing conditions used in the simulation. In order to fully accommodate models such as the EEMB dissolution model, the parser should be able to let user define functions which relate the parameters in the rate functions to the processing variables. For example, for the SAL-601-ER7 resist, one possible way to let the user define the rate functions is illustrated here:

```
eblfundef R0 = (15.9 - 0.45 * Temp - 0.31 * time + 7.1 * C
               -0.28 * C^2 - 0.32 * Temp * time + 2.5 * B)^2;
eblfundef E0 = 207 - 35.4 * Temp + 9.0 * Temp^2 - 7.7 * time
               + 13.3 * C - 19.2 * B;
eblratdef R0 / (1.0 + (E / E0)^1.5)^31;
eblvardef Temp 120 time 90 C 0.27;
ebldevelop;
```

Here, the `eblfundef` command defines  $R_0$  and  $E_0$  which are functions of PEB temperature (Temp), time (time), and developer concentration (C). The `eblratdef` command then defines the rate function in terms of  $R_0$  and  $E_0$ . Next, the processing variables are specified in the `eblvardef` statement. If a different PEB condition is used, then only the `eblvardef` statement needs to be changed.

Similarly, the “cage effect” model can also be defined using the following statements:

```
eblfundef k1 = 4.3e9 * exp (- 0.694/(8.62e-5 * T));
eblfundef k2 = 1.7e5 * exp (- 0.370/(8.62e-5 * T));
eblfundef C0 = 0.25 * (1 - exp(D / 0.95));
eblfundef Ca = E;
eblfundef Xe = k2 * Ca^0.5;
```

```

eblfundef temp1 = exp(-(1 - Xe) * k1 * time * Ca^1.42 / Xe);
eblfundef temp2 = (1 - C0)/(1 - C0/Xe);
eblfundef temp3 = (1 - C0)/(Xe - C0);
eblfundef C = (temp1 - temp2)/(temp1 - temp3);
eblfundef CE = 15 * C^2 - 20 * C^3 + 15 * C^4
              - 6 * C^5 + C^6;
eblratdef 550 / (1.0 - CE/7.5)^6.5;
eblvardef Temp 120 time 90;
ebldevelop;

```

In this case,  $C$  is the normalized extent of the crosslinking reaction,  $C_0$  is the initial crosslinking,  $C_a$  is the acid concentration, and  $CE$  is the number of crosslinking events. This set of commands is a more complicated example but it demonstrates the flexibility of the user-specified functions. Since most of the function definitions are involved in the calculation of the parameters in the dissolution rate function, they would not degrade the performance of the program significantly if care are taken to avoid repeatedly calling these user-defined functions. Although the implementation to be compatible with the existing FORTRAN code will be quite difficult, the effort is well justified for the advantage gained with this new parser.

The results from the experiments of the interrupted development of the IBM DQN resist suggest that the dissolution of the resist is a strong function of the strength of the developer which reaches the resist profile surface. The increase in bias of the resist profiles when the development technique changed from dip to spray is another possible indication of this effect. As a result, a dissolution model which takes transport phenomena into account could be an improvement over the dissolution rate function of absorbed energy alone. This approach has recently been demonstrated by Ushirogouchi *et al.* [1]. A dissolution model based on the diffusion of developer ions and ionized resin molecules could be used to explore the mechanism of the formation of the surface induction layer such as the closing of the diffusion channels after the interruption treatment.

*SAMPLE* produces, principally, the two-dimensional cross-sections of line-edge profiles exposed with one-dimensional electron beams. In order to explore the interactions of electron-beam induced heating and proximity effects, three-dimensional (3-D) simulations of the exposure, heating and development processes are needed. Fortunately, many simulation modules such as the 3-D Monte Carlo simulation [2], the 3-D heat equation solver, and the 3-D resist etching algorithms [3][4] have already been developed. All that is required is a pattern generator which can take the exposure patterns and perform the convolution with energy matrix. For more sophisticated resist kinetics with no closed-form solution or simulation of the diffusion of catalyst during the post-exposure bake of a chemically-amplified resist, the algorithm for solving advanced resist kinetics developed by Ferguson in the *SAMPLE-ARK* program [5] could also be included. The combinations of these features would provide a major advancement in the simulation of electron-beam lithography.

### 9.3 A Final Perspective

The goal of establishing quantitative characterization methods and a mechanistic foundation to support resist profile simulation and processing optimization of the state-of-the-art e-beam lithography has been attained. The new extensions to the *SAMPLE* program increase the range of profile modeling capability of the program with both empirical and mechanistic models. From a process development engineer's point of view, the EEMB dissolution rate model should provide an efficient and robust model for the optimization of resist processing. The mechanistic models for chemically-amplified resists and interrupted development are hopefully also of immediate use to the process engineer. From a resist engineer's point of view, the understanding from the mechanistic nature of these modeling approaches should also aid in the development of lithographic materials. It is hoped that these extensions will contribute to the further advance of electron-beam lithography.

## References

- [1] T. Ushirogouchi, Y. Onishi, and T. Tada, "Resist Profile Simulation for Photoresist Composition Optimization," *J. Vac. Sci. Technol. B*, vol. 8, no. 6, pp. 1418-1422, Nov/Dec 1990.
- [2] E. W. Scheckler, N. N. Tam, A. K. Pfau, and A. R. Neureuther, "An Efficient Volume-Removal Algorithm for Three-Dimensional Lithography Simulation with Experimental Verification," Submitted to *IEEE Trans. on CAD*, 1991.
- [3] Kenny K.H. Toh, "Algorithm for Three-Dimensional Simulation of Photoresist Development," *Ph.D. Dissertation*, Department of Electrical Engineering and Computer Sciences, University of California, Berkeley, 1990.
- [4] Edward W. Scheckler, "Algorithms for Three-Dimensional Simulation of Etching and Deposition Processes in Integrated Circuit Fabrication," *Ph.D. Dissertation*, Department of Electrical Engineering and Computer Sciences, University of California, Berkeley, 1991.
- [5] Richard A. Ferguson, "Modeling and Simulation of Reaction Kinetics in Advanced Resist Processes For Optical Lithography," *Ph.D. Dissertation*, Department of Electrical Engineering and Computer Sciences, University of California, Berkeley, 1991.